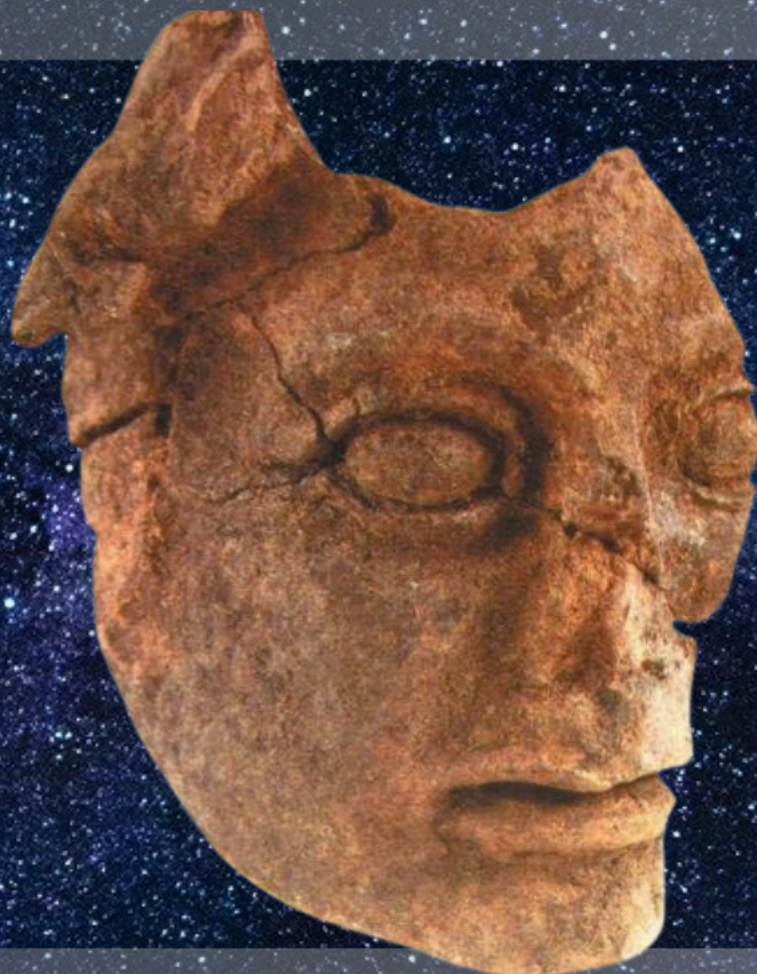




Istituto Nazionale di Fisica Nucleare
LABORATORI NAZIONALI DI FRASCATI

FRASCATI PHYSICS SERIES



VULCANO 2022 **Frontier Objects in Astrophysics and Particle Physics**

Editors:

Antonella Antonelli, Roberto Fusco Femiano, Aldo Morselli, Gian Carlo Trinchero

VULCANO Workshop
Frontier Objects in Astrophysics and Particle Physics
2022

FOREWORD

The 18th edition of the Vulcano workshop: Frontier objects in Astro-physics and Particle Physics was organized jointly by the National Institute for Nuclear Physics (INFN) and the National Institute for Astrophysics (INAF). The workshop was held in the Conference Room of the Hotel del Golfo (Elba Island, Toscana, Italy) from September 25th to October 1st and was attended by more than 80 scientists world wide. We were particularly glad to have been able to organize this edition of the workshop in presence after that the previous edition 2020 was cancelled for Covid. This edition was held in Elba Island and not in the Vulcano Island for several reasons. One of these is because of the increased activity of the volcano in the Vulcano Island. This workshop is certainly one of the first that since 1986 has the aim to gather people from High Energy Astrophysics and Particle Physics to discuss the most recent highlights in these fields. Since the 80s the Universe has been regarded as a great particle accelerator to test the Grand Unified Theories ideas. Of course a machine hard to use because most the experiments happened only once, a long time ago. Today, the astro-particle connection is probed everyday by underground accelerators and spacecrafts. As never before, these two fields of knowledge complement and integrate each other. The discovery of new particles may unveil some cosmic mysteries, conversely, astrophysical observations may give new information on the infinitely small. In the last years, several observations have triggered a fruitful collaboration between scientists from particle physics and astrophysics: in August 2017 gravitational waves have been detected by LIGO and VIRGO due to Neutron Stars coalescence accompanied for the first time by electromagnetic emission. These observations are considered the act of birth of a new era for astrophysics, the multimessenger astronomy. Then IceCube observed a high energy neutrino in coincidence with a flaring blazar and accompanied by gamma rays emission, and other events likely associated to supernovae. These detections are considered the beginning of the neutrino astronomy thereby enlarging the field of the multimessenger astronomy. These two windows will help us to deepen further our knowledge of the universe, In the next decades this new season for physics and astrophysics with simultaneous observations with the most advanced astronomical instruments and particle detectors will bring us to many discoveries that we can barely imagine now, and that we hope to discuss in the next editions of the Vulcano workshop. The final scientific program was selected by the Scientific Organizing Committee, chaired by Antonella Antonelli (INFN) and Roberto Fusco-Femiano (INAF), and composed by: Simone DellAgnello (INFN), Pino Di Sciascio (INFN), Nicola Menci (INAF), Aldo Morselli (INFN), Luigi Piro (INAF), Marco Ricci (INFN), Gian Carlo Trinchero (INAF), and Francesco Vissani (INFN). The Local Organizing Committee was composed by Antonella Antonelli, Maria Cristina DAMato (INFN), Roberto Fusco-Femiano, and Lia Sabatini (INFN) with the precious help of Alessio Gorgi (INAF). A special thank to Maria Cristina DAMato and Lia Sabatini to whom a large part of the compliments received from the participants are due, for the precious work done in the preparatory phase, during and after the conclusion of the eighteenth edition of the workshop.

Antonella Antonelli and Roberto Fusco-Femiano

CONFERENCE PROGRAM

GRAVITATIONAL WAVES AND MULTIMESSENGER ASTRONOMY

E. Troja	Multiwavelength Observations of Afterglow of GW counterparts (GW170817)
M.A. Papa	Gravitational Waves: Recent Results
F. Ricci	Gravitational Waves with the Interferometer Detectors on the Earth
M. Punturo	Einstein Telescope: Science, Technologies and Perspectives
H. Van Eeerten	Relativistic Jets and Gamma-Ray Bursts from Neutron Star Mergers
M. Della Valle	Observations of Kilonovae and Theoretical Implications
I. Di Palma	Core-Collapse Supernova Detection: a Deep Learning Approach
P. Ubertini	Integral Observations of GW and Transient Phenomena
S. Mastrogiovanni	Implications for Cosmology following Recent Gravitational Wave Observations
A. Mangiagli	LISA-Athena Synergy for Detecting GW and HE Counterparts of Supermassive Binary BH Mergers
S. Katsanevas	GW Detection at the Moon
L. Piro	Athena Multimessenger Science
R. Peron	METRIC: an Italian Proposal for an Atmosphere/Gravity/Geodesy small Mission in LEO
L. Porcelli	Three Lunar Laser Ranging Mission in 2023-2024 by NASA, ESA and CNSA for Precision Test of General Relativity

ASTROPHYSICS AND COSMOLOGY

R. Jimenez	Do We Understand the Universe?
B. Allen	Will Pulsar Timing Arrays Observe the Hellings-Downs Correlation Curve??
S. Fabiani	First Results from IXPE
C. Pittori	New Results from AGILE
F. Panessa	Massive BH in AGNs: Multiwavelength Observations
R. Iuppa	The CSES Space Missions for Investigating the near-Earth Electromagnetic Plasma and Particle Environment Hot Filamentary Large Scale Structures in the Universe
F. Nicastro	Hot Filamentary Large Scale Structures in the Universe
D. Jones	Searching for New Physics with Local Measurements of the Hubble Constant
A. Fontanai	Exploring the Frontiers of Astrophysics with JWST END
S. Bhandari	Recent Developments of Fast Radio Bursts
A. Moiseev	New Mission Concept: Compton Telescope with Coded Aperture Mask and its Science Perspectives
E.S. Battistelli	Status of Cosmic Microwave Background Observations for the Search of Primordial Gravitational Waves
L. Graziani	First Stars in the Universe

COSMIC RAYS AND GAMMA RAYS

M.Teshima	Status of the CTA LST Project
L. Olivera Nieto	Highlights from Gamma Ray Atmospheric Cherenkov Telescopes
F. Longo	The Cherenkov Telescope Array: Status and Perspectives
E. Bissaldi	GRB at High Energies
R. Sparvoli	Recent Results on Cosmic Ray Direct Observation

F. Alemanno	Measurement of Cosmic Ray Spectra with DAMPE and Prospects with the HERD Space Mission
Z. Cao	LHAASO Results
O. Tibolla	High Altitude Water Cherenkov Observatory (HAWC): Recent Results
U. Barres de Almeida	Status of the Southern Wide-Field Gamma-ray Observatory (SWG0)
M. Unger	UHE Cosmic Ray Observations
J. Hoerandel	Radio Detection of Cosmic Rays
S. Celli	Hadronic Pevatrons (and their Radiation Signatures)
M. Kachelriess	Extragalactic Cosmic Ray Sources
J. Vink	What Sources are the Dominant Galactic Cosmic-Ray Accelerators?
H. Yan	Cosmic Ray Transport in Interstellar Turbulence

NEUTRINO

V. Hannen	First Sub-eV Neutrino Mass Limit from the KATRIN Experiment
S. Bertolucci	Neutrino Physics at FNAL
M. Agostini	Present and Future of Neutrinoless Double Beta Decay
D. D'Angelo	Results from Borexino
F. Sanchez	Long-baseline Neutrino Oscillations Review
J. Cao	Reactor Neutrino Experiments Review
A. Capone	HE Nu Experimental Status
E. Lisi	Phenomenology of neutrino Oscillations
A. Lamastra	Models of Neutrino Sources
S. Buson	Beginning a Journey Across the Universe: The Discovery of Extragalactic Neutrino Factories
R. Stein	Neutrinos and Tidal Disruption Events

DARK MATTER AND DARK ENERGY

M. Selvi	Dark Matter Direct Detection Review
M. Vecchi	Intriguing Hints from Indirect Dark Matter Searches
S. Capozziello	A Cosmographic Outlook on Dark Energy and Modified Gravity
R. Scaramella	EUCLID, Mapping the Geometry of the Dark Universe
D. Gilman	Constraints on Dark Matter from Gravitational Lensing
M. Castellano	Constraints on Dark Matter From Reionization
V. Gammaldi	A review of Multiple Dark Matter Signatures: Indirect Searches and Machine Learning
P. Santini	Constraints On Dark Energy From The Abundance Of Massive Galaxies
F. G. Saturni	Measuring The Dark Matter Content of Dwarf Spheroidal Galaxies
L. Covi	Theory Introduction on Dark Matter Models
F. Kuhnel	Primordial BHs and Dark Matter
E. Skorda	Dark Matter Search at LHC
P. Branchini	Recent Dark-Sector Results at Belle II
J. Jerhot	NA62 Results on Dark Sector Searches
P. Valente	PADME Results and Perspectives
C. Gatti	Search for Axion Dark Matter
P. Camarri	Searches for Ultra Long-Lived Particles

PARTICLE PHYSICS

- E. Goudzovski Search for New Physics in Kaon Decay
R. Quagliani Search for New Physics in B Meson Decay
M. Incagli New Physics Search in High Precision Measurements: the Muon $g - 2$ Factor

FUTURE PROJECTS

- E. Cavazzuti ASI Future Programs in Astrophysics and Fundamental Physics
R. Tenchini Future INFN Projects in Particle Physics at Accelerators
R. Scaramella INAF Scientific Projects and Future Programs

Slides are available at:

<https://agenda.infn.it/event/30175/contributions/>

**FRONTIER OBJECTS IN ASTROPHYSICS AND PARTICLE PHYSICS
CONFERENCE PROCEEDINGS**

F. Ricci	Gravitational Waves with the Interferometer Detectors on the Earth	1
H. Van Eerten	Relativistic Jets and Gamma-Ray Bursts from Neutron Star Mergers	15
S. Mastrogiovanni	Implications for Cosmology following Recent Gravitational Wave Observations	27
E. Battistelli	Status of Cosmic Microwave Background Observations for the Search of Primordial Gravitational Waves	47
B. Allen	Will Pulsar Timing Arrays Observe the Hellings-Downs Correlation Curve?	65
A. Moiseev	New Mission Concept: Compton Telescope with Coded Aperture Mask and its Science Perspectives	81
L. Olivera Nieto	Highlights from Gamma Ray Atmospheric Cherenkov Telescopes	97
O. Tibolla	High Altitude Water Cherenkov Observatory (HAWC): Recent Results	107
U. Barres de Almeida	Status of the Southern Wide-Field Gamma-ray Observatory (SWG0)	123
S. Celli	Hadronic Pevatrons (and their Radiation Signatures)	137
J. Vink	What Sources are the Dominant Galactic Cosmic-Ray Accelerators?	153
A. Lamastra	Models of Neutrino Sources	169
M. Vecchi	Intriguing Hints from Indirect Dark Matter Searches	179
S. Capozziello	A Cosmographic Outlook on Dark Energy and Modified Gravity	193
PM. Castellano	Constraints on Dark Matter From Reionization	209
V. Gammaldi	A review of multiple dark matter signatures: indirect searches and machine learning	225
P. Santini	Constraints On Dark Energy From The Abundance Of Massive Galaxies	239
F. G. Saturni	Measuring The Dark Matter Content of Dwarf Spheroidal Galaxies	253
J. Jerhot	NA62 Results on Dark Sector Searches	269
P. Valente	PADME Results and Perspectives	285
C. Gatti	Search for Axion Dark Matter	295
P. Camarri	Searches for Ultra Long-Lived Particles	307
M. Incagli	New Physics Search in High Precision Measurements: the Muon $g - 2$ Factor	323

GRAVITATIONAL WAVES WITH THE INTERFEROMETER DETECTORS ON THE EARTH

Fulvio Ricci

*Sapienza Università di Roma, INFN Sezione di Roma, Roma, Italy
on behalf of the LIGO-Virgo-KAGRA collaborations*

Abstract

We present the plans for upgrading the Gravitational Wave detectors on the Earth in view of the next observation run O4 planned to start in 2023. Then, we highlight the main results obtained during the previous three observation runs. We conclude focusing on the future evolution of these detectors in the next decades.

1 Introduction

To detect gravitational waves emitted by stellar compact objects, large-scale laser interferometers are organised to compose a global network of advanced detectors. Two LIGO interferometers in USA are located, the first in Livingstone (Louisiana) and the second in Hanford (Washington state); Virgo is in Cascina, near Pisa in Italy and KAGRA is the new Japanese detector, which

started to be operative in 2015. KAGRA is installed in two orthogonal galleries, 3 km long, excavated near Kamioka in the Gifu prefecture. The KAGRA location is near the caverns hosting the neutrino detectors Super-Kamiokande and Hyper-Kamiokande, the first in operation in the Kamioka mine and the second under construction in the Tohibora mine.

The network of GW interferometers has the advantages to better define the location of the sources emitting transient GW signal, to disentangle the polarisation components of the GW signal and increase further the event detection rate by improving the network duty cycle. In 2015, the first gravitational-wave signals were detected by the two US Advanced LIGO instruments, and two years later the network LIGO-Virgo permitted to pinpoint in the sky the binary neutron star coalescence, then observed across the whole electromagnetic spectrum by a impressive numbers of astronomical detectors on the Earth and in the space, opening the era of the multi-messenger astronomy. At present, the catalog of events detected by the network accounts for 90 signals that, as we will see in the next section, have already a significant impact on several fronts in fundamental physics and astrophysics. The advanced GW interferometers alternate periods of time devoted to observation to upgrade phases for improving the detector sensitivity. A gain of a factor 2 on the minimum detectable value of GW strain expands the explored volume of the Universe of a factor 8, and as consequence, increases the detection rate of the GW signals. At the time of writing this article, all the detectors are preparing the new observation run O4 that will start in 2023 and in the following section we highlight the most significant changes of the experimental set-ups for LIGO, Virgo and KAGRA .

2 LIGO, Virgo and KAGRA Upgrades

In general, the planned hardware changes are different for LIGO, Virgo and KAGRA. However, some strategic choices are in common as the injection through the output port of the interferometer an electromagnetic (e.m.) vacuum with a frequency dependent squeezing. During the last run O3 ended in 2020, a *phase* quadrature squeezed vacuum was successfully utilised in LIGO and Virgo, allowing for a 3 dB quantum noise reduction above ~ 100 Hz. However, at the same time, the low frequency quantum noise originating from *amplitude* quadrature vacuum fluctuation was increased due to the Heisenberg uncertainty principle, potentially spoiling the limit of the low frequency noise budget. To

have a reduction of the optical noise on the entire detection bandwidth, the use of frequency dependent squeezed vacuum is required. It will allow to preserve the low-frequency sensitivity even when the light power stored in the cavity will be increased, a standard approach to gain in sensitivity at high frequencies (see fig 1). Preserving the low-frequency sensitivity will guarantee the possibility to observe binary black holes (BBHs) with higher masses and collect signals emitted in the far Universe.

The frequency dependency is obtained by reflecting the squeezed vacuum (generated outside the main GW interferometer) from a Fabry-Perot filter cavity having low optical losses. The rotation of the ellipse representing the combined phase and amplitude fluctuations of e.m. field in the quadrature space, was obtained for the first time in the MHz region in 2005 ¹⁾ and then it has been observed in the kHz region in the LIGO laboratory of the Massachusetts Institute of Technology ²⁾. At present both LIGO and Virgo are implementing this technique in their detectors. The task is not simple: the interface between the squeezing system and the interferometer requires optical junction benches, both to inject the beam into the cavity and send it to the bench hosting the detection photodiodes. Losses and stray light in the filter cavity as in the whole optical set-up must be limited.

Moreover, the list of the other planned upgrades for all the detectors is long: here we will present for each detector just an incomplete list.

2.1 LIGO

LIGO has set for O4 the sensitivity goal for the two US interferometer to achieve an horizon range of 160 to 190 Mpc for the detection 1.4-1.4 coalescent binary neutron stars (BNS). To fulfil this goal it is needed to:

- reduce or even eliminate inhomogeneous coating absorption in the mirrors acting as test masses, by replacing one of them in the interferometer installed in Hanford and all the test masses in Louisiana;
- change the pre-stabilised lasers in the two LIGO detectors. The new light sources will provide 140 W output into the interferometer;
- achieve a value of 400 kW for the light power stored in the arm cavities;
- deploy many baffles to minimise stray light;

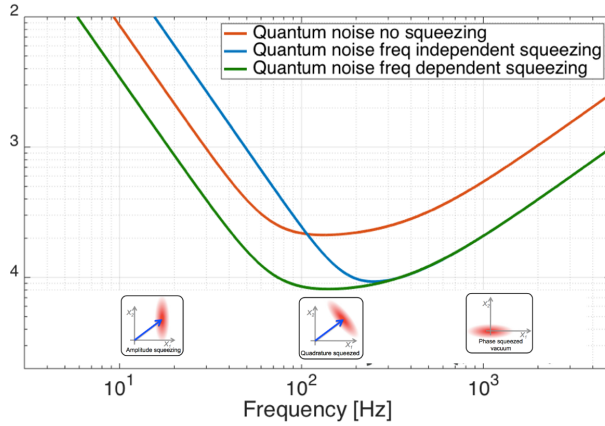


Figure 1: Comparison of the sensitivity gain of the interferometer in the three configurations: without squeezing (red curves), with frequency independent squeezing (blue curve) and with an optimised frequency dependent squeezing (green curve).

- install a new Faraday isolator for reducing the optical loss at the output port of the interferometer;
- implement adjustably deformable mirrors in the output port to tune up and maximise the matching of the beams in the output mode cleaner and in the filter cavity of the squeezing system.

The installation of the new hardware is completed; the following step is the commissioning of the detector and the noise hunting.

2.2 Virgo

The Virgo sensitivity goal is to achieve a horizon range of 80 - 110 Mpc, for the detection 1.4-1.4 coalescent binary neutron stars (BNS). The main innovation for Virgo is the installation of the signal recycling at the interferometer output. This is a significant change in the optical configuration: it implies a deep review of the control strategy of the whole interferometer. The signal recycling allows

the resonance of the whole interferometer to boost the detector sensitivity in the desired frequency interval. The reflectivity chosen for the signal recycling mirror determines the sharpness of the tuning: the present choice concerns the detection of signals from coalescing BBH and BNS. As for LIGO, the list of the other upgrades is long and here we report just few of them:

- a new output mode cleaner is installed with reduced optical loss;
- the payload of the input mode is new and it is equipped with instrumented baffles to mitigate and monitor the stray light;
- the thermal compensation system has been reviewed and upgraded;
- an array of several velocimeters has been deployed close to the vacuum chambers hosting the end test masses of the interferometer. The scientific target is to develop a method to subtract the Newtonian noise arising from terrestrial gravity fluctuations from the interferometer data. The Newtonian noise is affecting the detector bandwidth below 20 Hz. The success of this method will increase the chance to detect the continuous GW signals emitted by rotating NS and to increase the detection rate of BBH at higher masses.

2.3 KAGRA

The O4 goal is less ambitious than LIGO and Virgo: KAGRA started the first operation in 2015 and it is improving progressively the detector sensitivity. The detector has been designed to include new technological features: KAGRA is located in an underground environment to reduce the seismic noise and it makes use of cryogenic techniques to cool the mirrors in the range of 20 K. They have installed a 30 W laser at the input of the interferometer and they plan to start the run having replaced the signal recycling mirror and with the Fabry-Perot mirrors (acting as test masses of the space-time metric) at room temperature. In the second part of the run they plan to cool down the mirrors to improve the sensitivity in the low frequency region and even increase the power laser. As for LIGO and Virgo, KAGRA has a dedicated plan for deploying several baffles to minimise the stray light.

Table 1: *Table 1: Estimated ranges of the merge rates for BBH, NSBH and BNS ⁴⁾*

BBH	17.9 – 44	$\text{Gpc}^{-3} \text{yr}^{-1}$
NSBH	7.8 – 140	$\text{Gpc}^{-3} \text{yr}^{-1}$
BNS	10 – 1700	$\text{Gpc}^{-3} \text{yr}^{-1}$

3 The Gravitational Wave Observations

The GW events detected in the previous run of the network are collected in the catalog GWTC-3 ³⁾. It contains a total of 90 signals: 11 events from the first and second observing runs (O1 and O2), 44 from the first part of O3 and 35 from the second part. It includes BBH events plus two BNS events, 3 coalescences of neutron star - black hole (NSBH) and 1 event with the companion mass to be classified in between neutron star (NS) and black hole (BH). These observations are used to predict both the extrinsic and intrinsic properties of the GW sources. Extrinsic properties describe how we observed the event from Earth, i.e. the location of the source on the sky, its distance from the Earth, and the orientation of the plane in which the two compact objects orbit around one another. The extrinsic parameters and the intrinsic ones (as masses, spins and deformability of the compact objects), are derived on statistical basis (mainly via a Bayesian approach) by defining the 90% region where the inferred values of the source parameters are compatible with the data. In the following subsections, we will highlight some of the results obtained by analysing these data. They are related to studies on the population of compact objects, fundamental physics and search for primordial black holes.

3.1 Populations Studies

In the table 1 we report the merger rates for the three categories of compact objects as derived on the base of the actual observations reported in the catalog GWTC-3 and published in ⁴⁾. The intervals of the BNS and NSBH merger rates are estimated with a large uncertainty because of the poor number of events available: here it was assumed a constant rate density versus co-moving volume and it was taken the union of 90% credible intervals for all the methods

used in this analysis. For the BBH merger, the rate interval is computed at a redshift $z = 0.2$, accounting for the evolution of the merger rate to with redshift z , while it changes slightly as $\sim (1+z)^{2.7}$.

A large fraction of the BBH events are related to binary systems with mass ratio q near 1. Indeed, two events, GW190412 and GW190814, have $q = 0.28_{0.06}^{+0.12}$ and $q = 0.112_{-0.009}^{+0.008}$ respectively. In addition, the secondary mass of the system emitting the GW198014 results to be $M_2 = 2.59_{-0.09}^{+0.08} M_\odot$: a BH mass value is much lower than those of the galactic X-ray binary population or a NS mass too high asking for a significantly high spin to be compatible with the NS hypothesis.

The study of the spin distribution should help to discriminate among the various formation scenarios of these binary systems. For example, the dynamical formation of BBHs requires a dense stellar environments where the original binary system interacts with a third body, which replaces one of the binary components. Simulations show that the dynamical exchange involved in this process, is compatible with a random distribution of the spin directions for the final states. The BBH formation in isolation, a scenario complicated by several different processes occurring during the evolution of the system, pushes toward the observation of binary systems with spins well aligned to the orbital angular momentum and nearly zero orbital eccentricity.

The spin distribution of the BBH population is obtained by marginalising (in a statical sense) over the joint estimate of the mass and spin distribution $P(m_1, m_2, \chi_1, \chi_2)$, where m_i , $i = 1, 2$ are the masses and χ_i , $i = 1, 2$ the adimensional spins of the two compact objects. We have to note also that the inference of the spin population is affected by a selection bias, because BBHs with high, aligned spins can be observed at greater distances (at fixed distance and equal masses, the spin aligned events can be detected at higher signal to noise ratio). What we can conclude on the base of the present data, is that the spin distribution seems to advocate for a multiple formation scenario.

3.2 Fundamental Physics

Another interesting aspect one can probe are GW polarisations. In GR, there are only two tensor polarisation modes, which are typically decomposed as plus and cross modes (see fig. 2).

In theories beyond GR, two scalar polarisation modes (breathing and longi-

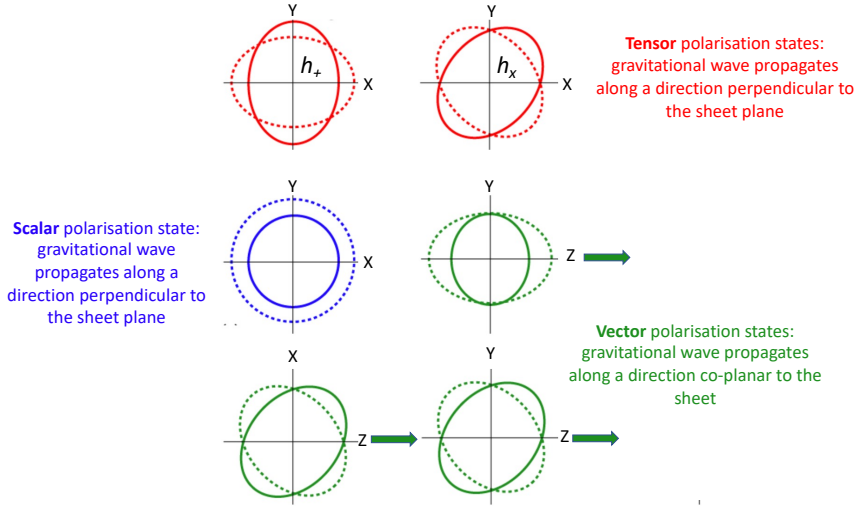


Figure 2: *General Relativity predicts the existence of two fundamental states of polarisation, the tensor modes h_+ and h_\times . Other theories of gravitation include four extra modes, scalar and vector ones* ⁵⁾.

tudinal) and two vector modes can exist in addition. Examples of breathing modes are reported in blue in the fig. 2. The LVC has used GW170817 and carried out a model selection analysis among three different models: tensor only, vector only, and scalar only models. It was found ⁶⁾ that a fully tensor wave was significantly preferred from the data over the other two hypothesis, consistent with the GR prediction. KAGRA has recently joined the collaboration and started its operation. This additional detector will help to further test additional polarisations. For example, one will be able to compare the tensor-only model against tensor + scalar model, the most popular hypothesis among the alternative theories of gravity.

The speed of gravitational waves in the general theory of relativity is equal to c , the light speed in a vacuum. In alternative theories of gravity often the dispersion relation is not as simple and a difference between c and the GW

propagation velocity v_{GW} should appear at some orders of the measurement accuracy.

In August 2017, the LIGO and Virgo detectors received the GW170817 signal. Data have been interpreted as due to the coalescence of two neutron stars located at a distance between 26 to 49 Mpc from Earth. Later the location was confirmed in the shell of the elliptical galaxy NGC 4993. The chirp mass of the system was extracted from the data resulting to be $1.188^{+0.004}_{-0.002} M_{\odot}$. The masses of the component stars have greater uncertainty. The larger (has a 90% chance of being between 1.36 and 2.26 M_{\odot} , and the smaller has a 90% chance of being between 0.86 and 1.36 M_{\odot} . 1.7 seconds after the GW merger signal, a short (2 seconds duration) gamma-ray burst, designated GRB 170817A, was detected by the Fermi and INTEGRAL spacecrafts: the gamma ray detection confirmed roughly that the e.m. burst was coming from the same patch of the sky pointed by the LIGO-Virgo network.

The delay between the e.m. and GW signals and the large distance between the Earth and the galaxy NGC 4993, provided the strong limit on the difference between the speed of light and that of gravity:

$$-3 \cdot 10^{-15} < \frac{v_{GW} - c}{c} < +7 \cdot 10^{-16}$$

Later , this results was revisited 7) to give the upper limit on the graviton mass:

$$m_g < 1.76 \cdot 10^{-23}$$

3.3 Primordial Black Holes

Apparently there is no mechanism for the formation of ultracompact objects with masses $< 1 M_{\odot}$ within the standard model of particle physics and the Λ CDM cosmological model or at least this is a controversial point. A possibility to have black holes with masses accessible to ground based interferometers is that they could have formed deep in the radiation era of the Universe from the prompt collapse of large primordial over-densities on the scale of the early time Hubble volume 9) 10). In addition, it has been argued, on the base of micro-lensing observations, that the primordial black holes (PBH) outside the mass range of $0.05 M_{\odot} \lesssim M \lesssim 0.45 M_{\odot}$ cannot contribute significantly to explain the dark matter mystery 8). Other constraints have been set on the PBH existence. PBHs lighter than $\sim 10^{15}$ g , which have not evaporated yet

or are in the final state of evaporation by the Hawking radiation, leave some signals from which an upper limit on their PBH abundance can be placed. They can change the abundance of the light elements produced by the big bang nucleosynthesis ($10^9 g < M_{PBH} < 10^{13} g$), extragalactic photon background ($10^{14} g < M_{PBH} < 10^{15} g$), and damping of the CMB temperature anisotropies on small scales by modifying the cosmic ionisation history ($10^{13} g < M_{PBH} < 10^{14} g$). By comparing these effects with observations, upper limits on the PBH fraction for various PBH mass can be obtained (under specific assumptions of their mass function) ^{11), 12)}. Except for the constraints from the entropy production and the primordial helium abundance, these limits are severe in the sense that they allow only a tiny fraction of PBHs in dark matter at any cosmic time before the PBHs evaporate.

Nevertheless, the search of PBH as dark matter contributors gained attention ¹⁴⁾ and, since the detections of gravitational waves is a novel tool to observationally search for PBHs complementary to the electromagnetic waves, we expect to make significant progresses even on this domain (for a comprehensive review of this topic see ¹³⁾). The existence of sub-solar-mass black holes would be considered to be a definitive proof that they were produced in the primordial Universe, as stellar evolution cannot produce black holes below about $3 M_{\odot}$.

To date, searches have been performed for sub-solar-mass black holes, but no detection has been made so far, leading to some of the best upper limits on the fraction of dark matter in black holes of mass $0.2 - 1.0 M_{\odot}$ ¹⁵⁾. In ¹⁵⁾, assuming a particular primordial black hole (PBH) formation model, it has concluded that a population of merging $0.2 M_{\odot}$ black holes can account for less than 16% of the dark matter density and a population of merging $1.0 M_{\odot}$ BHs can account for less than 2% of the dark matter density.

4 Future plans

Using as figure of merit the horizon of standard coalescent BNS events at a signal to noise ratio equal to 8, the final goal is to go from 60 Mpc achieved in O3 to 260 Mpc target for O5. Moreover, we must say that the present GW facilities have the potentiality to get a further increase in sensitivity for an extra factor 2 in amplitude. The instrumental set-up in a post O5 run can include larger light beams impinging on the Fabry-Perot mirrors acting as

test masses of the space-time geometry. These mirrors will have heavier masses with monolithic suspensions and better low-loss coatings. The combination of these actions, with a robust campaign to reduce the technical noises mainly affecting the sensitivity at low frequency, will permit to reduce the intrinsic limit due to the thermal noise. In addition higher light power can be stored in the arm cavities and improvements can be implemented on the readout scheme, detection benches seismically isolated and under vacuum. Newtonian noise subtraction will be implemented, improving further the low frequency region.

This sensitivity increment will permit to discover and characterise thousands of BBH events per year such to increase our understanding of the black hole population in the Universe and achieve new fundamental physics results.

Despite the amount of scientific results produced with GW170817, this event remains the only conclusive multimessenger observation with GWs to date. The increase in the detector sensitivity will multiply the chance to observe this category of events, enhancing our understanding of the inner core of neutron stars. Another class of multimessenger observation, reach of physics information, will be the detection of GWs in connection with e.m. and neutrino emissions from a core collapse supernova. Although the event rate is low for an observation limited to the local group of galaxies, even the joint detection of one event, will be a huge boost in our understanding of the explosion mechanism. In fact, despite the huge theoretical effort done in the simulation domain, the supernova explosion is far to be fully understood: the only direct measurement, guiding in a sense the simulation efforts of the core engine of the explosion, comes from SN 1987A. Neutrinos and GWs leave the core around the time of collapse and a joint detection of the two messengers will probe directly the inner dynamics of the SN process: neutrinos will allow us to probe mainly the thermodynamics of the collapse and from the GW data we will infer the matter dynamics.

The post-O5 plans are under preparation: they are conceived for extending the life of the network of the advanced detectors at least up to 2040. At that time the network will include also the LIGO-India detector, which is now under construction. The GW observations of the Earth based interferometers will continue to produce results, paving the way of the future detectors as Einstein Telescope and Cosmic Explorer, able to explore the whole Universe.

5 Acknowledgements

The author gratefully acknowledge the support of the Italian National Institute of Nuclear Physics - INFN for the support to attend the conference.

References

1. Chelkowski S., Vahlbruch H., Hage B., Franzen A., Lastzka N., Danzmann K. and Schnabel R., *Experimental characterization of frequency-dependent squeezed light* Phys. Rev. A **71** 013806 (2005)
2. Oelker E. , Isogai T., Miller J., Tse M., Barsotti L., Mavalvala N. , Evans M. *Audio-Band Frequency-Dependent Squeezing for Gravitational-Wave Detectors* Phys.Rev.Lett. **116** 041102 (2016)
3. Abbott B.P. et al. *GWTC-3: Compact Binary Coalescences Observed by LIGO and Virgo During the Second Part of the Third Observing Run.* arXiv 2021, arXiv:2111.03606
4. Abbott B.P. et al. *The population of merging compact binaries inferred using gravitational waves through GWTC-3* arXiv 2022, arXiv:2111.03634v4, Accepted for publication on December 2022 in Physical Review X
5. Will, Clifford M. *Theory and experiment in gravitational physics.* 2nd Edition. Cambridge: Cambridge University Press. (1981)
6. Abbott B. P. et al. *GW170814: A Three-Detector Observation of Gravitational Waves from a Binary Black Hole Coalescence* Physical review letters, **119** (14) (2017)
7. Abbott B. P. et al. *Tests of general relativity with binary black holes from the second LIGO-Virgo gravitational-wave transient catalog* Phys.Rev.D **103** 12, 122002 (2021)
8. Mediavilla E., Jimenez-Vicente J., A.Munoz J.A., Vives-Ariasand H., Calderon-Infante J. *Limits on the Mass and Abundance of Primordial Black Holes from Quasar Gravitational Microlensing* arXiv:1702.00947v1 [astro-ph.GA], (2017)

9. Carr B. J., *The primordial black hole mass spectrum* *Astrophys. J.* **201**, 1 (1975).
10. Nakamura T., Sasaki M., Tanaka T., Thorne K.S. *Gravitational waves from coalescing black hole macho binaries* *Astrophys. J. Lett.* **487**, L139 (1997).
11. Carr B. J., Kohri K., Sendouda Y., Yokoyama J., *New cosmological constraints on primordial black holes* *Phys. Rev. D* **81**, 104019 (2010)
12. Josan A.S., Green A. M., Malik K. A., *Generalized constraints on the curvature perturbation from primordial black holes* *Phys. Rev. D* **79**, 103520 (2009)
13. Sasaki M., Suyama T., Tanaka T., Yokoyama S. *Primordial Black Holes - Perspectives in Gravitational Wave Astronomy* *Class. Quantum Grav.* **35** 063001 (2018)
14. Carr B. J., Kühnel, F. *Primordial black holes as dark matter: recent developments.* *Annu. Rev. Nucl. Part. Sci.* **70**, 355-394 (2020)
15. Abbott B. P. et al. *Search for subsolar mass ultracompact binaries in advanced LIGO's second observing run.* *Phys. Rev. Lett.* **123**, 161102 (2019).

RELATIVISTIC JETS AND GAMMA-RAY BURSTS FROM NEUTRON STAR MERGERS

Hendrik van Eerten

University of Bath, Claverton Down, Bath BA2 7AY, United Kingdom

Abstract

A defining characteristic of gamma-ray bursts (GRBs) is the presence of jetted outflows. These jets are shaped by their launching mechanism and interactions with the environment (both close and further distant) of the GRB, as revealed to us when the jets decelerate from the ultra-relativistic to the non-relativistic. Due to its close proximity and off-axis orientation, multi-messenger event GRB 170817A has been particularly informative in this regard. In this talk I will review the characteristics of GRB jets, paying special attention to recent developments in the field prompted by observation and numerical study of the afterglow of short GRBs from neutron star mergers.

1 Introduction

Gamma-ray bursts (GRBs) have long been associated with neutron stars. A well-established dichotomy exists between long GRBs from collapsing mas-

sive stars (“collapsars”), lasting more than about two seconds in the observer frame, and short GRBs that last less than two seconds ²¹). It is the latter category that has been linked to the merging of two neutron stars ^{33, 10}). For both categories the brief or permanent creation of a highly magnetic neutron star (“magnetar”) has been a persistent alternative in the literature to the direct formation of a black hole. The connection between short GRBs and the merging of neutron stars has been confirmed directly by the recent detection of gravitational waves from a merger pair along with a short GRB in GW170817 / GRB 170817A ¹), but the evidence for possible neutron star remnants remains indirect.

GRBs are produced by non-thermal emission from relativistic flows. Over the years, evidence has accumulated that these flows are collimated in the form of jets, even if this has to be inferred indirectly in close to all events. Due to strong relativistic beaming, the emission from a GRB jet is dominated by a small area of surface where the balance happens to be optimal between beaming angle and intrinsic strength of emission at the time of the departure of the radiation. At first, the geometry of the outflow is therefore not apparent to the observer, but the large luminosity of the source renders it unlikely that its emission was released in all directions (relativistic beaming that emphasises the observer direction notwithstanding). Following the prompt GRB emission in gamma rays, bursts normally produce a fading afterglow peaking at progressively longer wavelengths from X-rays to radio. A second indication of jetted emission therefore can be found in the light curves of the afterglows, which at some point (the “jet break”) fade faster than they would have for spherical outflows (this is both because there is no more material available at larger angle to enter into the line of sight and because jetted outflow will at some point begin to spread sideways and dissipate faster than purely radial flow would). Finally, and again involving GRB 170817A, very large baseline interferometry (VLBI) observations have been able to reveal motion of the centroid of emission consistent with outflow with at least some degree of collimation ^{29, 13}).

In these proceedings I briefly review some developments in GRB jets from neutron star-neutron star (NS-NS) mergers associated with short GRBs.

2 How solid is the short-long divide?

Given the clearly different formation channels between short and long bursts referred to above, one would expect that long GRBs are unrelated to neutron stars at least as far as their progenitor systems are concerned. Nevertheless, in the past years a surprisingly large number of events have been reported that appear to blur the divide.

Normally, the bulk characteristics of the populations are as follows. The short bursts are spectrally harder in their prompt emission, have less temporal lag between soft and hard gamma ray arrival times (hard gamma rays are often delayed relative to soft gamma rays for both burst types) and have shorter timescales in their variability. Long bursts are spectrally softer, have larger temporal lag and variability timescales (the latter two are indicative of a larger emission radius). Long bursts release significantly more isotropic equivalent energy $E_{\gamma,iso}$ (which relates to the jetted energy E_{γ} according to $E_{\gamma} = (2\Omega/4\pi) E_{\gamma,iso}$ for a bi-polar jet of solid opening angle Ω per jet; the isotropic equivalent energy does not require knowledge of Ω to determine). Both long and short bursts obey a relation between their prompt emission peak energy and total prompt energy release (the “Amati” relation and variations thereof ⁵⁾) where a higher frequency peak corresponds to a larger total energy release, but both relationships are calibrated differently. The long bursts population peaks around redshift $z \sim 2$, comparable to the peak of star formation, as expected for a phenomenon associated with short-lived massive stars. Being intrinsically fainter, short bursts are detected at smaller redshifts and often at an offset from their host galaxy (not unexpected for an event produced by a binary pair of neutron stars that previously experienced two supernova explosions that will have imparted a net momentum to the pair). The most utterly unambiguous determinant of the origin of a given long burst remains the observation of a supernova (of broad-lined type Ic, in practice) spatially coincident with the burst. For short bursts, a detection of gravitational waves and/or a kilonova would be similarly unambiguous.

And yet, as said, the odd cases appear to pile up (they are of course of interest from the perspective of aiming for a high-profile publication, so there is some selection bias at play here). Among them are the following, to name a few with publication titles that speak for themselves. *No supernovae associated with two long-duration γ -ray bursts* (GRB 060505, GRB 060614) ¹²⁾, *The*

second-closest gamma-ray burst: sub-luminous GRB 111005A with no supernova in a super-solar metallicity environment ²⁷⁾, Discovery and confirmation of the shortest gamma-ray burst from a collapsar ²⁾ and A peculiarly short-duration gamma-ray burst from massive star core collapse ⁵²⁾ (GRB 200826A). A particularly promising recent case is A nearby long gamma-ray burst from a merger of compact objects ⁴⁵⁾, A long-duration gamma-ray burst with a peculiar origin ⁴⁹⁾, A kilonova following a long-duration gamma-ray burst at 350 Mpc ³⁷⁾ and The case for a minute-long merger-driven gamma-ray burst from fast-cooling synchrotron emission ¹⁵⁾ (all GRB 211211A). This burst is unambiguously of long duration (lasting over 50 seconds), most likely associated with a host galaxy at 350 Mpc but lacking a supernova that at this distance really should have been detected. Instead, a kilonova of similar properties as the well-studied kilonova AT 2017gfo associated with GRB 170817A appears to stand out among the afterglow emission. Its temporal lag, minimum variability timescale and placement on the Amati relation calibration are also consistent with the neutron star merger population rather than the collapsar population. What makes this event so promising is that it therefore potentially signals a population of bursts directly detectable in gravitational waves in forthcoming runs ³⁶⁾ that was previously not recognized as such. Given that we currently still have only one solid multi-messenger detection in GW170817 / GRB 170817A, this additional neutron star connection is a quite appealing prospect.

3 Basic jet features since 170817

Certainly at the toy model level, the jet model of GRB outflows scales straightforwardly between bursts from neutron star mergers and from collapsars. On the one hand, collapsar jets are presumed to be more energetic (at least in the isotropic equivalent sense, the general distribution of opening angles of short GRBs is not well enough constrained to make too strong statements on how their jet energies relate). On the other hand, happening on the outskirts of galaxies, short bursts are presumed to occur in a more dilute environment than their long counterparts. Because jet (isotropic equivalent) energy and circumburst density ρ always occur in the form of a ratio E_{iso}/ρ in expressions for characteristic times and radii of the jet model, such as jet break times and the transition point to non-relativistic flow, in these aspects the differences between

short and long burst jet are maybe less than one would expect from considering the different density and energy scales separately. The reason for this ratio, by the way, is to eliminate the mass dimension of both variables in expressions that only carry dimensions of time and/or distance.

A big reveal of GRB 170817A has been the observability of the lateral energy distribution of the jetted outflow, which is of interest in that it carries the fingerprints of jet launching and propagation. Being cosmologically distant sources, a strong observational bias exists for GRBs to be seen on-axis. Relativistic beaming strongly depends on angle, so jets not directed towards observers are significantly less likely to trigger a gamma-ray detector. When seen on-axis, afterglow emission from near the centre of the jet will dominate the received flux, while emission from higher latitudes gradually comes into view. As a consequence, subtleties in the lateral distribution of energy that set apart a “top-hat” jet (constant energy up to a truncation angle) from structured jets (e.g. a Gaussian, power law or other more gradual decrease in energy with angle), have little noticeable impact on the light curve temporal slope other than a slight modification of the temporal curvature around the jet break ²³).

If a GRB jet is observed at an angle, the imprint of lateral jet structure is more stark ^{38, 39}). Jets observed at a slight angle (i.e. within the opening angle θ_0 of a top-hat flow, or the characteristic width θ_c of a Gaussian energy distribution, reflect their orientation angle θ_{obs} in their temporal slope and delayed jet break ^{47, 38, 51}) (the far angle is now $\theta_0 + \theta_{obs}$, rather than θ_0). If the jet is observed further off-axis, like GRB 170817A was, then an earlier rising stage of the light curve exists whose slope directly constrains ³⁹) θ_{obs}/θ_c . The fact that the afterglow light curves in radio and X-rays for this event rose gradually for the length of time that they did, immediately rules out top-hat jets that would have appeared into view far more abruptly. At the gradually rising light curve stage, a quasi-spherical outflow fits the data equally well, perhaps produced by a “choked jet” or outflow dominated by a cocoon of energy dissipated during the early propagation stages of the jet through the NS merger debris ^{22, 30, 24}). However, such a scenario would not be able to produce the later decay stage slope of GRB 170817A ^{42, 43, 44}) in the manner a Gaussian structured jet model can.

The jet structure need not be exactly Gaussian, though, and such a structure is mostly introduced as a convenient means to capture a potentially more

complicated profile inferred from more detailed physical models (mostly detailed relativistic magnetohydrodynamics simulations). In fact, observations can be used to constrain the jet profile more generally and the local rising light curve slope of a GRB 170817-like event can be inverted to infer a local energy distribution slope ⁴¹).

4 Simulating jets from neutron star mergers

The conditions of formation and propagation of afterglow jets of GRBs have been simulated numerically for decades by now, including seminal papers on long and short GRBs ^{25, 3, 50, 4}). Jetted flow from a neutron star remnant has been studied in depth ^{7, 8}), but many works in the literature concentrate on black holes as the central jet engine. There are various research questions of interest accessible through high-resolution jet simulations. The launching mechanism of relativistic jets remains an open question. There is no clear consensus on the degree of collimation of afterglow jets, neither from observations nor from simulations and it is not known whether there is naturally a broad or narrow range of collimation angles to be expected. The discovery of GRB 170817A and its implication for jet structure have provided new impetus for the simulation of jets from short GRBs. For example, broad wings of low energy relative to the jet tip can indicate the presence surrounding the jet of a lot of material produced by the neutron star merger.

Power-law and Gaussian lateral energy distributions can be seen to map well onto a diversity in simulation results (see e.g. ³⁹), comparing to simulations from ^{4, 28, 9, 24, 26}). A few things should be kept in mind however when doing so. Obviously, actual jets will have a radial fluid profile as well as an angular fluid profile, but the assumption of a homogeneous shell can be quite effective when predicting broadband afterglow emission. GRB jets differ from jets from, for example, active galactic nuclei in that the engine powering the jet is only active briefly relative to the lifetime of the jet. After the engine switches off, at a timescale comparable to the duration of the prompt burst, the jet will evolve towards a blast wave shell.

It is only when the energy powering the flow along a given radial line has on balance been conferred to swept-up circumburst medium that the energy profile alone fully capture the large-scale flow dynamics. At earlier time, the velocity of the original ejecta still shapes the outflow Lorentz profile. The

Lorentz factor might well differ in its angular distribution from the energy distribution, and thus provide more freedom to model to prompt emission if it is extracted from the same jetted flow. All afterglow observations of GRB 170817 are following the deceleration of the ejecta and thus of a shock-wave in the external medium.

Another thing to keep in mind is that the simulation inspiring a simplified energy profile might not represent the end stage of “sculpting” of the jet. There might be more strong interactions with the burster environment that are not accounted for in the modelling, or beyond the range of the computational grid during a simulation run. This aspect has received a lot of attention in recent years. Focusing on neutron star merger simulations, the major players are the accretion disc ¹¹⁾, the dynamical ejecta from the mergers ¹⁸⁾ and the neutrino-driven wind from the disc ³⁵⁾. General relativistic magnetohydrodynamics simulations of the jet-accretion disc interaction ²⁰⁾ already produce a jet with lateral energy structure. This is not unexpected, given that, really, a top-hat jet is as unrealistic as it is simplistic; top-hat models ignore the presence of structure under the assumption that it is of minor importance for jet dynamics and emission predictions, which is not the same as asserting the structure does not exist.

However, recent simulations show examples of how a subsequent encounter of the jet with a neutrino-drive wind effectively resets and replaces the launch structure by the imprint of this later interaction ³²⁾. For these particular simulations, which inject the jet into a detailed simulation including neutrino leakage scheme of neutrino-driven winds ³⁴⁾, the emerging profile reveals a slight energy spike at the tip on a central plateau, flanked by a drop in energy that holds an intermediate between a sharp top-hat distribution and a gradual Gaussian jet profile.

The question of whether jets end up choked or not by the presence of merger debris is likewise of interest for jet simulations. Recent work ¹⁶⁾ explores whether a jet, sculpted by neutrino-driven wind interaction, manages to get past the ejecta. According to this study, the ejecta interaction is not as key to shaping the lateral energy profile as the wind, but might indeed end up choking the jet, leading to a mildly relativistic cocoon emerging rather than a highly relativistic and tightly collimated jet.

Finally, these simulation outputs can be used to predict the afterglow

light curve. However, in most cases it is not possible to simply continue the simulation up to the relevant radii and times, since the jet evolves over many orders of magnitude (from $< 10^7$ cm to the parsec scale and well beyond), unless specialized moving mesh techniques are deployed ^{48, 6)}. When not starting from a simplified shell model or analytical description of the jet lateral profile, the afterglow stage dynamics therefore need to be modelled by extrapolating simulations. This extrapolation needs to properly account for jet spreading dynamics though, because when not included this would result in an artificially shallow late-time lightcurve slope ³¹⁾. When spreading dynamics are included when extrapolating from a simulation (e.g. as in ³²⁾), the late time slope steepens on account of the faster dissipation relative to non-spreading flow.

5 Jet models and neutron star merger afterglow emission modelling

The issue raised about jet simulations and afterglow modelling in the previous section is of interest in view of the long-term observations of GRB 170817A, the one nearby off-axis multi-messenger event that we have data for. Data from last year potentially suggested the emergence of an additional component in the X-ray emission, still visible at 3.3 years following the merger. This component could have been emission from another blast wave, this time associated with the kilonova, and thus constrain the kilonova physics. The evidence for this extra component, however, is not statistically strong ^{17, 46)}, and where based on a tension with jet model predictions, subject to caveats such as the uncertainty in long-term jet spreading behaviour mentioned above. Other aspects also impact the late time slope of the afterglow light curve and can help alleviate a tension between model and data (assuming one would actually emerge). These include the details of the emission modelling, which, like long-term jet evolution across many scales, is underresolved if no special mesh techniques are deployed ⁶⁾ and which might need a reparametrization in the non-relativistic regime ^{40, 17, 6)}.

Which data and which *priors* and weights are attached to these data also matters in modelling. As always when comparing models to a diverse data set, it remains a challenge to find the most appropriate approach to weighing data points from separate sources (e.g. gravitational waves versus broadband afterglow versus centroid position) and to deciding how strongly to penalize or reward features from a model that ultimately remains an idealized approximation of an actual jet (no matter how elaborate the simulation underpinning the

model). There are by now multiple efforts to combine multi-messenger data, VLBI, gravitational waves and broadband afterglow altogether, within a single framework (e.g. ¹⁹). Future analysis is likely to include a full joint-fit of these data, for GRB 170817A or upcoming NS-mergers, rather than a “pipeline” approach (as was done first by ⁴²) where the posterior from the one analysis enters the other in the form of a prior. This ensures that all information is used even when constraining parameters that are not shared by models of different facets of the merger ¹⁴). A joint fit of gravitational wave data and afterglow, for example, means fitting a merger model of gravitational wave emission (i.e. templates for the latter) that shares system orientation with an afterglow jet model, but does not share e.g. neutron star spin on the gravitational wave side or synchrotron emission efficiency on the afterglow side.

6 Acknowledgments

The author acknowledges support by the European Union horizon 2020 programme under the AHEAD2020 project (grant agreement number 871158).

References

1. B. P. Abbott *et al*, ApJ **848**, L12 (2017),
2. T. Ahumada *et al*, Nature Astronomy **5**, 917 (2021)
3. M. A. Aloy *et al*, ApJ *531*, L119 (2000)
4. M. A. Aloy *et al*, A&A **436**, 273 (2005)
5. L. Amati *et al*, A&A **390**, 81 (2002)
6. E. Ayache *et al*, MNRAS **510**, 1315 (2022)
7. N. Bucciantini *et al*, MNRAS **396**, 2038 (2009)
8. N. Bucciantini *et al*, MNRAS **419**, 1537 (2012)
9. P. C. Duffell & A. I. MacFadyen, ApJL **776**, L9 (2013)
10. D. Eichler *et al*, Nature **340**, 126 (1989)
11. E. Fernandez *et al*, MNRAS **482**, 3373 (2019)

12. J. Fynbo *et al* Nature **444**, 1047 (2006)
13. G. Ghirlanda *et al*, Science **363**, 968 (2019)
14. G. Gianfagna *et al*, eprint arXiv:2212.01104 (2022)
15. B. Gompertz *et al*, Nature Astronomy, Advanced Online Publication (2022)
16. O. Gottlieb *et al* ApJL **933**, L2 (2022)
17. A. Hajela *et al*, ApJL **927**, L17 (2022)
18. K. Hotokezaka *et al*, Physical Review D **87**, 024001 (2013)
19. K. Hotokezaka *et al*, Nature Astronomy **3**, 940 (2019)
20. A. Kathirgamaraju *et al*, MNRAS **484**, L98 (2019)
21. C. Kouveliotou, C. *et al*, ApJ **413**, L101 (1993)
22. G. P. Lamb & S.Kobayashi, ApJ **829**, 112 (2016)
23. G. P. Lamb *et al*, MNRAS **506**, 4163 (2021)
24. D. Lazzati *et al*, ApJL **848**, L6 (2017)
25. A. I. MacFadyen & S. E. Woosley, ApJ **524**, 262 (1999)
26. R. Margutti *et al*, ApJ **856**, L18 (2018)
27. M. J. Michalowski *et al*, A & A **616**, A169 (2018)
28. A. Mizuta & M. A. Aloy *et al*, **2009**, 1261 (2009)
29. K.P. Mooley *et al*, Nature, **561**, 355 (2018)
30. E. Nakar & T. Piran, ApJ **834**, 28 (2017)
31. A. Nathanail *et al*, MNRAS **495**, 3780 (2020)
32. L. Nativi *et al*, MNRAS **509**, 903 (2022)
33. B. Paczynski, ApJ **308**, L43 (1986)
34. A. Perego *et al*, MNRAS **443**, 3134 (2014)

35. A. Perego *et al*, MNRAS **443**, 3134 (2017)
36. P. Petrov *et al*, ApJ **924**, 54 (2022)
37. J. C. Rastinejad *et al*, Nature **612**, 223 (2022)
38. G. S. Ryan *et al*, ApJ **799**, 3 (2015)
39. G. S. Ryan *et al*, ApJ **896**, 166 (2020)
40. L. Sironi & D. Giannios, ApJ **778**, 107 (2013)
41. K. Takahashi & K. Ioka **497**, 1217 (2020)
42. E. Troja *et al*, MNRAS **478**, L18 (2018)
43. E. Troja *et al*, MNRAS **489**, 1919 (2019)
44. E. Troja *et al*, MNRAS **498**, 5643 (2020)
45. E. Troja *et al*, Nature **612**, 228 (2022)
46. E. Troja *et al*, MNRAS **510** 1902 (2022)
47. H. J. van Eerten *et al*, ApJ **722**, 235 (2010)
48. X. Xie *et al*, ApJ **863**, 58 (2018)
49. J. Yang *et al*, Nature **612**, 232 (2022)
50. W. Zhang *et al*, ApJ **586**, 356 (2003)s
51. B. B. Zhang *et al*, ApJ **806**, 15 (2015)
52. B. B. Zhang *et al*, Nature Astronomy Letters **5**, 911 (2021)

IMPLICATIONS FOR COSMOLOGY FOLLOWING RECENT GRAVITATIONAL WAVE OBSERVATIONS

S. Mastrogiovanni

INFN, Sezione di Roma, I-00185 Roma, Italy

Artemis, Universit Cte dAzur, Observatoire de la Cte dAzur, CNRS, F-06304 Nice, France

Abstract

Standard sirens are a central paradigm in gravitational-wave (GW) cosmology. From the GW signature detected from compact binary mergers, it is possible to directly measure the luminosity distance of the source, and if additional information on the source redshift is provided, a measurement of the cosmological expansion can be performed. In this article, I will provide an intuitive introduction to current analysis methods for GW standard siren cosmology. I will also present the most recent results on cosmology using the latest LIGO-Virgo-KAGRA GW events.

1 Introduction

The LIGO, Virgo and KAGRA detectors ^{1, 2, 3, 4} have recently presented their third gravitational wave transient catalog (GWTC-3 ⁵). The catalog

presents almost 100 GWs detected from the coalescence of Binary Black Holes (BBHs), Binary Neutron stars (BNSs) ⁶⁾ and neutron star black hole (NSBH) ⁷⁾ binaries. These observations allowed us to shed light on possible formation mechanisms of compact binaries ^{8, 9, 10)}, as well as tests General Relativity (GR) on cosmological scales ¹¹⁾.

Among the various implications, GWs can also be used to probe cosmology. Although the cosmological expansion has been studied in detail using Supernovae in the “local” Universe ¹²⁾ and the Cosmic Microwave Background (CMB) ¹³⁾, the Standard cosmological model still suffers theoretical and observational difficulties. From the theoretical point of view, we observe that 70% of the energy content Universe is dominated by a form of Energy, *Dark Energy*, that is causing an accelerated expansion. From the observational point of view, there is a discrepancy in the value of the expansion rate of the Universe today, the Hubble constant (H_0), between measures from Supernovae and the CMB. The tension is at the level of 4.2σ the value inferred from the CMB ¹³⁾

$$H_0 = 67.8 \pm 0.9 \text{ km s}^{-1} \text{ Mpc}^{-1}, \quad (1)$$

and the value inferred from Supernovae ¹²⁾

$$H_0 = 73.0 \pm 1.4 \text{ km s}^{-1} \text{ Mpc}^{-1}. \quad (2)$$

GW sources provide an independent new channel to probe this tension and it has been argued that can potentially shed light on the 20-year-long issue of the H_0 tension ¹⁴⁾.

In this paper, I review the most recent results on cosmology using GW observations. I will focus on the three methods for GW cosmology that have been applied so far in literature: the bright, dark, and spectral siren methods. In Sec. 2, I will provide a pedagogic and intuitive introduction to current methods for GW cosmology. In Sec. 3, I will discuss the most updated results on the measurement of the Hubble constant. Finally in Sec.4 I will conclude with a discussion on future prospects for this field.

2 Basics of standard sirens

Compact binary coalescences at cosmological distances are the only known, and observed, type of source for which it is possible to directly measure the

luminosity distance (d_L)¹⁵⁾. In analogy to Type Ia Supernovae, often referred to as standard candles, GW sources are referred to as *standard sirens*. In order to probe cosmology, however, we should be provided also with the *redshift* of the source, i.e. the recessional velocity of the source with respect to the observer due to the Universe expansion. Once a redshift is provided, we can infer the parameters of a cosmological model by fitting the $d_L - z$ relation. For a flat Universe with Dark Energy and Dark matter components, the luminosity distance is linked to the redshift by

$$d_L = \frac{c(1+z)}{H_0} \int_0^z \frac{dz'}{\sqrt{\Omega_m(1+z')^3 + \Omega_\Lambda}}, \quad (3)$$

where Ω_m is the dark matter energy density, $\Omega_\Lambda = 1 - \Omega_m$ the Dark Energy density and c the speed of light. Another relevant aspect, peculiar to GW sources, is that from the GW waveform it is possible to measure the *redshift masses* m_d of the compact objects. These are related to the intrinsic masses m_s by

$$m_d = m(1+z). \quad (4)$$

GW techniques for cosmology are classified according to the method used to obtain the redshift. In the following, I will give a pedagogical and intuitive introduction to these techniques, for more details on their derivation and implementation I defer the reader to¹⁶⁾ and the literature referenced in the next sections. Although in this review I focus on measures of H_0 using the standard cosmological model, the methods discussed can also be applied to probe GR deviations on cosmological scales^{17, 18, 19, 20)}.

A central aspect of inferential techniques involving standard sirens is the correction of selection biases. Selection biases arise when a given experiment (in our case GW detectors), is not able to detect all the compact binary coalescences in the Universe. This might cause a lack of GW events, e.g. after a given luminosity distance, that might introduce a bias in the estimation of the H_0 . In order to correct for selection biases, it is crucial to have an astrophysical population model for the GW sources as well as a robust knowledge of the selection biases involved in each detection process. For a more in-depth discussion and derivation of selection bias correction is provided in²¹⁾. In this review, I will only give an intuitive introduction to the selection biases involved in each standard siren method and I defer the reader to the literature referenced in the following sections.

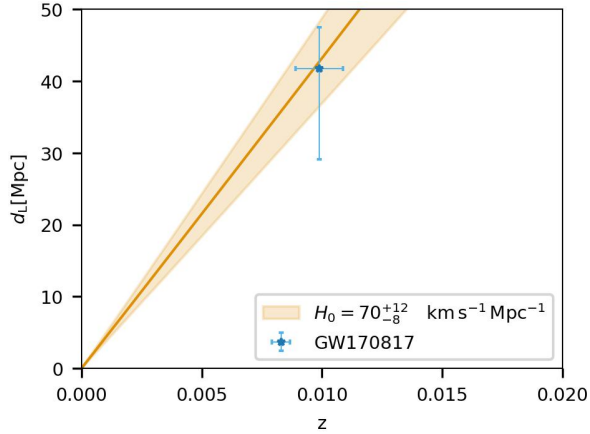


Figure 1: An Hubble diagram adapted to the case of GW170817 and its EM counterpart. The redshift is reported on the horizontal axis and the luminosity distance is on the vertical axis. The blue scatter indicates the observed values for GW170817 and the orange contour is the 68% credible interval contour for the inferred H_0 (22).

2.1 Bright sirens method

The bright sirens method assigns the redshift to the GW events by using the observations of an observed associated electromagnetic (EM) counterpart. Typically, we expect EM counterparts for BNS mergers (22), and possibly some NSBH, consisting in short γ -ray burst (GRB) and kilonovae. Indeed, these two types of EM emissions were observed from the BNS merger GW170817. The EM counterparts might allow us to identify the host galaxy of the GW events and therefore their redshift.

Once we measure the luminosity distance and redshift of the source, we can construct a *Hubble diagram* (a diagram that relates luminosity distance to redshift). Fig. 1 shows an example of a Hubble diagram for the bright siren GW170817 (more details are provided Sec. 3). The figure reports the measure of the luminosity distance from the GW waveform and the measure of the redshift from the identification of its hosting galaxy. The figure also reports (orange contours) a fit for H_0 using Eq. 3.

Bright standard sirens are the optimal sources to probe cosmology as the

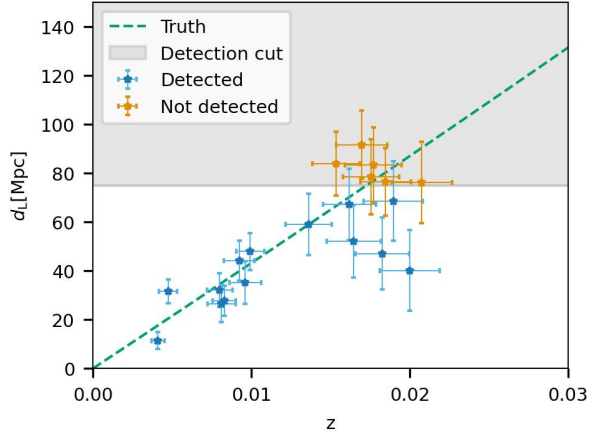


Figure 2: Illustration of the impact of a selection bias on the luminosity distance on the Hubble diagram. The plot reports GW sources detected (blue points) and not detected (orange points) in presence of a selection cut on luminosity distance at 75 Mpc. The dashed line indicates the $d_L - z$ relation for simulated cosmology.

source redshift is accurately determined. Currently, the precision on the H_0 measure is dominated by the large uncertainties on the luminosity distance on the GW side²³⁾. The uncertainty on the d_L can be improved by exploiting the afterglow light curve of the EM counterpart that carries information on the binary viewing angle²⁴⁾. Another bottleneck of this method is the rareness of this type of observation. This is due to the fact that the detection of EM counterparts is really challenging, in particular when the GW sky localization is not precise enough²⁵⁾. Indeed, so far the only bright siren observed out of ~ 100 GW events is GW170817.

Even for bright sirens, it is crucial to correct selection effects. Fig. 2 shows an example, generated with a toy model to illustrate the impact of a selection bias on the source luminosity distance for the H_0 estimation. In the toy model, GWs are not detected if their *measured* (it includes noise fluctuations) luminosity distance exceeds a detection threshold of 75 Mpc. The Figure displays multiple detected GW events with distance and redshift estimates as well as the signals which are missed. Close to the detection threshold, we are missing some GW events. This lack of GW events introduces a bias in the

fitting process for H_0 that must be corrected.

2.2 Dark sirens method

The first method that has been proposed using GW for cosmology even in absence of EM counterparts is the Dark Sirens method ⁽²⁶⁾. The idea behind this method is to identify possible GW host galaxies by making use of galaxy surveys. In fact, GWs will provide a sky localization in which potential host galaxies can be extracted from the galaxy catalog. The galaxy catalog will provide a list of potential host galaxies for the GW event that can be used to infer H_0 .

The dark sirens method is particularly efficient for GW events that are well localized. In Fig. 3 I report the localization skymap for GW190814 ⁽²⁷⁾, one of the best localized GW events. The 90% credible interval covers an area of $\sim 20 \text{ deg}^2$ ⁽²⁸⁾. The skymap can be used to select possible host galaxies

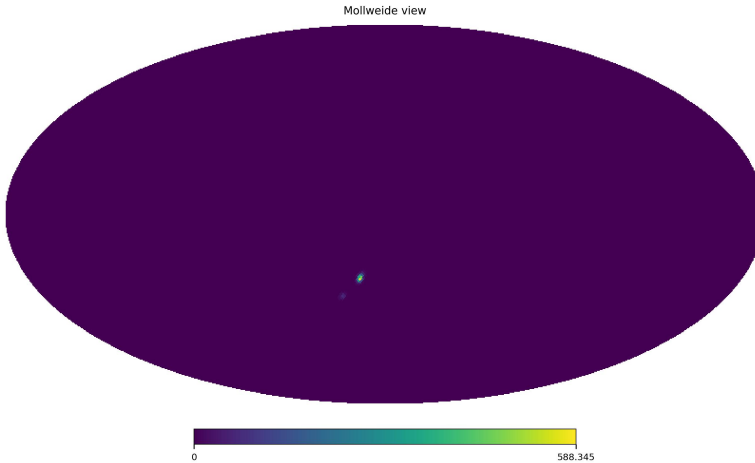


Figure 3: The skymap shows the posterior probability density distribution for the localization in right ascension and declination of GW190814. The pixel size of the map is $\sim 3.5 \text{ deg}^2$. The 90% credible interval covers an area of $\sim 20 \text{ deg}^2$.

from a galaxy survey. In Fig. 4, I report in the 3-dimensional volume, all the galaxies present in the infrared “K” band from the GLADE+ galaxy catalog ⁽²⁹⁾. Overdensities and underdensities of galaxies along the GW sky localization

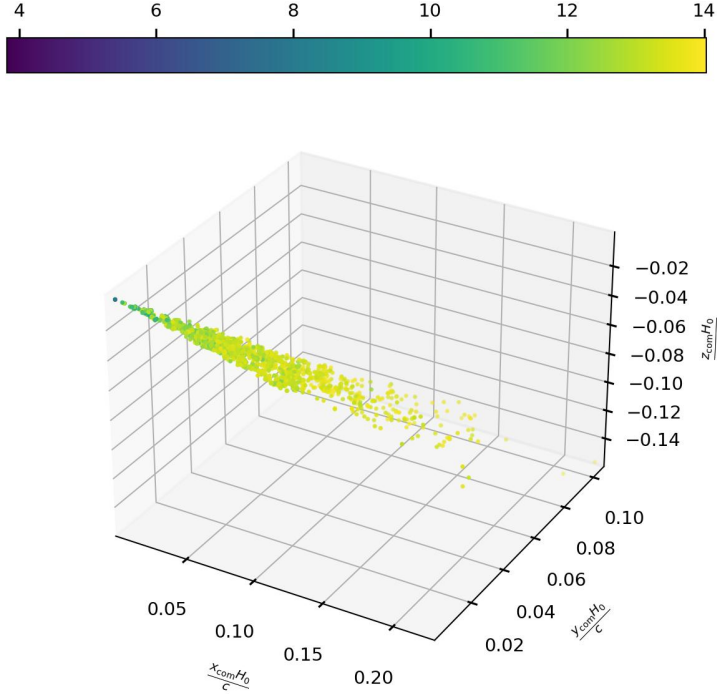


Figure 4: Galaxies reported by the galaxy catalog GLADE+ in the 90% credible sky area of GW190814. The plots report the galaxy distribution in terms of (dimensionless) comoving distance. The color bar indicates the apparent magnitude reported for each galaxy.

volume can be used to assign the most probable redshift to GW events.

Another important aspect to note from Fig. 4 is that as we go farther in distance, galaxies tend to be less and less. This is expected as current observational facilities can not detect faint galaxies at higher distances. This introduces a selection effect that will preferentially place GW events at lower redshifts, thus systematically favoring low H_0 values. This selection effect is often referred to as “completeness” correction³⁰⁾ since it arises from the fact that the galaxy catalog does not contain all the possible hosts of GW events.

2.3 Spectral sirens

Another method to study cosmology with GW signals alone has been proposed in ³¹⁾. The basic idea behind this method is to exploit the relation in Eq. 4 between source mass and detector mass. By measuring the detector frame masses, and using some hypothesis on the astrophysical distribution of source masses, it is possible to implicitly obtain the redshift for a population of GW sources. The narrower the distribution of the source mass spectrum, the more precise the implicit redshift information will be. This is the motivation for which the method has been originally proposed and studied in light of BNS mergers ³²⁾ that are expected to have a narrower mass spectrum than the one of BBHs. However, recently it has been recognized that, even if the BBHs mass spectrum spans ~ 2 order of magnitudes in mass, it presents local overdensities that can be used to set a scale for the redshift of GW events. The BBHs mass spectrum overdensities, not only can be used to probe cosmology even in absence of any complementary EM observations ³³⁾, but can also potentially introduce systematic biases in the estimation of H_0 if not properly accounted for ³⁴⁾.

In Fig. 5, I show an example of how the mass-redshift relation can be used to fit a cosmological model with only GW signals. The plot reports the detector mass and luminosity distance for all the BBHs with an Inverse False Alarm rate higher than 4 yr reported in GWTC-3 ⁵⁾. Let us assume that there is an overdensity of BBHs produced at a source mass of $35M_\odot$. At a luminosity distance of ~ 1 Gpc, which corresponds to a redshift of ~ 0.2 for a Planck Cosmology ($H_0 = 67.7\text{km s}^{-1} \text{Mpc}^{-1}$), this overdensity will be located around $m_d = 35M_\odot(1 + 0.2) \approx 42M_\odot$. As it can be seen from the plots, given a cosmological model, a fixed overdensity in the source frame mass is mapped differently in the detector-frame vs luminosity distance plane. This allows us to identify cosmological models which are able to the observed detector masses and distances of the GW events.

Of course, in real analyses such as ^{28, 18)}, cosmological studies are not performed with a trivial fitting as described in the previous paragraph. Current analyses use hierarchical Bayesian statistics to deconvolve selection biases given by the fact that GW detectors are not equally sensitive to detect all the masses. Moreover, current algorithms do not assume known the mass spectrum of compact binaries but are able to fit flexible phenomenological

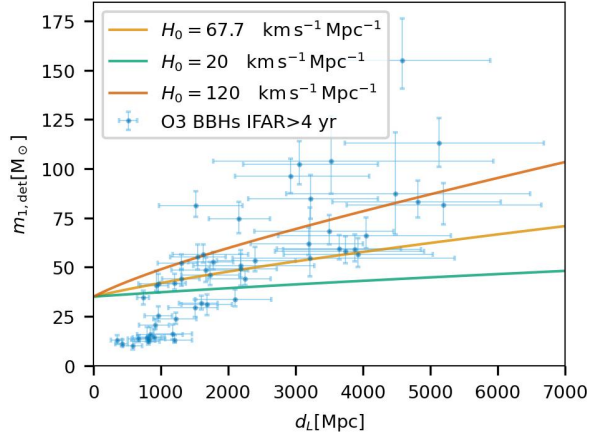


Figure 5: Detector frame mass (vertical axis) and luminosity distance (horizontal axis) measured for the GW events (blue scatters) present in GWTC–3 with inverse false alarm rate higher than 4 yr. The different solid lines map an overdensity of BBHs produced at $35M_{\odot}$ in the detector mass/distance plane for different cosmological models.

models.

3 Recent results

3.1 Bright sirens

GW cosmology was officially opened by the BNS merger GW170817 and its EM counterparts⁶⁾. About ~ 1.7 s after the GW luminosity peak of GW170817, *Fermi* Gamma-ray Burst Monitor³⁵⁾ and *International Gamma-Ray Astrophysics Laboratory*³⁶⁾ detected a Gamma-ray Burst (GRB 170817A)²²⁾. After about ~ 11 hours, the One-Meter Two-Hemisphere team first identified a bright optical transient consistent with the localization of GW170817. Confirmations from several other teams swiftly followed this²²⁾. The counterpart, now known as AT 2017gfo, was confidently associated with the host Galaxy NGC 4993.

NGC4993 is a galaxy in the Hydra constellation with an average radial peculiar velocity of ~ 310 km/s. The recessional velocity of NGC4993 is about 3327 ± 72 km/s. By combining observations of the galaxy’s proper motion and

observed recessional velocity, we can obtain a value of the galaxy’s recessional due to the expansion of the Universe ($v_r = 3017 \pm 166 \text{ km/s}$). From this estimation, we can obtain a measurement of the galaxy cosmological redshift of $z = 0.0101 \pm 0.0005$ (37).

The maximum a posteriori of GW170817 luminosity distance, when fixing the sky position of NGC4993 is $43.8^{+2.9}_{-6.9} \text{ Mpc}$ at 68% confidence level (38). By combining this information with the cosmological redshift measurement from NGC4993, it is possible to infer the value of the $H_0 = 70^{+12}_{-8} \text{ km s}^{-1} \text{ Mpc}^{-1}$ (38). This result has been updated with an extended analysis at a lower frequency in the LIGO and Virgo sensitivity bands. The results are $H_0 = 70^{+13}_{-7} \text{ km s}^{-1} \text{ Mpc}^{-1}$ using high-spin priors (magnitude of the dimensionless spin parameters ≤ 0.89), and $H_0 = 70^{+19}_{-8} \text{ km s}^{-1} \text{ Mpc}^{-1}$ using low-spin priors (magnitude of the dimensionless spin parameters ≤ 0.05) (37). One can note that low-spin priors (well motivated from the observations of galactic radio pulsars (39)) display a broader constraint on the Hubble constant. While the opposite is true for high-spin priors. This is caused by the absence of strong precession in the high-spin analysis which results in a stronger constraint on the viewing angle of the system. Indeed, there is a strong degeneracy between the determination of the luminosity distance and the binary viewing angle (40, 38).

For GW170817, follow-up measurements of the Kilonova afterglow enabled an additional measure of the binary viewing angle (41). In fact, radio band observations using Very Long Baseline Interferometry (VLBI) reported the observation of a narrow-collimated jet associated with the merger (41). The orbital inclination angle could then be determined by assuming that the jet is emitted perpendicularly to the orbital plane of the merger. This improves the d_L measure and provides an improved value for $H_0 = 68.4^{+4.7}_{-4.6} \text{ km s}^{-1} \text{ Mpc}^{-1}$ (42) in contrast to the GW-alone value of $H_0 = 70^{+19}_{-8} \text{ km s}^{-1} \text{ Mpc}^{-1}$.

GW170817 remains the only gravitational-wave event with a confirmed electromagnetic counterpart. Recently it has some of the most massive BBHs could be associated with active galactic nuclei flares (43) caused by the interaction of the kicked remnant black hole with the accretion of disk (44). If these EM counterparts are confirmed, they can still be used to measure the H_0 (45, 46, 47). However, there seems to be currently no statistical for the associations of some of these events (48).

3.2 Dark sirens

The first application of the dark sirens galaxy catalog method was during the first two runs of the LIGO and Virgo with the support of the GLADE ⁴⁹⁾ galaxy catalog. GLADE is an all-sky catalog composed of several surveys estimating the galaxies' redshift with photometric and spectroscopic techniques.

One of the first applications of the dark sirens method to a population of BBHs, has been done with 6 BBHs (without EM counterpart) from the first and second observing runs of Advanced LIGO and Virgo. The estimated H_0 , in combination with the estimation of GW170817 obtained was $H_0 = 68.7_{-7.8}^{+17.0}$ km s⁻¹ Mpc⁻¹. For this analysis, the primary mass component of the binary was chosen to be a power-law distribution with a slope of -1.6 between $m_{\min} = 5 M_{\odot}$ and $m_{\max} = 100 M_{\odot}$, while the distribution for the light component was selected to be uniform within the same range and with the condition $m_2 \leq m_1$.

One of the last applications of the galaxy catalog method was with 47 compact binary coalescences from the first 3 runs of LIGO, Virgo, and KAGRA and using the GLADE+ galaxy catalog ²⁹⁾ (an improved and more complete version of the GLADE). Differently from the previous analyses, in ²⁸⁾, the H_0 inference is done with a more complex model for the mass spectrum of BBHs. The primary component mass of BBHs was selected as a power law with an additional Gaussian peak; see ²⁸⁾ for more details. In fact, in ³⁴⁾, it has been shown that in the case that the galaxy catalog is not complete and the mass spectrum is not accurately modeled, the H_0 estimation can present strong biases. In ²⁸⁾ a value of $H_0 = 68_{-6}^{+8}$ km s⁻¹ Mpc⁻¹ was found with the GLADE+ catalog. This is an improvement of 40% with respect to the GW170817 case ³⁸⁾. However, one has to note that most of the information on H_0 is coming from the choice of the BBH mass spectrum, as I will detail in the next section. In ²⁸⁾ this is shown by varying the BBHs mass spectra and showing that the H_0 measure is highly sensitive to it.

There were also additional cosmological studies with GW events. In ¹⁹⁾, by using the GLADE and a selection of GW events that are supported in a 70% complete region of GLADE, it is found $H_0 = 72.2_{-7.5}^{+13.9}$ km s⁻¹ Mpc⁻¹ (in combination with GW170817). In ^{50, 51)} well-localized GW events are used from the first 3 runs of the LIGO, Virgo, and KAGRA to estimate H_0 with the Dark Energy Survey Imaging (DESI) Legacy survey reporting a value of

$$H_0 = 72.8_{-7.6}^{+11.0} \text{ km s}^{-1} \text{ Mpc}^{-1}.$$

3.3 Spectral sirens

For the first time in ²⁸⁾, a joint estimation of H_0 and mass spectrum of BBHs is presented using 42 BBHs from GWTC-3. The analysis used 3 different population models for the mass spectrum of BBHs finding that, among all the models, the preferred ones are the ones that display an overdensity of BBHs produced around $35M_\odot$. In ²⁸⁾, it has been shown that the localization of this peak-like structure is crucial to measure the H_0 . The estimation of the H_0 from the preferred mass model is $H_0 = 50_{-30}^{+37} \text{ km s}^{-1} \text{ Mpc}^{-1}$. Moreover, it is found in ²⁸⁾ that other cosmological parameters such as the matter-energy density Ω_m and Dark Energy Equation of State parameter w could not be constrained by current GW observations. When combining this H_0 estimation with GW170817 and its EM counterpart, we obtain a value of $H_0 = 68_{-8}^{+12} \text{ km s}^{-1} \text{ Mpc}^{-1}$. This measure represents an improvement of $\sim 17\%$ with respect to GW170817 alone. A similar analysis using several population models for BBHs is performed in ¹⁸⁾ finding consistent constraints on the Hubble constant.

4 Conclusions

In this paper, I have provided a pedagogical introduction to current techniques and results for GW cosmology: the bright, dark, and spectral sirens methods. I have described the basics and working principles for each of these methods and shortly introduced their difficulties and prospects. I have discussed the most recent results using current GW events and these methods.

Gravitational Wave signals for compact binary coalescences are becoming a central tool to probe cosmology. This is of great scientific interest given that GW sources do not share the same systematics with the current two measures from CMB and Supernova which are found to be in tension. Moreover, as I described in this paper, several methods for studying cosmology with GWs can be used. These methods will not completely share the same type of systematics and can be used to additionally corroborate cosmological measures.

References

1. A. Buikema *et al.*, “Sensitivity and performance of the Advanced LIGO detectors in the third observing run,” *Phys. Rev. D*, vol. 102, no. 6, p. 062003, 2020.
2. M. Tse *et al.*, “Quantum-Enhanced Advanced LIGO Detectors in the Era of Gravitational-Wave Astronomy,” *Phys. Rev. Lett.*, vol. 123, no. 23, p. 231107, 2019.
3. F. Acernese *et al.*, “Advanced Virgo: a second-generation interferometric gravitational wave detector,” *Class. Quant. Grav.*, vol. 32, no. 2, p. 024001, 2015.
4. F. Acernese *et al.*, “Increasing the Astrophysical Reach of the Advanced Virgo Detector via the Application of Squeezed Vacuum States of Light,” *Phys. Rev. Lett.*, vol. 123, no. 23, p. 231108, 2019.
5. R. Abbott *et al.*, “GWTC-3: Compact Binary Coalescences Observed by LIGO and Virgo During the Second Part of the Third Observing Run,” 11 2021.
6. B. P. Abbott *et al.*, “GW170817: Observation of Gravitational Waves from a Binary Neutron Star Inspiral,” *Phys. Rev. Lett.*, vol. 119, no. 16, p. 161101, 2017.
7. R. Abbott *et al.*, “Observation of Gravitational Waves from Two Neutron Star–Black Hole Coalescences,” *Astrophys. J. Lett.*, vol. 915, no. 1, p. L5, 2021.
8. B. P. Abbott *et al.*, “Binary Black Hole Population Properties Inferred from the First and Second Observing Runs of Advanced LIGO and Advanced Virgo,” *Astrophys. J. Lett.*, vol. 882, no. 2, p. L24, 2019.
9. R. Abbott *et al.*, “Population Properties of Compact Objects from the Second LIGO–Virgo Gravitational-Wave Transient Catalog,” *Astrophys. J. Lett.*, vol. 913, no. 1, p. L7, 2021.
10. R. Abbott *et al.*, “The population of merging compact binaries inferred using gravitational waves through GWTC-3,” 11 2021.

11. The LIGO Scientific Collaboration, the Virgo Collaboration, the KAGRA Collaboration, R. Abbott, H. Abe, F. Acernese, K. Ackley, N. Adhikari, R. X. Adhikari, V. K. Adkins, and et al., “Tests of General Relativity with GWTC-3,” *arXiv*, p. arXiv:2112.06861, Dec. 2021.
12. A. G. Riess, S. Casertano, W. Yuan, J. B. Bowers, L. Macri, J. C. Zinn, and D. Scolnic, “Cosmic Distances Calibrated to 1% Precision with Gaia EDR3 Parallaxes and Hubble Space Telescope Photometry of 75 Milky Way Cepheids Confirm Tension with Λ CDM,” *ApJ*, vol. 908, p. L6, Feb. 2021.
13. Planck Collaboration, P. A. R. Ade, N. Aghanim, M. Arnaud, M. Ashdown, J. Aumont, C. Baccigalupi, A. J. Banday, R. B. Barreiro, J. G. Bartlett, and et al., “Planck 2015 results. XIII. Cosmological parameters,” *A&A*, vol. 594, p. A13, Sept. 2016.
14. H.-Y. Chen, M. Fishbach, and D. E. Holz, “A two per cent Hubble constant measurement from standard sirens within five years,” *Nature*, vol. 562, no. 7728, pp. 545–547, 2018.
15. D. E. Holz and S. A. Hughes, “Using gravitational-wave standard sirens,” *Astrophys. J.*, vol. 629, pp. 15–22, 2005.
16. S. Mastrogiovanni and D. A. Steer, “Measuring Cosmological Parameters with Gravitational Waves,” in *Handbook of Gravitational Wave Astronomy. Edited by C. Bambi*, p. 48, 2022.
17. S. Mastrogiovanni, L. Haegel, C. Karathanasis, I. Magaña Hernandez, and D. A. Steer, “Gravitational wave friction in light of GW170817 and GW190521,” *JCAP*, vol. 2021, p. 043, Feb. 2021.
18. M. Mancarella, E. Genoud-Prachex, and M. Maggiore, “Cosmology and modified gravitational wave propagation from binary black hole population models,” *arXiv e-prints*, p. arXiv:2112.05728, Dec. 2021.
19. A. Finke, S. Foffa, F. Iacovelli, M. Maggiore, and M. Mancarella, “Cosmology with LIGO/Virgo dark sirens: Hubble parameter and modified gravitational wave propagation,” *J. Cosmology Astropart. Phys.*, vol. 2021, p. 026, Aug. 2021.

20. K. Leyde, S. Mastrogiovanni, D. A. Steer, E. Chassande-Mottin, and C. Karathanasis, “Current and future constraints on cosmology and modified gravitational wave friction from binary black holes,” *arXiv*, p. arXiv:2203.11680, Mar. 2022.
21. S. Vitale, D. Gerosa, W. M. Farr, and S. R. Taylor, “Inferring the Properties of a Population of Compact Binaries in Presence of Selection Effects,” in *Handbook of Gravitational Wave Astronomy. Edited by C. Bambi*, p. 45, 2022.
22. B. P. Abbott *et al.*, “Multi-messenger Observations of a Binary Neutron Star Merger,” *Astrophys. J. Lett.*, vol. 848, no. 2, p. L12, 2017.
23. E. Chassande-Mottin, K. Leyde, S. Mastrogiovanni, and D. A. Steer, “Gravitational wave observations, distance measurement uncertainties, and cosmology,” *Phys. Rev. D*, vol. 100, p. 083514, Oct. 2019.
24. K. Hotokezaka, E. Nakar, O. Gottlieb, S. Nissanke, K. Masuda, G. Hallinan, K. P. Mooley, and A. T. Deller, “A Hubble constant measurement from superluminal motion of the jet in GW170817,” *Nature Astron.*, vol. 3, no. 10, pp. 940–944, 2019.
25. B. Patricelli, M. G. Bernardini, M. Mapelli, P. D’Avanzo, F. Santoliquido, G. Cella, M. Razzano, and E. Cuoco, “Prospects for multimessenger detection of binary neutron star mergers in the fourth LIGO-Virgo-KAGRA observing run,” *MNRAS*, vol. 513, pp. 4159–4168, July 2022.
26. B. F. Schutz, “Determining the Hubble Constant from Gravitational Wave Observations,” *Nature*, vol. 323, pp. 310–311, 1986.
27. R. Abbott, T. D. Abbott, S. Abraham, F. Acernese, K. Ackley, C. Adams, R. X. Adhikari, V. B. Adya, C. Affeldt, M. Agathos, and et al., “GW190814: Gravitational Waves from the Coalescence of a 23 Solar Mass Black Hole with a 2.6 Solar Mass Compact Object,” *ApJL*, vol. 896, p. L44, June 2020.
28. The LIGO Scientific Collaboration, the Virgo Collaboration, the KAGRA Collaboration, R. Abbott, H. Abe, F. Acernese, K. Ackley, N. Adhikari,

- R. X. Adhikari, V. K. Adkins, and et al., “Constraints on the cosmic expansion history from GWTC-3,” *arXiv e-prints*, p. arXiv:2111.03604, Nov. 2021.
29. G. Dály, R. Díaz, F. R. Bouchet, Z. Frei, J. Jasche, G. Lavaux, R. Macas, S. Mukherjee, M. Pálfi, R. S. de Souza, and et al., “GLADE+: An Extended Galaxy Catalogue for Multimessenger Searches with Advanced Gravitational-wave Detectors,” *arXiv e-prints*, p. arXiv:2110.06184, Oct. 2021.
30. R. Gray *et al.*, “Cosmological inference using gravitational wave standard sirens: A mock data analysis,” *Phys. Rev. D*, vol. 101, no. 12, p. 122001, 2020.
31. D. F. Chernoff and L. S. Finn, “Gravitational Radiation, Inspiring Binaries, and Cosmology,” *ApJL*, vol. 411, p. L5, July 1993.
32. S. R. Taylor, J. R. Gair, and I. Mandel, “Cosmology using advanced gravitational-wave detectors alone,” *Phys. Rev. D*, vol. 85, p. 023535, Jan. 2012.
33. W. M. Farr, M. Fishbach, J. Ye, and D. E. Holz, “A Future Percent-level Measurement of the Hubble Expansion at Redshift 0.8 with Advanced LIGO,” *ApJ*, vol. 883, p. L42, Oct. 2019.
34. S. Mastrogiovanni, K. Leyde, C. Karathanasis, E. Chassande-Mottin, D. A. Steer, J. Gair, A. Ghosh, R. Gray, S. Mukherjee, and S. Rinaldi, “On the importance of source population models for gravitational-wave cosmology,” *Phys. Rev. D*, vol. 104, p. 062009, Sept. 2021.
35. C. Meegan *et al.*, “The Fermi Gamma-Ray Burst Monitor,” *Astrophys. J.*, vol. 702, pp. 791–804, 2009.
36. A. von Kienlin *et al.*, “INTEGRAL spectrometer SPI’s GRB detection capabilities. GRBs detected inside SPI’s FoV and with the anticoincidence system ACS,” *Astron. Astrophys.*, vol. 411, pp. L299–L306, 2003.
37. B. P. Abbott *et al.*, “Properties of the binary neutron star merger GW170817,” *Phys. Rev.*, vol. X9, no. 1, p. 011001, 2019.

38. B. P. Abbott *et al.*, “A gravitational-wave standard siren measurement of the Hubble constant,” *Nature*, vol. 551, no. 7678, pp. 85–88, 2017.
39. X. Zhu, E. Thrane, S. Osłowski, Y. Levin, and P. D. Lasky, “Inferring the population properties of binary neutron stars with gravitational-wave measurements of spin,” *Phys. Rev. D*, vol. 98, p. 043002, 2018.
40. S. Nissanke, D. E. Holz, S. A. Hughes, N. Dalal, and J. L. Sievers, “Exploring short gamma-ray bursts as gravitational-wave standard sirens,” *Astrophys. J.*, vol. 725, pp. 496–514, 2010.
41. K. Hotokezaka, E. Nakar, O. Gottlieb, S. Nissanke, K. Masuda, G. Hallinan, K. P. Mooley, and A. T. Deller, “A Hubble constant measurement from superluminal motion of the jet in GW170817,” *Nature Astronomy*, vol. 3, pp. 940–944, July 2019.
42. S. Mukherjee, G. Lavaux, F. R. Bouchet, J. Jasche, B. D. Wandelt, S. M. Nissanke, F. Leclercq, and K. Hotokezaka, “Velocity correction for Hubble constant measurements from standard sirens,” *Astron. Astrophys.*, vol. 646, p. A65, 2021.
43. M. J. Graham, B. McKernan, K. E. S. Ford, D. Stern, S. G. Djorgovski, M. Coughlin, K. B. Burdge, E. C. Bellm, G. Helou, A. A. Mahabal, and et al., “A light in the dark: searching for electromagnetic counterparts to black hole-black hole mergers in LIGO/Virgo O3 with the Zwicky Transient Facility,” *arXiv*, p. arXiv:2209.13004, Sept. 2022.
44. B. McKernan, K. E. S. Ford, I. Bartos, M. J. Graham, W. Lyra, S. Marka, Z. Marka, N. P. Ross, D. Stern, and Y. Yang, “Ram-pressure stripping of a kicked Hill sphere: Prompt electromagnetic emission from the merger of stellar mass black holes in an AGN accretion disk,” *Astrophys. J. Lett.*, vol. 884, no. 2, p. L50, 2019.
45. H.-Y. Chen, C.-J. Haster, S. Vitale, W. M. Farr, and M. Isi, “A Standard Siren Cosmological Measurement from the Potential GW190521 Electromagnetic Counterpart ZTF19abanrhr,” 9 2020.
46. V. Gayathri, J. Healy, J. Lange, B. O’Brien, M. Szczepanczyk, I. Bartos, M. Campanelli, S. Klimentko, C. O. Lousto, and R. O’Shaughnessy,

- “Measuring the Hubble Constant with GW190521 as an Eccentric black hole Merger and Its Potential Electromagnetic Counterpart,” *Astrophys. J. Lett.*, vol. 908, no. 2, p. L34, 2021.
47. S. Mukherjee, A. Ghosh, M. J. Graham, C. Karathanasis, M. M. Kasliwal, I. Magaña Hernandez, S. M. Nissanke, A. Silvestri, and B. D. Wandelt, “First measurement of the Hubble parameter from bright binary black hole GW190521,” 9 2020.
48. G. Ashton, K. Ackley, I. M. n. Hernandez, and B. Piotrkowski, “Current observations are insufficient to confidently associate the binary black hole merger GW190521 with AGN J124942.3 + 344929,” *Class. Quant. Grav.*, vol. 38, no. 23, p. 235004, 2021.
49. G. Dály, G. Galgóczi, L. Dobos, Z. Frei, I. S. Heng, R. Macas, C. Messenger, P. Raffai, and R. S. de Souza, “GLADE: A galaxy catalogue for multimessenger searches in the advanced gravitational-wave detector era,” *MNRAS*, vol. 479, pp. 2374–2381, Sept. 2018.
50. A. Palmese, J. deVicente, M. E. S. Pereira, J. Annis, W. Hartley, K. Herner, M. Soares-Santos, M. Crocce, D. Huterer, I. Magaña Hernandez, and et al., “A Statistical Standard Siren Measurement of the Hubble Constant from the LIGO/Virgo Gravitational Wave Compact Object Merger GW190814 and Dark Energy Survey Galaxies,” *ApJ*, vol. 900, p. L33, Sept. 2020.
51. A. Palmese, C. R. Bom, S. Mucesh, and W. G. Hartley, “A standard siren measurement of the Hubble constant using gravitational wave events from the first three LIGO/Virgo observing runs and the DESI Legacy Survey,” *arXiv e-prints*, p. arXiv:2111.06445, Nov. 2021.

**Status of Cosmic Microwave Background observations for the
search of primordial Gravitational Waves**

Elia Stefano Battistelli
*Physics Department, Sapienza University of Rome
P.le Aldo Moro, 5, I-00185, Rome, Italy*

Abstract

The cosmic microwave background (CMB) is one of the most powerful tools for cosmology. Its polarization could have imprinted the sign of an inflationary background of gravitational waves which is supposed to have originated at $10^{-38}/10^{-35}$ seconds after the Big Bang. Detecting this background is extremely difficult because of the weakness of the signal (if any) left on the CMB polarization and because of the need to control the systematic effects. Also, the presence of astrophysical foregrounds, the possibility of leakage from curl-free to curl-like component, including gravitational lensing, and the instrumental noise and systematics, requires sensitive detectors and smart systematic effect control. I will discuss the experimental efforts spent in this field highlighting the key observational difference and the choice that could lead, in the near future, to the detection of the curl component of the CMB polarization, a clear sign of the inflationary expansion.

1 Introduction

Cosmic inflation is a theory of exponential expansion of the Universe invoked in the cosmological standard model to explain some paradoxes and odd coincidences in the way we see our Universe. In addition, cosmic inflation makes firm predictions that all cosmologists would like to prove or confute. Inflation predicts a background of gravitational waves that could be detected using the cosmic microwave background (CMB) radiation as a giant antenna being the CMB itself everywhere in the Universe. Unfortunately, the amplitude of the gravitational waves background, in turn responsible for polarization of the CMB, is only mildly predicted. The weakness of this prediction arises from the inflationary energy scale being possibly close to the GUT energy scale.

The CMB is in fact an ether of photons which permeates the Universe. It can be considered as a relic of the early Universe as it mainly remained unchanged since its origin when the Universe was only 380000 years old, when radiation and matter decoupled. It was discovered in 1965 by Arno Penzias and Robert Wilson, two American physicists working at the Bell Laboratories, during tests and noise measurements on an antenna developed for radio-communications ³²⁾. Penzias and Wilson found a temperature of 3.5 K higher than expected and assigned this excess to the CMB. They were awarded of the Nobel prize for Physics in 1978 for this discovery. Curiously enough, the actual first measurement of the CMB was made earlier, in 1941, by the Canadian Andrew McKellar. He measured a temperature of 2.3 K using CN stellar absorption lines ²⁹⁾. Apparently McKellar made no connection to the CMB and the significance of this measurement was recognized only after the measurement of Penzias and Wilson.

Soon after its discovery, the study of the fine structures of the CMB was fully recognized to be among the most powerful tools for cosmology. The CMB frequency spectrum was clearly measured for the first time by the FIRAS experiment on board of the COBE satellite ²⁸⁾. This frequency spectrum brings in it information about the thermal history of the Universe. The frequency spectrum is that of a perfect black body, better than one part in ten thousands, at a temperature of 2.72548 ± 0.00057 K ¹⁷⁾. The same COBE satellite, actually discovered another feature of the CMB: tiny anisotropies imprinted in its map ³⁶⁾. Since then, measurements of the CMB anisotropies and the power spectrum that describes their sky distribution have enormously improved until

the recent full sky measurements made by Planck satellite ³⁵⁾, see e.g. figure 1.

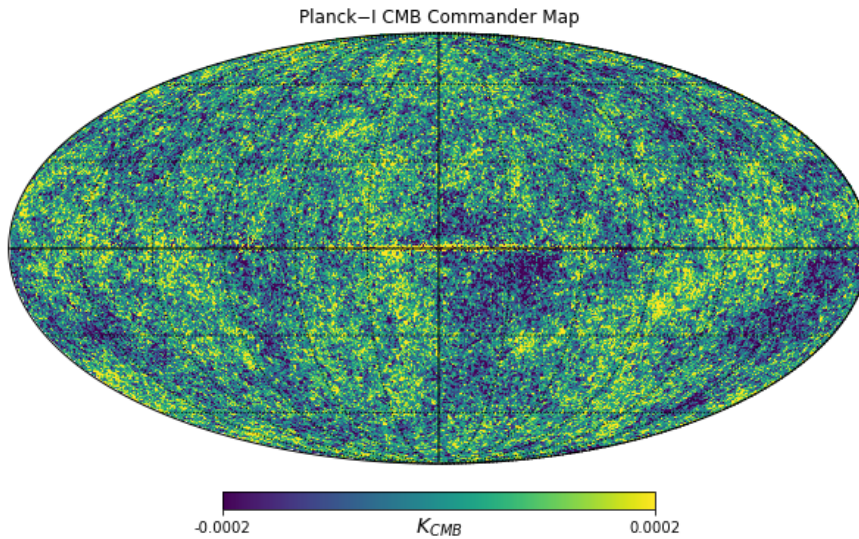


Figure 1: CMB anisotropies map obtained from Planck satellite analyzed with commander pipeline

Another feature in the CMB maps is a tiny level of polarization present in there. Because of the physics of acoustic oscillations which creates CMB anisotropies (scalar perturbations), a certain degree of polarization is expected, and observed, in the CMB maps ²⁴⁾. This can be actually observed only if a local quadrupole moment is present in the primordial plasma. Because of the symmetry in the collapsing fluid, a level of polarization is expected to be spatially correlated with primary anisotropies, to have a curl-free polarization pattern with an even parity: this polarization patterns are called E-modes for similarity to electric field, in opposition to the curl component, odd parity, which are called B-modes. B-modes are not expected to be originated by the motion of the oscillating primordial fluid. However, a stochastic background of gravitational waves, because of their symmetry properties, could create the conditions for which B-modes polarization is created.

2 Inflation

Inflation (19, 25, 38) is a theory which was invoked to explain evidences in our Universe, otherwise difficult to explain, such as the horizon problem, the absence of magnetic monopoles, and the apparent flatness in the geometry of the Universe. Why our Universe consists of many very similar regions which were not causally connected among them? How can the Universe be so uniform and its geometry very close to a flat geometry if this would be an unstable solution of the cosmological standard model? Inflation can explain these apparent paradoxes and can in principle be observed by means of the detection of the curl component of the polarization of the CMB, the B-modes, originated by a stochastic background of gravitational waves (tensor perturbations) generated during the inflationary exponential expansion of the Universe. The search for the signature of an inflationary expansion of the Universe is in its very early stage. It is the next milestone in modern cosmology. Inflation should have occurred when the Universe was only $\sim 10^{-33}$ s old and should have lasted $\sim 10^{-36}$ s (21). Inflation is driven by a negative-pressure vacuum energy density. One of the most popular scalar fields, responsible for inflation, is a slow rolling scalar field which should, among the rest, create the quantum fluctuations at the origin of the scalar perturbations responsible for the primary CMB anisotropies. In other words, the Cosmological Standard Model is self-consistent but fails to explain what has happened at the quantum gravity energy at $T > 10^{27}$ K or $E > 10^{14}$ GeV when the Universe was $\sim 10^{-33}$ s old (38).

The energy scale (the potential V) at which inflation took place, can be described in terms of the ratio between the amplitude of tensor and scalar fluctuations, the tensor-to-scalar ratio r (25):

$$V^{1/4} \approx \left(\frac{r}{0.01} \right)^{1/4} (10^{16} \text{ GeV}) \quad (1)$$

Since inflation was first proposed, several models were proposed at different energy scales. Given the limits of the energy scale of inflation more and more stringent, most proposed models are not considered anymore. A simple model is the Single-Field Slow-Roll, SFSR. Inflation is associated to the displacement of the scalar field from the minimum of its potential V (43). A value of r close to 0.01 would imply an energy scale close to what is theoretically foreseen by grand unified theories of fundamental interactions. It is worth stressing, however, that there is no firm prediction for the value of r

in inflationary models. Also, it is unclear what particle drives inflation. The best candidate is a spin-zero field, a boson, and it was proposed that Higgs boson, under certain circumstances of non-minimal coupling of the Higgs field to gravity, is at the origin of the exponential expansion of the Universe and the creation of the background of gravitational waves we all are looking for. It should be stressed however, that the scalar field responsible for inflation has a value of about the Planck mass. The Higgs mass is $\simeq 125$ GeV, a factor 10^{17} smaller so the connection between the Higgs field and the inflationary field is still unclear.

Another important connection that should be established is the possibility to use multimessenger astronomy to increase the sensitivity of the search for gravitational background and have a clearer insight into the physics of inflation. The possibility to cross correlate gravitational waves data from experiments such as LIGO or Virgo ²⁾ with those of CMB polarization such as Planck ³⁵⁾ is a fascinating possibility. This cross-correlation should leverage the power of cross correlating two data sets, to go inside the noise of either the Gravitational Waves data set produced by Ligo or Virgo collaborations, or the CMB polarization full-sky maps, for instance by Planck, in order to extract primordial gravitational wave background signature. This method could increase the sensitivity and the systematic control of such a search.

3 Cosmic Microwave Background observations

Observations of the CMB in the last $\simeq 30$ years have gone through an enormous improvement in terms of sensitivity, number of detectors and observational techniques, allowing us to enter in the era of the so-called precision cosmology. The measurement of the CMB frequency spectrum is probably the only field where not such improvement have been produced, leaving us at a similar upper limits, for the deviation from a pure Black Body, as those observed by FIRAS experiment ¹⁷⁾. The reason for this difficulty has to be searched in the extreme arduousness of making monopole (the absolute CMB temperature averaged all over the sky) measurements from ground as opposed to differential measurements which more easily remove common mode emission from atmosphere. On the other hand, CMB anisotropies have reached an unprecedented level of precision and angular resolution. In Fig. 2 it is reported the observational status on CMB anisotropies obtained from experiments with different frequency and

angular resolution capabilities such as Planck, ACTPol, and SPT experiments. The low- l uncertainties is due to the Cosmic Variance and not to the experiment noise. This is the uncertainty due to the fact that we can only observe one realization of all the possible realizations of observable universes and it is clearly stronger at large angular scales where this effect gets maximized. At multipoles l up to 500/600, the measurement is dominated by the full-sky maps of Planck Satellite ³⁵⁾, which set the ultimate limit. At higher multipoles, the higher angular resolution of experiments such as the Atacama Cosmology Telescope (ACT ⁴⁰⁾) or the South Pole Telescope (SPT ¹¹⁾) allow us to detect several acoustic peaks of the CMB angular power spectrum. However, observations can still be improved as only $\simeq 10\%$ of the sky has been observed at high resolution.

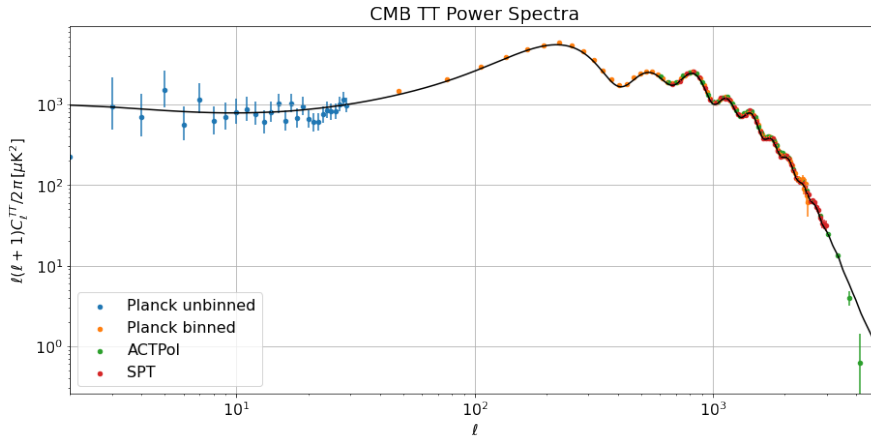


Figure 2: CMB anisotropies power spectrum. Data were obtained from ACT-Pol, Planck and SPT experiments. At low multipoles l , large angular scales, Planck data have been left unbinned (not averaged over the multipoles l) while at large multipoles l , small angular scales, the data have been binned (averaged) over $\Delta l = 30$). Data credit: NASA / LAMBDA Science Team

4 Cosmic Microwave Background Polarization: E-modes and B-modes

The CMB is characterized by some degree of polarization. Primary anisotropies are produced by acoustic oscillations of primordial plasma in or out dense and less dense over-densities²¹⁾. The motion of fluid creates the conditions of a local quadrupole because of Doppler shifts, leading to a net E-modes polarization. A local quadrupole is the condition necessary to drive to a net polarization which otherwise would be averaged out by the isotropy around the last scattering electrons. This kind of polarization is correlated to temperature anisotropies²²⁾.

Because of gravitational lensing from cosmic structures, part of the curl-free E-modes convert into a curl component: B-modes²²⁾. The effect is much larger at small angular scales and can become a problem if the value of the tensor-to-scalar ratio r is below 10^{-2} . This effect is starting being delineated by high angular resolution experiments such as ACT⁴⁰⁾, SPT¹¹⁾, or Polarbear⁴⁾.

The effect of primordial gravitational waves on CMB is however visible both at medium ($\simeq 1^\circ$) and at large (several degrees) angular scales. The primordial power spectrum has two characteristic peaks, at multipole $l \simeq 100$ and at lower multipole $l \simeq 4$, this latter due to the reionization of the Universe and thus of interest at much larger angular scales. The amplitude of these peaks is directly related to the energy scale at which inflation took place, then to tensor-to-scalar ratio r as expressed in equation 1²²⁾.

Another important point in observational CMB studies is the possibility to de-lens high angular resolutions observations to be able to infer the primordial recombination peak of the B-modes power spectrum. Also, the complementarity of the experiments in terms of foreground removal capability, spectral coverage, sky coverage and angular resolution is of great importance. Large coverage telescopes may more easily point to the reionization bump, although it is more difficult to clean a sky patch from foreground when single features are not resolved.

From the observational point of view, in fact, it is extremely difficult to hunt the reionization peak because it is necessary to map a large sky patch with good systematic control allowing observations to retrieve large angular scales. Nevertheless, a few experiments have as a goal a large sky fraction

map. Among the others, it should be mentioned CLASS¹⁵⁾, LSPE²⁶⁾, or LiteBIRD³⁹⁾ which will be discussed in the next section.

5 Experimental effort toward B-modes detection

In the following there is a list of several experiments that are now, and since some time, setting the agenda in the field of B-modes detection. This is not an exhaustive list of the existing (or planned) experiments but gives the idea of the huge world wide effort that is being spent for this detection. Most of the instruments take data with Transition Edge Sensor (TES) detectors (see e.g. 34, 10, 26, 6, 15, 40, 11, 4, 41, 23)). TES are superconductor detectors held at their critical temperature between their normal state, and their superconducting state. In this way, we have a very steep dependence of the detector resistance with temperature which makes TES extremely sensitive thermometers. TES are the state of the art for millimetric astronomy. However, new techniques have recently started to be developed, such as Kinetic Inductance Detectors³¹⁾. The desire to improve the sensitivity of experiments is a major driver in this field. In order to improve sensitivity, dry and high altitude sites are selected in order to reduce the effect of atmosphere emission and fluctuations. Once the detectors are limited by the incoming radiation (photon noise limited), the only way to improve an experiment sensitivity is to increase the number of detectors and effectively increase the integration time. TES allow to field large arrays of detectors and, consequently, large field of views, thanks also to the easiness in multiplexing the SQUIDs that are used to read the TES. Large cryogenic detector arrays carry the difficulty to read them out, as well as a large thermal input for cryostat. In order to overcome this issue, multiplexing techniques have been developed to reduce number of wires and thermal input into the coldest stages of a cryostat. Dedicated Read-out electronics based on Field Programmable Gate Array (FPGA) have been and will be key toward this development.

Another important point is the complementarity of different experiments. Large fractions of the sky need to be mapped to obtain sensitive results, however, only with high angular resolution one can hope to reach large multipoles and remove foreground from the CMB maps. Large fractions of the sky can be obtained with dedicated scanning strategy, from particular site on Earth or from satellite, however, large telescopes, required for high angular resolu-

tions, cannot be sent on a space borne platform. Many experiments observe the sky from the southern hemisphere but there are few that aim to observe large fraction of the northern hemisphere sky. In the following, it is given specific examples of the interplay between large sky coverage and large telescope aperture.

5.1 High angular resolution CMB polarimeters

The possibility to detect CMB anisotropies and their polarization with high enough angular resolution (*i.e.* $\sim 1'$) opens great possibility, among the rest, to effectively perform the de-lensing activity necessary for an effective B-modes detection. Gravitational structures, in fact, act to smooth the acoustic peaks in temperature and E-mode CMB polarization power spectra, in addition to convert part of the E-modes into B-modes. Also, if telescopes are designed with large enough field of view, they can definitely hunt for primordial recombination bump in the B-modes power spectrum. Among other instruments, it should be cited the Atacama Cosmology Telescope (ACT ⁴⁰), the South Pole Telescope (SPT ¹¹) and PolarBear ⁴.

From 2008, ACT, a 6m telescope fielded in the Atacama Desert at 5200m a.s.l., has been taking data with three instruments: the first, Millimeter Bolometer Array Camera (MBAC ⁴⁰) had three independent sets of optics with filled arrays of detectors, cooled at 300 mK, at frequencies of 148, 218 and 277 GHz, and was not sensitive to polarization. The second, ACTPol ⁴¹, started taking data in 2013 and has used feedhorn-coupled, polarization-sensitive detectors, 100 mK cryogenics with continuous cooling: two arrays centered at 148 GHz and one array operating at both 97 and 148 GHz. The third instrument, AdvACT, takes data in five frequency bands, from 27 to 230 GHz: one high-frequency 150/230 GHz and two mid-frequency 90/150 GHz feedhorn-coupled, polarization-sensitive multichroic detectors, with low-frequency 27/39 GHz arrays which recently replaced one 90/150 GHz array for synchrotron monitoring. ACT uses TES with Time Domain Multiplexing technique.

The SPT is a 10m telescope taking data from the South Pole station in Antarctica. It also has fielded three generation of instruments: SPT-SZ, SPTpol, and SPT-3G ³⁷). With 1.2' FWHM beam at 150 GHz, SPT can reach high multipole with its 2690 dual-polarization detectors, with triple frequency capability. SPT-3G has currently about 16,000 TES read out using frequency-

domain multiplexing readout.

The Polarbear experiment measures CMB polarization using 1274 TES cooled at 0.3 K through a lenslet-coupled double-slot dipole antennas working at 150 GHz. Polarbear uses frequency-domain multiplexing to read its TES 3).

All these three experiments are carrying out very precise measurements which are allowing and will allow soon to measuring or setting upper limits in the B-modes power spectrum, especially for the lensing part at large multipoles, as shown in Fig. 3. Further improvements are then expected from data of these three experiments plus experiments such as Simons Observatory 5) and Stage 4 1) whose experimental effort starts from the aforementioned experiments (see later for details).

5.2 Hunting the recombination bump from ground

The best sites on Earth to do sensitive CMB measurements are those with low content of precipitable water vapour. The most sensitive experiments are located in the Atacama Desert and in the Antarctic continent. In the Amundsen-Scott base, in the South Pole in Antarctica, the BICEP-Keck collaboration has been installing instruments since 2008 10). The BICEP-Keck instruments are expressly and uniquely devoted to the B-modes search. They are nowadays giving the most stringent upper limit on the value of the tensor-to-scalar ratio r . The BICEP2, Keck Array and BICEP3 instruments recently released their ultimate upper limit joining the data from BICEP2, Keck Array, and BICEP3, up to 2018, with those of Planck and WMAP. BICEP/Keck Array results reach depths of 2.8, 2.8 and 8.8 $\mu\text{K}_{cmb}/\text{arcmin}$ at 95, 150 and 220 GHz over an area of $\simeq 600$ square degrees at 95 GHz and $\simeq 400$ square degrees at 150 and 220 GHz. They set an upper limit of $r < 0.036$ which is so far the most stringent limit on r .

On the Argentinian site of the Atacama Desert, an international collaboration is installing a new experiment which is devoted to the search of the B-modes: the Q and U Bolometric Interferometer for Cosmology (QUBIC 20, 30, 42, 34, 27, 14, 12, 33). QUBIC is a novel instrument which combines the sensitivity of TES bolometers with the high control of systematics that only interferometers can have. It will take data at 150 GHz and 220 GHz and it is now undergoing diffuse calibration. QUBIC will take data with 2048

TES at the two frequencies with 128:1 time domain multiplexing technology based on 128 SQUIDs cooled at 1 K. With three years of integration, simulations show that QUBIC can achieve a statistical sensitivity to the effective tensor-to-scalar ratio of $\sigma(r) = 0.015$. This is another example of complementarity. Besides the sensitivity that QUBIC will be able to reach, it will be a unique experiment for efficiently removing systematic effects and, thank to its spectral capability, another feature intrinsic to interferometry ³⁰⁾, will allow more efficiently to disentangle CMB from foregrounds.

5.3 Hunting the recombination bump from the stratosphere

Since Boomerang experiment ⁹⁾, and probably even earlier ⁸⁾, the stratosphere has been recognized to be a great place to make CMB measurements. A Long Duration Balloon (LDB) experiment has the advantage of being substantially outside the atmosphere (LDB's fly at $\simeq 40$ km altitude in the stratosphere) with the cost of an instrument which is similar to that of a ground experiment, and much lower than that of a satellite. In addition, LDB can field new technology relaxing the mandatory requirements for space borne experiments concerning the readiness level of new technologies. The request for appropriate sub-orbital technological readiness level is still a driver but not as stringent as for space borne experiments and this allows the scientific community even to make progress in the readiness levels.

The SPIDER experiment ⁶⁾ flew from Antarctica in 2015 with different arrays of TES bolometers in two different frequencies: 815 TES at 150 GHz and 675 TES at 95 GHz. SPIDER set an upper limit on B-modes at a level of $r < 0.11$. SPIDER uses Time Domain Multiplexing and dedicated electronics to read its detectors ⁷⁾.

The Primordial Inflation Polarization Explorer (PIPER ²³⁾) is another balloon-borne experiment which aims at measuring the B-modes of the CMB from the stratosphere. It consists of two telescopes cooled at 1.7 K thanks to a liquid helium bucket dewar with no windows between the LHe-cooled telescope and the ambient environment. Each telescope uses a pair of 32×40 TES in a range of 4 frequency bands: 200, 270, 350 and 600 GHz. Through a series of conventional balloon flights, the PIPER collaboration aims to measure the primordial tensor-to-scalar ratio at a level of $r < 0.007$ at 95% CL.

5.4 Reionization bump

Another possibility to detect the inflationary gravitational wave background is to try to measure the reionization bump at large angular scale, i.e. $l < 10$ (see Fig. 3). This bump originates from gravitational waves interacting with ionized matter at later times and thus it is a signal which characterizes a large portion of the sky.

The Large Scale Polarization Explorer (LSPE ²⁶) is another B-modes experiment composed by a ground based coherent receiver, STRIP ¹⁸), and a balloon borne experiment, SWIPE ¹³), which will map a large portion of the sky. STRIP takes advantage of its observational location at Tenerife (latitude 28° North), allowing it to use the earth rotation to map a large fraction of the sky. SWIPE will scan the sky by rotating the entire experiment flying from the northern hemisphere during winter. In this way, LSPE can perform the observations without interference from the sun entering the field of view. In order to enlarge the radiation modes reaching the detectors, SWIPE employs multimoded TES which increase the modes of radiation (and thus the sensitivity) of the detectors while paying the price of the reduced angular resolution. This happens because the amount of radiation sums coherently with the number of modes, while noise sums incoherently so the net effect is an increase of the S/N ratio and the square root of the number of modes. This is an alternative way to improve the sensitivity of an experiment.

The Cosmology Large Angular Scale Surveyor (CLASS ¹⁵) is operational in the Atacama Desert since 2016, and since 2019 with 4 frequency bands: 40, 90, 150 and 220 GHz, last two frequency bands employing dichroic detectors. CLASS takes advantage of its geographical position in the Atacama Desert, at latitude $\simeq 23^\circ$ South, to use the earth rotation to make a large map of the sky. In this way, CLASS is the only ground-based experiment to be able to address both the reionization peak and the primordial peak. CLASS recently presented calibration and on sky performance using the moon and planets ¹⁵).

5.5 Large ground-based efforts toward inflationary B-modes

The weakness of the signal to be detected, requires a joint venture of the several ground base experiments already mentioned so far. Two efforts have been funded or partially funded to try to use the different capability of the aforementioned experiments: they are the Simons Observatory, located in the

Atacama Desert, and the CMB Stage4 effort, which will be distributed in the Atacama Desert and in Antarctica.

The Simons Observatory (SO ⁵⁾) is a large effort which is being build to take data from the Atacama Desert, in the same location where ACT and PolarBear are seeing the sky. It will take data within 6 bands: 27, 39, 93, 145, 225 and 280 GHz. SO will have three small-aperture telescopes of 0.5 m and one large-aperture telescope of 6 m. It will take data with 60,000 bolometers. The small aperture telescopes will have a large sky coverage and will thus hunt the largest angular scales with a high mapping speed. Their forecast predict a level on sensitivity in r of the order of $\sigma(r) = 0.003$.

The CMB Stage4 (CMB-S4, ¹⁾) is a project which aims at unifying the large effort already spent for ground observation of the CMB. It is the next generation experiment and is formed by a series of telescopes located both in the Atacama Desert and in South Pole. It intends to be the definitive ground-based CMB polarization experiment. CMB-S4 plans to measure the sky with 500,000 detectors in seven years using fourteen small aperture telescope and one "delensing" telescope. CMB-S4 is predicted to see a tensor-to-scalar ratio r greater than 0.003 at more than 5σ and, in the absence of a detection, to place an upper limit of $r < 0.001$ at 95% CL.

5.6 Hunting B-modes from space

LiteBIRD ³⁹⁾ is the next CMB space mission after COBE, WMAP and Planck. It was selected by the Japan Aerospace Exploration Agency (JAXA) in May 2019. LiteBIRD will orbit around the Sun-Earth Lagrangian point L2 and it will measure the CMB using three telescopes. A reflective telescope for the lower frequencies (Low Frequency Telescope, LFT) with 400 mm aperture and angular resolution ranging from 24 to 71 arcminutes. LFT will take data in nine frequency bands spanning from 34 to 161 GHz in order to be able to detect both CMB and synchrotron radiation. Two refractive telescopes have been designed for the Medium and High Frequency ranges (MHFT). The frequency band is divided in 89 to 224 GHz for the Medium and Frequency Telescope (MFT), and 166 to 448 GHz for the High Frequency Telescope (HFT). LiteBIRD will reach unprecedented total sensitivity to CMB polarization with a typical angular resolution of 0.5° . LiteBIRD will take data with 1030 multi-chroic pixels for a total of 4508 TES, distributed over the three telescopes. The TES will be read

out using a Frequency Domain Multiplexing scheme borrowing from a scheme already in use with the SPT or PolarBear.

Forecasts predict that LiteBIRD will reach a tensor-to-scalar ratio limit of $r < 0.001$. This would be done probing both the recombination bump and the reionization. This sensitivity will either detect primordial gravitational waves or rule out inflationary models within the currently predicted scenarios. Favorable scenarios predict models with $r \simeq 0.01$ (22). In this case, LiteBIRD would detect them with more than 10σ precision.

6 Conclusions

As we have seen, the hunt for B-modes is in its greatest development thanks to balloon born, ground based and satellite experiments which are planned and taking data. Optical design, polarization modulators, and cryogenic techniques have been increasingly matured but the field that is probably giving the strongest impulse is the design of detectors. Progress on detectors sensitivity is impressive and improved technologies are being developed and deployed in addition to the standard TES technology which is the one that for the moment is filling the instruments focal planes. Detectors need to get a sensitivity of few $10^{-18}W/\sqrt{Hz}$. Focal planes are saturated so we need multiple telescopes and/or parallel processing or multimoded approach. TES are the most mature technology but Kinetic Inductance Detectors (KIDs) promise a great development for their easiness in building and in multiplexing.

Predictions affirm that Stage 3 experiments (those who are now taking data) will probably reach a sensitivity of $\sigma(r) \simeq 0.01$. We have to wait until SO and Stage 4 to reach a sensitivity of $\sigma(r) \simeq 0.001$. In this contest we should ask ourselves: will the systematic control be able to catch up? We need a fiducial model which would include multiple components such as thermal dust, synchrotron, and Anomalous Microwave Emission (AME). In fact, thermal dust and synchrotron polarized emission can be orders of magnitude larger than CMB B-modes depending on the frequency and on the sky portion it is observed. For instance, in a particularly clean region of the sky, at the minimum of their summed emission (i.e. $\simeq 70\text{GHz}$) synchrotron and thermal dust emission can be a few μK while B-modes can be a few tens of nK for $r=0.01$. On the other hand, AME, is still an emission which lacks of predictivity. It will have to be understood and monitored especially if it comes to be polarized. If there are

departures from the fiducial model than AME will be a problem for B-modes detection¹⁶). Also, will the data-analysis effort follow?

The quest for B-modes is clearly very challenging. So far, no single experiment could lead to a detection but only upper limits could be established. A possibility to amplify experiments sensitivity, would be to use the aforementioned cross-correlation between CMB polarimeters and gravitational waves experiments. Once a full sky map of gravitational waves will be available, this still unexplored technique could start giving results in a separate work. In any case, the joint effort of several different experiments could lead to a significant improvement of the sensitivity but another important point is the capability to control of the systematics and especially when this is carried out with different observational techniques. An example of this is the bolometric interferometry that QUBIC is implementing. Also, the spectral capability and the wide number of bands is going to be key to disentangle CMB B-modes from foreground signals.

Acknowledgements

ESB would like to acknowledge the organizers of the Vulcano workshop for the kind invitation.

References

1. Abazajian K., et al., CMB-S4 Science Case, Reference Design, and Project Plan. *arXiv:1907.04473* (2019).
2. Abbott B.P. et al., GWTC-1: A Gravitational-Wave Transient Catalog of Compact Binary Mergers Observed by LIGO and Virgo during the First and Second Observing Runs. *Phys. Rev. X*, **9**, 031040 (2019).
3. Adachi S. et al., A Measurement of the Degree-scale CMB B-mode Angular Power Spectrum with Polarbear. *ApJ*, **897** 1 (2020).
4. Ade P.A.R. et al., A Measurement of the Cosmic Microwave Background B-Mode Polarization Power Spectrum at Sub-Degree Scales with POLARBEAR. *ApJ*, **794**, 171 (2014).

5. Ade P.A.R. et al., The Simons Observatory: science goals and forecasts. *JCAP*, **2**, 56 (2019).
6. Ade P.A.R. et al., A Constraint on Primordial B-modes from the First Flight of the SPIDER Balloon-borne Telescope. *ApJ*, **927**, 2, 174 (2022).
7. Battistelli E.S. et al., Functional Description of Read-out Electronics for Time-Domain Multiplexed Bolometers for Millimeter and Sub-millimeter Astronomy. *Journal of Low Temperature Physics*, **151**, 3-4, 908-914 (2008).
8. de Bernardis P. et al., The ARGO project: Scientific targets, first results and future perspectives. *Il Nuovo Cimento C*, **15**, 993-1011 (1992).
9. de Bernardis P. et al., A flat Universe from high-resolution maps of the cosmic microwave background radiation. *Nature*, **404**, 6781, 955 (2000).
10. BICEP Keck collaboration et al., BICEP / Keck XIII: Improved Constraints on Primordial Gravitational Waves using Planck, WMAP, and BICEP/Keck Observations through the 2018 Observing Season. *Phys. Rev. Lett.*, **127** 151301 (2021).
11. Carlstrom J. et al., The 10 Meter South Pole Telescope. *PASP*, **123**, 568 (2011).
12. Cavaliere F. et al., QUBIC VII: The feedhorn-switch system of the technological demonstrator. *JCAP*, **2022** , 04, 40 (2022).
13. Columbro F. et al., SWIPE Multi-mode Pixel Assembly Design and Beam Pattern Measurements at Cryogenic Temperature. *Journal of Low Temperature Physics*, **199** , 1-2, 312-319 (2020).
14. D'Alessandro G. et al. QUBIC VI: Cryogenic half wave plate rotator, design and performance. *JCAP*, **2022** , 04, 39 (2022).
15. Dahal S. et al., Four-year Cosmology Large Angular Scale Surveyor (CLASS) Observations: On-sky Receiver Performance at 40, 90, 150, and 220 GHz Frequency Bands. *ApJ*, **926**, 33 (2022).
16. Dickinson C. et al., The State-of-Play of Anomalous Microwave Emission (AME) research. *New Astronomy Reviews*, **80**, 1-28 (2018).

17. Fixsen, D. J., The Temperature of the Cosmic Microwave Background. *ApJ*, **707**, 2, 916-920 (2009).
18. Franceschet, C., The LSPE-Strip feed horn array. *Journal of Instrumentation*, **17**, 01, P01029 (2022).
19. Guth A.H., The inflationary universe: a possible solution to the horizon and flatness problems. *Phys. Rev. D*, **23** (1981).
20. Hamilton J-C. et al. ,QUBIC I: Overview and science program. *JCAP*, **2022** , 04, 34 (2022).
21. Hu Wayne, and Martin White, A CMB Polarization Primer. *New Astronomy*, **2**, 323 (1997).
22. Kamionkowski M. et al., The Quest for B Modes from Inflationary Gravitational Waves.*Ann. Rev. Astron. Astrophys*, **54**, 227 (2016).
23. Kogut A. et al., The Primordial Inflation Polarization Explorer (PIPER): Science Goals. *Bulletin of the AAS*, **52**, 3 (2020).
24. Kovac J. et al., Detection of Polarization in the Cosmic Microwave Background using DASI. *Nature*, **420**, 772-787 (2002).
25. Linde A.D., A new inflationary universe scenario: a possible solution of the horizon, flatness, homogeneity, isotropy and primordial monopole problems. *Phys. Rev. D*, **108** (1982).
26. The LSPE collaboration, The large scale polarization explorer (LSPE) for CMB measurements: performance forecast. *JCAP*, **2021** (2021).
27. Masi S. et al., QUBIC V: Cryogenic system design and performance. *JCAP*, **2022** , 04, 38 (2022).
28. Mather, J. C., et al., Measurement of the Cosmic Microwave Background Spectrum by the COBE FIRAS Instrument. *ApJ*, **420**, 2, 439 (1994).
29. McKellar A., Molecular Lines from the Lowest States of Diatomic Molecules Composed of Atoms Probably Present in Interstellar Space. *Publications of the Dominion Astrophysical Observatory* **1941**, 251, 32-58 (1941).

30. Mousset L. et al., QUBIC II: Spectral polarimetry with bolometric interferometry. *JCAP*, **2022** , 04, 35 (2022).
31. Paiella A. et al., In-Flight Performance of the LEKIDs of the OLIMPO Experiment. *Journal of Low Temperature Physics* **199**, 1-2, , 491-501 (2020)
32. Penzias A. A. and Wilson R. W., A Measurement of Excess Antenna Temperature at 4080 Mc/s. *ApJ* **1965**, 142, 419–421 (1965).
33. O’Sullivan C. et al., QUBIC VIII: Optical design and performance. *JCAP*, **2022** , 04, 41 (2022).
34. Piat M. et al., QUBIC IV: Performance of TES bolometers and readout electronics. *JCAP*, **2022** , 04, 37 (2022).
35. Planck collaboration, Planck 2018 results I: Overview and the cosmological legacy of Planck. *A&A*, **641**, A1 (2020).
36. Smooth, G. F., et al., Structure in the COBE differential microwave radiometer first-year maps. *ApJL*, **396**, L1-L5 (1992).
37. Sobrin J.A. et al., The Design and Integrated Performance of SPT-3G. *ApJS*, **258** 2 (2022).
38. Starobinsky A.A., Spectrum of relict gravitational radiation and the early state of the universe. *JETP Lett.*, **30**, 682-685 (1980).
39. Sugai H. et al., Updated Design of the CMB Polarization Experiment Satellite LiteBIRD. *JLTP*, **199** 1107 (2020).
40. Swetz D. et al., OVERVIEW OF THE ATACAMA COSMOLOGY TELESCOPE: RECEIVER, INSTRUMENTATION, AND TELESCOPE SYSTEMS. *ApJS*, **194**, 41 (2011).
41. Thornton R.J. et al., THE ATACAMA COSMOLOGY TELESCOPE: THE POLARIZATION-SENSITIVE ACTPol INSTRUMENT. *ApJS*, **227** 21 (2016).
42. Torchinsky S. et al., QUBIC III: Laboratory characterization *JCAP*, **2022** , 04, 36 (2022).

43. Tristram M. et al., Planck constraints on the tensor-to-scalar ratio. *A&A*, **647**, A128 (2021).

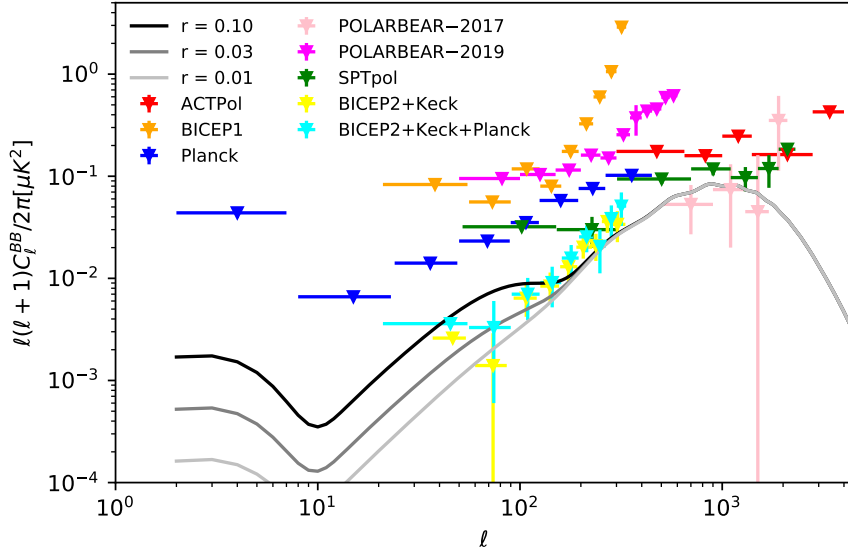


Figure 3: Some observed B-mode power from CMB experiments. x-axis is a logarithmic scale of the multipoles l while y-axis reports the temperature fluctuations of B-modes. The factor $l(l+1)$ ensures that $l(l+1)C_l$ is constant at low l for a nearly scale-invariant spectrum of density perturbations. Data with error bars on the y-axis are significant detections, while the remaining are 95% upper limits. Data were taken from NASA/LAMBDA website. Theoretical curves for $r = 0.1$ and $r = 0.01$ are shown respectively with black and grey lines.

WILL PULSAR TIMING ARRAYS OBSERVE THE HELLINGS AND DOWNS CORRELATION CURVE?

Bruce Allen

MPI for Gravitational Physics, Callinstrasse 38, 30167 Hannover, Germany

Abstract

Pulsar timing arrays seek to detect gravitational waves (GW) by observing correlations which were predicted by Hellings and Downs in 1983. Here, we address the question, are these correlations going to be exactly what was predicted in 1983? The answer is no: interference between different GW sources creates a pattern of correlation that does not average to give the Hellings and Downs curve. We explain this effect, calculate the variance, and show that it is potentially observable.

1 Introduction

Thank you for inviting me to this wonderful place. The Vulcano workshops are famous not just for the interesting physics, but also for the friendly colleagues, the fantastic food, and the beautiful venue.¹ I am enjoying this a

¹This sentence remains correct under all 120 permutations of the adjectives.

lot, and really hope that you ask me to return for the next workshop in 2024.

My talk concerns pulsar timing arrays (PTAs), which are a way to detect low frequency (nHz) gravitational waves (GW). These waves have periods of years, meaning frequencies that lie far below the sensitivity band of detectors such as LIGO and LISA.

The results are described in detail in two arXiv preprints. The first of those is by me ¹⁾ and the second is work done in collaboration with Joe Romano ²⁾. All of the ideas and most of the figures in my talk come from those two preprints. So if some details are lacking, or if you want to learn more about this topic, please look there.

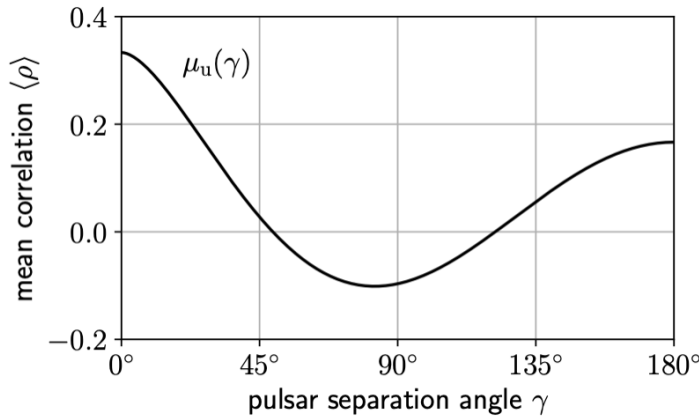


Figure 1: *The Hellings and Downs curve.*

This is the only talk about PTAs in this workshop, so I will spend some time introducing those. But I first want to show you the most important thing in my talk, which you may have seen before. This is the Hellings and Downs curve $\mu_u(\gamma)$, illustrated in Fig. 1. This function shows the average (hence the symbol “ μ ” for “mean”) correlation between the pulse arrival times (or pulsation frequency Doppler shifts) from two different pulsars, separated on the sky by angle γ as seen from Earth, induced by an unpolarized (hence the subscript “u”) isotropic GW stochastic background. For example, for two pulsars that are almost in the same direction on the sky (γ near 0°) you can see that, on the average, GWs induce correlated variations in the arrival times of the pulses. In contrast, for pulsars that are separated by about 90° on the

sky, on the average the effects of the GWs on the pulses is anticorrelated.

Observing this Hellings and Downs curve is important for PTAs. It plays the same role that the famous “chirp waveform” did for the first LIGO detection³⁾ of GWs. When we see this Hellings and Downs curve clearly, we can confidently proclaim “we have detected GWs”.

My talk addresses a simple question: should we expect to see *exactly* this curve? Or only something *close* to it? My conclusion: we will see this curve, but when enough good data is available, we will also see a certain deviation from it. While I can’t predict the sign of that deviation, I can predict its expected magnitude. Here, that expected (squared) deviation from the Hellings and Downs curve is called the variance, and is denoted by σ^2 .

2 Pulsar Timing Arrays

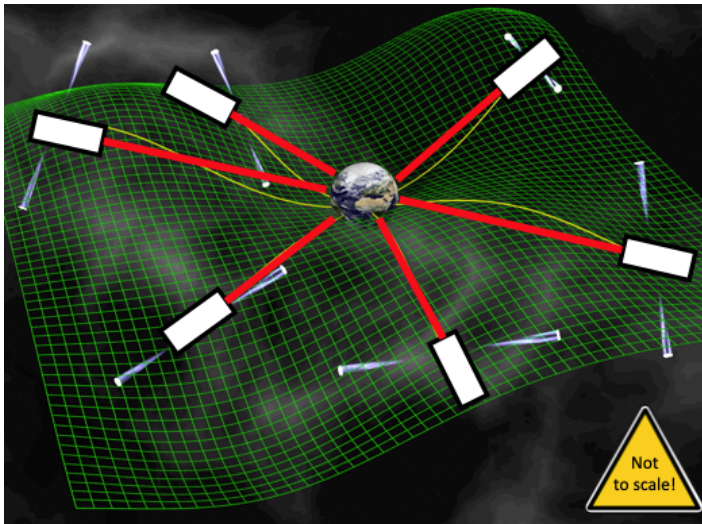


Figure 2: A pulsar timing array (PTA) made from six pulsars (a modified version of David J. Champion’s original illustration).

PTAs are galactic-scale gravitational wave detectors. Fig. 2 is a schematic diagram of a PTA made from six pulsars.² The GW sources are not shown –

²This figure is not to scale. For example, typical PTA pulsars are thousands

the nearest ones are probably at distances that are five orders of magnitude larger than the Earth-pulsar separations.

To stress that this is like a six-arm LIGO detector, in the figure I have replaced the pulsars with lasers. Conceptually, one could also replace the pulsars with perfect clocks, which tick at a few hundred Hz rather than at typical laser frequencies of 10^{15} Hz. The idea is that when a GW goes flying by, it redshifts or blueshifts those clocks.³ Because the clock frequency is so low, there is no light or color, so it might be better to say “Doppler shift”. But I keep to the tradition of the literature, which uses “redshift” and “blueshift”.

The data stream from each pulsar is a redshift $Z = \Delta f/f$ as a function of time, where f is the mean pulsation frequency and Δf is the decrease in the frequency at time t . Typical PTA pulsars are observed every week or two for decades, so the time series consists of hundreds or thousands of redshift measurements.

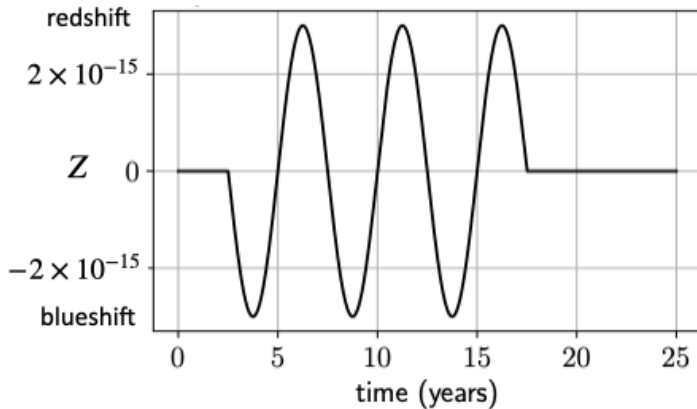


Figure 3: *Redshift/blueshift of a pulsar signal induced by a GW that oscillates through three cycles with an oscillation period of five years.*

Here is an example. Suppose that a fixed-frequency GW, consisting of

of years from Earth, but the GWs they detect, shown by the green ripples, should have wavelengths that are $O(10^2)$ times smaller.

³While pulsars are observed with terrestrial radio telescopes, their pulsation frequencies are then determined at the solar system barycenter, to remove effects of Earth’s motion and the gravitational effects of the Sun and planets.

three cycles with an oscillation period of five years, went flying by this detector. Fig. 3 shows the pattern of redshift/blueshift observed in one of these pulsars, in the absence of any noise. The maximum redshift corresponds to a lowering of the observed pulsar rotation frequency by three parts in 10^{15} . The maximum blueshift is the same fractional increase in the observed rotation frequency.

If you had a single perfect noise-free pulsar, then you could observe GWs simply by monitoring the pulse arrival times. The GW frequency is the frequency of this redshift/blueshift oscillation. The GW strain amplitude h is the maximum fractional frequency change, which in my example is $O(10^{-15})$. Because pulsars are monitored for decades with a timing precision of hundreds of nanoseconds, these small shifts are observable. However, because pulsars are not free of noise, PTAs must search for GWs by looking for a common signal, which appears the same in the different “pulsar arms”.

There are three active PTAs. The European Pulsar Timing Array (EPTA) currently monitors 42 pulsars ⁴⁾. The North American nanoHz Gravitational Wave Observatory (NANOGrav) currently monitors 66 pulsars ⁵⁾. The Parkes Pulsar Timing Array (PPTA) currently monitors 26 pulsars ⁶⁾. In all, the International Pulsar Timing Array (IPTA), which is an umbrella organization for all three PTAs, monitors 88 pulsars. (This number is smaller than you might have expected because many of the pulsars are common to two or more of the PTAs.)

The PTA data sets, which span several decades, show intriguing evidence for a stochastic background of GWs. A plausible source of these GWs is the slow orbital decay of supermassive black hole binaries ⁷⁾. We know that most galaxies have supermassive black holes at their centers. When galaxies merge, the black holes at their centers form binary systems, whose orbits decay due to interactions with other stars and with their environment. Those binaries eventually become close enough to orbit with periods of years or decades, emitting continuous gravitational waves at twice the orbital frequency. This would create a signal in the PTA band.

We expect that the closest of these supermassive black hole binaries is at a distance of order 50 Mpc, and there would be a much larger number of similar sources at greater distances, extending out to near the Hubble radius. The GW signals that these produce sum up to create a stochastic confusion-noise GW background, which has the statistical properties of a central-limit-theorem

Gaussian ensemble 8).

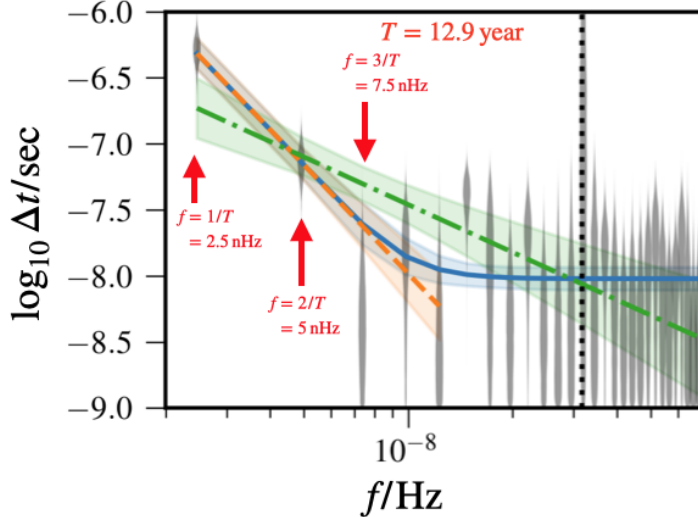


Figure 4: *The timing noise seen in the NANOGrav 12.5 year data set is consistent with a GW stochastic background. Reproduced from 5).*

Shown in Fig. 4 is $T = 12.9$ years of NANOGrav data 5); the data from other PTAs is similar 4, 6). This shows the result of Fourier-transforming the time series of pulsar timing residuals Δt , which are the time integrals of the redshift Z . The amplitudes are shown for frequency bins corresponding to the fundamental mode at $f = 1/T = 2.5$ nHz, $2/T = 5$ nHz and so on. This data, which only shows autocorrelations, has the sort of increasing amplitude at low frequencies which would be expected from a supermassive binary black hole background. The best fit power law (orange line) to the first five harmonics has a slope $\approx f^{-2.6}$. This is close to the $f^{-13/6}$ power law expected from supermassive black hole binaries. The characteristic strain amplitude $h_c \approx 1.9 \times 10^{-15}$ is also consistent with expectations for that source.

In my opinion, this is good evidence for a GW background. But there are other possible explanations. Perhaps, for example, all pulsars have some intrinsic source of rotation noise, with a power-law spectrum similar to that which would be produced by merging black hole binaries.

3 The Hellings and Downs curve $\mu_u(\gamma)$

Fortunately there is a simple way to understand if the source of these observed pulsar timing fluctuations is a GW background, and, if it is due to GWs, to gain confidence. This is to observe the pattern of correlation shown in Fig. 1. This pattern was first calculated by Ron Hellings and George Downs in 1983⁹, and is called the ‘‘Hellings and Downs curve’’. I want to describe how pulsar timing arrays might see this curve, which is described by the function

$$\mu_u(\gamma) = \frac{1}{4} + \frac{1}{12} \cos \gamma + \frac{1}{2} (1 - \cos \gamma) \log \left(\frac{1 - \cos \gamma}{2} \right). \quad (1)$$

The take-home message from my talk is that PTAs will not observe exactly this curve. However, they will observe something close to this curve, and we can predict and calculate the magnitude of the expected deviations away from it. This is what I mean by the variance in the Hellings and Downs correlation.

Here is what Hellings and Downs did in 1983. First, they placed a single distant unit-amplitude unpolarized GW source at a point Ω on the sky. (Here Ω is a unit-length three-dimensional vector.) Next, they wrote down the correlation ρ between the redshifts (or timing residuals) of two pulsars a and b , separated by an angle γ on the sky, which is

$$\begin{aligned} \rho &= \Re(F_a(\Omega)F_b^*(\Omega)) \\ &= F_a^+(\Omega)F_b^+(\Omega) + F_a^\times(\Omega)F_b^\times(\Omega). \end{aligned} \quad (2)$$

This is the product of the response of pulsar a to a GW point source at direction Ω with the response of pulsar b to that same source. The appearance of the real part, and the complex conjugate on the first line of Eq. (2), are because I use a complex polarization basis for the GWs. The real part of F is the response to the plus polarization, and (minus) the imaginary part is the response to the cross polarization: $F = F^+ - iF^\times$. The second line expresses this correlation in terms of these (real) linear polarizations. The functions F correspond to what are called ‘‘antenna patterns’’ in the context of LIGO or LISA. They depend upon the sky direction to the pulsar, as well as on the source direction Ω .

Finally, Hellings and Downs averaged the correlation ρ over all pairs of pulsars a and b separated by angle γ , assuming that these were uniformly distributed around the sky.⁴ We call this a ‘‘pulsar sky average’’. What they

⁴In fact Hellings and Downs fixed the pulsar positions and averaged over

found is exactly the function given in Eq. (1). That is to say, $\mu_u(\gamma) = \langle \rho \rangle$, where angle brackets denote the average over all pulsar pairs a, b separated by angle γ . People often call this a “quadrupole response pattern”, which is roughly correct. While it also includes higher modes, the quadrupole term is the largest one ²⁾.

The calculation corresponds to observational practice. Imagine that you are a PTA observer with access to many pulsars, distributed all around the sky. To determine the mean correlation at angle γ , you take all pairs that (within some tolerance window) are separated by angle γ , and average their correlations. This observational average can be directly compared to $h^2 \mu_u(\gamma)$, where h^2 is the characteristic squared amplitude of the GWs. (This factor of h^2 appears because the calculation that led to Eq. (1) is for a unit amplitude source of GWs.)

However, it is surely the case that our Universe is not like this simple model. As explained earlier, we expect that the Universe contains a very large number of GW point sources, rather than a single point source. So, what does the Hellings and Downs calculation and curve have to do with reality? Let us investigate this question.

4 The Hellings and Downs correlation for two GW sources

Imagine now that we have two GW sources, rather than one. For example, put the first source directly over the North pole (direction Ω_1) and the second source directly overhead us, here in Elba (direction Ω_2). We’re going to repeat the Hellings and Downs calculation, to find the average correlation of two pulsars separated by angle γ , under the influence of two GW sources.

The sources have complex waveforms $h_1(t)$ and $h_2(t)$; the real part is the plus polarization and the imaginary part is the cross polarization: $h = h^+ + ih^\times$. For simplicity, assume that both sources are unpolarized, which implies $\overline{h_1 h_1} = \overline{h_2 h_2} = 0$. (Here, the overline means “average over time”.) The real parts of these equation ensure that the average plus and cross intensities are equal, and the imaginary parts ensure that the product of the plus and cross amplitudes averages to zero. (If you look at the definition of the Stokes parameters, you’ll

source directions on the celestial sphere. From symmetry these are equivalent ¹⁰⁾.

see that this is what is meant by “unpolarized”.) The squared strain of the two GW sources are real quantities, given by $\overline{h_1 h_1^*} = |\overline{h_1}|^2$ and $\overline{h_2 h_2^*} = |\overline{h_2}|^2$ respectively.

The redshifts of pulsars a and b are obtained by summing the effects of the two GW sources:

$$\begin{aligned} Z_a &= \Re(h_1 F_a(\Omega_1) + h_2 F_a(\Omega_2)) \\ &= \frac{1}{2} (h_1 F_a(\Omega_1) + h_1^* F_a^*(\Omega_1) + h_2 F_a(\Omega_2) + h_2^* F_a^*(\Omega_2)) \\ Z_b &= \frac{1}{2} (h_1 F_b(\Omega_1) + h_1^* F_b^*(\Omega_1) + h_2 F_b(\Omega_2) + h_2^* F_b^*(\Omega_2)). \end{aligned} \quad (3)$$

Note that the final line is just the previous one with pulsar a replaced by pulsar b .

Now, we are going to consider two different possibilities for the behavior of these GW sources. In the first case, the two sources are not going to interfere with each other. This means that they are radiating at different frequencies: if we multiply their GW waveforms together and integrate over time, we get zero. Thus, $\overline{h_1 h_2} = \overline{h_1 h_2^*} = 0$. Later, I’ll consider the case where they do interfere.

By multiplying the final two lines of Eq. (3) and then time averaging the product, you can calculate the correlation $\overline{Z_a Z_b}$ between pulsars a and b . It might sound complicated, but it’s simple – you can do it in your head. There are 16 possible terms in the product, but after taking the time average, 12 terms vanish. The only nonzero terms are when h_1 multiplies h_1^* or h_2 multiplies h_2^* , giving

$$\rho = \overline{Z_a Z_b} = \frac{1}{2} \overline{|h_1|^2} \Re(F_a(\Omega_1) F_b^*(\Omega_1)) + \frac{1}{2} \overline{|h_2|^2} \Re(F_a(\Omega_2) F_b^*(\Omega_2)). \quad (4)$$

These two terms look exactly the same as Eq. (2), which Hellings and Downs used in their 1983 calculation. So if we average Eq. (4) over all pulsar pairs separated by angle γ , then we get *exactly* the Hellings and Downs curve, $\langle \rho \rangle = \frac{1}{2} (|\overline{h_1}|^2 + |\overline{h_2}|^2) \mu_u(\gamma)$. It does not matter where the independent GW sources are located on the sky relative to each other: the pulsar average always gives exactly the Hellings and Downs curve.

Now, let us repeat the calculation for GW sources that interfere. For this, assume that $\overline{h_1 h_2} = 0$ but that $\overline{h_1 h_2^*}$ is real and positive. (These equations imply that the plus components of h_1 are uncorrelated with the cross components of h_2 and vice versa. However, they also imply that the plus components of

h_1 and h_2 are correlated with each other, and that their cross components have that same degree of correlation.) As before, we need to multiply the last two lines of Eq. (3) and average over time. Again, while this might sound complicated, you can do it in your head. In addition to the four terms that appeared for uncorrelated sources, we now get four additional terms where an h_1 multiplies the complex conjugate of h_2 , or vice versa. This gives

$$\rho = \overline{Z_a Z_b} = \frac{1}{2} \overline{|h_1|^2} \Re(F_a(\Omega_1) F_b^*(\Omega_1)) + \frac{1}{2} \overline{|h_2|^2} \Re(F_a(\Omega_2) F_b^*(\Omega_2)) + \frac{1}{2} \overline{h_1 h_2^*} \Re(F_a(\Omega_1) F_b^*(\Omega_2) + F_a(\Omega_2) F_b^*(\Omega_1)). \quad (5)$$

In contrast to the case of independent sources, the cross term, proportional to the (real) time average $\overline{h_1 h_2^*}$, is nonzero. If we average this correlation ρ over all pulsar pairs separated by angle γ , the first line, which is the same as in the independent source case, averages to give the Hellings and Downs curve, *but the second line does not*. If you average the second line over all pairs of pulsars separated by angle γ , it gives a different function of angle γ than the Hellings and Downs curve. In a minute, I'll show you what that function looks like.

That's the take-home message of my talk. After the various PTAs have observed enough pulsars, and determined the average correlation at angle γ , this interference term means that they won't observe exactly the Hellings and Downs curve. This is because our Universe contains many GW sources, with independent positions and GW phases, radiating in the lowest frequency bins. These generate a standing wave pattern whose pulsar average, in any representative universe, is not the Hellings and Downs curve.

5 Variance of the Hellings and Downs correlation for many GW sources

Let us now consider what happens when there are many GW sources radiating at the same frequency, so there is lots of interference. I'll denote the number of these sources by the integer N . So now, the response of each pulsar has N terms, and the time-averaged correlation, obtained as a product, has N^2 terms. If we label the sources by $j = 1, \dots, N$, then the pulsar-averaged correlation curve is

$$\langle \rho \rangle = \sum_j h_j^2 \mu_u(\gamma) + \sum_{j \neq k} h_j h_k \cos(\phi_j - \phi_k) \mu(\gamma, \beta_{jk}). \quad (6)$$

Here, the two-point function $\mu(\gamma, \beta)$ is shown in Fig. 5, h_j is the GW amplitude of the j 'th source, $\phi_j \in [0, 2\pi)$ is the GW phase of that source, and β_{jk} is the angle on the sky between sources j and k . (From here on, h_j is just a positive real number, whereas in Sec. 4, h_1 and h_2 denoted functions of time.)

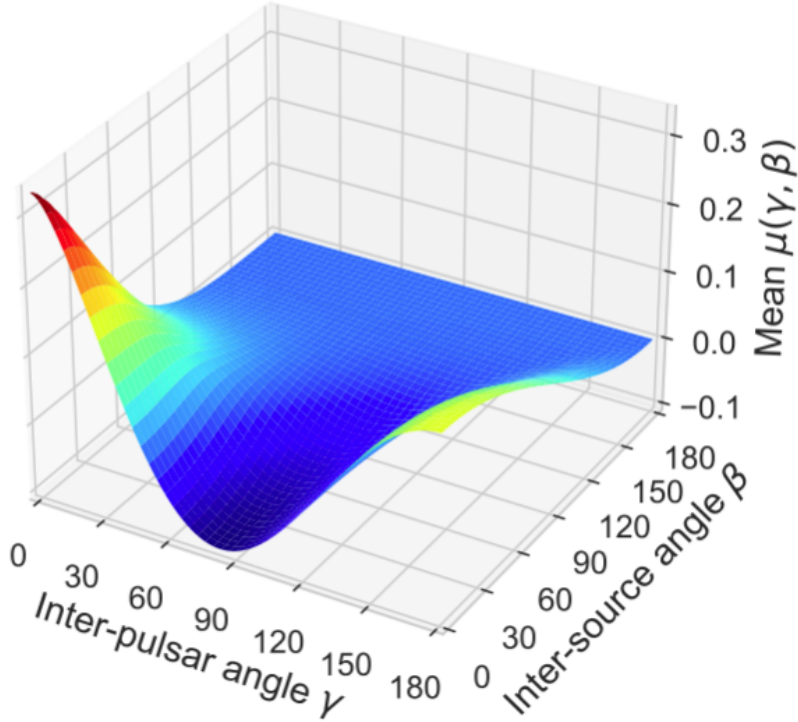


Figure 5: The two-point function $\mu(\gamma, \beta)$. The cross-section at $\beta = 0$ is the Hellings-Downs curve: $\mu_u(\gamma) = \mu(\gamma, 0)$. An explicit formula for $\mu(\gamma, \beta)$ is derived in ¹.

Look carefully at Eq. (6). The first sum is the “diagonal” terms, where source j interferes with itself. The pulsar average of these gives exactly the Hellings and Downs curve. Then there are the “off-diagonal” terms, meaning the sum over $j \neq k$. These come from different sources interfering with each other. The product of the amplitudes of those two sources is multiplied by the cosine of the phase difference between the sources. These phases are indepen-

dent random numbers, different for each source, so that the value of the cosine is uniformly distributed in the interval $[-1, 1]$. Finally, this is multiplied by a function which I call the two-point function, which is illustrated in Fig. 5.

The function $\mu(\gamma, \beta)$ is a function of the angle γ between the two pulsars, and of the angle β between the two sources. It is defined by the pulsar average

$$\mu(\gamma, \beta_{jk}) = \langle F_a(\Omega_j) F_b^*(\Omega_k) \rangle . \quad (7)$$

Here β_{jk} is the angle between the sources: $\cos \beta_{jk} = \Omega_j \cdot \Omega_k$. The angle brackets mean “average over uniformly distributed pulsars a and b separated by angle γ on the sky”. You will recognize that this is precisely the pulsar average of the extra “interference” term that appeared in Eq. (5), when we looked at two interfering GW sources. (Note: after the pulsar average in Eq. (7), only the real part remains.)

The important thing about Eq. (6) is this. The first sum, the diagonal terms, gives us something proportional to the Hellings and Downs curve. But the second sum, the off-diagonal terms, adds up different cross-sections of the plot in Fig. 5, at values of $\beta \neq 0$. Those cross-sections are *not* proportional to the Hellings and Downs curve $\mu_u(\gamma)$. So, because of the interference between different GW sources, the pulsar-averaged correlation is *not* proportional to the Hellings and Downs curve.

6 Cosmic variance in the Hellings and Downs correlation

We can calculate the variance of the pulsar-averaged correlation from the Hellings and Downs curve. Start with Eq. (6), subtract the diagonal term, which *is* proportional to the Hellings and Downs curve, square the difference, and average over sources with independent random phases uniformly distributed on the sky. One obtains the cosmic variance ¹⁾

$$\begin{aligned} \sigma_{\text{cosmic}}^2(\gamma) &= \int_0^\pi d\beta \sin \beta \mu^2(\gamma, \beta) \\ &= -\frac{5}{48} + \frac{49}{432} \cos^2 \gamma - \frac{1}{6} (\cos^2 \gamma + 3) \log\left(\frac{1 - \cos \gamma}{2}\right) \log\left(\frac{1 + \cos \gamma}{2}\right) + \\ &\quad \frac{1}{12} (\cos \gamma - 1) (\cos \gamma + 3) \log\left(\frac{1 - \cos \gamma}{2}\right) + \\ &\quad \frac{1}{12} (\cos \gamma + 1) (\cos \gamma - 3) \log\left(\frac{1 + \cos \gamma}{2}\right) . \end{aligned} \quad (8)$$

This is the typical (squared) deviation away from the Hellings and Downs curve, for a universe filled with interfering GW sources, and is shown in Fig. 6 and Fig. 7. (Note: it might appear that there is no cosmic variance around $\gamma = 50^\circ$ and $\gamma = 130^\circ$. In fact, the variance there is small, but positive.)

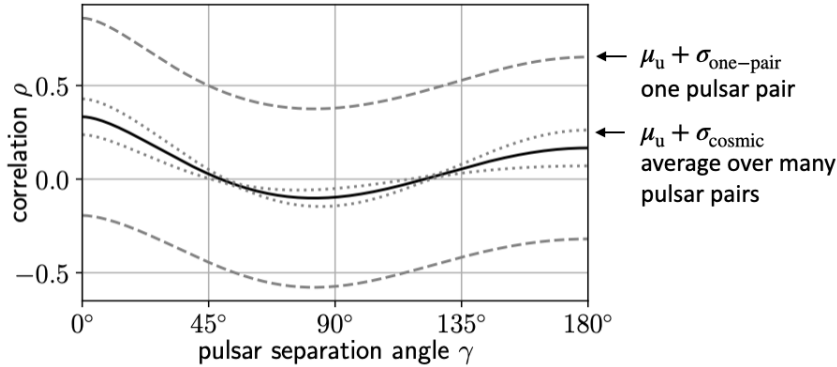


Figure 6: *The cosmic variance characterizes the expected deviation from the Hellings and Downs curve. (Plot is for a GW confusion-noise model, with $h^2 = 1$ and $h^4/h^4 = 1/2$, see ²).*

I want to give you an idea of the size of the cosmic variance. This is shown in Fig. 6. The solid black line is the Hellings and Downs curve. If you pick a random pair of pulsars separated by angle γ , they will have a correlation which lies (± 1 sigma) in between the two outer dashed lines. If you are a PTA observer, and you average over many pulsars on the sky separated by angle γ , you'll end up at the Hellings and Downs curve, plus or minus the amount shown by the dotted line, which is the (square root of the) cosmic variance of Eq. (8). This difference arises from the interference between GW sources radiating at the same frequency. That interference generates a standing wave pattern which doesn't average to give the Hellings and Downs curve.

7 How close can PTAs get to the Hellings and Downs curve?

Real pulsar timing arrays don't have access to an infinite set of pulsars, uniformly distributed on the sky. They only observe a finite number of pulsars. What happens is that as you add more pulsars to your array, you decrease the

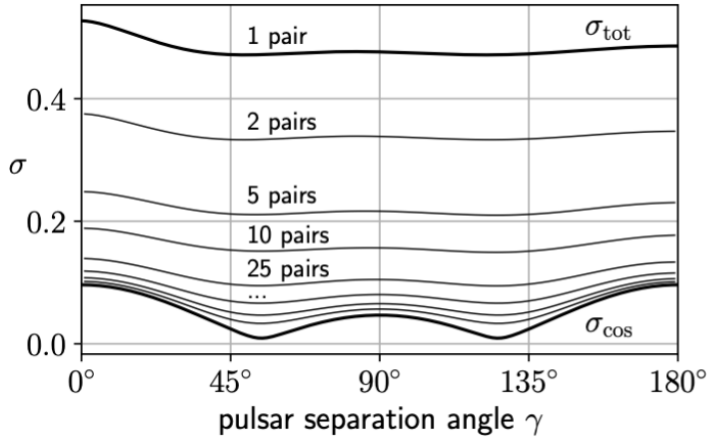


Figure 7: *The variance decreases as more pulsar pairs are added, but does not decrease to zero. Instead, it converges to the cosmic variance. (Plot is for a GW confusion-noise model, with $h^2 = 1$ and $h^4/h^4 = 1/2$, see ²⁾.)*

variance away from the Hellings and Downs curve. This is shown in Fig. 7. If you start with a single pair of pulsars at angle γ , then the variance is the top curve. As more pairs of pulsars are added, the variance decreases as shown, eventually converging to the cosmic variance, shown by the bottom curve.

There is another way to think about and to derive the cosmic variance ²⁾: it arises from the correlations between different pairs of pulsars. Once you have enough pulsar pairs, adding additional pairs at similar angular separations does not provide new information. So adding pairs does not reduce the variance to zero: there is always some remaining difference. At angles (say around $\gamma = 0^\circ$) where the cosmic variance is large, you only need a hundred pairs to get pretty close to the cosmic variance. In contrast, at angles (say around $\gamma = 50^\circ$) where the cosmic variance is small, thousands of pulsar pairs are required.

I'd like to illustrate the situation for four different PTAs ²⁾. This is shown in Fig. 8, where we have assumed that there is no timing noise, and no experimental noise of any kind. So this represents the absolute best-case limit of what might be achieved. The expected precision to which those PTAs, with their pulsar sky locations, can find the Hellings and Downs curve is represented by the distance between the “+” symbols. Let's look first at the PPTA, which

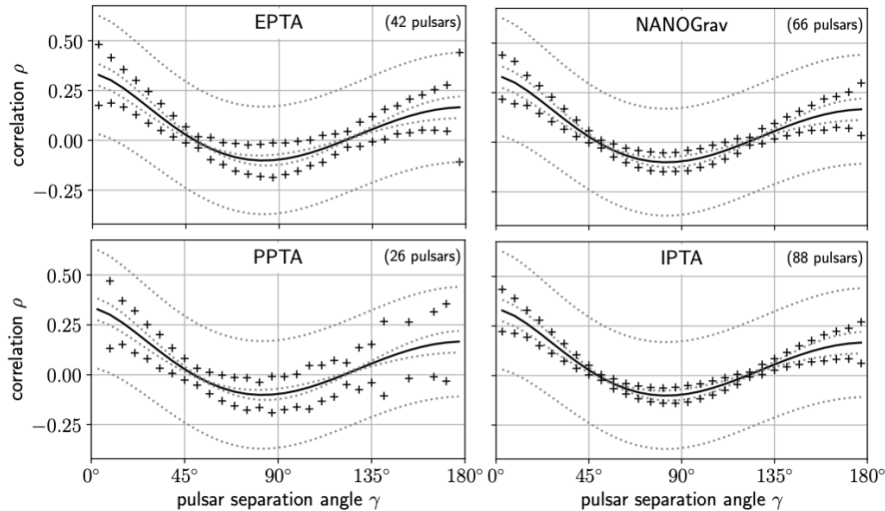


Figure 8: *Best-case variance for current PTAs, using $30 \times 6^\circ$ angular bins, and assuming noise-free measurements, plotted with “+” symbols. This assumes a GW Gaussian ensemble with a binary inspiral spectrum, and plots timing residual correlations with $h^2/h^2 = 0.4$ and $h^2 = 1$, see ²⁾.*

has the smallest number of pulsars, and can form 861 distinct pairs. Since there are 30 angular bins, on the average this is only 29 pairs per bin. Note that some bins, for example the $0^\circ - 6^\circ$ bin, are empty, because the PPTA does not have any pulsar pairs separated by an angle under 6° . So while PPTA does get well below the single-pair variance, shown by the outer dotted lines, it does not get really close to the cosmic variance, shown by the inner dotted lines. In contrast, the IPTA, which has 88 pulsars, can form 3828 distinct pairs, so the average bin contains about 128 pairs. You can see from the crosses that it can, in principle, get much closer to the cosmic variance than the PPTA.

The good news is that these predicted deviations away from the Hellings and Downs curve are not enough to prevent one from recognizing it, and from announcing a confident GW detection. However these deviations are also interesting, because they are a fundamental prediction. If our Universe matches the Hellings and Downs curve much more closely than predicted by the cosmic variance, or if it differs from that curve by much more than the cosmic vari-

ance, then this implies that our Universe is not dominated by many weak GW sources forming a confusion-noise background.

8 Conclusion

I am fairly sure that the Hellings and Downs correlations will be confidently detected in the coming decade, and hope that the organizers of this workshop will invite me to provide updates over that time. In the longer term, as the Square Kilometer Array (SKA) discovers more pulsars and they are timed with greater precision, I am also confident that the cosmic variance will be measured, and will be found to agree with these predictions. If the observed deviations from the Hellings and Downs curve are much smaller or larger than I have predicted, then it means that our Universe does not have a GW background which is described by a Gaussian ensemble, as would be expected from many supermassive black hole binaries, radiating incoherently.

9 Acknowledgments

Parts of this work ²⁾ were done with my friend and colleague Joe Romano.

References

1. B. Allen, arXiv:2205.05637, *to appear in Phys. Rev. D* (2022).
2. B. Allen and J. D. Romano, arXiv:2208.07230 (2022).
3. LIGO/Virgo Scientific Collab., *Phys. Rev. Lett.* **116**, 061102 (2016).
4. S. Chen *et al.*, *Mon. Notices Royal Astron. Soc.* **508**, 4970 (2021).
5. Z. Arzoumanian *et al.*, *Astrophys. J. Lett.* **905**, L34 (2020).
6. B. Goncharov *et al.*, *Astrophys. J. Lett.* **917**, L19 (2021).
7. C. M. F. Mingarelli *et al.*, *Nat. Astron* **1**, 886 (2017).
8. B. Allen and J. D. Romano, *Phys. Rev. D* **59**, 102001 (1999).
9. R. W. Hellings and G. S. Downs, *Astrophys. J. Lett.* **265**, L39 (1983).
10. N. J. Cornish and A. Sesana, *Class Quantum Gravity* **30**, 224005 (2013).

**NEW MISSION CONCEPT: COMPTON TELESCOPE WITH
CODED APERTURE MASK AND ITS SCIENCE
PERSPECTIVES**

Alexander Moiseev *
University of Maryland, College Park, MD, USA,
and CRESST/NASA/Goddard Space Flight Center, Greenbelt, MD, USA
for the GECCO Collaboration †

Abstract

The Galactic Explorer with a Coded Aperture Mask Compton Telescope (GECCO) is a novel Explorer-class concept for a next-generation telescope covering the poorly explored hard X-ray and soft γ -ray energies (0.1 MeV – 10 MeV). This concept builds upon the heritage of past and current missions, improving sensitivity and angular resolution. GECCO uses the combined Coded Aperture Mask and Compton telescope techniques to employ the benefits of both: superior angular resolution provided by the Coded Aperture, and good background rejection and wide field-of-view provided by the Compton telescope. It is being developed at NASA/GSFC in collaboration with other US and foreign institutions. GECCO observations will extend arcminute angular resolution to high-energy images of the Galactic plane, and will make a bridge between X-ray optics instruments and the high-energy γ -ray instruments, enabling a broad potential for discoveries in the MeV γ -ray sky.

* email:amoiseev@umd.edu

† Full list of the Collaboration is given at the end of the paper

1 Science Motivation

The coming of age of modern γ -ray astronomy, in particular by the ground-breaking achievements of Fermi-LAT ¹⁾, has dramatically increased the breadth and depth of our understanding of a variety of sources which radiate at γ -ray energies and the underlying fundamental mechanisms of their operation. However, as usual, newly revealed information has resulted in the appearance of deeper questions.

The γ -ray energy range from a few hundred keV to a few tens MeV has remained largely unexplored since the pioneering but limited observations by COMPTEL ²⁾ on CGRO (1991- 2000), while the neighboring energy ranges have been deeply investigated by NuSTAR ³⁾, Gehrels-Swift ⁵⁾, INTEGRAL ⁶⁾, AGILE ⁷⁾, and Fermi-LAT (Fig.1).

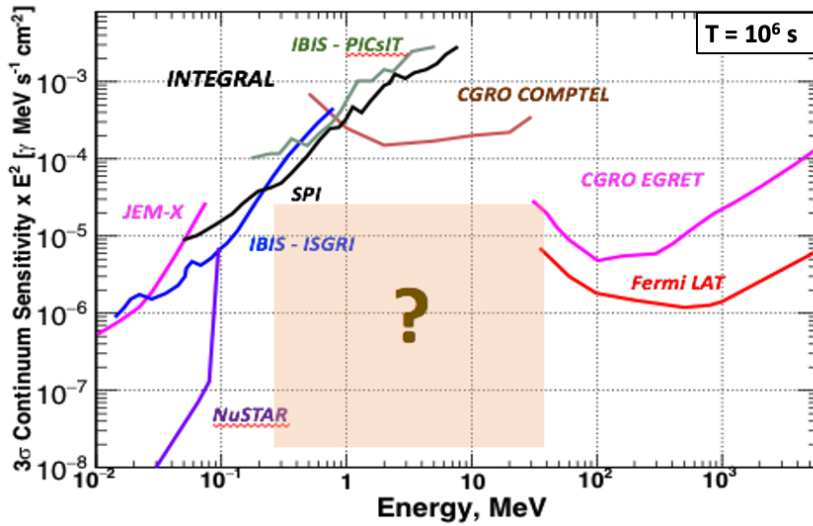


Figure 1: *Currently available capabilities in MeV γ -ray astronomy. GECCO focuses on the highlighted under-explored energy range.*

However, the lack of measurements in this band results not from a paucity of interesting science, since many sources of great astrophysical interest have

energy output that peaks in the MeV-range, with expected spectral and temporal features, but rather from technological constraints that limit instrumental performance. In fact, this energy range offers great potential for astrophysics discovery in the areas of nucleosynthesis, multimessenger/gravitational waves, jets, and compact objects, see *e.g.*, an excellent eASTROGAM ⁸⁾ review of the scientific targets in MeV γ -ray astronomy. In addition, the rapidly widening search for the sources of gravitational waves ⁹⁾ and high-energy neutrinos ¹⁰⁾ requires their accurate and precise localization and identification, which can be provided by X-ray and γ -ray instruments.

There are several unresolved problems connected with the dynamic structure and composition of the inner Galaxy, including the Galactic Center region and active star-forming regions that require high spatial resolution to address: the nature of unassociated Fermi-LAT sources (approximately one third of all detected sources, primarily in the Galactic plane), the nature of the Fermi-eROSITA Bubbles, the nature of the Galactic Center GeV-excess, the origin of the 511-keV positron annihilation line, and the origin of enigmatic dark matter. High-sensitivity measurements of nuclear lines in the MeV range will also lead to resolving Galactic chemical evolution and sites of explosive element synthesis, such as supernova. High angular resolution and good spectral resolution, along with high sensitivity, are critical in these studies.

The arguments and science objectives listed above prove the need for a wide-aperture, high angular and energy resolution MeV-instrument, to fill the poorly explored yet full of scientific potential energy gap between X-ray optics instruments (NuSTAR, eROSITA ¹¹⁾, future HEP-X ¹²⁾), and high-energy γ -ray instruments (Fermi-LAT, AGILE, ground-based γ -ray telescopes). An important argument is also that the operation of the ESA mission INTEGRAL, the only one currently providing measurements in high keV-low MeV energy range, can be terminated in 2023. COSI ¹³⁾, with excellent energy resolution but limited sensitivity and Compton-only modest angular resolution, is planned for a 2026-2027 launch and should provide results that will set the stage for a GECCO mission ^{14, 15)}.

2 GECCO concept inputs

2.1 Limits to Compton telescope angular resolution at MeV energies

The measurement concepts for X- and γ -ray instruments are different, depending on the photon energy of interest. Below 200 keV focusing optics provide the best performance ^{3, 12}). For energies above 10 MeV and up to the TeV range, pair-production is suitable for direct detection, competing at the high end with ground-based Cherenkov and large-array detectors. For high-keV and low-MeV energies, Compton scattering is the dominant photon interaction mechanism with matter, and photon detection using the Compton effect is a well-established observation method (²) and references therein). Unlike pair-production telescopes like Fermi-LAT ¹), the photon arrival direction can only be constrained to an "event circle" (Fig.2a). The uncertainty in the event circle is reflected in its thickness and is due to uncertainties in the scattering angle arising from energy and location measurement uncertainties, as well as Doppler broadening. The direction of a point source can be determined by the overlap from combining the event circles (or arcs) of many detected photons. While the measurement uncertainties can be improved, the resulting point source resolution is ultimately limited by "Doppler" broadening. This effect is due to uncertainty in the initial electron momentum, where the incident photon Compton scattering occurs. This effect imposes a fundamental limit on the angular resolution for Compton telescopes that for semiconductor detectors (*e.g.*, Si, Ge, or CdZnTe) varies in the range 0.4 – 3.5 degrees for energies 0.2 – 10 MeV. For this reason, arcminute angular resolution cannot be achieved in a Compton telescope alone, and arcminute resolution is typically needed in order to associate a source confidently with a multiwavelength counterpart.

2.2 Coded Aperture Imaging

Spatial modulation of the incident flux and deconvolution of the measurement from a position-sensitive detector at the detector plane is an established method for imaging with fine angular resolution, and usage of coded-aperture (CA) masks is widespread in X-ray instruments ^{16, 17}). A mask is an array of opaque and transparent elements set between the source field and a position-sensitive detector plane (PSD), also called the Focal Plane Detector (FPD). Every source within the instrument's FoV projects a shadow image of the mask

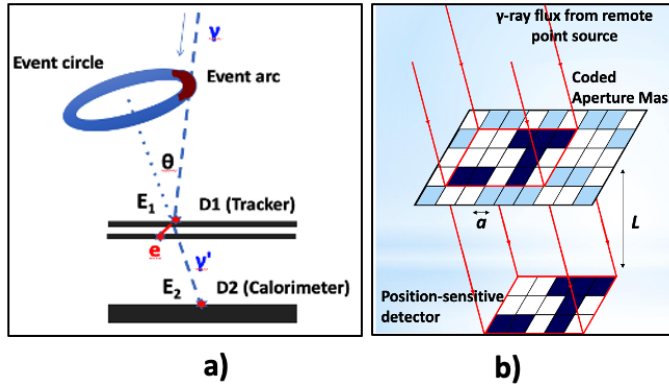


Figure 2: a) Principle of operation of the Compton telescope. Incident photon undergoes Compton scattering in D1 and then is detected in D2; b) CA principle of operation. The angular resolution is constrained by the Mask element size “ a ” and Mask-Focal Plane detector separation “ L ”

onto the PSD (Fig.2b). There are several data analysis approaches for such systems that are widely discussed in the literature, many based on Fourier-based deconvolution.

The fundamental angular resolution of the system is determined by the ratio of the mask pixel size to the distance from the mask to the FPD. The pixel size is constrained by the PSD position resolution, and is usually set 2-3 times larger to provide reasonable signal-to-noise ratio (SNR). The availability of a PSD with high-position resolution is one of the cornerstones of CA-based instruments. The other key parameter is the distance between the mask and the PSD. For space-borne instruments this distance is constrained by the launcher geometry and cannot exceed 3-4 meters.

The challenges for an MeV-energy CA Imager. At MeV energies, CA imagers face difficulties not present in X-ray applications. The amount of material required to significantly attenuate MeV photons is much thicker than is needed for X-rays, with a minimal mask thickness on the order of a few cm of tungsten. The resulting mask will be heavy, with a fully-coded FoV that is limited by the ratio of the mask pixel size to its thickness (that is, the opening angle of a given transparent mask element), as well as by the ratio of

the mask size to the FPD size. The effective change in mask thickness with photon incidence angle furthermore creates non-uniformity in the system response (self-collimation effect). If the CA design for X-ray instruments is rather straightforward, for MeV energies it requires careful design and fabrication optimization to maximize the instrument performance.

2.3 CZT Imaging Calorimeter

During last several years, our team has been developing a modular, crate-based architecture for the CZT Imaging Calorimeter (ImCal). ImCal is based on combining many position-sensitive Virtual Frisch-grid (VFG) CZT bar detectors with a large geometrical aspect ratio, e.g., $6 \times 6 \times 20$ or $8 \times 8 \times 30$ mm^3 [18, 19]. These are oriented with the long axis parallel to the incident γ -ray direction, making the detector effective thickness equal to the bar length, providing high detection efficiency. The distinguishing feature of the detector is the use of four conducting pads attached to the sides of the encapsulated CZT crystal bar near its anode (Fig.3). The pads are virtually grounded through the ASIC front end and act as a virtual Frisch-grid. The induced signals on the pads, anode, and the cathode (6 signals in total per bar) are read out to provide X, Y, and Z coordinates by combining the signal ratios. An important advantage of the position-sensitive VFG detectors is the ability to correct for non-uniformity of the response caused by crystal defects. Such a correction allows us to use standard grade crystals produced with higher acceptance yields and, thus, to reduce the overall cost of the instrument [18].

Crate Design. The CZT bars are tightly packed inside the cells of the egg-crate structure (Fig.3). As a result of joint GSFC-BNL efforts, we have integrated a fully functional prototype of the Imaging Calorimeter comprised of 3×3 crates. The crates are plugged into a motherboard, which also carries low-voltage power regulators, ADCs, an FPGA, and a fiber-optics communication interface.

While good spectroscopic performance has been achieved with this prototype, measurements clearly indicated that the analog ASICs used previously have inherent limitations for the reconstruction of the X and Y event locations. To address this problem, we chose to use a new “smart” ASIC concept based on waveform sampling of the unshaped signals. With the digitized data, we can use time-correlated samples of the signals captured from pads for reconstruct-

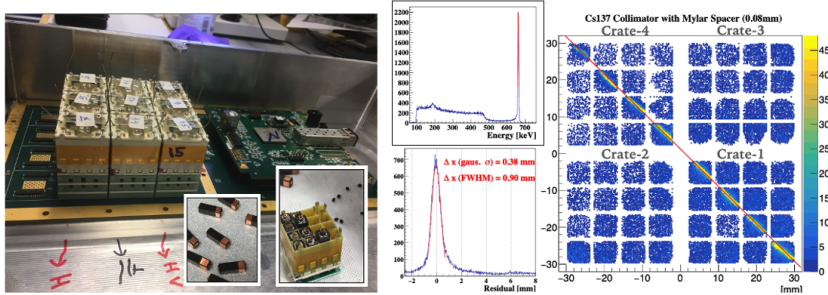


Figure 3: *Left: 9-crate prototype assembled, with inserts: CZT bars with copper sensing pads attached, and crate, half-populated with bars. Upper middle: the ^{137}Cs spectrum with $\sim 0.9\%$ FWHM energy resolution, obtained with IDEAS readout. Right: image of 0.08mm wide collimator obtained with 4 crates, each blue square corresponds to cross-section of CZT bar ($6 \times 6\text{mm}^2$). The red line is the best fit linear function. Bottom middle: corresponding residual distance of the reconstructed hit from the red line (position resolution), 0.9mm FWHM*

ing X and Y coordinates with much higher accuracy. To develop the waveform digitizing approach, we integrated and tested a 2×2 prototype crate with a customized GDS-100 front-end readout system provided by IDEAS²⁰⁾. The results obtained with radioactive sources in the laboratory, and in our recent test at the TUNL/HIGS polarized photon beam encouraged our team to use the GDS readout system as the baseline for the GECCO ImCal (Fig.3).

With the ImCal prototype built and tested, we demonstrated the basic principles and benefits of this technology for γ -ray space telescopes, and its ability to measure with high efficiency both the photon interaction sites and the deposited energy with good accuracy: $< 1\text{mm}$ for the 3D position resolution, and $\leq 1\%$ FWHM for the energy resolution. Arrays of such detectors have been recognized as promising for use in various γ -ray telescopes as a stand-alone Compton detector and as a focal-plane detector for CA instruments (Fig. 5), with direct application in GECCO¹⁴⁾ and AMEGO²¹⁾. Furthermore, using the crate-based modular design allows for flexibility in selecting array configurations and sizes for large-area detector systems.

3 GECCO Concept

The GECCO concept combines the best of the Compton and CA imaging modalities, mutually enhancing the performance of each modality and enabling previously inaccessible measurements^{14, 15}, its baseline design is shown in Fig.4. Compton telescopes provide good, low-noise performance over a wide FoV, while CA telescopes achieve arcmin-level and better angular resolution but have no inherent background rejection. In GECCO we are developing a novel approach, over most of GECCO energy band, where CA imaging will be performed using only Compton-scattered γ -rays, whose rings of incidence cross the CA mask, allowing significant background rejection and improved signal-to-noise ratio (SNR).

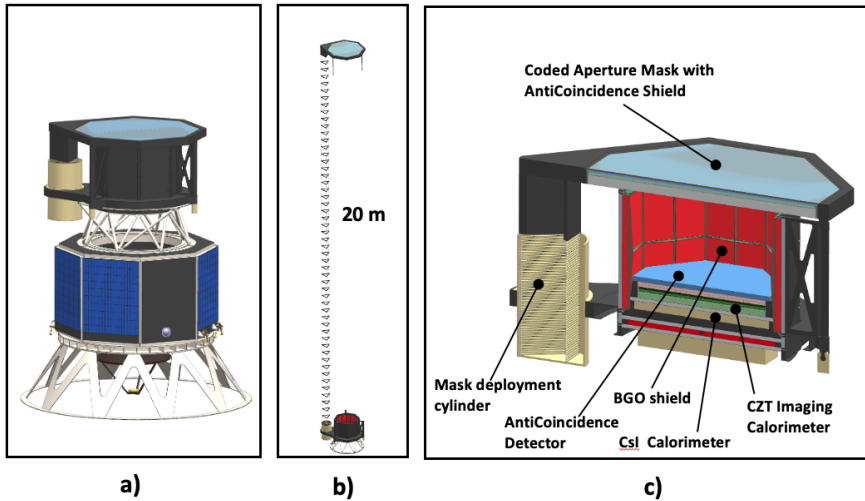


Figure 4: *GECCO conceptual design: a) GECCO with the mask in stowed position and notional spacecraft bus, b) GECCO with the mask in deployed position, c) GECCO, cutaway.*

This approach will enable the use of a longer focal length to achieve sub-arcminute angular resolution without requiring heavy, full side shielding, by deploying the mask post-launch on an extensible boom, similar to the well-

developed designs used in NuSTAR and other X-ray optics instruments. The method of using Compton imaging to suppress side-entering background (bright off-angle sources, diffuse γ -radiation) is illustrated in Fig.6. In the GECCO baseline design we assume the CA mask to be deployed at 20m, with the mask pixel size 3mm. These numbers provide ~ 0.5 arcmin angular resolution and $2^\circ \times 2^\circ$ fully-coded field-of-view. It is critical for achieving high sensitivity CA observations and its efficacy and efficiency have been validated in simulations performed by our team. The method of “Compton pointing” has been demonstrated earlier in simulations^{22, 23}, and tested with INTEGRAL/IBIS data²⁴), but the mature concept has never been implemented as the central motivation for a telescope design.

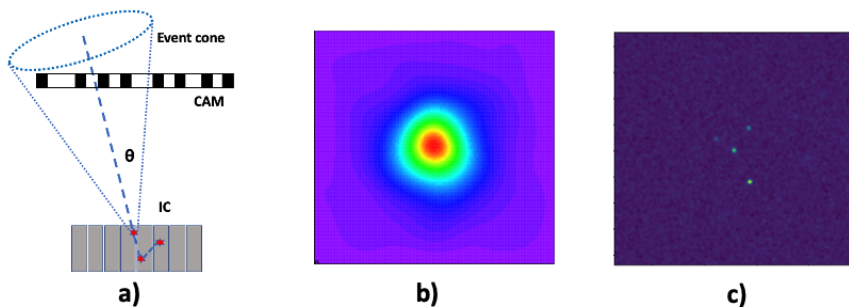


Figure 5: *a): Illustration of ImCal dual imaging capability. Red stars show the points of photon interactions detected in the ImCal, which are used to reconstruct the cone of possible incident photon directions, enabling Compton imaging. The point of the first photon interaction is used to create the CA image, with ImCal operation as the CA FPD. The dashed line shows the scattered photon direction detected by ImCal. The dotted lines show the event cone. b) Compton observation of 4 point sources of different intensities, separated by $3' - 5'$, and c) – the same 4 point sources as detected by the CA (simulations).*

In GECCO the ImCal detects γ -rays from 50 keV to 10 MeV providing the (multi-site) energy and location of interactions. It serves as the detector plane for the CAM telescope and, above ~ 200 keV, as a standalone Compton telescope (Fig.5). The CsI Calorimeter supports the ImCal by measuring the

energy and interaction positions of radiation escaping from the ImCal: 2-10 MeV photons have the lowest attenuation length and most of them are not fully contained in the ImCal and so cannot be correctly reconstructed. Monte Carlo simulations of the instrument have been performed by our team with the MEGAlib toolkit ²⁵⁾.

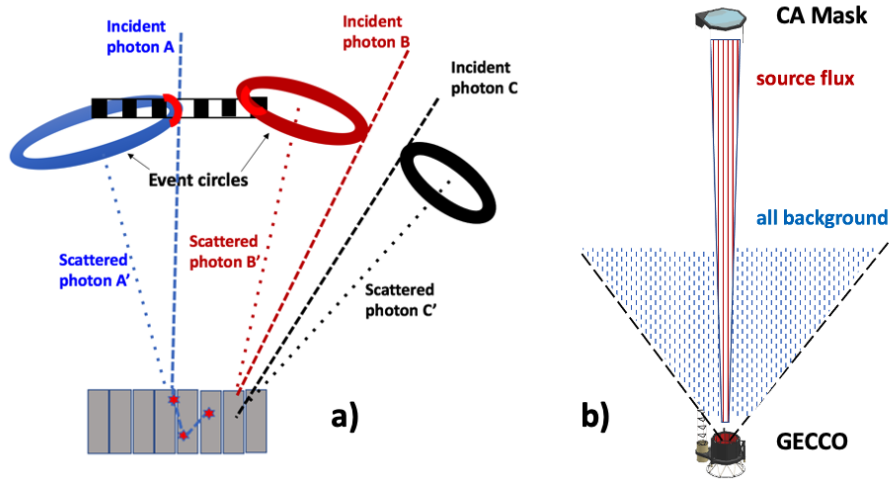


Figure 6: *Background removal method: a) Photon A, shown in blue - accepted good photon from the source, with its event circle crossing the CA mask location. Photon B, shown in red - accepted background photon, because its event circle crosses the CA mask location. Photon C, shown in black - rejected background photon. b) Source and background fluxes, shown in red, entering the GECCO ImCal FoV within the CA mask FoV, accepted for the analysis. The background flux, entering the GECCO ImCal FoV but outside of the CA mask FoV, is shown in blue and is rejected by the Compton pointing method.*

The ImCal, serving for GECCO as a standalone Compton telescope and as a FPD, is also a powerful tool to measure the γ -radiation polarization. The first results of our simulations are very encouraging, and we will pursue this topic for GECCO, following the steps COSI ¹³⁾ is taking.

The GECCO BGO shield consists of eight, thick BGO detectors config-

ured to create an octagonal well (shown in dark red in Fig.4). It shields the detectors from the bright Earth radiation, and serves as a veto detector for incident charged cosmic rays and for vetoing not-fully contained and otherwise accepted Compton events. The BGO shield will also serve as an excellent γ -ray burst (GRB) detector (BurstOctagon), capable of locating GRBs with 1-2 degree accuracy (burst type, location, and brightness dependent, our team simulations). If the GRB is in a heavy-populated sky region where such resolution is insufficient, GECCO can be re-pointed in that direction for more accurate localization using the full power of the CA mode.

Presently, our team is developing the GECCO prototype, called Proto-GECCO, to test and demonstrate the performance and conduct the design optimization if found necessary ²⁶⁾.

4 GECCO Expected performance and Conclusions

GECCO's observational capabilities will be of paramount importance for disentangling astrophysical and dark matter explanations of emission from the Galactic Center and potentially providing a key to discovering as-of-yet unexplored dark matter candidates ²⁷⁾. GECCO will operate in the 100 keV - 10 MeV energy range, with energy resolution of $\approx 1\%$ in 0.5 - 5 MeV. The Coded Aperture Mask provides the angular resolution of ≈ 0.5 arcmin with a $2^\circ \times 2^\circ$ fully-coded FoV, while the Compton telescope provides the angular resolution of $4^\circ - 8^\circ$ with a ≈ 2 sr FoV, see ¹⁵⁾ for the details. The $3\sigma, 10^6 s$ sensitivity is expected to be about $10^{-5} MeV \times cm^{-2} \times s^{-1}$ over the entire energy range.

In order to exploit GECCO's unique (for this energy range) angular resolution and pursue its main science objective of resolving heavily-populated sky regions, its primary mode of observation is fixed pointing, with extended exposure of such regions. Also, the pointed mode will be used to either increase observation time for special regions of interest, or to observe transient events such as flares of various origins or gamma-ray bursts. However, as a standalone Compton telescope with wide FoV, ImCal will simultaneously provide wide-area sky exploration, significantly broadening GECCO's observational scope.

With the unprecedented angular resolution of the coded mask telescope combined with the sensitive Compton telescope, GECCO will be able to disentangle discrete sources from truly diffuse emission, contributing to understanding the gamma-ray Galactic Center excess and the Fermi Bubbles, and

to tracing low-energy cosmic rays and their propagation in the Galaxy ¹⁵). Nuclear and annihilation lines will be spatially and spectrally resolved from continuum emission and from sources, addressing the role of low-energy cosmic rays in star formation and galaxy evolution, the origin of the 511 keV positron line, fundamental physics, and Galactic chemical evolution. Of special interest will be the exploration of sites of explosive element synthesis by conducting high-sensitivity measurements of nuclear lines from Type 1a supernovae and from other objects.

GECCO will be able of addressing practically all of the science problems described in the Section 1, but will be focused on two primary objectives. One is to explore heavily populated sky regions, mainly the Galactic Center (the illustration of GECCO's capability to detect closely situated sources is shown in Fig.5c). Here, the important goals are to resolve the nature and environment of the central massive black hole, and to understand if some emissions are due to dark matter, or multiple point sources. The presence of dark matter in close vicinity of the GC has been advocated in numerous papers and GECCO will be able to resolve this ²⁷). GECCO is the only instrument, able to investigate this problem at MeV energies by resolving potentially contributing point sources, that would have an expected \sim arcmin population density ^{4, 28, 29}). The other primary objective for GECCO will be large FoV monitoring for transient events, detected with high sensitivity, and accurate localization, performing multimessenger investigations to support GW and neutrino discoveries.

5 Acknowledgements

The UMCP/CRESST/GSFC GECCO team members were supported by NASA award 80GSFC17M0002 and NASA/APRA award 80NSSC20K0573.

The BNL team members were supported by U.S. Department of Energy, Office of Defense Nuclear Nonproliferation Research & Development (DNN R&D).

The UCSC team members (Dark matter analysis) were partly supported by the U.S. Department of Energy grant number desc0010107. Adam Coogan was partially funded by the Netherlands eScience Center (grant number ETEC.2019.018) and by the Schmidt Futures Foundation.

Israel Martinez-Castellanos provided a very valuable help in the BurstOctagon GRB detection capability simulations.

The GECCO team is grateful to the GSFC engineers and technicians (S. Shu-

man, P. Goodwin, K. Simms, G. Lotkin), and BNL engineers and technicians (Don Pinelli, Bill Weldon, Connie-Rose Deane, Joe Pinz), for their critical contribution to the CZT Calorimeter development.

The team is grateful to the IDEAS leadership and engineers (Aage Kalsæg, Gunnar Maehlum, Tor Magnus Johansen, and others) and to the TUNL/HIGS scientists and engineers (Ying Wu, Calvin Howell, Stepan Mikhailov, and others) for their invaluable support in the instrument development and testing. Our project would not be possible without high-quality CZT detectors, provided by Redlen and KROMEK companies.

6 GECCO Team

D.M. Asner¹, M.G. Baring², P.F. Bloser³, A.E. Bolotnikov¹, E. Bottacini^{4,5}, N. Cannady^{7,8}, G.A. Carini¹, W. Collmar⁹, A. Coogan¹⁰, G. DeNolfo⁶, S. Digel¹¹, V. Eberle⁹, T. Enßlin⁹, I. Grenier¹², A. Harding³, D. Hartmann¹³, S. Herrmann¹, D. Kazanas⁶, M. Kerr¹⁴, R. Krivonos¹⁵, P. Laurent¹², O. Limousin¹², F. Longo¹⁶, J.W. Mitchell⁶, A.A. Moiseev^{8,17,*}, L. Morrison¹⁹, A. Morselli¹⁸, I.V. Moskalenko⁵, R.F. Mushotzky¹⁷, M. Negro^{7,8}, E. Orlando^{5,16}, B. Philips¹⁴, S. Profumo¹⁹, K. Sakai^{7,8}, M. Sasaki^{8,17}, P. Shawhan¹⁷, C.R. Shrader^{8,20}, D. Shy¹⁴, G.K. Skinner²¹, L. Smith¹⁷, F. Stecker⁶, S. J. Stochaj²⁵, A.W. Strong⁹, S. Sturmer^{7,8}, H. Tajima²², D. Thompson⁶, J. Tomsick²³, A. Vigliano¹⁶, Z. Wadiasingh^{8,17}, R. Woolf¹⁴, E. Yates¹⁷, K.-P. Ziock²⁴, A. Zoglauer²³

¹ Brookhaven National Laboratory (BNL), USA

² Rice University, Houston, USA

³ Los Alamos National Laboratory (LANL), USA

⁴ University of Padova, Italy

⁵ Stanford University, USA

⁶ NASA/Goddard Space Flight Center, USA

⁷ University of Maryland, Baltimore County, USA

⁸ CRESST/NASA/Goddard Space Flight Center, USA

⁹ Max Planck Institute for Astrophysics, Garching, Germany

¹⁰ GRAPPA, University of Amsterdam, the Netherlands

¹¹ Stanford Linear Accelerator Center (SLAC), USA

¹² CEA Saclay, France

¹³ Clemson University, USA

- ¹⁴ Naval Research Laboratory (NRL), USA
¹⁵ Space Research Institute (IKI), Russia
¹⁶ University of Udine and INFN, Trieste, Italy
¹⁷ University of Maryland, College Park, USA
¹⁸ INFN Roma Tor Vergata, Italy
¹⁹ University of California at Santa Cruz, USA
²⁰ Catholic University, Washington DC, USA
²¹ University of Birmingham, United Kingdom
²² Nagoya University, Japan
²³ University of California, Berkeley, USA
²⁴ Oak Ridge National Laboratory, USA
²⁵ New Mexico State University, USA
* Principal Investigator, amoiseev@umd.edu

References

1. W.B. Atwood, *et al*, (Fermi-LAT Collaboration), The Large Area Telescope on the Fermi Gamma-ray Space Telescope Mission, *ApJ* **697**, 1071 (2009)
2. V. Schonfelder, *et al*, Instrument Description and Performance of the Imaging Gamma-ray Telescope COMPTEL aboard the COMPTON Gamma-Ray Observatory, *ApJS* **86**, 657 (1993)
3. F.A. Harrison *et al*, The Nuclear Spectroscopic Telescope Array (NuSTAR) High-energy X-ray mission, *ApJ* **770**, 103, (2013)
4. J.S. Hong, *et al*, NuSTAR Hard X-Ray Survey of the Galactic Center Region II: X-Ray Point Sources, *ApJ* **825**, 2, 132 (2016), arXiv:1605.03882
5. S.D. Barthelmy, *et al*, The Burst Alert Telescope (BAT) on the SWIFT Midex Mission, *Space Science Reviews* **120**, 143-164 (2005)
6. C. Winkler, *et al*, INTEGRAL: Science Highlights and Future Prospects, *Space Science Reviews* **161**, 149 (2011)
7. M. Tavani, *et al*, The AGILE Mission, *A&A* **502**, 995 (2009)
8. A. De Angelis, *et al*, (The e-ASTROGAM Collaboration), Exploring the extreme Universe with gamma rays in the MeV – GeV range, *Experimental Astronomy* **44**, 25 (2017), DOI 10.1007/s10686-017-9533-6

9. B. P. Abbott, *et al*, Gravitational Waves and Gamma-Rays from a Binary Neutron Star Merger: GW170817 and GRB 170817A, *ApJL* **848**, L13 (2017)
10. S. Garrappa, *et al*, Investigation of Two Fermi-LAT Gamma-Ray Blazars Coincident with High-Energy Neutrinos Detected by IceCube, *ApJ* **880**, 103 (2019)
11. P. Predehl, *et al*, The eROSITA X-ray telescope on SRG, *A&A* (2020), arXiv:2010.03477v1
12. K.K. Madsen, *et al*, Optical instrument design of the High-Energy X-ray Probe (HEX-P), In Proc. SPIE 10699, 106996M (6 July 2018); doi: 10.1117/12.2314117
13. J. Tomsick, A. Zoglauer, *et al*, The Compton Spectrometer and Imager, *Bulletin of the American Astronomical Society*, **51**, 98 (2019); arXiv: 1908.04334
14. A. Moiseev, (GECCO Collaboration), New mission concept: Galactic Explorer with a Coded aperture mask Compton telescope (GECCO), *PoS ICRC2021* **648** (2021)
15. E. Orlando, E. Bottacini, A.A. Moiseev, *et al*, Exploring the MeV sky with a combined coded mask and Compton telescope: the Galactic Explorer with a Coded aperture mask Compton telescope (GECCO), *JCAP07* **036** (2022)
16. G. K. Skinner, Imaging with Coded-Aperture Masks, *NIM* **221**, 33 (1984)
17. E. Caroli, *et al*, Coded Aperture Imaging in X-ray and Gamma-ray astronomy, *Space Science Reviews* **45**, 349 (1987)
18. A.E. Bolotnikov, *et al*, A 4×4 array module of position-sensitive virtual Frisch-grid CdZnTe detectors for gamma-ray imaging spectrometers, *NIM in Physics Research*, **A 954**, 161036 (2020)
19. A. E. Bolotnikov, *et al*, Performance of 8×8×32 and 10×10×32 mm³ CdZnTe position-sensitive virtual Frisch-grid detectors for high-energy gamma-ray cameras, *NIM A* **969**, 164005 (2020).

20. <https://ideas.no/products/gds-100/>
21. J. E. McEnery, *et al*, (AMEGO collaboration), All-sky Medium Energy Gamma-ray Observatory: exploring the extreme multimessenger universe, *Bull. Amer. Astron. Soc.* **51**, 245 (2019); arXiv:1907.07558
22. E. Aprile, *et al*, A Monte Carlo analysis of the liquid xenon TPC as gamma-ray telescope, *NiM A* **327**, 216 (1993)
23. M. Galloway, *et al*, A Combined Compton and Coded-aperture Telescope for Medium- energy Gamma-ray Astrophysics, arXiv:1705.02652 (2017)
24. M. Forot, *et al*, Compton Telescope with a coded aperture mask: imaging with the INTEGRAL/IBIS Compton mode, *ApJ* **668**, 1259 (2007)
25. <https://megalibtoolkit.com/home.html>
26. R. Woolf, *et al*, Development of the balloon-borne Galactic Explorer Coded Aperture Mask and Compton Telescope (GECCO) prototype, In *SPIE Proceedings*, 12181, *Space Telescopes and Instrumentation 2022: Ultraviolet to Gamma Ray*, 121812J (2022); doi:10.1117/12.2630681
27. A. Cogan, A. Moiseev, L. Morrison, S. Profumo, *et al*, Hunting for Dark Matter and New Physics with GECCO, *Physical Review D*, in press, arXiv:2101.10370 (2022)
28. R. Krivonos, *et al*, INTEGRAL/IBIS nine-year Galactic Hard X-Ray Survey, *Astronomy & Astrophysics* **545**, A27 (2012)
29. E. Churazov, *et al*, INTEGRAL results on the electron-positron annihilation radiation and X-ray & Gamma-ray diffuse emission of the Milky Way, *New Astronomy Reviews* **90**, 101548 (2020)

Highlights from Gamma-Ray Atmospheric Cherenkov Telescopes

Laura Olivera-Nieto 

*Max-Planck-Institut für Kernphysik, Saupfercheckweg 1, 69117
Heidelberg, Germany*

Abstract

Ground-based gamma-ray astronomy is a very active field of research. As the field prepares for the upcoming Cherenkov Telescope Array (CTA), the previous generation of instruments continues to take data and produce significant scientific results. Here we present a summary of some of the recent highlights from imaging atmospheric Cherenkov telescopes.

1 Introduction

Imaging Atmospheric Cherenkov Telescope (IACT) arrays have been instrumental to the progress achieved in gamma-ray astronomy in the last decades ¹). Despite their relatively low duty-cycle and limited field of view, they are able to provide deep exposures with relatively short observation times thanks to the very large collection areas. Additionally, their angular resolution is superior to

that of other ground based gamma-ray instruments such as water Cherenkov detector (WCD) arrays. This allows for detailed studies of the morphology of sources, as well as their spectral and temporal behavior.

In this proceedings I will present a short summary of some recent highlights from IACT observations, focusing on the three largest arrays that are currently in operation: the Major Atmospheric Gamma-ray Imaging Cherenkov (MAGIC) telescopes, the Very Energetic Radiation Imaging Telescope Array System (VERITAS) and the High Energy Stereoscopic System (H.E.S.S.).

2 Galactic Science

2.1 Binary Systems

One of the most remarkable results coming from IACT arrays in the recent years was the detection of very-high energy (VHE) gamma-rays from the recurrent nova RS Ophiuchi during its latest eruption in August 2021. Recurrent novae are a class of binary systems in which a white dwarf is orbiting closely another star, while accreting matter from it onto its surface. After a number of years, which differs from system to system, a runaway thermonuclear reaction takes place which ejects the accreted material into a rapidly-expanding shell around the white dwarf.

The event was detected by both the MAGIC telescopes and H.E.S.S., with the interpretation in both cases being consistent with a hadronic origin for the gamma-ray emission. The H.E.S.S. and Fermi-LAT lightcurves can be seen in Figure 1. More information can be found in ²⁾ and ³⁾.

Another special class of binary systems are those referred to as microquasars. Such systems host a compact object, usually a black hole, from the vicinity of which jets are launched. The most studied such system in our Galaxy is arguably the microquasar SS 433, the first microquasar ever discovered and the only one known to be a VHE gamma-ray source ⁴⁾.

Following the discovery of gamma-ray emission from the lobes of SS 433 by the HAWC Collaboration, deep observations of the system led to its detection by the H.E.S.S. array of telescopes ⁵⁾. The superior energy and angular resolution of H.E.S.S. compared to that of HAWC will allow for a detailed study of the properties of the source.

The final result concerning binary systems chosen to be highlighted here

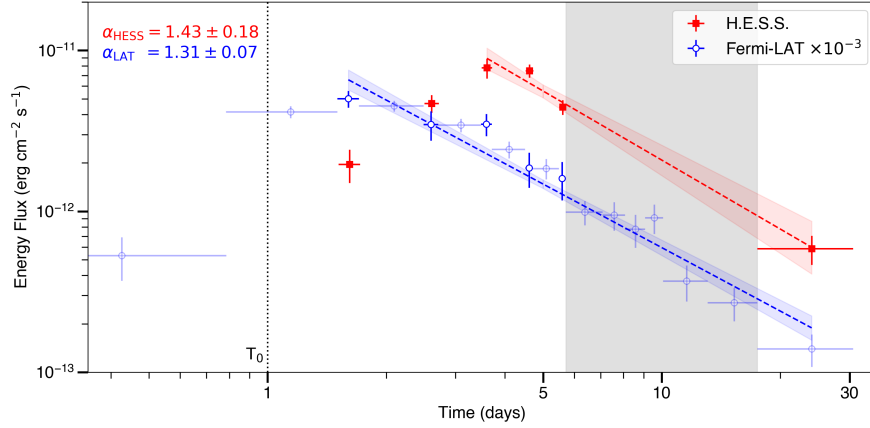


Figure 1: Light curves of gamma-ray emission from RS Ophiuchi, including data from Fermi-LAT and H.E.S.S. observations. Figure from [2\)](#).

is the outcome of collaboration between all the three experiments covered. A deep exposure on the region of HESS 0632+057 was obtained by combining observations from H.E.S.S., MAGIC and VERITAS. Combining the observations also allowed to probe the complete orbital phase of the binary, revealing variability in the gamma-ray flux with a period and amplitude correlated to the modulation previously observed in the x-ray band [6\)](#).

2.2 Stellar Clusters

A recent development in the study of Galactic sources with IACT arrays is the application of combined spectro-morphological (or "3D") analysis techniques [7\)](#). The application of this technique to the region of the massive stellar cluster Westerlund 1 allowed to conclude that only the cluster can explain the majority of the observed gamma-ray emission. Interestingly, the morphology of the emission does not correlate with the distribution of gas in the region, favoring a leptonic origin in the emission [8\)](#).

2.3 PeVatron Candidates

PeVatrons are sources capable of accelerating particles to PeV energies, a signature of which is the presence of radiation with energies of hundreds of TeV. There are many such candidates, many of which have been the subject of recent studies. Here I will highlight only two examples, selected for being an example of synergies between wide-field WCDs and IACT arrays.

WCDs survey a large fraction of the sky continuously, thanks to their high duty cycle and wide field of view. They are also able to reach higher energies than IACTs thanks to the consequently increased exposure time. However, they have worse angular and energy resolution than IACTs. This means that, while WCDs are the ideal instrument to discover new sources and extend spectra above hundreds of TeV, they often lack the precision to identify e.g. the morphology of the emission and consequently the sources responsible for it. For this reason, synergies between both instrument classes are crucial to the study of gamma-ray sources.

A good example of this is the SNR G106.3+2.7 region, where emission above 500 TeV has been reported by LHAASO ⁹⁾. MAGIC observations were able to disentangle the emission into two components, as shown in Figure 2. The emission is split into a low energy (<6 TeV) component consistent with a region dubbed the *head*, and a high energy one (>6 TeV), likely responsible for the emission seen by LHAASO, coming from a region dubbed as the *tail*. The nature of the emission is unclear for the low energy component, whereas a hadronic nature is preferred for the high energy one ¹⁰⁾.

Another such example is the case of LHAASO J2108+5157, which was detected by LHAASO above 100 TeV ⁹⁾ but for which no lower energy counterpart has been identified. VERITAS observations of the region resulted in no detection, placing very strict upper limits that rule out a hadronic interpretation for the emission ¹¹⁾.

2.4 The Galactic Center

The Galactic Center (GC) is arguably one of the most important and well studied Galactic sources. There have been many observations of this region in previous years, mainly by the H.E.S.S. array since it is the only one located in the southern hemisphere ¹²⁾. However, the GC is also visible by northern observatories, such as VERITAS at very high zenith angles, that is, closer to the

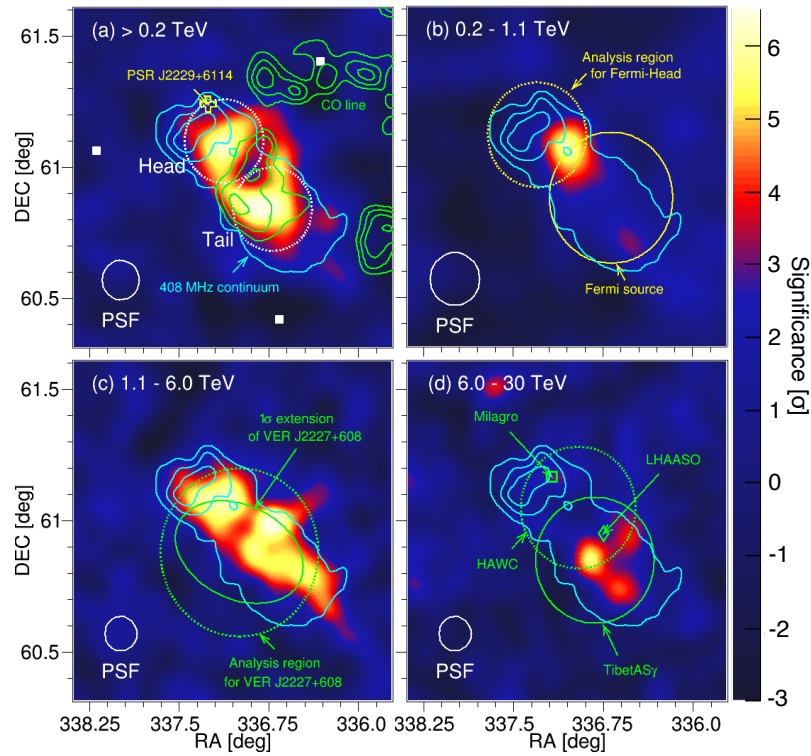


Figure 2: Energy-dependent pre-trial significance maps of SNR G106.3+2.7 observed with the MAGIC telescopes. Figure from [10](#).

horizon. Recent observations by VERITAS report consistent results with the previous measurements, with no evidence for a spectral cutoff. This indicates that the spectra likely extends to higher energies, reaffirming the status of the GC as a solid PeVatron candidate [13](#).

3 Extragalactic Science

3.1 Gamma-Ray Bursts

One of the biggest results to come out of IACTs in the recent years is the discovery of a VHE component in the afterglow of long gamma-ray bursts (GRBs), bright explosions associated with core-collapse supernovae. Here I will focus on the observation of three GRBs for which there is a refereed publication reporting a significant detection, but note that more candidates are being considered at the moment.

3.1.1 GRB 180729B

The first GRB to be detected, GRB 180729B was detected with a significance of 5σ by the H.E.S.S. array of telescopes. The relatively low significance did not allow for a detailed study of the properties of the emission, which was observed 10 hours after the initial burst and with maximum energies of ~ 440 GeV ¹⁴).

3.1.2 GRB 190114C

The first GRB detection to be reported, GRB 190114C was observed by the MAGIC telescopes only 60 seconds after the initial burst and detected with significance of over 50σ ¹⁵). Photons were detected with energies up to ~ 1 TeV, well above the so-called synchrotron burn off limit, that is, the theoretically predicted maximum energy for photons produced via synchrotron emission. The VHE and X-ray fluxes present a similar, yet not identical, time evolution. This evidence is used to justify the need for a second component, additional to the synchrotron one, produced by inverse Compton (IC) to model the observed spectrum, as shown in Figure 3.

3.1.3 GRB 190829A

GRB 190829A was observed by the H.E.S.S. array for three consecutive nights with a total significance of 20σ . The observations reveal a remarkably similar time evolution in the VHE and X-ray fluxes, with photons of energies up to ~ 3.3 TeV detected. The measured spectral index of the H.E.S.S. range is inconsistent with the predictions of a model invoking IC to explain the VHE emission, and matches instead the prediction of the synchrotron emission if

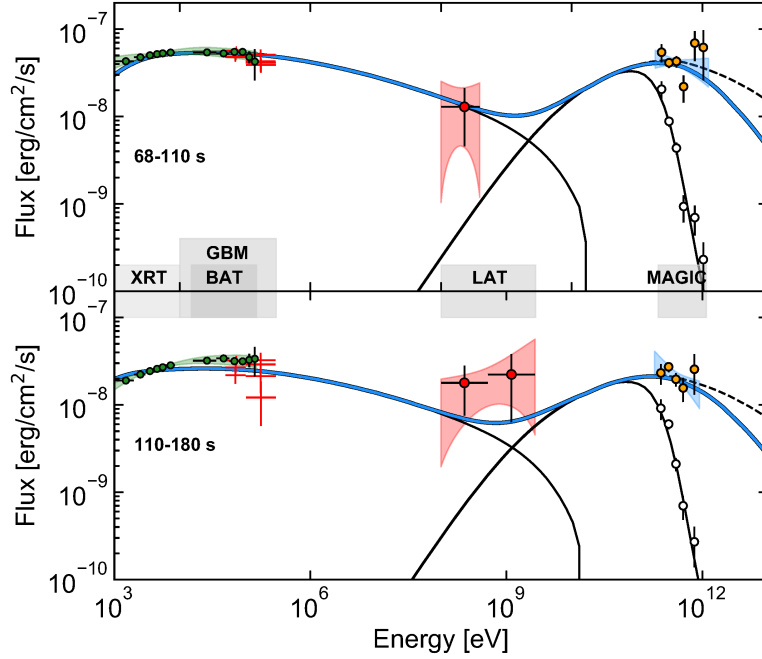


Figure 3: Measured and modeled spectral energy distribution of GRB 190114C in two different time intervals. Figure from [15](#)).

extrapolated to that energy range, as seen in Figure 4. This would contradict the expected maximum energy achievable via synchrotron emission [16](#)).

4 Fundamental physics

4.1 Dark Matter Searches

Gamma-ray observations of regions expected to contain a high fraction of dark matter, such as dwarf spheroidal galaxies [17](#)), or the inner Galaxy [18](#)) are used to constrain the properties of the posited Weakly Interacting Massive Particles (WIMPs), a candidate for dark matter.

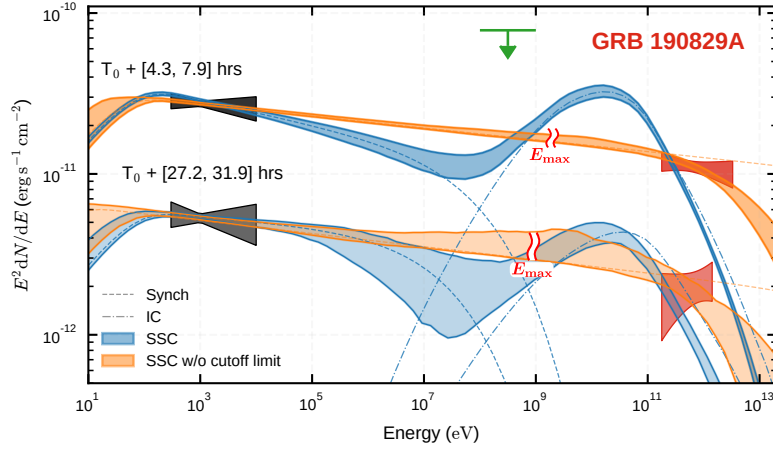


Figure 4: Measured and modeled spectral energy distribution of GRB 190829A. Figure from [16](#)).

4.2 Lorentz Invariance Violation

The observation of photons from GRB 190114C was used by to probe a possible energy dependence of the speed of light, obtaining competitive limits for this effect [19](#)).

5 Conclusions

The currently operating generation of IACTs continues to deliver novel and exciting results, partially via exploiting synergies with different instrument classes or new analysis techniques. In the years leading up to CTA, this generation of IACTs will continue to provide the high resolution view, both angular and spectral, needed to improve our understanding of the gamma-ray sky.

6 Acknowledgements

The author acknowledges the support of the Max Planck Institut für Kernphysik and thanks the organizers of the Vulcano Workshop for the invitation to participate.

References

1. Hillas, A. Evolution of ground-based gamma-ray astronomy from the early days to the Cherenkov Telescope Arrays. *Astroparticle Physics*. **43** pp. 19-43 (2013).
2. H. E. S. S. Collaboration, Time-resolved hadronic particle acceleration in the recurrent nova RS Ophiuchi. *Science*. **376**, 77-80 (2022).
3. MAGIC Collaboration, Proton acceleration in thermonuclear nova explosions revealed by gamma rays. *Nature Astronomy*. **6** pp. 689-697 (2022).
4. HAWC Collaboration, Very-high-energy particle acceleration powered by the jets of the microquasar SS 433. *Nature*. **562**, 82-85 (2018).
5. Olivera-Nieto, L., for the H.E.S.S. Collaboration. Contributed presentation at the 7th Heidelberg International Symposium on High-Energy Gamma-Ray Astronomy 2022. <https://indico.icc.ub.edu/event/46/contributions/1302/>
6. VERITAS, MAGIC and H.E.S.S. Collaborations, Observation of the Gamma-Ray Binary HESS J0632+057 with the H.E.S.S., MAGIC, and VERITAS Telescopes. *The Astrophysical Journal*. **923**, e241 (2021).
7. Mohrmann, L., Specovius, A., Tiziani, D., Funk, S., Malyshev, D., Nakashima, K. and Eldik, C. Validation of open-source science tools and background model construction in γ -ray astronomy. *A&A*. **632** pp. eA72 (2019).
8. H.E.S.S. Collaboration, A deep spectromorphological study of the γ -ray emission surrounding the young massive stellar cluster Westerlund 1. *A&A*. **666** pp. eA124 (2022).

9. Cao, Z. Ultrahigh-energy photons up to 1.4 petaelectronvolts from 12 γ -ray Galactic sources. *Nature*. (2021).
10. MAGIC Collaboration, MAGIC observations provide compelling evidence of the hadronic multi-TeV emission from the putative PeVatron SNR G106.3+2.7. *ArXiv E-prints*. pp. earXiv:2211.15321 (2022).
11. Park, N., for the VERITAS Collaboration. Contributed presentation at the 7th Heidelberg International Symposium on High-Energy Gamma-Ray Astronomy 2022. <https://indico.icc.ub.edu/event/46/contributions/1304/>
12. HESS Collaboration, Acceleration of petaelectronvolt protons in the Galactic Centre. *Nature*. **531**, 476-479 (2016).
13. VERITAS Collaboration VERITAS Observations of the Galactic Center Region at Multi-TeV Gamma-Ray Energies. *ApJ*. **913**, e115 (2021).
14. H.E.S.S. Collaboration, A very-high-energy component deep in the γ -ray burst afterglow. *Nature*. **575**, 464-467 (2019).
15. MAGIC Collaboration, Observation of inverse Compton emission from a long γ -ray burst. *Nature*. **575**, 459-463 (2019).
16. H.E.S.S. Collaboration, Revealing x-ray and gamma ray temporal and spectral similarities in the GRB 190829A afterglow. *Science*. **372**, 1081-1085 (2021).
17. MAGIC Collaboration, Combined searches for dark matter in dwarf spheroidal galaxies observed with the MAGIC telescopes, including new data from Coma Berenices and Draco. *Physics Of The Dark Universe*. **35** pp. e100912 (2022).
18. H.E.S.S. Collaboration, Search for Dark Matter Annihilation Signals in the H.E.S.S. Inner Galaxy Survey. *Phys. Rev. Lett.* **129**, e111101 (2022).
19. MAGIC Collaboration, Bounds on Lorentz Invariance Violation from MAGIC Observation of GRB 190114C. *Phys. Rev. Lett.* **125**, 021301 (2020).

HIGH ALTITUDE WATER CHERENKOV OBSERVATORY (HAWC): RECENT RESULTS

Omar Tibolla on behalf of HAWC collaboration
Universidad Politécnica de Pachuca, Pachuca, Hidalgo, Mexico
Dept. of Physics, Durham University, UK

Abstract

The acronym HAWC stands for High Altitude Water Cherenkov Observatory. HAWC is a wide field of view observatory and consists of an array of 300 water Cherenkov detectors and 345 smaller water Cherenkov detectors to scan the sky to search for transient and steady emission of TeV and multi TeV gamma rays: in fact HAWC can detect gamma-rays up to very high energies of several hundreds TeV. HAWC is a great survey instrument, since it continuously observes almost $2/3$ of the entire sky every sidereal day. Therefore, after the first seven years of operation, several great scientific achievements have been reached with HAWC, such as many new TeV gamma-ray emitters are now detected, moreover known TeV gamma-ray sources can be studied in more detail and up to higher energies. Some highlights of the most recent results are presented.

1 The High Altitude Water Cherenkov Observatory

HAWC is located between Sierra Negra (4640 m above sea level, a.s.l.) and Pico de Orizaba (5636 m a.s.l.) at 4100 m a.s.l., at a latitude of +19 deg, covering an area of almost 22000 m² with water Cherenkov tanks. HAWC consists of an array of 300 water tanks that detects particles created in atmospheric particles showers, both electro-magnetic and hadronic cosmic-ray atmospheric showers: each tank is 5 meters tall and is filled with 200000 liters of purified water. In each tank the atmospheric showers particles produce Cherenkov radiation which is detected by the photomultiplier tubes (PMT). HAWC operates days and night at any weather conditions (which is a significant advantage when comparing it with instruments in the same and in the adjacent energy band such as the Imaging Atmospheric Cherenkov Telescopes), i.e. it does not have limited duty cycle, with an instantaneous Field of View (FoV) of ~ 2 Sr (i.e. almost 15% of the entire sky). Therefore HAWC scans 2/3 of the sky every 24 hours to a depth of 1 Crab at 5σ ; this deep sensitivity is crucial to study both extended diffuse sources and transient events. HAWC is ~ 15 times more sensitive than the first generation water Cherenkov observatory such as Milagro experiment. HAWC registers 25000 cosmic rays per second, generating ~ 2 Terabytes of data per day, every day, operating in a nominal energy range between ~ 300 GeV and ~ 100 TeV. The operations with HAWC with a partial array started in 2013, while HAWC array was completed in 2015. The official inauguration was in March 2015. In ¹⁾ more information on the HAWC observatory, its operations, performances, air shower event data reconstruction can be found.

Then, in 2017-2018 a hardware upgrade occurred; a sparse outrigger array of 345 smaller (i.e. 1.65 meters tall, containing ~ 2500 liters of purified water) water Cherenkov detectors was added around the HAWC main array, extending its detection area by a factor of ~ 4 , i.e. covering an area of ~ 100000 m². This major hardware upgrade increases the sensitivity to the highest energy events by determining the core position for showers that fall off the main array, i.e. this low cost HAWC extension significantly improves its sensitivity above 10 TeV, e.g. at 50 TeV HAWC sensitivity increases by a factor 3-4. The outrigger upgrade is described in details in ²⁾.

2 An improved reconstruction algorithm: Pass 5

Recently, the HAWC Collaboration underwent a major technical software update. This collection of improved reconstruction algorithms is known as "Pass 5". The rest of this article uses results from Pass 5. While the vast majority of previously published HAWC results were based on our previous, Pass 4, event reconstruction ¹⁾, with the update to Pass 5, HAWC reconstruction algorithm performance significant improved in several aspects:

- Improved gamma/hadron separation efficiency at all energies, especially for high zenith angles and for larger events (which means at higher energies);
- Enhanced high zenith angle reconstruction which drastically improves the high-energy pointing which leads to a much narrower Angular Resolution which does not degrade at high zenith angles;
- Analysis extended to smaller (which means fewer PMTs hit) events with a new methodology to identify and remove noise;
- Addressing the PMT saturation effect that was limiting HAWC effective area at higher energies;

Pass 5 improved reconstruction algorithm is described in more details in ⁴⁾; Fig. 1. clearly shows some of its crucial consequences such as the astonishing improvements in both significance (which implies a much more performant gamma/hadron separation) and angular resolution.

The new Pass 5 reconstruction algorithm is used in all the recent results shown in this article, as recently shown in ³⁾ as well.

3 Solar Physics with HAWC

I start this brief review on the recent astrophysical results from the HAWC experiment with the counterintuitive example about the possibility of performing solar physics studies with HAWC.

Fermi-LAT detected GeV gamma-rays from the Sun up to ~ 100 GeV. A correlation of this emission to the solar cycle was determined: at the Solar Minimum higher GeV gamma-ray flux was detected from the Sun and viceversa.

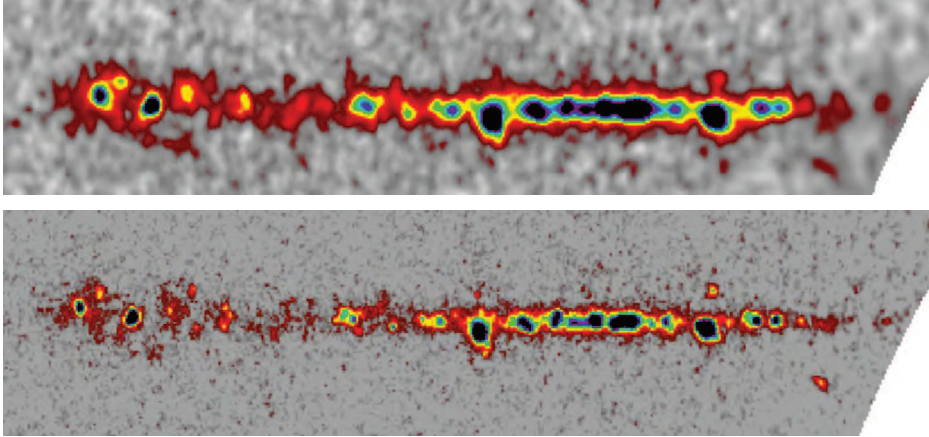


Figure 1: Comparison between the significance map of 1523 days of observations of the Galactic Plane with Pass 4 (upper plot) and the significance map of 2090 days of observations of the same region with Pass 5 (lower plot). Fig. 3 shows more details about the improved HAWC observations of the Galactic Plane.

Hence the emission mechanism seems rather clear and straightforward: CRs hadrons interact with the Sun's atmosphere producing the gamma-ray emission. Therefore, at the Solar Maximum with a higher solar magnetic field, more CRs are deflected and therefore the gamma-ray luminosity of the Sun is lower (and viceversa).

However EAS detectors see the shadow of the Sun in the CR sky, e.g. ²²⁾, since the Sun is mainly a "negative source" at multi-TeV energies. Hence we can detect the Sun in TeV and multi-TeV gamma rays simply subtracting from the map the well known Sun's shadow amplitude and shape. With HAWC we can significantly detect ($\sim 5.9\sigma$) the Sun in VHE gamma-rays from the Sun with the advent of Pass 5. Furthermore, as shown in Fig. 2, we can compare the fluxes and spectra at the Solar Minimum and Maximum.

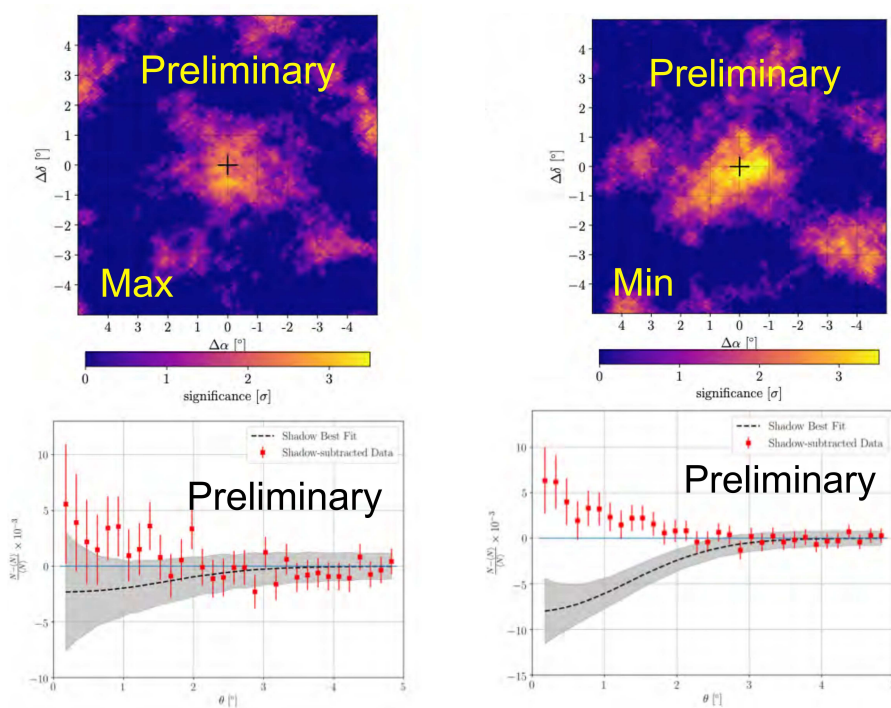


Figure 2: Preliminary gamma-ray map of the Sun showing the multi-TeV significance after subtracting the Sun shadow. In the lower plots the significance profile compared to the Sun shadow are shown. The preliminary peak significance for the Solar Maximum is $\sim 3.5\sigma$ and for the Solar Minimum is $\sim 4.9\sigma$, respectively.

4 Pushing to the highest energies and consequences for the Galactic science

Fig. 3 shows the preliminary HAWC significance map of the Galactic Plane with our new Pass 5 event reconstruction algorithm. Because of the improved gamma/hadron separation, e.g. as a comparison with the previous HAWC Galactic Plane results ⁵⁾, fainter gamma-ray sources are now clearly detected. Moreover several large TeV gamma-ray extended sources, such as HAWC J2227+610, are now disentangled in two or more sources, thanks to the

upgraded angular resolution.

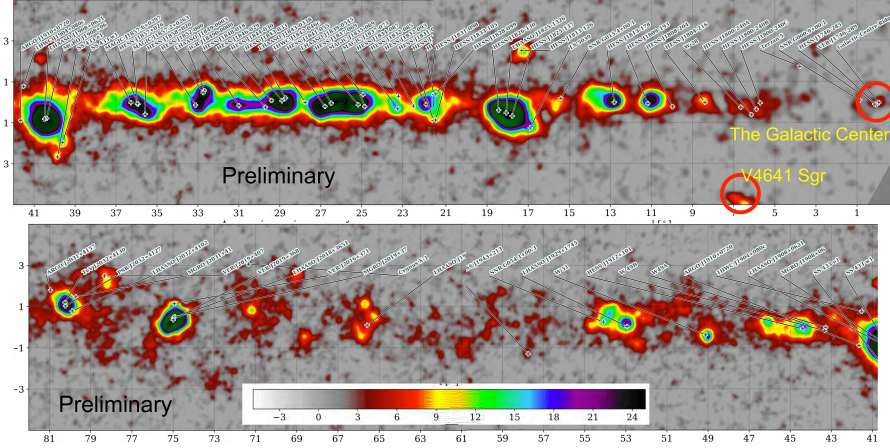


Figure 3: The preliminary HAWC significance map of the Galactic Plane in Galactic coordinates with Pass 5 event reconstruction of 2090 days observations; the significance in standard deviations, σ , is represented in the color bar. The red circles mark the Galactic Center region and V4641 Sgr.

In Fig. 3 the Galactic Center region and the newly discovered TeV microquasar V4641 Sgr (shortly described in the next sections) are highlighted. At HAWC latitude, the Galactic Center transits with a minimum zenith angle of 47 deg and now, with better reconstruction algorithms, we can study this region with much higher accuracy: its energy spectrum is still under investigation, however the preliminary results are compatible with H.E.S.S. energy spectrum beyond 20 TeV.

Moreover, as underlined in the previous section, especially HAWC highest energies bands are the one that benefit most from Pass 5 great improvements. It is remarkable that, with the preliminary works using Pass 5, we can significantly detect 20-30 gamma-ray sources above 56 TeV, which is a great results when considering that 9 sources were detected in the same energy band using Pass 4, as published in ⁶⁾. Most of these sources, which appear to be mostly extended, are either Pulsar Wind Nebulae (PWN) systems and unidentified Galactic gamma-ray sources, with the only exceptions of a Star Forming

Region and a binary system. This is a remarkable result if we consider the adjacent TeV band. In the last two decades more than 200 gamma-ray sources have been detected at TeV energies using the recent generation of Imaging Atmospheric Cherenkov Telescopes (IACTs, such as VERITAS, H.E.S.S. and MAGIC) detected and $\sim 50\%$ of the detected Galactic sources are still unidentified, i.e. they are not yet firmly identified. Now, with the advent of Pass 5, the dominance in number of unidentified sources is even stronger in the adjacent multi-TeV band: in fact $\sim 60\%$ of the newly detected multi-TeV gamma-ray sources are unidentified. In general, while on one hand the unidentified very high energy gamma-ray sources can often be effectively described as relic PWNe (especially the very high energy unidentified sources that lack of any lower energy plausible counterparts in particular in X-rays and at radio wavelengths, the the so-called dark sources, can be realistically explained only as ancient PWNe), e.g. ⁷⁾ the hadronic scenarios generally encounter greater difficulties, e.g. ⁸⁾, in most of the cases evidenced by the lack of evidence of plausible target material.

Pushing to higher energies both the tremendous improvements due to Pass 5 and the dominance of the leptonic scenarios (PWNe and likely leptonic unidentified sources) become more and more remarkable. While 3 gamma-ray sources were detected with Pass 4 ⁶⁾, now, using Pass 5, we can preliminarily detect 18 gamma-ray sources above 100 TeV and all of them seem to be either PWNe or unidentified gamma-ray sources (most of these sources appear to be extended as well). Finally, 4 gamma-ray sources are significantly detected above 177 TeV for the first time with HAWC. These sources are 3 PWNe and 1 (candidate PWN) Unidentified gamma-ray source. This apparent predominance of leptonic accelerators in this energy band is a considerable preliminary result from HAWC; in fact, at first sight, we notice a clear dominance of leptonic accelerators in the highest HAWC energy bands, i.e. approaching the so-called knee of Cosmic Ray (CR) spectrum at ~ 1 PeV which is so crucial for understanding the origin of cosmic rays. This could surprise when searching CR accelerators within the so-called standard models, e.g. ⁹⁾, and hence searching for hadronic PeVatrons, however it should not because this result has been widely anticipated and foreseen by two decades of IACTs observations. Moreover previous HAWC studies clearly went in this direction: in order to give a clear example, Fig. 3 of ⁶⁾ describes the multi-TeV energy spectra of

the 3 above mentioned sources detected above 100 TeV with Pass 4 reconstruction algorithm (with the energy spectrum of the Crab Nebula as a reference): as well in that case two of the sources are PWNe and the remaining one is an unidentified (candidate PWN) source.

Speaking about PWNe systems, it is important to underline the new HAWC discovery of a multi-TeV gamma-ray source which surrounds the radio-quiet pulsar PSR J0359+5414, which exhibits a high spin-down power ($\dot{E} \simeq 1.3 \times 10^{36}$ erg s¹). At a distance from us of 3.45 kpc, PSR J0359+5414 is isolated and slightly off-set from the Galactic plane (~ 1 deg). This pulsar has been detected at GeV energies with Fermi-LAT, however no emission from this region of the sky has been detected before in VHE TeV and multi-TeV gamma rays, i.e. by any Extensive Air Shower (EAS) or IACT observatory. Moreover an analysis of subthreshold HAWC data has shown that leptonic ultra-high-energy emission is a universal feature around pulsars ³³).

5 Where are hadronic Galactic PeVatrons?

Never the less, one of the most crucial questions for the CR origin still remains: where are the hadronic Galactic PeVatrons? On this topic HAWC recent results are outstanding as well.

5.1 The Boomerang region

The region around the pulsar PSR J2229+6114 and the supernovae remnant (SNR) G106.3+2.7, which at radio wavelengths appears as comet-shaped source, is generally known as the Boomerang region and it has been longly studied at TeV energies, e.g. ¹⁰). With HAWC we detect a very bright multi-TeV gamma-ray source in the Boomerang region ¹¹) as well. Fig. 4 summarizes recent HAWC observations of the region. The PWN formed by the relativistic electrons and positrons accelerated by the high spin-down luminosity pulsar PSR J2229+6114, is called Boomerang Nebula; this PWN is clearly visible at radio wavelengths, in X-rays and gamma rays. Boomerang PWN is fully contained in its SNR, G106.3+2.7. Hence, even if the source often is simply considered as a PWN, e.g. ¹²), both hadronic and leptonic scenarios are plausible, as mentioned in ¹¹).

The joint VERITAS-HAWC energy spectrum is well fit by a pure power law from 800 GeV to 180 TeV as shown in Fig. 2 of ¹¹); therefore, in case of

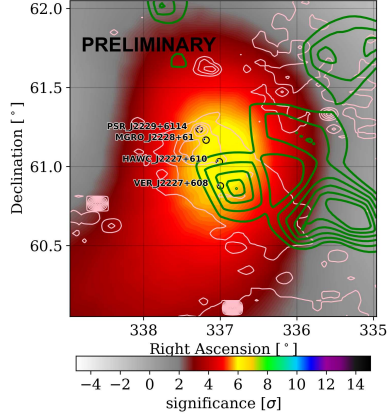


Figure 4: The preliminary significance map of 1347 days of observations of the Boomerang region with Pass 4; the green contours refer to the DAME CO survey ¹³⁾ and the pink contours indicate the 1.4 GHz continuum brightness temperature from the Canadian Galactic Plane Survey ¹⁴⁾; the relevance of both these multi-wavelength observations for this scientific case is described in details in ¹¹⁾.

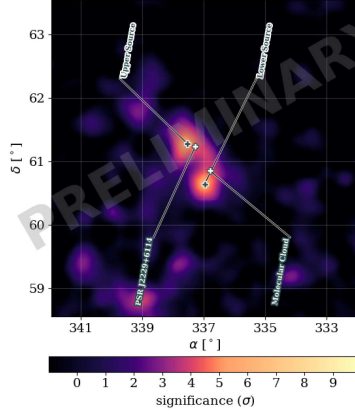


Figure 5: The preliminary multi-TeV significance map of the Boomerang region with Pass 5 clearly indicates two distinct gamma-ray sources.

hadronic acceleration, this will constrain the cutoff energy in the underlying proton spectrum to be above 800 TeV. The advent of Pass 5 increases the plausibility to study Boomerang region as a potential hadronic PeVatron: in fact now the previously published HAWC source can be resolved into two distinct sources, as shown in Fig. 5. Moreover, in the adjacent energy band, MAGIC telescopes detect these two distinct sources of TeV gamma-rays as well ¹⁵⁾.

- The Head Region (North West Source) which contains the pulsar and its PWN; their presence would clearly suggest a leptonic scenario, i.e. the

IC scattering of relativistic leptons accelerated by PSR J2229+6114 on background photons

- The Tail Region (South East Source) seems instead spatially coincident to the molecular cloud shown in Fig. 3; the presence of a dense molecular cloud suggests hadronic scenarios to explain the gamma-ray emission.

5.2 LHAASO J2108+5157

LHAASO J2108+5157 was discovered in LHAASO-KM2A survey ¹⁶⁾ up to 200 TeV. This intriguing source is located north of Cygnus region, 3 deg off-set from the Galactic plane. LHAASO J2108+5157 is now significantly detected with HAWC Pass 5 reconstruction algorithm as well; given its is spatial coincidence with a giant molecular cloud, this intriguing source represents an ideal scientific case for a plausible hadronic Pevatron as origin of the multi-TeV gamma-ray emission. On the other hand, a relic PSR/PWN system, such as ⁷⁾ or ⁸⁾, cannot be disproved so far and very recently it been suggested as a possible explanation for LHAASO J2108+5157 in ¹⁷⁾.

A joint HAWC - VERITAS analysis is undergoing. Notably the preliminary HAWC (only) spectrum indicates harder and lower flux than seen by LHAASO. It is relevant to mention here that moreover a harder spectrum would likely strengthen a hadronic interpretation of the multi-TeV gamma-ray emission, not only because hadronic models generally prefer harder spectra, but also because a harder energy spectrum seems requested at lower energies considering Fermi-LAT flux upper limits ¹⁶⁾; moreover the lower energy upper limits described in ¹⁷⁾ might impose very strong constraints on hadronic scenarios of accelerated protons interacting with the giant molecular cloud.

5.3 HESS J1809-193

With HAWC we can detect another potential PeVatron candidate: HESS J1809-193. As well as for the previous scientific cases, the TeV and multi-TeV gamma-ray emission can be explained within several and competing scenarios:

- A PWN leptonic scenario can be assumed taking into account the quite powerful $\dot{E} \simeq 1.8 \times 10^{36}$ erg s⁻¹) 51 kyr pulsar PSR J1809-1917 which is located close to the H.E.S.S. emission peak.

- A hadronic PeVatron scenario can be considered due to the fact, that several SNRs are indeed located in the region of HESS J1809-193. In particular, the peak of the gamma-ray emission detected by H.E.S.S. is spatially coincident with G11.0-0.0.

We notice good agreement between our preliminary spectrum and the H.E.S.S. energy spectrum. Moreover, the combined spectral energy distribution (SED) reaches an energy of up to 100 TeV and no significant sign of cutoff is found. Notably LHAASO was not detecting multi-TeV gamma-rays from HESS J1809-193, most probably because of the location of this VHE gamma-ray source at the edge of the field of view of LHAASO.

6 Binary systems

Exceptional improvements with the new Pass 5 have been achieved for another class of Galactic emitters: binary systems. With Pass 4, in 1523 days of HAWC observations, significant emission was detected only in the case of SS 433¹⁸⁾, while no other known high-mass microquasars were detected significantly¹⁹⁾. With Pass 5 instead, multi-TeV gamma-rays could be detected with HAWC from several binary systems.

6.1 LS 5039

The radio quiet binary system LS 5039 consists of massive O-type main-sequence star and a compact object, which could be either a black hole or a pulsar. These two objects orbit each other in an eccentric orbit every 3.9 days. LS 5039 is located near the extended PWN HESS J1825-138, which has very bright TeV gamma-ray emission. We could now disentangle the gamma-ray emission from LS 5039 and HESS J1825-138 due to the improved angular resolution. Furthermore, the energy spectra of both high and low states of LS 5039 can be studied.

More than a decade ago the H.E.S.S. collaboration separately studied the high and low states of the LS 5039 energy spectra²⁰⁾ defining two broad phase intervals: INFC, encompassing inferior conjunction, and SUPC: superior conjunction. The preliminary spectra extracted by HAWC data are in good agreement with the spectra measured by H.E.S.S.

6.2 SS 433

The discovery of VHE emission from the microquasar SS 433 was published in 19). This peculiar source is located nearby to the very bright and extended gamma-ray source MGRO J1908+06.

The binary system SS 433 consist of a supergiant star that is overflowing its Roche lobe with matter accreting onto a compact object (presumably a black hole). Perpendicular to the line of sight, two jets of ionized matter can be detected; moreover the SNR W50 is disorted by the jets which terminate inside it. Both X-ray and gamma-ray emission could be detected from the lobes of the jets. With Pass 4 analysis we could reach a marginal detection of the lobes (i.e. 5.8σ for the lobes simultaneously, below 5σ for the lobes separately 19)), while with the advent of Pass 5, the lobes have been detected significantly with 7 and 9σ , respectively (see Fig. 6).

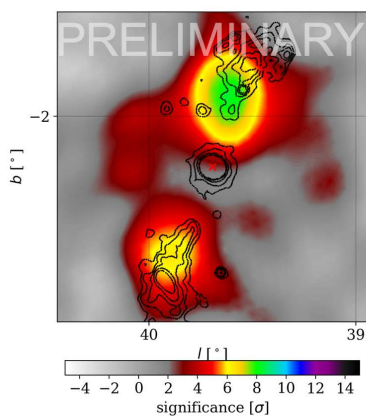


Figure 6: The preliminary significance map as measured by HAWC of the SS 433 region. The red X marks the location of the compact object. The black contours illustrate the X-ray emission observed by ROSAT (33).

6.3 V4641 Sgr

V4641 Sagittarii is a famous variable binary system located in the Sagittarius constellation and now a newly discovered multi-TeV microquasar. V4641 Sgr exhibits one of the fastest superluminal jets known in our Galaxy. The high velocity of the superluminal motion implies that a jet is pointing towards us, moreover this is in line with the very small angular size of the radio jet (21). V4641 Sgr is observed at high zenith angle (~ 45 deg) with HAWC and a significant 9.7σ with Pass 5 detection was obtained with Pass 5.

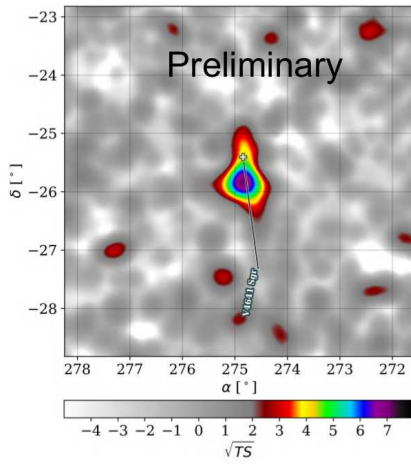


Figure 7: Preliminary significance map of V4641 Sgr.

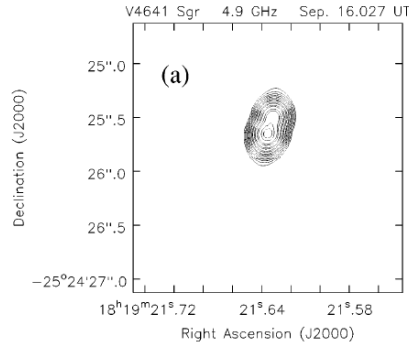


Figure 8: September 16.027 UT image of V4641 Sgr at 4.9 GHz with peak at 0.248 Jy, contouring at $\pm 2^{n/2} \times 0.005$ Jy for $n = -1, 1, 2, \dots$ from (21)

7 Extragalactic astrophysics with HAWC

With of Pass 5 updated algorithms, there are significant improvements for extragalactic astrophysics as well; in fact after monitoring Mrk 421 and Mrk 501 for several years, now three Active Galactic Nuclei (AGN) are significantly detected with HAWC:

- M87 is classified as a giant Fanaroff–Riley I radio galaxy and is the central dominant galaxy of the Virgo Cluster; hence M87 and its central

supermassive black hole (SMBH) M87* are one of the best studied AGN in the whole sky at every wavelengths. E.g., in fact the radio galaxy Messier 87 was one of the best candidate to localize the origin of the VHE particle acceleration in the immediate vicinity of the black hole ³⁴⁾ and the shadow of M87* was the first imaged by the Event Horizon Telescope ³⁵⁾. After the marginal detection at multi-TeV gamma-rays ³⁶⁾, with Pass 5 M87 is significantly detected with HAWC at $\sim 6\sigma$ level (TS= 35.7).

- 1ES 1215+303, also known as ON 325, is a high synchrotron peaking BL Lac object and has been already observed by IACTs at VHE TeV gamma-rays ³⁷⁾. Now 1ES 1215+303 is significantly detected with HAWC at $\sim 6.7\sigma$ level (TS= 45.2) and its preliminary spectral energy distribution is compatible with VERITAS spectra ³⁸⁾.
- VER J0521+211 represents a peculiar case of discovery of a BL Lac-type blazar triggered by VHE observations ³⁹⁾; with Pass 5, VER J0521+211 is marginally detected with HAWC at $> 4\sigma$ level (TS= 18.2). Preliminary HAWC energy spectrum exhibits lower fluxes than VERITAS ⁴⁰⁾.

8 Final remarks

Additionally to the recent results described in this proceedings paper (i.e. the search for hadronic Pevatrons, VHE Pulsar Wind Nebulae, Galactic Center, Solar Physics, Active Galactic Nuclei, Binary Systems and Microquasars), there are several other HAWC recent results, such as:

- Cosmic Rays studies: in ²³⁾ we presented our H + He energy spectrum and now we exam the "all particle" ²⁴⁾ energy spectrum with Pass 5
- Dark Matter studies: upper limits on possible Dark Matter contributions have been determined for dwarf galaxies ²⁵⁾, the Andromeda galaxy ²⁶⁾ and the Galactic Halo ²⁷⁾.
- Fundamental Physics: e.g. constraints on the Lorentz invariance violations ²⁸⁾.
- Multimessenger activities: crucial for e.g. gamma-ray counterparts of gravitational waves (GW), e.g. ²⁹⁾, and neutrino events, e.g. ³⁰⁾.

- Geophysics with HAWC: in fact HAWC was recently used to trace large atmospheric transient waves as created by the explosion of the Hunga volcano ³¹).

9 Acknowledgments

The authors acknowledge The Royal Society Newton Advanced Fellowship 180385.

References

1. Abeysekara A. U. et al. *ApJ* **843** 39 (2017).
2. Marandon V. et al. *arXiv:1908.07634* (2019).
3. Tibolla O. et al. *procs of CRIS 2022* to be publ. in *Journal of Phys.* (2022).
4. Sohyoun L.Y.C. and Smith A. *Bulletin of the APS* **67** 6 (2022).
5. Abeysekara A. U. et al. *ApJ* **843** 40 (2017).
6. Abeysekara A. U. et al. *PRL* **124** 021102 (2020).
7. Vorster M., Tibolla O., Kaufmann S. and Ferreira S. *ApJ* **773** 139 (2013).
8. Tibolla O., Kaufmann S. and Chadwick P. *J* **5(3)** 318 (2022).
9. Tibolla O., Blandford R. et al. *Cosmic Ray Origin - Beyond the Standard Models* (Amsterdam: Elsevier), *Nucl. and Part. Phys.* **297-299** (2018).
10. Acciari V. A. et al. *ApJ* **703** L6 (2009).
11. Albert A. et al. *ApJ* **896** L29 (2020).
12. Acero F. et al. *ApJ* **773** 77 (2013).
13. Dame T. M., Hartmann D. and Thaddeus P. *ApJ* **547** 792 (2001).
14. Taylor A. R. et al. *AJ* **125** 3145 (2003).
15. Oka T. et al. *Proc. of 37th Inter. CR Conf.* **395** 796 (2021).
16. Cao Z. et al. *ApJ* **919** L22 (2021).

17. Abe S. et al. *arXiv:2210.00775* (2022).
18. Abeysekara A. U. et al. *Nature* **562** 82 (2018).
19. Albert A. et al. *ApJ* **912** L4 (2021).
20. Ahronian F. et al. *A&A* **460** 743 (2006).
21. Hjellming R. M. et al. *ApJ* **544** 977 (2000).
22. Albert A. et al. *Phys. Rev. D* **98** 123011 (2018).
23. Albert A. et al. *Phys. Rev. D* **105** 063021 (2021).
24. Alfaro R. et al. *Phys. Rev. D* **96** 122001 (2017).
25. Albert et al. *Phys. Rev. D* **101** 103001 (2020).
26. Abeysekara A. U. et al. *JCAP Issue* **06** 043 (2018).
27. Abeysekara A. U. et al. *JCAP Issue* **02** 049 (2018).
28. Albert A. et al. *PRL* **124** 131101 (2020).
29. Abbott B. P. et al. *ApJ* **848** L12 (2017).
30. Aartsen M. G. et al. *A&A* **607** 115 (2017).
31. Alfaro R. et al. *arXiv:2209.15110* (2022).
32. Brinkmann W., Aschenbach B. and Kawai N. *A&A* **312** 306 (1996).
33. Albert A. et al. *ApJ* **911** L27 (2021).
34. Acciari V. A. et al., *Science*, **325**, 444 (2009).
35. The EHT Collaboration et al. *ApJ*, **875**, L1 (2019).
36. Alfaro R. et al. *ApJ*, **934**, 158 (2022).
37. The MAGIC Collaboration *A&A*, **544**, id.A142 (2012).
38. Valverde J. et al. *ApJ* **891** 170 (2020).
39. Archambault S. et al. *ApJ* **776** 69 (2013).
40. Adams C. B. et al. *ApJ* **932** 129 (2022).

STATUS OF THE SOUTHERN WIDE-FIELD GAMMA-RAY OBSERVATORY (SWGGO)

Ulisses Barres de Almeida
Brazilian Center for Physics Research (CBPF)
Rua Dr. Xavier Sigaud 150, 22290-180 Rio de Janeiro, Brazil
on behalf of the SWGO Collaboration

Abstract

The Southern Wide-field Gamma-ray Observatory (SWGGO) is the Collaboration to build a new extensive air shower array in South America for the observation of very- to ultra-high-energy gamma-rays, and is currently engaged in the design and prototyping work towards the realisation of this future facility. SWGGO will use an array of water-Cherenkov-based particle detectors to provide a wide field and high duty cycle view of the southern sky, complementing CTA and the existing particle arrays of the Northern Hemisphere, such as HAWC and LHAASO. Towards the lower energies, SWGGO aims to push the observational range of wide-field ground-based gamma-ray facilities down to a few hundred GeV, thus bridging the gap with space-based instruments in the monitoring of the VHE sky. In this contribution, I will provide an overview of the status of the project and plans for the future, including performance expectations and science goals, as well as ongoing activities towards the site search and technological developments.

1 A wide-field gamma-ray observatory in the south

Astrophysics' most extreme accelerators can be effectively probed with ground-based gamma-ray facilities, which provide a diagnosis of the high-energy processes ongoing in the sources. Both cosmic rays and gamma-rays initiate extensive air showers (EASs) in the atmosphere, consisting of a large number of secondary relativistic particles that can be measured by terrestrial detectors using a variety of experimental techniques. These particles create Cherenkov light that can be imaged from the ground using telescopes with large reflective surfaces – the imaging atmospheric Cherenkov technique, IACT. The secondary particles distribution can also be directly measured at ground-level using particle detectors. Together, these observational approaches cover a wide range of energies, from about 30 GeV to a few PeV.

The advantage of the air-Cherenkov method is that light can be detected over the entire shower development, thus exploiting the whole atmosphere as calorimeter. Due to the large number of Cherenkov photons emitted, energy resolutions of the order of 15% are typically achieved. The air-Cherenkov pulses are short close to the shower core (order of 10 ns), allowing to achieve a good angular resolution of 0.1° over a wide energy range. Furthermore, most of the emitted light in the optical range (mainly blue) reaches the ground with only little absorption, so that the energy threshold is lower compared to the particle detection technique, which requires the charged secondary particles to have sufficient energy to reach observation level.

The conventional extensive air shower (EAS) array is a particle sampler that measures the secondary particles of the shower front reaching the ground. Many technologies can be applied to such purpose, the most common ones employing water-Cherenkov detectors (WCD) or scintillator units. From the basic working principle of these technologies, it results that particle samplers operate as transit observatories with continuous duty cycle and a wide field-of-view (FoV) of \gtrsim sr. Such detectors also have typically high energy thresholds, since only the most energetic showers penetrate deep enough in the atmosphere to produce measurable signals from charged particles or secondary high-energy photons at ground level. One of the principal advantages of the particle detection technique is the possibility of directly measuring the muon component of the EAS, which allows for effective background rejection and operation into the ultra-high energy range, above several tens of TeV.

The differences between air-Cherenkov detectors and ground particle arrays highlight the importance that both types of instruments be operated in synergy. To ensure an adequate global latitude-longitude coverage with both experimental approaches is therefore one of the main objectives of the field for the near future. From the side of ground particle arrays, this means the installation of the first instrument of its kind in the southern hemisphere.

High-altitude EAS arrays have recently opened-up a new observational window in Astronomy, significantly increasing the number of detected gamma-ray sources in the very- to ultra-high energy domain (VHE to UHE) ¹⁾. In particular, these instruments have been successful in detecting very extended emission around bright sources ²⁾, and achieved unprecedented sensitivity above 100 TeV, detecting the first Galactic sources up to the PeV ³⁾. These remarkable results have all been obtained in the Northern sky, increasing the expectations towards the development of a new instrument in the South, from where most of the Galaxy is visible, and many prominent targets such as the Galactic Center and the Fermi Bubbles can be accessed. Other primary targets, which would benefit from an all-sky coverage for the monitoring and triggering of transient sources, and which motivate an improved sensitivity below 1 TeV, are Active Galactic Nuclei (AGN) and Gamma-ray Bursts (GRBs), as recently demonstrated by LHAASO ⁴⁾.

2 Status of the SWGO Collaboration

SWGO is an international collaboration for the planning and design of a major ground-based gamma-ray observatory in the Andes. It resulted from the joint effort between members of two initiatives targeting the construction of a wide-field air shower array in the Southern Hemisphere, namely the SGSO Alliance ⁵⁾ and the LATTES Project ⁶⁾. Today, SWGO is a strong international collaboration with over 60 institutes distributed in 14 countries, numbering almost 200 scientists, which bring together the experience of previous experiments such as the Pierre Auger Observatory, HAWC, and LHAASO. A large contingent of the participating scientists are from Latin America.

The observatory proposal consists on a baseline design ⁷⁾ that would significantly increase the effective area of the observatory with respect that of HAWC, and lower its detection energy threshold, through a combination of a high fill factor core array (well above 50%, within an area of *sim* 10^{4-5} m²)

and installation at higher elevation site, near 5 km above sea level. Another main objective of the Collaboration's research programme is to improve the background rejection power by, e.g. cost-effective solutions to the identification of muons at individual detector units. In order to achieve greater energy sensitivity for PeVatron searches, the proposal also involves complementing the core detector with a large sparse array, of up to 1 km².

3 Research and Development for SWGO

The SWGO Collaboration is currently in the research and development stage of the project, which seeks to provide a complete plan for the building and operation of the future gamma-ray facility. Following the considerations presented above, the baseline design that will guide the R&D of the observatory consists of:

- a ground-level particle detector array with duty cycle close to 100% and order steradian field of view, to be installed in South America above 4.4 km altitude, between latitudes -30° and -15°.
- to cover a broad energy range, from about 100 GeV to over 100 TeV, and possibly extending up to the PeV scale.
- to be based mostly on water Cherenkov detector units, consisting on a high fill-factor core with an area far greater than that of HAWC and significantly superior sensitivity, surrounded by a low-density outer array.

3.1 General Progress Status

The reference configuration presented in ⁷⁾ guides the SWGO R&D programme, and serves as baseline for the array design optimisation and detector technology options. Table 1 describes the key characteristics of this reference array configuration, which is composed of an outer array with at least 800 detectors placed 16 meters apart from each other, surrounding a core array with circa 5,700 water tanks arranged in a compact regular grid.

There are two primary choices being investigated for the water-Cherenkov detector (WCD) units, with the core and outer arrays sharing the same fundamental unit design. The first is a double-layer cylindrical tank with 3.8 m diameter and top and lower heights of 2.5 m and 0.5 m, respectively ^{8, 9)}. The

Table 1: SWGO reference configuration. Two WCD unit options are listed.

Component	Parameter	Reference design
Core Array	Geometry	160 m radius circle = 80,400 m ²
	Fill Factor	≈ 80%, ~ 5,700 units
Outer Array	Geometry	at least 300 m outer radius = 202,200 m ²
	Fill Factor	≈ 5%, ~ 880 units
WCD units	Double-layer	∅ 3.8 m; 0.5 m (bottom) + 2.5 m (top) height
	Multi-PMT	∅ 3.8 m; 2.75 m height
Photodetectors	Option	Large-area 8" PMT
	Geometry	Central up/downward facing or 3-pt star (Υ)
Electronics	Requirement	Nano-second inter-cell timing
Reference Site	Altitude	4,700 m a.sl.

upper layer of the WCD is used for calorimetry of the electromagnetic shower component, whereas the bottom layer is mostly used for muon tagging. A single, large-area PMT is placed centrally in each layer. Deployment in an artificial pond or a natural lake is being investigated to increase shielding against laterally penetrating particles. The second alternative is a multi-PMT, shallow WCD tank, with diameter of 3.8 m and a height of 1.75 m, which aims to identify the passage of muons by means of the asymmetrical illumination of three upward-facing PMTs placed at its base ¹⁰⁾.

Project R&D is anticipated to be concluded in 2024, along with the choice of the installation site. It should be followed by a Preparatory Phase for finalisation of the engineering array and identification of resources, aiming at a start of observatory construction in as early as 2026.

Site shortlisting and candidate configurations for optimisation simulations have just been concluded. The final array and detector unit configuration will be optimised based on scientific performance, following a series of science benchmarks that have been defined according to the core science cases chosen for the observatory ¹¹⁾. The detailed plans for construction and operations of the SWGO observatory will be consolidated into a Conceptual Design Report, to be delivered at the end of R&D.

3.2 Candidate site investigations

The site selection process for SWGO was separated in a three-step process consisting on candidate sites identification, site shortlisting and final selection of primary and backup site for the observatory installation. Site shortlisting has just been completed at Q3 2022.

Two fundamental site requirements can be derived from the basic concept of sampling the shower front: that of a large flat available area (i.e., for an extended array with a good fraction of instrumented surface) and the requirement of high altitude installation sites, both of which are necessary to achieve satisfactory shower reconstruction and overall performance.

As a result of its Southern Hemisphere location, SWGO will be able to fully exploit the synergies with CTA, while extending the range of Northern wide-field installations like LHAASO, for an all-sky coverage. SWGO is therefore anticipated to be deployed at a latitude range between -15° and -30° , in order to maximize the exposure to galactic sources, and in particular the Galactic Center ($\delta = -28.9^\circ$), and to concurrently optimize overlap with LHAASO. This criteria, together with the altitude restrictions, for which a location above 4.4 km a.s.l. is desirable, leaves the Andes, in South America, as the only possible choice for sites.

Preliminary site identification studies have found suitable options in Argentina, Bolivia, Chile, and Peru, each of which has unique qualities and more closely matches some of the alternatives for the array design or detector technology under consideration. Table 2 indicates the preferred and back-up sites, as defined after the shortlisting process. Preferred sites will now undergo in-depth studies towards final site selection. Generally speaking, the biggest elements under consideration to a final choice are water access, of which $\sim 10^5 \text{ m}^3$ will be required, flatness over a large available area of at least 1 km^2 , and general availability of local infrastructure and quality of site accessibility¹²⁾.

4 Detector Development Options

As seen in the Figure 1, various technological options are being investigated for the individual WCD units¹³⁾. In particular, two mechanical concepts are being considered: bladders installed in surface tanks, which can be made of metal as in HAWC or rotomolded plastic as in the Pierre Auger Observatory;

Table 2: SWGO candidate sites.

Country	Site Name	Latitude	Altitude [m a.s.l.]	Notes
Argentina	Alto Tocomar	24.19 S	4,430	
	Cerro Vecar	24.19 S	4,800	Primary
Bolivia	Chacaltaya	16.23 S	4,740	
Chile	Pajonales	22.57 S	4,600	
	Pampa La Bola	22.56 S	4,770	Primary
Peru	Imata	15.50 S	4,450	
	Sibinacocha	13.51 S	4,900	Lake site
	Yanque	15.44S	4,800	Primary

and floating bladders deployed directly into a natural lake ¹⁴⁾ or an artificial pool.

The capability to discriminate between gamma and CR-induced air showers is the fundamental element of the technique, essential to achieve good sensitivity. Above several TeV, gamma/hadron discrimination can be greatly improved by exploring the low muon content of gamma-ray induced air-showers, using muon detection as a veto to suppress the CR background. At lower energies, cosmic-ray showers are muon-poor, so that gamma/hadron discrimination must be based on the distribution of particles at ground. Here, one relies on the observable differences in the structure of secondary particles at ground, which depends on the nature of the EAS-initiating particle and, in the case of hadronic cascades, present pronounced sub-structures from the decay of neutral pions. In both cases, a good sampling of the shower front, by means of sufficient array fill-factors, is essential.

Two methods are under evaluation to identify muons within the individual detector units: the dual-layer WCD, with a gamma-hadron separation technique based on the use of vertical segmentation to identify energetic muons (of typically a few GeV) that reach the bottom layer detector ^{8, 9)}; and the use of shallow, multi-channel WCDs ¹⁰⁾, which would distinguish muons from electromagnetic particles based on the rise times of the signals and the charge asymmetry between the PMTs. Additionally, new analysis techniques are being researched ^{15, 16)}. Figure 2 shows a schematic depiction of the different

SWG0 R&D Detector Options			
	WCD mechanics	Photodetectors	Electronics chain
	Water Container { Metal Tank (bladders) Plastic Tank (bladders) Lake (bladders)	Detector { Large-area PMT SiPM array Multi-sensor	Photodetector supply { Active base Multi-channel HV
	Segmentation { Double-layer None	Light guide { None WLS plate / fibers	Digitiser { High-rate sampling Medium-rate sampling + TDC
			Clock distribution { White Rabbit RapCal

Figure 1: SWGO detector components and main options under study ¹³⁾.

WCD unit configurations under consideration in the array simulations.

5 Analysis and simulations for array configuration

The definition of a baseline configuration for the array layout and detector unit design, as presented earlier, serves as the basis for performance evaluation and project development during the R&D phase. Further investigation into array configuration options is then guided by a set of predetermined quantitative scientific benchmarks designed to evaluate observatory performance ¹¹⁾. The phase space under study is bracketed by the set of configurations shown in Figure 3.

The fundamental design elements to consider are the overall array area, fill factor, and site elevation. The effective area, gamma/hadron discrimination efficiency, and the angular resolution, over a target energy range, will be the main quantities considered in evaluating the performance of the array.

The key array configuration trade-offs (at a fixed cost) are anticipated to play out between the performance at low energies (>1 TeV), dependent largely on site elevation, fill factor, and detector unit threshold, and at high energies (>100 TeV), driven by the total area of the array and the background rejection efficiency. As already mentioned, a crucial component of the study will be the capability to distinguish between air showers started by cosmic rays and gammas over the entire energy range of operations.

Simulation work is currently ongoing ¹⁷⁾ to assess the performance of

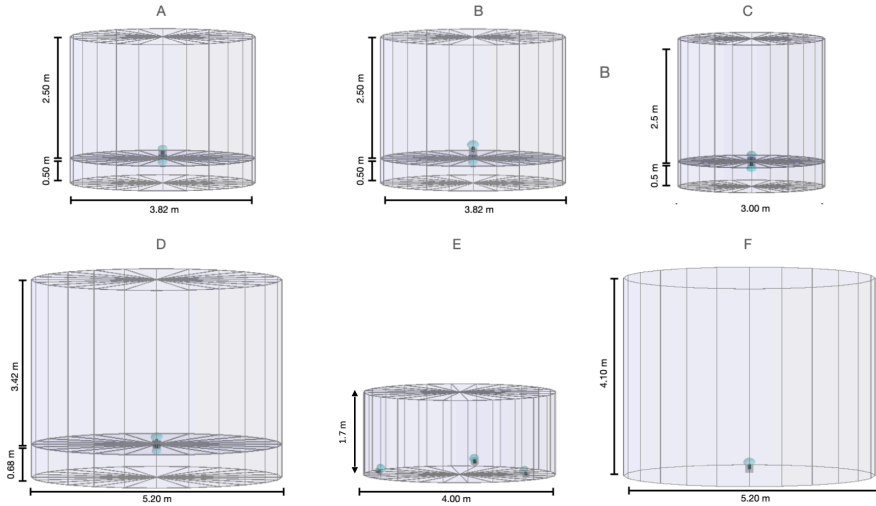


Figure 2: SWGO water-Cherenkov detector unit configurations under study.

the different array designs and detector choices. In terms of array sensitivity to point sources, the phase space bracketed by the options under investigation are shown in Figure 4. The Array A1 configuration in Figure 3 serves as the minimal configuration stated in Table 1, which establishes the performance baseline. In general, decreasing the threshold for individual units and deployment at higher altitude locations can reduce the gamma-ray energy detection threshold. Gains in overall sensitivity will result from improvements in angular resolution and background rejection. The size of the external array and the background rejection efficiency at UHE, which scales with the total available muon detection area, will determine the amount of energy increase reported over 100 TeV.

The optimisation work is being carried out at predetermined altitudes, between 4.1 and 5.2 km, for a same observatory site and magnetic field, and for a fixed estimated total array cost.

6 Science perspectives

The key scientific topics that the SWGO Collaboration plans to focus on, some of which are unique to facilities in the Southern Hemisphere, include:

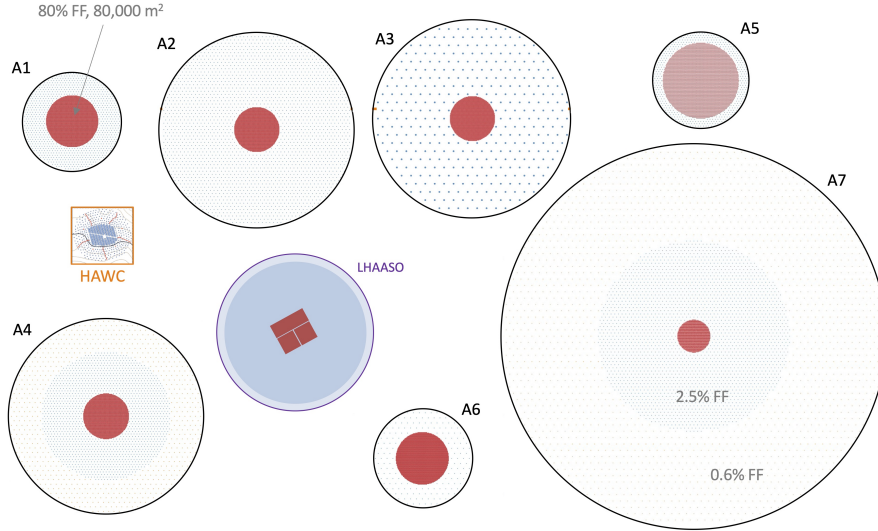


Figure 3: Illustration of the range of array configuration options currently under investigation by the SWGO Collaboration. The baseline array configuration described in Table 1 refers to option A1 of Figure 2. Image Credits: The SWGO Collaboration.

- At lower energies, <1 TeV, transient sources are the main goal, making use of the observatory's wide field of view and nearly constant duty cycle to serve as a complementary monitoring and triggering tool for CTA. The primary scientific objectives are gamma-ray bursts (GRBs) and active galactic nuclei (AGN), which are also the potential multi-messenger counterparts of gravitational waves and VHE neutrinos, respectively.
- At the high-energy end of the spectrum, >100 TeV, the search for PeVatrons, the purported sources responsible for the acceleration of the most energetic cosmic ray particles of the Galaxy, dominates the scientific objectives.
- Deep searches for Dark Matter signals up to 100 TeV are possible thanks to access to the Galactic Center and Halo, covering the entire energy range of WIMP models.
- The improvement in angular resolution at energies higher than a few

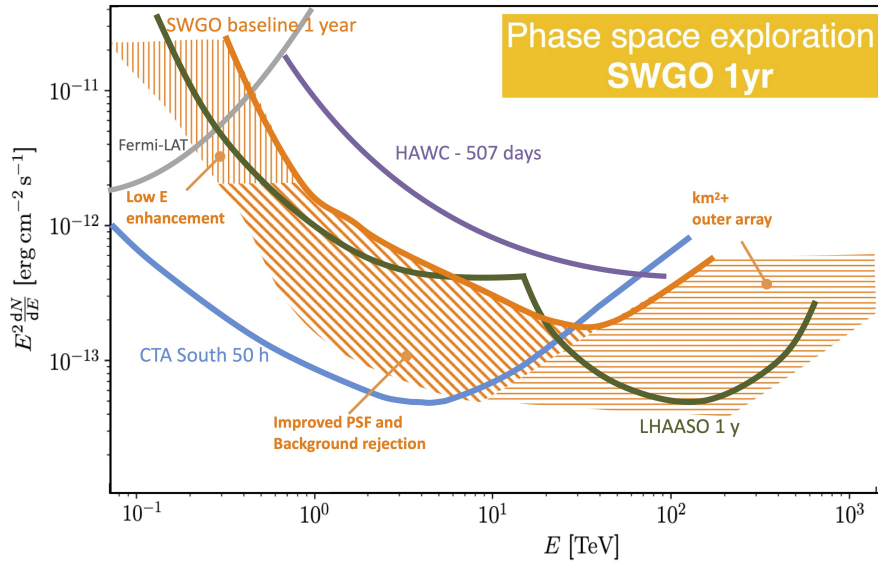


Figure 4: Phase-space explored for SWGO. The orange bracketed phase-space is compared to the differential point-source sensitivity of various experiments ¹⁷⁾. The "baseline" curve refers to the reference configuration, equivalent to array A1. The lower limit of the orange band corresponds to a factor of 30% improvement in the PSF and a factor of 10× improvement in background rejection efficiency. The size of the outer array is the main parameter driving the high-energy enhancement.

tens of TeV will be useful for the study of galactic diffuse emission and extended sources, like PWNe and TeV Halos.

- The accurate measurement of the muon content in hadronic showers will be made possible by the effective single-muon detection capability of detector units, allowing for studies of mass-resolved cosmic rays from tens of TeV to the PeV scale.

7 Conclusions and Outlook

Significant work has already been made toward the final SWGO design, and the prospects from the current stage of the R&D phase point to an instrument of

exceptional performance to be realized in the Andes within this decade. Over the next year we will apply the science benchmarks describing the key science goals of SWGO, to evaluate the trade-offs associated with the various detector unit and array design options under investigation, in order to deliver SWGO as the most valuable tool across a wide range of key scientific areas.

Once ready, SWGO will be a powerful complement to CTA, and the combined SWGO and LHAASO data will provide crucial full-sky coverage for population studies, mapping of the diffuse emission of the Galaxy, measurement of cosmic ray anisotropy, and monitoring of the VHE to UHE transient sky. Alongside the array and detector options evaluations, prototype detector units are being developed at member institutions around the globe, and prepared for deployment and testing at candidate sites over the course of the next several months. At the end of 2023, or early in 2024, all these work fronts are expected to converge towards the final site-detector option definition for SWGO. This will mark the conclusion of the project R&D, and give way to the building of an engineering array for final design optimisation.

8 Acknowledgements

U. Barres de Almeida acknowledges partial funding from a FAPERJ Thematic Grant E-26/211.342/2021 and a FAPERJ Young Scientists Excellence Fellowship E-26/202.818/2019.

References

1. A. Albert *et al*, *Astrophys. J.* **905**, 76 (2020).
2. A.U. Abeysekara *et al*, *Science* **358**, 6365 (2017).
3. Z. Cao *et al*, *Nature* **594**, 33 (2021).
4. Y. Huang *et al*, *GCN Circular* **32677**, 22/10/11 (2022).
5. A. Albert *et al*, eprint arXiv:1902.08429 (2019).
6. P. Assis *et al*, *Astrop. Phys.* **99**, 34 (2018).
7. H. Schoorlemmer *et al*, *PoS(ICRC2021)* **395**, 903 (2022)
8. F. Bisconti & A. Chiavassa eprint arXiv:2205.02148 (2022)

9. S. Kunwar *et al*, eprint arXiv:2209.09305 (2022)
10. P. Assis *et al*, Eur. Phys. J. C **82**, 899 (2022).
11. U. Barres de Almeida *et al*, PoS(ICRC2021) **395**, 893 (2022).
12. M. Doro *et al*, PoS(ICRC2021) **395**, 689 (2022).
13. F. Werner *et al*, PoS(ICRC2021) **395**, 714 (2022).
14. H. Goksul *et al*, PoS(ICRC2021) **395**, 708 (2022).
15. R. Conceição *et al*, Eur. Phys. J. C **81**, 542 (2021).
16. R. Conceição *et al*, J. Cosm. Astrop. Phys. **10**, 86 (2022).
17. H. Schoorlemmer *et al*, PoS(ICRC2021) **395**, 903 (2022).

HADRONIC PEVATRONS (AND THEIR RADIATION SIGNATURES)

Silvia Celli

*Sapienza Università di Roma and Istituto Nazionale di Fisica Nucleare
Piazzale Aldo Moro 5, 00185, Roma, Italy*

Abstract

Since its discovery more than hundred years ago, the origin of the cosmic-ray (CR) flux measured at Earth still remains unknown. To explain the energy region up the knee, located at few PeVs, supernova remnants (SNRs) are usually addressed as main CR accelerators. Despite experimental efforts devoted to the identification of PeV activity in SNRs through the search for radiative signatures at the highest energies, the PeVatron capabilities of SNRs are yet to be confirmed. Recently, renewed interest was raised towards Massive Star Clusters (MSCs) as an alternative candidate (perhaps major) class of PeVatrons, after the detection of gamma rays from some of such objects both in our Galaxy and in the Large Magellanic Cloud. In this contribution, I will discuss the physics of acceleration, propagation and radiation of high-energy particles in SNRs and MSCs.

1 Introduction

The standard paradigm for the origin of Galactic CRs assumes SNRs as main contributors of the particle flux ¹⁾, though still nowadays it remains unclear what is the maximum energy that these sources would be able to produce. In these regards, spectral and composition measurements of CRs are key to discriminate among different possible scenarios and build up a consistent astrophysical framework to explain their origin. The Occam's razor attributes to a unique source population the bulk of the CRs, given the featureless extension of their spectrum from some tens of GeV up to few PeVs: the most grounded scenario explains acceleration of particles up to *knee* energies with SNR shocks. Despite many experimental efforts, the exact location of the CR-knee for individual mass species is still a matter of debate: measurements from the last generation of Extensive Air Shower (EAS) array experiments, as KASCADE, indicated an all-particle knee at around 3 PeV, where the steepening seems to result from the light component of the CR flux, namely protons and He nuclei ²⁾. Observations by high-altitude experiments are in principle less affected by statistical fluctuations of the number of particles in the shower, being closer to the shower maximum: ARGO, for instance, has confirmed the energy of the all-particle knee, while providing indication for lower values of the proton spectral break, around 700 TeV ³⁾. Mass measurements across the knee region, despite being dependent on hadronic interaction models, seem to indicate a mixed composition of the CR spectrum, being dominated by protons at PeV energies, and progressively by heavier nuclei ⁴⁾. This result implies that the CR spectrum depends on the particle rigidity¹: according to the Peters cycle ⁵⁾ then, if the proton maximum rigidity is found at $R_{p,\max}$, for heavier nuclei the maximum energy allowed would correspond to $E_{\max} = ZeR_{p,\max}$. As protons represent the dominant particles in CRs, at least at the lowest energies, the value of $R_{p,\max}$ has a strong impact on the resulting CR spectrum. It hence appears of paramount importance to determine the knee location for individual mass components. A more accurate and improved knowledge about these issues is expected to be achieved in the next years ⁶⁾, thanks to the operations

¹Rigidity is defined as $R = pc/(Ze)$, p being the particle momentum, Ze the nucleus electric charge in terms of atomic number Z and elementary charge e , while c is the in-vacuum speed of light.

of the high-altitude experiment LHAASO ⁷⁾, that with a km² effective area at PeV energies configures as the most sensitive particle shower detector available to date. Measuring the exact location of the proton component is also crucial in the context of theoretical modelling, as to constrain the physical processes operating at the accelerators, particularly their domain of application and their limits.

This contribution is organized as it follows: in sec.2 I will introduce the orthodoxy, describing in details the view that places acceleration at SNR shocks at the origin of the Galactic CR flux and its main limitations. In fact, it is not guaranteed at all that particle acceleration at SNR shocks proceeds up to the PeV, as this would require the presence of sustained Magnetic Field Amplification (MFA) in the shock upstream, which is not necessarily the case for all SNRs. Alternative candidate PeVatron sources have been suggested through the years: in sec.3 MSCs are discussed, in terms of both compact and loose clusters, with a focus on the particle maximum energy that these sources are expected to provide and to the CR composition that would hence result. While we are still far from reaching a unified consistent picture, observations are becoming richer and richer: thus, in sec.4, I will report and comment on recent detections of PeVatrons in our Galaxy. Finally, conclusions are provided in sec.5.

2 Supernova Remnants

The pillars of the SNR paradigm for the origin of Galactic CRs have been formulated during the XXth century, starting as early as in 1934 ⁸⁾, when it became clear that a rate of 3 SuperNovae (SNe) per century, as expected in our Galaxy, characterised by a standard value for the released kinetic energy of 10⁵¹ erg and a 10% conversion efficiency into non-thermal particles, would suffice to explain the power embedded in the CR flux. Additionally, the supersonic blast wave emitted by the SN explosion constitutes an ideal location where particle acceleration can take place: the Diffusive Shock Acceleration (DSA), a special case of the I-order Fermi process, provides a possible mechanism operating at shocks ⁹⁾ (the reader is deferred to ¹⁰⁾ for a complete review on the topic). The powerfulness of this theory resides in the fact that the particle energy gain is found to be independent of the microphysics of the acceleration process, namely from the source of particle scattering. Additionally, DSA is

by construction rigidity-dependent, hence it naturally explain the *second-knee*, namely the CR spectral feature observed at $\simeq 2 \times 10^{17}$ eV, often interpreted as the Iron knee occurring at 26 times higher energy than proton knee. However, the simplest model of DSA, also so-called *test-particle* approach, fails to reproduce the PeV energies required to explain the CR knee. In fact, simply imposing the *Hillas criterion*² one obtains for the particle maximum energy:

$$E_{\max} = v_s R_s B_{\text{up}} \quad (1)$$

R_s and v_s being respectively the shock radius and speed, while B_{up} the value for the upstream magnetic field, which is responsible for the particle confinement. This condition is suitable for protons, which are not expected to be limited by energy losses, in contrast to electrons, for which magnetic and radiation fields affect in a crucial way the evolution of their maximum energy¹⁵). Note that the Hillas criterion reflects a hard upper limits on the maximum energy achievable: in fact, it is not a sufficient condition for acceleration to occur, as what is needed is actually enough time for the turbulence to grow up to the scale of the Larmor radius of the highest energy particles. For characteristic values of these quantities in SNRs, e.g. $v_s \simeq 3 \times 10^3$ km/s, $R_s \simeq 10$ pc and $B_{\text{up}} \simeq 10$ mG, values of the order of $E_{\max} \simeq 100$ TeV can at most be achieved. It is therefore evident that, in order to push the proton maximum energy to the PeV frontier, significant MFA occurring upstream of the shock is necessary.

A possible solution is represented by the fact that the accelerated particles themselves can amplify the magnetic field at shocks during the acceleration process via various plasma instabilities, and consequently the magnetic field strength at SNR shocks might increase as to allow the acceleration of particles up to PeV energies and beyond. Signatures of amplified magnetic fields are inferred from the observed narrow filaments of non-thermal X-ray emission in several young SNRs, the most striking evidence being in Tycho. Resonant and non-resonant streaming instabilities^{12, 13} (RSI and NRSI respectively) have been suggested as natural and effective mechanisms for MFA, the former being induced by spatial gradients of the particle distribution function, while the latter by the current of escaping CRs from the shock upstream.

Particle escape is one of the least understood pieces of DSA theory. While its

²This condition is necessary for particle acceleration to proceed, requiring the particle Larmor radius to be smaller than the accelerator size.

relevance is manifold, as the flux of escaping particles plays an essential role both to achieve PeV energies, as well as in the formation of the Galactic CR flux detected at Earth, the escape process has not yet been consistently integrated within the framework of DSA. If there were no escape from upstream, all particles accelerated in an SNR would be advected downstream and undergo severe adiabatic energy losses before being injected into the InterStellar Medium (ISM): in this case, the requirements to reach PeV energies would be even more severe than they already are from eq.1. In acting as a depletion process with respect to the energetic balance of SNRs, the escape process is also fundamental in shaping the spectra of secondary particles resulting from the hadronic collisions of the energised particles. In fact, gamma-ray spectral observations indicate that no SNR has differential energy distribution resembling the $dN/dE \propto E^{-2}$, as expected from linear DSA theory, showing rather steep spectra and energy breaks that evolve with the system age, being typically lower for more evolved systems. Both these observations can be reconciled by taking into considerations the escape process: in particular, energy breaks would be produced as a result of the maximum energy that the shock would be able to confine at the given age of the system. After the Sedov time t_{Sed} , in fact, $E_{\text{max}}(t)$ is expected to behave as a decreasing function of time because of the shock deceleration during this stage, that would consequently become less effective in generating magnetic turbulence (both RSI and NRSI), and hence in the particle confinement. A phenomenological description of such a behavior was adopted e.g. in [14, 15](#)), where a simplified power law behavior was assumed for the maximum momentum of protons confined by the shock, as:

$$p_{\text{max}}(t) = p_{\text{M}} \left(\frac{t}{t_{\text{Sed}}} \right)^{-\delta} \quad (2)$$

p_{M} being achieved at the Sedov time, and δ a parameter embedding the unknown evolution of magnetic turbulence, to be inferred from observations. The impact of assuming eq.2 on the spectrum of protons from the region inside of a standard SNR is shown in the left panel of fig.1: an energy break is visible in the emerging spectra, corresponding to the maximum energy of confined particles at the age of the accelerator. The computation was performed with standard assumptions, i.e. SNR age of 10^4 yr, expanding into a uniform environment with numeric density $n = 1 \text{ cm}^{-3}$. The acceleration spectrum was set to $f(p) \propto p^{-4}$, as demonstrated by the slope below the energy break, which

is produced by the *particles confined* inside the shock, namely those that are still subject to advection and adiabatic losses. Above the break, instead, the spectrum does not fall abruptly, it rather steepens because of the contribution from the *escaping particles*, that despite being formally detached from the shock are still located in the remnant region. The amount and the duration of this confinement will clearly depend on the value of diffusion coefficient operating in that region: the figure was obtained under the assumption of a homogeneous diffusion coefficient with Kolmogorov spectrum and normalization equal to 10^{27} cm²/s at 10 GeV, which is about a factor 10 smaller than the average Galactic value. A suppression of diffusion coefficient with respect to the Galactic one, that is computed over propagation timescales of several Myr, is expected to be realized in highly-turbulent environments, as around the accelerators themselves. Such an effect has indeed been observed around Pulsar Wind Nebulae (PWNe), as Monogem and Geminga¹⁶).

In this scenario, the steep gamma-ray spectra observed in many middle-aged SNRs would be the result of hadronic interactions of both confined and escaping particles: the right panel of fig.1 shows gamma-ray fluxes resulting from proton-proton collisions inside the SNR shock among confined and escaping particles scattering off target gas. For the purpose of calculations, the SNR was located at a distance of $d = 1$ kpc. Note that the hadronic interpretation of the origin of the radiation from some middle-aged SNRs, as IC443 and W44, is also testified by the detection of the so-called *pion-bump*³ spectral feature¹⁷). Proton-proton collisions in these systems are expected to be boosted also because of the fact that these SNRs are interacting with complex molecular cloud systems. Middle-aged SNRs have hence been considered in the context of the present modelling of particle escape, as shown in fig.2: broadband gamma-ray fluxes observed from IC443 and W51C could be reproduced under reasonable assumptions for the particle acceleration (both spectrum and efficiency), as well as diffusion. In both cases, it is evident that the possible past PeV activity of the sources can only be probed with observations from more sensitive instruments in the energy band beyond 100 TeV gamma rays,

³Such a feature corresponds to a drop in the spectrum of secondary gamma rays produced in the hadronic decay of the neutral pion: the drop is related to the threshold condition for the pion production, i.e. when the meson results at rest in the center of mass frame.

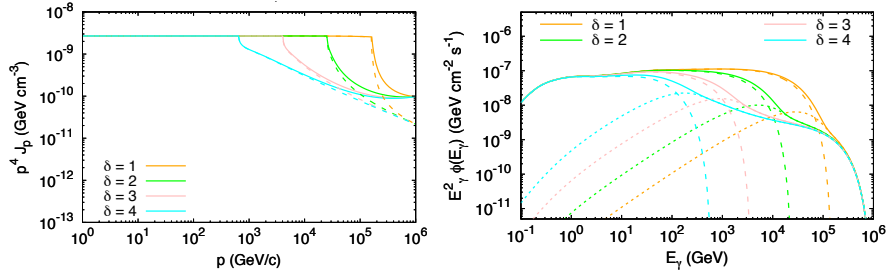


Figure 1: Particle escape modelling in a middle-aged SNR with age 10^4 yr, expanding into a uniform environment with numeric density $n = 1 \text{ cm}^{-3}$. In both panels, the acceleration spectrum has been set to $f(p) \propto p^{-4}$, while homogeneous diffusion coefficient is considered with Kolmogorov spectrum and normalization equal to $10^{27} \text{ cm}^2/\text{s}$ at 10 GeV. The maximum momentum temporal dependence has been parametrized according to eq. 2, with $p_M = 1 \text{ PeV}/c$ and δ as indicated in the legend. *Left*: Spectra of protons from inside the SNR. *Right*: Gamma-ray fluxes from hadronic collisions occurring inside the SNR, located at a distance of $d = 1 \text{ kpc}$. Dashed lines for confined particles, dotted for escaping ones, solid for their total contribution. Figures from (14).

as LHAASO and CTA. A consistent scenario should however be built to reproduce emissions from all messengers possibly resulting from pp collisions (19), including e.g. synchrotron emission from secondary electrons and neutrinos.

The time-integrated history of the particle escaping flux will reflect on the CR spectrum observed at Earth: in the context of SNRs, it seems now well established that the slope of relativistic CRs injected into the ISM is the same as at acceleration stage for spectra steeper than p^{-4} , while it is exactly p^{-4} in the case of linear DSA or harder (20, 21, 14). This spectrum has to be folded with transport across the Galaxy to compare with observations. The CR steepness observed at Earth can be reconciled only in the context of steep acceleration spectra, which are an inevitable consequence of the MFA required to get to PeV energies: in the energy transfer towards magnetic waves, the particle spectrum gets depleted in the number of particles.

Particularly in the early stages of an SNR evolution, namely at the transition to the Sedov phase, it is indeed the flux of escaping particles that drives NR-SIs, that in turn lead to the formation of resonant modes, capable of particle confinement. Even in the non-linear DSA regime, computations show that only

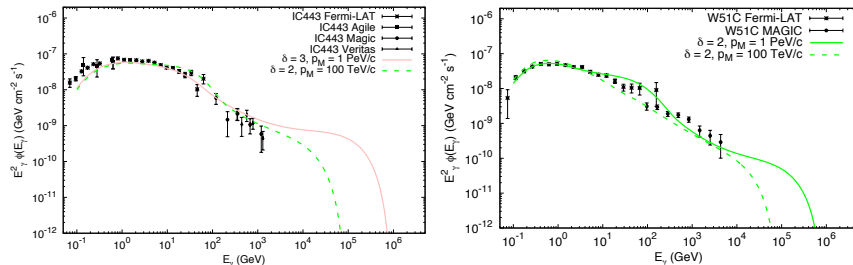


Figure 2: Gamma-ray fluxes from known SNRs compared with escape modelling from ¹⁴). *Left*: IC443, assumed with age 15 ky and distance 1.5 kpc, acceleration spectrum $f(p) \propto p^{-4}$, upstream density $n = 10 \text{ cm}^{-3}$ and Kolmogorov diffusion coefficient normalized to $10^{27} \text{ cm}^2/\text{s}$ at 10 GeV: the resulting modelling requires CR acceleration efficiency of 2%. *Right*: W51C, assumed with age 30 ky and distance 5.4 kpc, acceleration spectrum $f(p) \propto p^{-4.3}$, upstream density $n = 10 \text{ cm}^{-3}$ and Kolmogorov diffusion coefficient normalized to $3 \times 10^{26} \text{ cm}^2/\text{s}$ at 10 GeV: the resulting modelling requires CR acceleration efficiency of 12-15%. Figures from ¹⁸).

particular SNRs can achieve maximum energies in the knee range, i.e. those characterised by fast shocks expanding in highly dense environments ^{21, 22}, e.g. the wind of a red-supergiant (RSG) progenitor. In other words, a sub-class of potential PeVatrons is constituted by powerful and rare ($1/10^4 \text{ yr}$) type II remnants, namely young SNRs with $E_{\text{SN}} > 5 \times 10^{51} \text{ erg}$ and small ejecta mass (few solar masses), evolving into dense stellar winds (with high mass loss rates and slow wind velocities). Despite being an attracting possibility, the short duration of the PeVatron stage ²³) dramatically reduces the observational constraints in terms of high-energy detectable emission from the remnant itself. In such a case, to identify PeVatrons it might result more promising to look at radiative signatures from gas clouds located outside (but sufficiently nearby) the remnant, illuminated by the escaping CR flux ^{24, 25}).

To summarize, the capability of SNRs to act as PeVatrons has not yet been proven: no historical SNR seems to be acting right now as a PeV hadronic source. A possibility remains that SNRs provide the energetics to sustain most of the CR flux, but do not operate up to the PeV domain. In such a situation, an additional source population should be envisaged as to explain the CR knee. In the last decades, the idea that non-isolated SNRs can play this role

has emerged in the community: the best location to find them is constituted by clusters of massive stars, which are discussed in the next section.

3 Massive Stellar Clusters

Recently, a major success was obtained in the detection of gamma-ray sources with unattenuated spectra up to tens of TeV from several MSCs in our Galaxy and beyond, including the Cygnus Cocoon, the Central Molecular Zone, West-erlund I and II ²⁶). The presence of correlated gas strongly hints towards a hadronic interpretation for the origin of the radiation, despite in some cases this evidence has not been considered conclusive. De-convolving the gamma rays from the target gas allows to derive the CR density profile, which is found to be consistent with being linearly decreasing from cluster itself, indicating the presence of continuous accelerators over Myr long timescales: a wind luminosity of $L_w \sim 10^{38}$ erg/s maintained for such long timescales would provide comparable energetics to that injected by SNe. Considering three dimensional diffusion in spherical symmetry, the CR density function at equilibrium conditions (namely $\partial f/\partial t = 0$) satisfies the following equation

$$Q\delta(r) = \frac{1}{r^2} \frac{\partial}{\partial r} \left(r^2 D \frac{\partial f}{\partial r} \right) \quad (3)$$

where D represents the diffusion coefficient and Q the source flux, here assumed to originate at the very center of the system, namely in $r = 0$. Therefore, in all positions with $r \neq 0$, it holds that

$$r^2 D \frac{\partial f}{\partial r} = \text{const} \quad (4)$$

Furthermore, assuming the diffusion coefficient to be independent of the radial position (at least within the spatial scale where the gamma rays are observed), it follows that

$$f(r) \propto \frac{1}{r} \quad (5)$$

On the other hand, if CRs were advected into a wind one would expect $f(r) \propto 1/r^2$, while the case of a burst-like CR injection would result into a constant radial profile up to the typical diffusion length $\sqrt{D\tau_{\text{burst}}}$. Hence, the linearly decreasing radial profile observed in CRs around MSCs coupled with the observations of quite hard gamma-ray spectra ($E^{-2.2-2.4}$) without visible cut-offs

offer a strong indication of ongoing particle acceleration up to high energies. Stellar clusters have been investigated as potential particle accelerators since the early 1980s, when the maximum energy limitations connected with isolated SNR scenarios were already clear ^{28, 29}). The fact that stars inject kinetic energy not only as SN explosions, but also due to the presence of stellar winds through their entire lives constituted a motivation for the investigation of the properties of wind-blown bubbles ²⁷). Recently, several theoretical efforts have been dedicated to understanding where particle acceleration could possibly take place in these systems and up to which maximum energy. Two main scenarios have emerged, namely:

- i) acceleration could take place around compact and massive stellar associations, which are capable of forming a strong collective wind terminating into a shock (the so-called Wind Termination Shock, WTS);
- ii) acceleration can occur within superbubbles (SBs), low-density multi-parsec scale cavities blown by the combined effect of stellar winds and supernovae explosions; candidate locations for effective particle acceleration are e.g. SNR shocks launched into the WTS of a compact cluster, and (more rarely) multiple interacting shocks of different SNRs.

The term *massive* refers to clusters hosting SN progenitors, namely zero age main sequence stars with mass $M > 8M_{\odot}$, while *compact* indicates that the stellar density is high enough (e.g. hundreds of stars in parsec scale) such that the WTS radius is larger than the core radius, hence a strong collective WTS is actually formed ³⁰). 3D simulations have shown that these systems are characterised by highly isotropic magnetic turbulence, which may potentially boost the maximum energy of CR protons to few PeVs, under reasonable assumptions with regards to the dissipation of energy from winds to magnetic perturbations, and if the particle transport proceeds in the Bohm domain ³¹). In particular, WTSs dominate the energetics of young MSCs and of their host SB for the first 3 Myr ³²) from formation: after this time, in fact, SNe explosions start to come into play, adding turbulence and stochasticity to the system evolution. At such later stage, also loosely bounded clusters are expected to accelerate particles, e.g. as a result of particle scattering across multiple SNR shocks ³³): this condition is however not expected to be realised frequently. On a general ground, the large size of SBs (tens to hundreds of pc) represents

the ideal location for the Hillas criterion to ensure potentially maximum energies even beyond the PeV scale; however, the forward shock is typically not strong, hence no efficient particle acceleration is realised there ³⁴). A more promising acceleration scenario might in turn take place at individual SNRs shock launched though the highly turbulent upstream wind of the WTS ³⁴). Such a situation is not uncommon given that most of core-collapse SNe are born within cluster cores. From this process, stochastic particle spectra and intermittent injection into the ISM result, possibly explaining the variety of observations from different gamma-ray bright MSCs ²⁶).

An additional element to consider the contribution of MSCs to the Galactic CR flux is represented by mass composition studies, that are well know to deviate from Solar composition in correspondence of particular isotope ratios. The $^{22}\text{Ne}/^{20}\text{Ne}$ abundance, for instance, is about five times higher in CRs than for the Solar wind ³⁰). This observation might indicate that at least part of the CR flux is accelerated out of the material contained in the winds of massive stars: e.g. WTS around WR stars are enriched in helium-burning products as ^{22}Ne . With respect to the overall CR composition, Voyager data have shed light into the ISM phases that the majority of CRs are accelerated from ³⁵): in particular, volatile elements (namely those found in a gaseous phase, as H, He, N, Ne and Ar) results to be mainly accelerated from a plasma with typical temperatures of the hot medium found in Galactic SBs, while refractory elements (Mg, Al, Si, Ca, Fe, Co, and Ni) most likely originate from the acceleration and sputtering of interstellar dust grains in SNR shocks (namely dust grains that result from an ISM mixture where they are continuously incorporated through thermal evaporation of embedded molecular clouds).

To summarize, the energy and composition of CRs provide crucial constraints to the source populations at their origin. Isolated SNRs provide the majority of the power needed to sustain the CR flux, but can hardly achieve PeV energies, unless in the case of very special and rare explosions. As the majority of CRs appear to be accelerated from the hot ISM, isolated SNRs within SBs have to be preferred as dominant sources contributing at the lowest energies. The collective effects of winds from compact MSCs resulting into WTSs can explain CR energies up to few PeVs, provided the clusters are luminous enough ($L_w > 3 \times 10^{38}$ erg/s) and turbulence ensures particle scattering to proceed in Bohm domain: this source contribution is required by CR composition mea-

surements, as to explain the $^{22}\text{Ne}/^{20}\text{Ne}$ anomaly. The exact transition from Galactic to extra-Galactic CRs is not yet known: nonetheless, at energies above the *ankle*, CRs are believed to come from outside the Galaxy as these would not be confined in the disc thickness ($h \sim 300$ pc); it is however likely that the transition to extra-Galactic sources occurs even before the ankle, given the indication of almost pure proton composition in there. Beyond 100 PeV, the modest amplitude of the CR dipole anisotropy measured disfavours a Galactic origin for the light CR component ³⁶). Still from 1 PeV to 100 PeV, Galactic accelerators can in principle constitute the dominant contribution to CRs. A viable option to reach such energies is constituted by acceleration occurring at SNR shocks embedded in MSCs, namely when an SNR shock expands in the strongly magnetised and turbulent environments shaped by the stellar wind. Nonetheless, the relative contribution among the different sources and the transition energies between each other represent still uncertain variables of current models, and possible clarifications will be provided by improved spectral and composition studies of the CR flux, particularly in the energy region where the detection method moves from direct to indirect.

4 Recent experimental results in the search for PeVatrons with gamma rays

The first ever detected PeVatron in our Galaxy was identified by the HESS telescopes in correspondence of the radio source SgrA*, the SuperMassive Black Hole (SMBH) at the center of the Milky Way ³⁷). This statement is supported by two observational results: i) the detection of very-high-energy (VHE, $E_\gamma > 10$ TeV) photons from a region extending $\sim 20 - 60$ pc away from the SMBH without a significant cut-off, up to ~ 30 TeV; and ii) the observation of a CR radial distribution around the source extending with a $1/r$ profile up to ~ 200 pc, witnessing the injection and diffusion of particles from a continuous accelerator operating over timescales longer than 10^4 yr (see eq.5). Given the large uncertainties that affect the very inner parsecs of our Galaxy (in both the gas and source distribution), the hypothesis that there might be sources other than the SMBH itself is realistic. The Galactic Center region is in fact a unique environment, populated by millions of stars, including RSGs, WRs, OB associations and SNRs (also the youngest known to date, G1.9+0.3). Some of these are also bright gamma-ray emitters. In this regard, the clusters of young

massive stars are of special interest, given the collective effects provided by the multiple SNRs and stellar wind shocks that characterise these regions, the MSCs located in the inner Galactic Center region PeVatron candidates, to be considered as either complementary or alternative candidates to the SMBH. However, even if the assumption of a PeVatron in the center of the Galaxy would be verified (independently of its nature of SMBH or MSCs or other), for instance through the observation of coincident VHE neutrinos, one should consider the fact that this source can not be responsible for the bulk of CR flux observed at Earth. In fact, in the standard picture of CR propagation in the Galactic halo, which is often referred to as the Galactic Halo model ^{38, 39}, we do expect that CRs propagate diffusively in the Galactic disc up to distances comparable with the halo size, which extends above and below the Galactic Plane for about $H \sim 3 - 4$ kpc. As a consequence, PeV protons accelerated in the Galactic Center would only travel Galactic distances of the order of few kpc, i.e. the Earth would not be within their reach, being located 8 kpc away from the Galactic Center. Alternative propagation scenarios may allow those particles to reach the Earth, as for instance in the case of anisotropic diffusion along the spiral arms of the Galaxy. However, these scenarios challenge the observations of the Boron over Carbon ratio (B/C). In fact, the B and C flux ratio is related to the amount of matter traversed by CRs in their travel, the so-called *grammage*, which is directly related to the matter density in the confinement volume. If CRs would diffuse mainly along the arms, they would in fact accumulate a grammage much larger than observed ¹).

Very recently, the LHAASO detector has been able to observe ultra-high-energy (UHE, $E_\gamma > 100$ TeV) photons from several regions of our Galaxy ⁴⁰). In particular, photons up to 1.4 PeV were observed from the Crab ⁴¹), a plerion powered by the electron-positron wind originated from the central pulsar. Besides this source, no other accelerator has been firmly identified, mostly because the angular resolution of the observations is not yet enough to pinpoint the exact acceleration region. Remarkably, the locations of most of the PeVatrons seem to be consistent with known pulsar/PWNe, with only few of them being located nearby of SNRs and just a couple spatially consistent with Star Forming Regions (SFRs). The questions remain open whether any SNR in our Galaxy behaves as a PeVatron or whether instead other sources should rather be considered to explain the CR knee. Clearly, the pure spatial coincidence

among LHAASO sources and SFRs does not guarantee these to behave as PeVatrons, though raising the question whether it might be so, or whether these might simply host SNR-PeVatrons. Next generation imaging instruments, as CTA ⁴²⁾, will likely provide definite answers to these major concerns, thanks to the unprecedented angular resolution it will achieve at such extreme energies.

5 Conclusions

CR and gamma-ray data provide us with a wealth of information that have to be consistently accounted for in the attempt to build a scenario explaining the origin of the most energetic particles ever observed. Current data seem to suggest that more than one source population contributes to the Galactic CR flux, here meant to extend up to 100 PeV, particularly SNRs and MSCs, occurring in different environments, e.g.:

- i) isolated SNRs, that are responsible for injecting the majority of the energetics required, while failing to achieve the PeV energy domain: the major contribution to this sample is expected to be provided by SNRs in wind-blown bubbles, accelerating particles from the hot ISM;
- ii) WTSs of compact star clusters, that in turn might be efficient particle accelerators in the PeV regime: a 5% contribution to the Galactic CR flux seems to be required in terms of both energetics and mass composition, particularly to reconcile the $^{22}\text{Ne}/^{20}\text{Ne}$ overabundance in CRs with respect to the Solar wind;
- iii) SNR shocks driven into the magnetised wind of compact MSCs, potentially responsible for proton energies beyond few PeVs, that would hence configure as Galactic superPeVatrons.

Despite the theoretical efforts dedicated to understanding particle acceleration in these realistic systems, the complexity and variety of possible realizations still prevent us from achieving a robust and complete development in terms of both models and simulations, the main limitation being represented by the unknown evolution of the magnetic turbulence at different spatial and temporal scales. At the same time, measurements are growing in both quality and quantity, providing more constraints to poorly known model parameters. While we're still far from reaching a general consensus on the origin of Galactic CRs, a

more structured scenario appears in front of us. The unique observational window that has just been opened in UHE gamma-ray astronomy is expected to shed new insights into this long-standing issue. Already with less than one year of data recorded, LHAASO has shown that there's plenty of PeVatrons in our Galaxy, and perhaps the detection of super-PeVatrons is just around the corner: it is now timely to complement this information with multi-wavelength and multi-messenger studies, as to unveil their nature.

References

1. P.Blasi, *A&A Rev.* **21**, 70 (2013).
2. W.D.Apel *et al*, *Astrop. Phys.* **31**, 86 (2009).
3. B.Bartoli *et al*, *PRD* **92** 092005 (2015).
4. A.D.Supanitsky, *Galaxies* **10** 75 (2022).
5. B.Peters, *Il Nuovo Cimento XXII*, **800** (1961).
6. G.Di Sciascio, *Nuclear Physics B Proceedings Supplement* **00** 1 (2019).
7. Z.Cao *et al*, *Chinese Physics C* **46**, 035001 (2022).
8. W.Baade *et al.*, *PNAS* **20**, 259 (1934).
9. R.Blandford *et al*, *ApJ* **221**, L29 (1978),
10. L.Drury, *Rep. Prog. Phys.* **46**, 973 (1983).
11. L.Drury, *Astropart. Phys.* **39**, 52 (2012).
12. A.R.Bell, *MNRAS* **353**, 550 (2004).
13. A.R.Bell *et al*, *MNRAS* **431**, 415 (2013).
14. S.Celli *et al*, *MNRAS* **490**, 4317 (2019).
15. G.Morlino *et al*, *MNRAS* **508**, 6142 (2021).
16. A.U.Abeysekara *et al*, *ApJ* **843**, 40 (2017).
17. M.Ackermann *et al*, *Science* **339**, 807 (2012).

18. S.Celli *et al*, Springer Thesis ISBN 978-3-030-33123-8 (2019).
19. S.Celli *et al*, ApJ **903**, 61 (2020).
20. K.M.Schure *et al*, MNRAS **437**, 2802 (2014).
21. M.Cardillo *et al*, Astropart. Phys. **69**, 1 (2015).
22. P.Cristofari *et al*, Astropart. Phys. **123**, 102492 (2020).
23. K.M.Schure *et al*, MNRAS **435**, 1174 (2013).
24. S.Gabici *et al*, MNRAS **396**, 1629 (2009).
25. A.M.Mitchell *et al*, MNRAS **503**, 3522 (2021).
26. F.Aharonian *et al*, Nature Astronomy **3**, 561 (2019).
27. R.Weaver *et al*, ApJ **218**, 377 (1977).
28. M.Casse *et al*, ApJ **237**, 236 (1980).
29. C.J.Cesarsky *et al*, Space Sci Rev **36**, 173 (1983).
30. S.Gupta *et al*, MNRAS **493**, 3159 (2020).
31. G.Morlino *et al*, MNRAS **504**, 6096 (2021).
32. T.Vieu *et al*, MNRAS **512**, 1275 (2022).
33. E.G.Klepach *et al*, Astropart. Phys. **13**, 161 (2000).
34. T.Vieu *et al*, MNRAS **515**, 2256 (2022).
35. V.Tatischeff *et al*, MNRAS **508**, 1321 (2021).
36. G.Giacinti *et al*, J. Cosmology Astropart. Phys. **1207**, 031 (2012).
37. A.Abramowsky *et al*, Nature **531**, 476 (2016).
38. V.L.Ginzburg *et al*, Prog Theor Phys Suppl **20**, 1 (1961).
39. V.S.Berezinskii *et al*, Astrophysics of cosmic rays (1990).
40. Z.Cao *et al*, Nature **594**, 33 (2021).
41. Z.Cao *et al*, Science **373**, 425 (2021).
42. B.S.Acharya *et al*, arXiv:1709.07997 (2017).

WHAT SOURCES ARE THE DOMINANT GALACTIC COSMIC-RAY ACCELERATORS?

Jacco Vink

Anton Pannekoek Institute & GRAPPA, University of Amsterdam, Netherlands

Abstract

Supernova remnants (SNRs) have long been considered to be the dominant source of Galactic cosmic rays, which implied that they provided most of the energy to power cosmic rays as well as being PeVatrons. The lack of evidence for PeV cosmic rays in SNRs, as well as theoretical considerations, has made this scenario untenable. At the same time the latest LHAASO and other gamma-ray results suggest that PeVatrons lurk inside starforming regions.

Here I will discuss why SNRs should still be considered the main sources of Galactic cosmic rays at least up to 10 TeV, but that the cosmic-ray data allow for a second component of cosmic rays with energies up to several PeV. This second component could be a subset of supernovae/SNRs, re-acceleration inside starforming regions, or pulsars. As a special case I show that the recent observations of Westerlund 1 by H.E.S.S. suggest a low value of the diffusion coefficient inside this region, which is, together with an Alfvén speed $\gtrsim 100 \text{ km s}^{-1}$, a prerequisite for making a starforming region collectively a PeVatron due to second order Fermi acceleration.

1 Introduction

The question about the origin of cosmic rays has been with us since their identification as an extraterrestrial source of ionization. ¹⁾ Cosmic rays have an energy distribution that is nearly a power law with index $q \approx -2.7$ from $\sim 10^9$ eV to $\sim 10^{20}$ eV. The deviations in the spectrum from a pure, single power law—and compositional changes as a function of energy—provide information on the the origin, transport and acceleration physics of cosmic rays. Important features are the steepening at $\sim 3 \times 10^{15}$ eV—the “knee”—and the flattening at $\sim 3 \times 10^{18}$ eV—the “ankle”. The “knee” has long been thought to be the maximum energy that protons can be accelerated to by the dominant class of Galactic cosmic-ray sources, whereas the “ankle” is regarded to mark the transition from Galactic to extragalactic cosmic rays. Although the sources of both Galactic and extragalactic cosmic rays remain topics of debate, supernova remnants (SNRs) are commonly considered to be the dominant source of Galactic, and active galactic nuclei (AGN) of extragalactic cosmic rays.

Here I will discuss that SNRs likely provide the bulk of Galactic cosmic rays, but that they do not accelerate up to the “knee”. Starforming regions provide observationally and theoretically good conditions for acceleration of PeV cosmic rays, as illustrated using new gamma-ray results on Westerlund 1.

2 Supernovae and the Galactic cosmic-ray energy budget

SNRs are long known to be radio synchrotron sources, and over the last 30 yr many have been identified as X-ray-synchrotron and very-high-energy (VHE) gamma-ray sources, indicating the presence of particles with energies of 10^8 eV to 10^{14} eV. ²⁾ The theory of diffusive shock acceleration ³⁾ (DSA) provides the theoretical framework to interpret the acceleration properties of SNRs.

For SNRs to be the dominant source class of Galactic cosmic rays, they must be able to transfer a substantial fraction of their energy ($\sim 10^{51}$ erg) to cosmic rays. The Galactic energy density of cosmic rays is estimated to be $U_{\text{cr}} \approx 1 \text{ eV cm}^{-3}$, mostly concentrated around energies of ~ 1 GeV. ⁴⁾ Composition measurements indicate that the typical escape time of cosmic rays with these energies is $\tau_{\text{esc}} \approx 1.5 \times 10^7$ yr, whereas the Galactic diffusion coefficient is $D \approx 3 \times 10^{28} (R/4 \text{ GV})^\delta \text{ cm}^2 \text{ s}^{-1}$, with $\delta \approx 0.3-0.7$. ⁵⁾ The one-dimensional diffusion length scale of cosmic rays is associated with the scale height of the cosmic-ray

populations above and below the Galactic plane: $H_{\text{cr}} = \sqrt{2D\tau_{\text{esc}}}$. The total energy budget to maintain the cosmic-ray energy density in the Galaxy is then

$$\begin{aligned} \frac{dE_{\text{cr}}}{dt} &\approx \frac{U_{\text{cr}}\pi R_{\text{disc}}^2 2H_{\text{cr}}}{\tau_{\text{esc}}} = U_{\text{cr}}\pi R^2 \sqrt{2D}\tau_{\text{esc}}^{-1/2} \\ &\approx 1.0 \cdot 10^{41} \left(\frac{U_{\text{cr}}}{\text{eV cm}^{-3}} \right) \left(\frac{R_{\text{disc}}}{10 \text{ kpc}} \right)^2 \\ &\quad \left(\frac{D}{3 \cdot 10^{28} \text{ cm}^2\text{s}^{-1}} \right)^{1/2} \left(\frac{\tau_{\text{esc}}}{1.5 \cdot 10^7 \text{ yr}} \right)^{-1/2} \text{ erg s}^{-1}, \end{aligned} \quad (1)$$

with R_{disc} the typical radius of the Milky Way.

The supernova rate in the Milky Way is estimated to be 2–3 per century, providing $\dot{E}_{\text{sn}} \approx 1.0 \times 10^{41} \text{ erg s}^{-1}$. So we find $\dot{E}_{\text{cr}} \approx 10\% \dot{E}_{\text{sn}}$.

3 The PeVatron problem

SNRs as the Galactic cosmic-ray sources are problematic when it comes to explaining the cosmic-ray “knee”, which is often taken as evidence that the dominant cosmic-ray sources should be able to accelerate protons beyond 10^{15} eV —i.e. they should be PeVatrons. However, SNRs are unlikely to be PeVatrons, both from an observational as well as from a theoretical point of view.

Gamma-ray spectra of SNRs are reasonably well described by power-law spectra with a break or a cutoff. The youngest known SNRs have gamma-ray spectrum extending up to $\sim 10 \text{ TeV}$ – 100 TeV , but show a turnover in their spectra below 10 TeV . This is both true for gamma-ray sources that are best modeled as hadronic gamma-ray sources—i.e. caused by pion production, such as Cas A ⁶⁾ and Tycho’s SNR ⁷⁾—and for leptonic gamma-ray sources. Since typically the gamma-ray photon energy is $\sim 10\%$ of the energy of the primary particle, the gamma-ray spectra of young SNRs indicate that the cosmic-ray spectrum inside young SNRs cuts off below 100 TeV , well below the “knee”.

Mature SNRs (~ 2000 – $20,000 \text{ yr}$), such as W44 and IC443, have breaks in their gamma-ray spectrum around 10 – 100 GeV , indicating the lack of cosmic-ray particles with energies in excess of 1 TeV . In these SNRs acceleration beyond 1 TeV has apparently stopped, and most previously accelerated particles have diffused out of the SNRs. Extended gamma-ray emission beyond the shock in the $\sim 2000 \text{ yr}$ old SNR RX J1713.7-3946 may indeed reveal escape of cosmic rays caught in the act. ⁸⁾ An interesting, but peculiar, counter example is

the relatively mature and luminous SNR N132D (~ 2500 yr) in the Large Magellanic Cloud, for which no gamma-ray break or cutoff is detected below 10 TeV. ⁹⁾ This is in contrast to the much younger—but in many other ways comparable—SNR Cas A, which has a cutoff at ~ 3 TeV. ⁶⁾

The theoretical problems of acceleration of cosmic rays by SNRs beyond 1 PeV, using reasonable assumptions, are at least four decades old. ^{10, 11)} The acceleration timescale according to DSA corresponds to the timescale for a shock-crossing cycle around the maximum energy: ¹²⁾

$$\tau_{\text{acc}} \approx \frac{8D_1}{V_s^2}, \quad (2)$$

with V_s the shock velocity and D_1 the upstream diffusion coefficient. The diffusion coefficient for relativistic particles can be expressed as

$$D_1 = \frac{1}{3}\lambda_{\text{mfp}}c = \frac{1}{3}\eta r_g c = \frac{1}{3}\eta \frac{E}{eB_1}c, \quad (3)$$

with c the particle speed/the speed of light, r_g the gyroradius, and $\lambda_{\text{mfp}} = \eta r_g$ a parametrisation of the mean-free path in terms of the gyroradius. The smallest realistic value for D is for $\eta = 1$, so-called Bohm diffusion, requiring a very turbulent magnetic field ($\delta B/B \approx 1$).

For SNRs we can approximate $V_s = mR_s/t_{\text{snr}}$, with R_s the shock radius and t_{snr} the SNR age. We can take Cas A as an example of a young cosmic-ray accelerator with $V_s \approx 5500$ km/s ¹³⁾, $R_s \approx 3$ pc, $m = 0.7$ ¹³⁾, and $B_1 \approx 100$ μG ^{14, 15)}. For the acceleration timescale we write $\tau_{\text{acc}} = ft_{\text{snr}}$, with $f < 1$ (typically $f = 10\%$). Rewriting eq. (2) gives:

$$\begin{aligned} E_{\text{cr,max}} &\approx \frac{3}{8}\eta^{-1} \frac{eB_1}{c} V_s^2 \tau_{\text{acc}} \approx \frac{3}{8}\eta^{-1} \frac{eB_1}{c} m^2 f \frac{R_s^2}{t_{\text{snr}}} \\ &= 1.4 \times 10^{14} \eta^{-1} \left(\frac{f}{10\%}\right) \left(\frac{m}{0.7}\right)^2 \left(\frac{B_1}{100 \mu\text{G}}\right) \left(\frac{R_s}{3 \text{ pc}}\right)^2 \left(\frac{t_{\text{snr}}}{350 \text{ yr}}\right)^{-1} \text{ eV}. \end{aligned} \quad (4)$$

Optimistically taking $\eta = 1$, we see that Cas A cannot accelerate to PeV energies. The situation is better than theorized 30 yr ago ¹⁰⁾, because X-ray synchrotron filamentary widths in Cas A, as measured by the Chandra X-ray Observatory, provide evidence for amplified magnetic fields. ^{14, 16)} Moreover, X-ray synchrotron radiation by itself requires $\eta \approx 1$. ¹⁷⁾

Although two ingredients for large $E_{\text{cr,max}}$ —magnetic-field amplification and turbulence—appear to be present, they are not sufficient to make SNRs

PeVatrons. In fact, the optimism regarding E_{\max} in SNRs is tempered by the fact that the measured gamma-ray cutoff energy for Cas A is consistent with $E_{\text{cr,max}} \approx 10$ TeV, ⁶⁾ rather than the expected ~ 100 TeV. This is peculiarly low for hadrons, as unlike electrons, they do not suffer radiative energy losses, but their maximum energy appears to be similar to the inferred maximum electron energy. ¹⁴⁾

4 Alternative Galactic cosmic-ray source candidates

Which energetic sources, other than SNRs, could be sources of Galactic cosmic rays? Clearly, Galactic PeVatrons do exist as LHAASO recently has reported the detection of PeV photons from various regions along the Galactic plane, including from the Crab Nebula or its pulsar. ¹⁸⁾ Alternative source classes often discussed are pulsars ¹⁹⁾, microquasars ²⁰⁾, stellar winds ²¹⁾, supernovae ²²⁾, superbubbles ^{23, 24, 25)}, and the supermassive black hole SGR A* ²⁶⁾.

Most of these source classes are advocated based on the idea that they can accelerate particles up to the “knee”, but not all of them are capable of explaining the Galactic cosmic-ray energy density, except “supernovae” and “superbubbles”, which are *grosso modo* powered by the same source of energy as SNRs. We ignore below SGR A*, which may indeed be a PeVatron, and may have been more powerful in the past. However, the LHAASO results require the presence of PeVatrons throughout the Galactic plane, and not just in the Galactic center.

4.1 Supernovae

The supernova hypothesis usually assumes that a subset of supernovae, those exploding in a dense stellar wind, start accelerating almost immediately after the explosion. ²²⁾ Typically these are Type IIb and Type IIn supernovae, which comprise $\sim 10\%$ of all supernovae. An important example of a potentially powerful accelerator was SN1993J, whose magnetic field at the shock was estimated to be ~ 10 G ²⁷⁾ with an initial shock velocity of $20,000 \text{ km s}^{-1}$. Essentially the supernova hypothesis is a “very young SNR” hypothesis, as in supernovae such as SN1993J a bright SNR shell immediately develops in the dense wind of the progenitor.

To get an idea of the maximum energy that can be reached under the right conditions, consider that the maximum distance traveled by $15,000 \text{ km/s}$

shock is $R_s = 4.7 \times 10^{16}$ cm in one year, and if the wind velocity and densities are high Bell’s instability ¹⁶⁾ could maintain a magnetic field of ~ 1 G near the shock. eq. (4) then gives $E_{\text{cr,max}} \approx 1.3 \times 10^{16}$ eV reached within one year. Observational proof for this hypothesis would be the detection of VHE gamma rays from a radio-emitting supernovae, but so far only upper limits have been reported. ²⁸⁾

4.2 Superbubbles and starforming regions

A substantial fraction of core-collapse supernovae probably explode inside of starforming regions. Collectively these regions have, therefore, somewhat less supernova energy available than SNRs, but this is offset by the energy input provided by stellar winds (sect. 4.3). The recent LHAASO detection of PeV photons associated with starforming regions ¹⁸⁾ provide observational evidence for the hypothesis that starforming regions/superbubbles are PeVatrons. ²⁵⁾ However, what needs to be proven is that the responsible multi-PeV cosmic rays are not originating from the sources contained in starforming regions—supernovae, SNRs and stellar winds—but that there are collective effects that keep on accelerating cosmic rays within the region as a whole. In other words, are starforming regions, from a cosmic-ray-acceleration point of view, more than the sum of their parts?

These “collective” effects are in all likelihood due to second order Fermi acceleration ²⁹⁾, which states that collisions of charged, relativistic cosmic rays with moving magnetic-field disturbances leads to energy gains of

$$\frac{\Delta E}{E} = \xi \left(\frac{v}{c}\right)^2, \quad (5)$$

with $\xi \approx 1$ a parameter hiding the details of the interactions, and c the speed of the relativistic particles. Since the magnetic disturbances are moving with the Alfvén speed we can set $v = V_A$. Second order Fermi acceleration takes into account gains due to head-on collisions, as well as losses due head-tail collisions. Although second order Fermi acceleration is slower than DSA, acceleration in starforming regions can take up to millions of years, rather than the few thousand year timescale of SNRs.

There have been some calculations of the expected spectra of cosmic rays due to this mechanism, taking into account diffusion in phase-space. ³⁰⁾ Here I present a heuristic approach to obtain $E_{\text{max,cr}}$. First note that the average

“collision time” is $\Delta t = \lambda_{\text{mfp}}/c$, with λ_{mfp} the mean free path. In reality, there are no discrete collisions, but we use the same approach as when we use a spatial diffusion coefficient, eq. 3. We can get rid of λ_{mfp} by stating $\Delta t = 3D/c^2$, and the aforementioned energy scaling $D = D_0(E/E_0)^\delta$. Combing Δt with eq. (5) we obtain

$$\frac{1}{E} \frac{dE}{dt} = \xi \frac{c^2}{3D_0} \left(\frac{E}{E_0} \right)^{-\delta} \left(\frac{V_A}{c} \right)^2, \quad (6)$$

which for $0 < \delta < 1$ has the solution

$$E_{\text{max,cr}} = E_1 + E_0 \left[\frac{\xi c^2}{3D_0} \left(\frac{V_A}{c} \right)^2 \tau_{\text{acc}} \right]^{1/\delta}, \quad (7)$$

with τ_{acc} the timescale available for acceleration, and E_1 the injection energy of the particle. We can parameterize this for $\delta = 1/2$, and $E_1 \ll E_{\text{max,cr}}$ as

$$E_{\text{max}} \approx 1.4\xi^2 \left(\frac{V_A}{150 \text{ km s}^{-1}} \right)^4 \left(\frac{D(10 \text{ TeV})}{10^{26} \text{ cm}^2 \text{ s}^{-1}} \right)^{-2} \left(\frac{\tau_{\text{acc}}}{1 \text{ Myr}} \right)^2 \text{ PeV}. \quad (8)$$

Note that we need a large Alfvén velocity ($\sim 150 \text{ km s}^{-1}$) and high level of magnetic-field turbulence— $D(10 \text{ TeV}) \lesssim 10^{26} \text{ cm}^2 \text{ s}^{-1}$ —to create a PeVatron.¹ Moreover, the particles need to be contained sufficient long to reach PeV energies. I come back to this when discussing Westerlund 1 (sect. 6.1).

4.3 Stellar winds

It is sometimes said that stellar winds may provide as much kinetic energy as supernova explosion. The reality is somewhat more complicated.

Best understood are the wind properties of massive main-sequence stars.³¹⁾

Fig. 4.2 provides the time-integrated wind-energy of main-sequence stars. Only for stellar masses approaching $100 M_\odot$ does the wind-energy approach the kinetic energy of supernova explosions. But given the steepness of the initial mass function, the fraction of these massive stars is very small. More common stars have $M_{\text{ms}} \lesssim 25 M_\odot$, which provide $\lesssim 2 \times 10^{49}$ erg.

Things are more confusing beyond the main sequence. Most massive stars will become a red supergiant, or sometimes a yellow supergiant. These

¹ Extrapolating the usual Galactic $D \approx 10^{28} \text{ cm}^2 \text{ s}^{-1}$ at $\sim 1 \text{ GeV}$ to 10 TeV gives $D(10 \text{ TeV}) \approx 10^{29} - 10^{31} \text{ cm}^2 \text{ s}^{-1}$, at least three orders of magnitude larger than used in eq. (8).

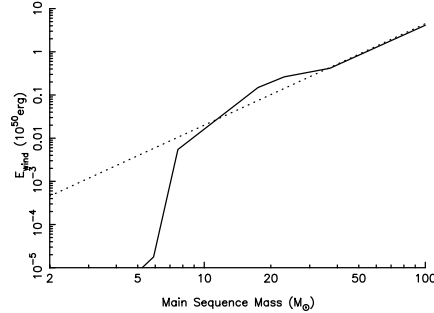


Figure 1: The time-integrated, main-sequence wind energy of massive stars as a function of main-sequence mass. The dotted line indicates the scaling $E_{\text{wind}} \propto M^{2.35}$. This figure is reproduced from ¹²⁾.

have enhanced mass losses, but their wind velocities are low— $\sim 10\text{--}50 \text{ km s}^{-1}$ compared to 100 km s^{-1} up to $\sim 3000 \text{ km s}^{-1}$ for main-sequence winds—and hence provide little kinetic energy. However, some massive stars end their lives in a Wolf-Rayet phase, characterized by large mass loss rates— $\dot{M} \sim 10^{-5} M_{\odot} \text{ yr}^{-1}$ —and very fast winds, 1000 km s^{-1} – 3000 km s^{-1} . The most massive stars ($M_{\text{ZAMS}} \gtrsim 25 M_{\odot}$?) are likely ending in a Wolf-Rayet star phase, but mass-stripping due to binary interactions provides an alternative channel for Wolf-Rayet star formation.

So how much kinetic energy is associated with Wolf-Rayet stars? The measured wind velocities are in the range $v_{\text{WR}} \approx 700 \text{ km s}^{-1}$ – 3000 km s^{-1} , with mass loss rates in the range $\dot{M}_{\text{w}} \approx (0.5\text{--}6) \times 10^{-5} M_{\odot} \text{ yr}^{-1}$.³²⁾ Typically a Wolf-Rayet star phase lasts a few 100,000 yr, implying a total time integrated energy of $E_{\text{w}} = 2 \times 10^{50} (\dot{M}_{\text{w}}/10^{-5} M_{\odot} \text{ yr}^{-1}) (v_{\text{w}}/2000 \text{ km/s})^2 (\tau_{\text{WR}}/500,000 \text{ yr}) \text{ erg}$. This is about $\sim 20\%$ of the canonical supernova explosion energy. If we take Type Ibc supernovae to be explosions of Wolf-Rayet stars, we use the Type Ibc supernova rate of 19% of the overall rate³³⁾, to suggest that $\sim 20\%$ of all massive stars become Wolf-Rayet stars. This implies that the Galactic power budget of Wolf-Rayet stars is $\sim 4\%$ of the supernova power—small but not negligible. Moreover, in young (few Myr) stellar clusters like Westerlund 1 (see below), the power of Wolf-Rayet stars precedes the supernova power, as the most-massive stars are in the Wolf-Rayet star phase, and the many less massive stars still need 5–20 Myr to evolve to the point of core collapse.

4.4 Microquasars

Microquasars are X-ray binaries containing an accreting neutron star or black hole, that develop jet outflows during certain accretion phases. They are regarded as nearby analogues to the radio galaxies and quasars (i.e. AGN). Given that AGN are the most likely sources for extragalactic cosmic rays, detected with energies up to $\sim 10^{20}$ eV, it is not unreasonable to assume that also microquasars are good Galactic accelerators. Indeed, radio and gamma-ray emission shows that they do accelerate at least electrons. ³⁴⁾ The shell found around Cygnus X-1 has also been used as evidence for energetic jets from these systems. ²⁰⁾ However, microquasars are a much less abundant gamma-ray source class than SNRs and pulsar-wind nebulae. ³⁵⁾ Moreover, the number of systems available at any given moment seem to be 50–100. ³⁶⁾ Together with a typical jet power of $\sim 10^{38}$ erg/s, this implies a typical Galactic kinetic power to be attributed to microquasars of $\dot{E}_{\mu q} \approx 10^{40}$ erg/s. If 10% of that power is transferred to cosmic rays, microquasars fall a factor hundred short of maintaining the Galactic cosmic-ray energy density.

4.5 Pulsars

Pulsar wind nebulae are among the most common Galactic gamma-ray sources. However, the canonical theory is that pulsar wind nebulae (PWNe) contain mostly electrons/positrons created by pair creation in the pulsar magnetospheres. Clearly they are efficiently accelerating electrons/positrons, and the archetypal Crab pulsar/PWN is even a confirmed PeVatron, given the detection of PeV photons from this source by LHAASO. ¹⁸⁾ It is possible that the pulsar winds do not solely consists of electrons/positrons and Poynting flux, but may also contain hadrons ³⁷⁾, potentially making pulsars hadronic PeVatrons. However, they are unlikely to be the dominant source of Galactic cosmic rays from an energy-budget point of view.

I illustrate this by pointing out that the pulsar birth rate is similar, but somewhat smaller than the supernova rate, i.e. about ~ 2 per century. For normal pulsars the energetic output comes at the expense of the rotational energy of the neutron star. The total initial rotational energy available is

$$E_{\text{rot}} = \frac{1}{2} I \Omega_0^2 = \frac{2\pi^2}{P_0^2} I \approx 8 \times 10^{48} \left(\frac{I}{10^{45} \text{ g cm}^2} \right) \left(\frac{P_0}{50 \text{ ms}} \right)^{-2} \text{ erg}, \quad (9)$$

with $P_0 = 2\pi/\Omega_0$ the initial spin period and I the moment of inertia. For pulsars to compete energetically with supernovae, they need $P_0 \lesssim 5$ ms. However, the initial spin period inferred from population synthesis models indicate a much longer initial period, 50–100 ms, or even 300 ms.³⁸⁾ Taking $P_0 \gtrsim 50$ ms gives $\dot{E}_{\text{psrs}} \lesssim 5 \times 10^{39}$ erg/s, insufficient for powering Galactic cosmic rays.

The above considerations suggest that pulsars are not prominent sources of Galactic cosmic rays, even if they accelerate hadrons. But in the latter case they could be a source of PeV protons. Pulsars are likely an important, perhaps even dominant, contributor to the electron-/positron cosmic-ray population. Moreover, the pulsar wind nebulae (PWNe) and pulsar wind haloes³⁹⁾ constitute an important class of VHE gamma-ray sources.³⁵⁾ There is no contradiction between being prominent gamma-ray sources and not providing enough energy to power Galactic cosmic rays: energetic electrons/positrons are radiatively much more efficient than energetic protons.

5 Do the sources of Galactic cosmic rays need to be PeVatrons?

For a long time it was considered that the dominant sources of Galactic cosmic rays must fulfill both the cosmic-ray energy budget and be PeVatrons. The reason was a lack of cosmic-ray spectral features between ~ 1 GeV and 3×10^{15} eV, whereas if there were two or more source classes fulfilling together these criteria, we would expect some breaks in the cosmic-ray spectrum.

It has now time to reconsider that idea, because of evidence that the cosmic-ray spectrum below the “knee” is not so featureless. First of all, the proton cosmic-ray spectrum has a different slope than the helium cosmic-ray spectrum.⁴⁰⁾ This suggests two different origins, although both could originate from SNRs in different environments, or forward shock versus reverse shock acceleration.⁴¹⁾ Secondly, the latest cosmic-ray measurements^{42, 43, 44)} indicate that the proton cosmic-ray spectrum hardens around ~ 0.7 TeV and softens again around 15 TeV.⁴⁵⁾ The situation regarding the proton spectrum around the “knee” is not clear. Certainly the break around 15 TeV is consistent with the maximum energy young SNRs can accelerate protons to.

These results open up the possibility that SNRs indeed provide the bulk of Galactic cosmic rays, a scenario that agrees with the cosmic-ray energy budget, and that other source classes—or subclasses of SNRs, including supernovae—are responsible for cosmic rays from 15 TeV up to the “knee”. Note that this

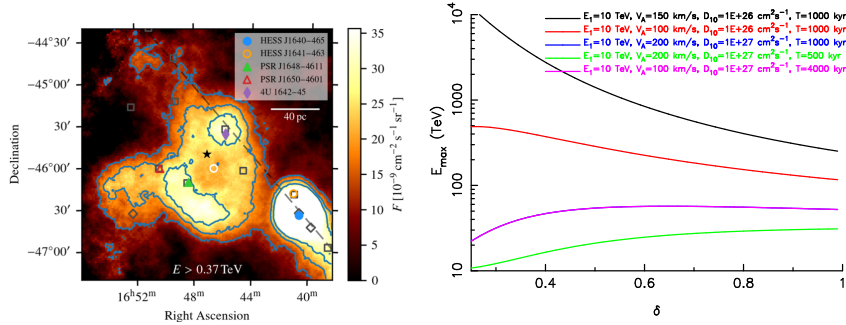


Figure 2: Left: VHE gamma-ray map of Westerlund 1 by H.E.S.S. ⁴⁷⁾ The cluster position is indicated by a black star. (Credit: H.E.S.S. Collaboration) Right: Maximum cosmic-ray energy by 2nd order Fermi acceleration according to eq. (8) as a function of δ and for various values of $D(10 \text{ TeV})$, V_A and τ .

requires PeVatrons to have harder (flatter slope) spectra than SNRs, in order for these PeVatron sources to be subdominant around 1 GeV.

6 Observational candidate PeVatrons: starforming regions

Since the detection of PeV photons from Galactic plane sources by LHAASO ¹⁸⁾ and some associations with starforming regions, starforming regions demand more attention as sources of cosmic rays and being potentially PeVatrons themselves (sect. 4.2)—as opposed to merely containing PeVatrons.

A notable source of PeV photons is LHAASO J2032+4102, which is positionally associated with the Cygnus Cocoon surrounding the Cyg OB2 star cluster. Imaging atmospheric Cherenkov telescope arrays also provide evidence for the existence of PeVatrons associated with starforming regions, and provide a better angular resolution. For example, recently H.E.S.S. detected VHE gamma-ray emission from HESS J1702-420(A) up to energies of 100 TeV, implying primary particles of up to or beyond 1 PeV. ⁴⁶⁾ But the nature of this source, which has a complex gamma-ray morphology, is not entirely clear. Although not a confirmed PeVatron, another interesting starforming region is Westerlund 1/HESS J1646-458, for which the gamma-ray spectrum extends at least up to 50 TeV. ⁴⁷⁾

6.1 Very-high energy gamma-ray emission from Westerlund 1

Westerlund 1 is the most massive young massive star cluster known in the Milky Way, $\sim 10^5 M_{\odot}$, which hosts many Wolf-Rayet stars and other evolved massive stars. Its age has been estimated to be ~ 4 Myr, but recent work suggests an age spread up to 10 Myr.² The VHE gamma-ray emission does not originate from the stellar cluster itself, but from a large shell-like region surrounding it, with peak radius of $\sim 0.5^{\circ}$ (fig. 2). At a distance of 4 kpc the shell has a physical radius of ~ 35 pc, whilst Westerlund 1 itself is much more compact, ~ 1 pc.

In the H.E.S.S. publication an interpretation is favored in which the shell-like emission is associated with a collective-wind termination shock,^{47, 48)} as a physical shell, consisting of swept-up gas, was considered unlikely, because the gamma-ray structure is too small for the energy input from Wolf-Rayet-star winds ($\dot{E}_{\text{WR}} \gtrsim 10^{39}$ erg s⁻¹⁴⁹⁾) and the age of the cluster, as based on the stellar-bubble expansion model by Weaver et al.⁵⁰⁾

However, some of the assumptions used to calculate the putative shell size may not be correct. The cluster age of ~ 4 Myr is a poor indicator for the total energy and shell creation timescale available for making a shell. As noted in sect. 4.3, the Wolf-Rayet star phase typically lasts for a few 100,000 yr, consistent with being about 2–10% of the stellar life time. Taking $\tau_{\text{SB}} \approx 200,000$ yr reduces the radius of the collective wind bubble from $R_{\text{SB}} = 185(n_{\text{H}}/5)^{-1/5}$ pc to $R_{\text{SB}} = 31(n_{\text{H}}/5 \text{ cm}^{-3})^{-1/5}$ pc. There is another reason to be suspicious about the predicted size of the bubble: observationally superbubbles appear to be smaller than predicted by wind-bubble expansion theories. This may be due to internal dissipation and radiative losses, as well as back pressure from the ambient medium.^{51, 52)}

The lack of an association of the VHE gamma-ray shell-like structure with an HI or CO structure is intriguing, but should also not be taken as evidence against the presence of a physical shell, as the intense UV light from the OB and Wolf-Rayet stars in Westerlund 1 likely photo-dissociated/ionize a large part of the surrounding CO and neutral hydrogen.

Assuming that Westerlund 1 itself is indeed accelerating cosmic rays, or further accelerating particles pre-accelerated by the colliding winds and past

²See the recent H.E.S.S. paper for references.⁴⁷⁾

SNRs, what can we learn from the VHE gamma-ray spectrum and morphology measured by H.E.S.S.?

The fact that the VHE gamma-ray morphology seems to have no or little dependence on gamma-ray energy suggest that the cosmic-ray particles have been well mixed within the emitting region and may have been accelerate throughout the bubble. The best-fit cutoff energy of ≈ 40 TeV—corresponding to proton energies above 100 TeV—indicates that escape is only important for particles above ~ 100 TeV. Equating the radius of the shell to the threedimensional diffusion length scale, $R_{\text{shell}} = \sqrt{6D\tau}$, and using $\tau \approx 200,000$ yr, we can estimate the diffusion coefficient at ~ 100 TeV to be $D \approx R_{\text{shell}}^2/(6\tau) \approx 3 \times 10^{26}(\tau/200,000 \text{ yr})^{-1} \text{ cm}^2\text{s}^{-1}$, corresponding to $D \approx 10^{26} \text{ cm}^2\text{s}^{-1}$ at 10 TeV. This is close to the value for which considerable energy gain due to second order Fermi acceleration is expected (eq. 8)!

The maximum energy as a function of the energy dependence of the diffusion coefficient, i.e. δ , is shown in fig. 2 (right) for different valued of D and V_A . It is clear that $V_A \gtrsim 100 \text{ km s}^{-1}$. From $V_A = B/\sqrt{4\pi \cdot 1.4 \cdot n_H m_p}$ we find that we need a low internal density: $n_H \lesssim 0.2(B/10 \mu\text{G})(V_A/100 \text{ km s}^{-1})^{-1} \text{ cm}^{-3}$. However, even densities of 10^{-3} cm^{-3} are possible in superbubbles of a few Myr old.⁵³⁾ Moreover, $10 \mu\text{G}$ is rather modest and corresponds to an internal magnetic-field energy density within the shell of 2×10^{49} erg. Interestingly, using eq. 3 with $B \approx 10 \mu\text{G}$ and $D(10 \text{ TeV}) = 10^{26} \text{ cm}^2\text{s}^{-1}$ provides a value of $\eta \approx 3$, which is very close to Bohm diffusion. Stronger magnetic fields are still consistent with the energy budget, required Alfvén speeds and a PeVatron hypothesis. Much lower strengths lead to inconsistencies, such as $\eta < 1$, or $D \gg 10^{26} \text{ cm}^2\text{s}^{-1}$.

To summarize, the VHE gamma-ray spectra and morphology of West-erlund 1 imply a small diffusion coefficient, whereas a low density inside the shell and amplified, turbulent magnetic field likely result in fast Alfvén velocity, setting the right conditions to (re)accelerate cosmic rays injected by primary sources to well beyond 100 TeV. As such West-erlund 1 may provide a model for other starforming regions as PeVatrons.

7 Conclusion

I have argued here that SNRs likely are the dominant sources of Galactic cosmic rays below ~ 10 TeV, as both observational and theoretical results are consis-

tent with young SNRs being able to accelerate to at least this energy. Moreover, the latest cosmic-ray measurements indicate that there is a hardening of the proton cosmic-ray spectrum around ~ 10 TeV, indicating the presence of additional sources of Galactic cosmic rays, which may be responsible for cosmic rays up to the “knee”.

If these additional sources accelerate cosmic rays with a relatively hard spectrum, this source class does not violate the energetic constraints. Like SNRs, this PeVatron source class may rely on the power input of supernovae, be its a subclass of SNRs, core-collapse supernovae exploding inside the dense stellar wind of the progenitor star, or the collective power of supernovae and stellar winds in starforming regions/superbubbles. Energetic pulsars should not be discarded as hadronic PeVatrons, but it first remains to be proven that pulsars are hadronic- and not just leptonic-accelerators. Both pulsars and starforming regions/superbubbles as PeVatron sources are consistent with the latest detections of Galactic PeV gamma-ray sources by LHAASO.

Several starforming regions/superbubbles have been associated with PeVatron candidate sources. It is not yet clear whether these are PeVatrons by themselves, or whether they merely contain(ed) PeVatrons sources (in the past), such as the aforementioned subclass of SNRs/supernovae and hadronic pulsar accelerators.

I argue that the recently reported VHE gamma-ray properties of HESS J1646-458—associated with Westerlund 1—indicates a small internal diffusion coefficient; small enough to accelerate protons up to the “knee” in a few 100,000 yr, provided that the Alfvén speed is $\gtrsim 100$ km s $^{-1}$. This suggests that starforming regions/superbubbles could be themselves PeVatrons. As cosmic-rays source, starforming regions may be more than the sum of their parts.

Acknowledgements

I am indebted to my involvement in and membership of H.E.S.S. However, this text is written on personal title. The author is supported by funding from the European Union’s Horizon 2020 research and innovation program, grant agreement No.101004131 (SHARP).

References

1. V. F. Hess, *Physik. Zeitschr.* **13**, 1084 (1912).

2. E. A. Helder, *et al*, SSRv **173**, 369 (2012).
3. M. A. Malkov and L. Drury, Rep. Prog. Phys. **64**, 429 (2001).
4. W. R. Webber, ApJ **506**, 329 (1998).
5. A. W. Strong, I. V. Moskalenko, and V. S. Ptuskin, Annual Review of Nuclear and Particle Science **57**, 285 (2007).
6. M. L. Ahnen *et al*, MNRAS **472**, 2956 (2017).
7. S. Archambault *et al*, ApJ **836**, 23 (2017).
8. H.E.S.S. Collaboration, H. Abdalla, *et al*, A&A **612**, A6 (2018).
9. H. E. S. S. Collaboration, H. Abdalla, *et al*, A&A **655**, A7 (2021).
10. P. O. Lagage and C. J. Cesarsky, A&A **125**, 249 (1983).
11. P. Cristofari, *et al*, Astropart. Phys. **123**, 102492 (2020).
12. J. Vink, Physics and Evolution of Supernova Remnants, (Springer International Publishing, 2020)
13. J. Vink, D. J. Patnaude, and D. Castro, ApJ **929**, 57 (2022).
14. J. Vink and J. M. Laming, ApJ **584**, 758 (2003).
15. H. J. Völk, E. G. Berezhko, and L. T. Ksenofontov, A&A **433**, 229 (2005).
16. A. R. Bell, MNRAS **353**, 550 (2004).
17. F. A. Aharonian and A. M. Atoyan, A&A **351**, 330 (1999).
18. A. F. A. Q. Cao, Z. *et al*, Nature **594** (2021).
19. K. Fang, K. Kotera, and A. V. Olinto, ApJ **750**, 118 (2012).
20. E. Gallo, R. Fender, C. Kaiser, and others, Nat **436**, 819 (2005).
21. G. M. Webb, W. I. Axford, and M. A. Forman, ApJ **298**, 684 (1985).
22. A. Marcowith, *et al*, MNRAS **479**, 4470 (2018).
23. A. M. Bykov and G. D. Fleishman, MNRAS **255**, 269 (1992).
24. E. Parizot, *et al*, A&A **424**, 747 (2004).
25. A. M. Bykov, *et al*, SSRv **216**, 42 (2020).
26. HESS Collaboration, A. Abramowski, *et al*, Nat **531**, 476 (2016).

27. C. Fransson and C.-I. Björnsson, *ApJ* **509**, 861 (1998).
28. H. E. S. S. Collaboration, H. Abdalla, *et al*, *A&A* **626**, A57 (2019).
29. E. Fermi, *Physical Review* **75**, 1169 (1949).
30. L. O. C. Drury and A. W. Strong, *A&A* **597**, A117 (2017).
31. J. S. Vink, *ARAA* **60**, 203 (2022).
32. T. Nugis and H. J. G. L. M. Lamers, *A&A* **360**, 227 (2000).
33. W. Li, *et al*, *MNRAS* **412**, 1473 (2011).
34. F. Aharonian *et al*, *Science* **309**, 746 (2005).
35. H. E. S. S. Collaboration, H. Abdalla, *et al*, *A&A* **612**, A1 (2018).
36. G. Dubus, N., *et al*, *A&A* **608**, A59 (2017).
37. E. Amato, The Theory of Pulsar Wind Nebulae, in *International Journal of Modern Physics Conference Series*, volume 28 (2014)
38. C. Faucher-Giguère and V. M. Kaspi, *ApJ* **643**, 332 (2006).
39. T. Linden, *PoS ICRC2021*, 931 (2022)
40. O. Adriani *et al*, *Science* **332**, 69 (2011).
41. V. Ptuskin, V. Zirakashvili, and E.-S. Seo, *ApJ* **763**, 47 (2013).
42. M. Aguilar *et al*, *Phys. Rev. L* **114**, 171103 (2015).
43. Q. An *et al*, *Science Advances* **5**, eaax3793 (2019).
44. K. Kobayashi, *et al*, *PoS ICRC2021*, 98 (2022)
45. P. Lipari and S. Vernetto, *Astropart. Phys.* **120**, 102441 (2020).
46. H. Abdalla *et al*, *A&A* **653**, A152 (2021).
47. F. Aharonian *et al*, *A&A* **666**, A124 (2022).
48. G. Morlino, *et al*, *MNRAS* **504**, 6096 (2021).
49. M. P. Muno, *et al*, *ApJ* **650**, 203 (2006).
50. R. Weaver, *et al*, *ApJ* **218**, 377 (1977).
51. M. G. H. Krause and R. Diehl, *ApJ* **794**, L21 (2014).
52. R. A. Chevalier, *ApJ* **511**, 798 (1999).
53. M. Krause, *et al*, *A&A* **566**, A94 (2014).

Models of neutrino sources

Alessandra Lamastra

*INAF - Osservatorio Astronomico di Roma
via di Frascati 33, 00078 Monte Porzio Catone, Italy*

Abstract

The detection of a diffuse flux of high-energy neutrinos by the IceCube observatory has opened a new window to the Universe, revealing the existence of extremely energetic astrophysical neutrino sources. While the isotropic distribution of the IceCube astrophysical neutrinos favors an extragalactic origin, the sources responsible for the observed flux are still almost entirely unresolved and pose a compelling mystery. High-energy neutrinos are produced by the interactions of energetic protons with surrounding photons and matter and are therefore a signature for hadronic cosmic accelerators. The IceCube Collaboration has reported high-energy neutrino events from the blazar TXS 0506+056 and the Seyfert galaxy NGC 1068. In this contribution, theoretical models for high-energy neutrino production in active galactic nuclei are presented and discussed, focusing on winds and jets, and on coronae and disks in the vicinity of the central supermassive black hole.

1 Introduction

The first observation of a diffuse flux of astrophysical neutrinos was announced in 2013 by the IceCube Collaboration ¹⁾. The analysis was based on high-energy neutrino events interacting within the detector during the first two years of IceCube operation. Later, the IceCube Neutrino Observatory confirmed this discovery with larger experimental data set and with different detection channels such as: high energy starting events ²⁾, through-going muon tracks ³⁾, and cascades ⁴⁾.

The measured flux of astrophysical neutrinos can be described by a single power-law energy distribution that extends from ~ 10 TeV to PeV energies. The best fit power-law normalization ($\phi_{@100TeV}^{\nu_{\mu}+\bar{\nu}_{\mu}}=1.44_{-0.26}^{+0.25} \times 10^{-18} \text{GeV}^{-1} \text{cm}^{-2} \text{s}^{-1} \text{sr}^{-1}$) and spectral index ($\gamma=2.37_{-0.09}^{+0.09}$) obtained by complementary analyses are consistent within uncertainties ⁵⁾.

The energy density in cosmic neutrinos is comparable to that of the isotropic gamma-ray background observed with the *Fermi* telescope and to that of ultra-high-energy cosmic rays (CRs above 10^9 GeV) observed, e.g., by the Auger observatory (see fig.1), and this might indicate a common origin of these messengers. Contrary to charged particles and gamma-rays, neutrinos are not deflected or absorbed during their travel so they can reach Earth unperturbed from cosmological distances making them useful messengers for studying galactic and extragalactic CR accelerators.

The arrival directions of astrophysical neutrinos are consistent with an isotropic distribution, suggesting that the signal is likely to originate from a population (or even multiple populations) of relatively weak extragalactic sources. However a small contribution from galactic sources cannot be excluded.

A specific source of high energy astrophysical neutrinos was reported after the spatial and temporal coincidence of a high-energy neutrino event and the blazar TXS 0506+056 ¹¹⁾. In September 2017 a very-high-energy muon event, of most probable neutrino energy of 290 TeV for an $E^{-2.13}$ spectrum, designated IceCube-170922A, generated an alert that was distributed worldwide and triggered a multi-wavelength campaign. Follow-up observations revealed that IceCube-170922A was spatially coincident with a known gamma-ray source, the blazar TXS 0506+056 that was active in almost all electromagnetic bands, most notably in the high-energy (HE) gamma-ray band monitored by the *Fermi* telescope, and in the very-high-energy (VHE) band detected by the Major Atmo-

spheric Gamma-ray Imaging Cherenkov (MAGIC) telescopes. The correlation of the neutrino event with the gamma-ray blazar is at 3σ statistical significance. Motivated by this correlation, the IceCube Collaboration investigated archival data for evidence of past neutrino emission from TXS 0506+056. This analysis revealed a neutrino flare (with higher significance) in 2014-2015 ¹²).

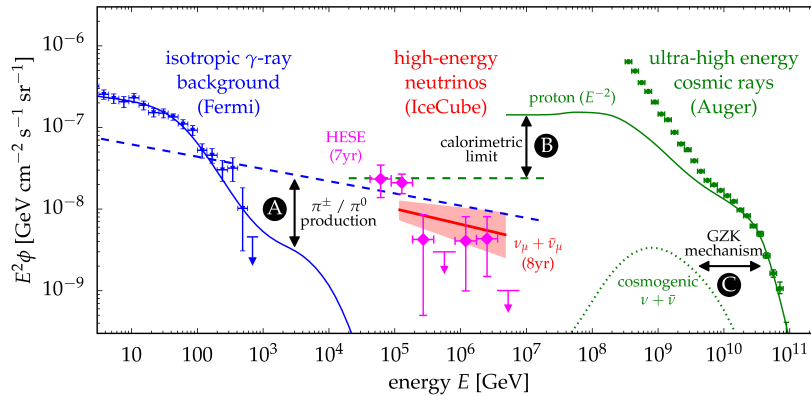


Figure 1: The flux of neutrinos per flavor ^{6, 7} (diamonds and shaded region) compared to the flux of unresolved extragalactic gamma-ray emission ⁸ (triangles) and UHE cosmic rays ⁹ (circles). Plot from ¹⁰.

A second piece of evidence comes from the all-sky analysis using 10 years of IceCube data. This analysis found an excess of neutrino events over expectations from the isotropic background 0.35 degrees away from the position of the Seyfert galaxy NGC 1068, with a 2.9σ statistical significance ¹³). Just over a month after the end of the workshop, the IceCube Collaboration reported an excess of 79^{+22}_{-20} neutrino events associated with NGC 1068 ¹⁴). The reported significance is 4.2σ which strengthens the previous report of a 2.9σ excess. NGC 1068 is a weak gamma-ray emitters in the *Fermi* band ¹⁵), and only upper limits on the gamma-ray flux are available in the VHE band ¹⁶). The best-fit neutrino flux measured by IceCube exceeds the observed gamma-ray emission in the HE and VHE band, and this finding places important constraints on the gamma-ray and neutrino emission models (see fig.2 and Section 2.1). NGC 1068 is a nearby composite Seyfert/starburst galaxy, as an active galaxy it is

classified as a Seyfert galaxy which is a class of active galactic nuclei (AGN) different from the blazar class to which TXS 0506+056 belongs to, as it will be described in the next section.

2 High-energy neutrinos from Active Galactic Nuclei

AGNs are among the most powerful emitters of radiation in the known universe, emitting a spectrum of electromagnetic radiation ranging from radio wavelengths to gamma-rays. They are fueled by accretion of matter onto supermassive black hole (SMBH), where the gravitational energy of the infalling material is released in the form of radiation and/or kinetic energy powering gas outflows. There are several classifications of AGN based on their morphological and spectral properties. For the purpose of this contribution it is convenient to make a classification based on the properties of the observed outflows. The first class includes non-jetted AGNs, such as Seyfert galaxies and quasars, which represent the bulk of the AGN population. These AGNs can accelerate multiphase wide-angle winds of velocities ranging from hundreds of km s^{-1} to few percent of the speed of light (ultra fast outflows, UFO), which are observed at different spatial scale (sub-pc to kpc) and ionization state. The electromagnetic emission in non-jetted AGN is dominated by thermal emission in the UV-optical band produced by the accretion disk around SMBH. In addition, accretion disk photons can inverse Compton (IC) scattered up to X-ray energies by a corona of hot electrons that surrounds the accretion disk.

The other class includes jetted AGNs. Jetted AGNs represent about the 10% of the AGN population. They have collimated relativistic outflows that power the strong gamma-ray and radio emission that we observe in blazars, and radio galaxies. Blazars are a class of relativistic jetted-AGNs in which the jet axis is aligned close to the line of sight.

AGN jets and winds, as well as the region very close to the SMBH composed of the accretion disk and the corona of hot electrons around it, have been proposed as possible sites of neutrino production. Here particles can be accelerated via diffusive shock acceleration, magnetic reconnections, and stochastic acceleration in plasma turbulence, and the presence of intense radiation fields and target matter ensures the conditions for high-energy neutrino production. Neutrinos are produced via hadronic interactions of accelerated protons with gas (hadronuclear interactions pp) or photon fields (photo-hadronic interac-

tions $p\gamma$). These hadronic interactions produce also gamma-rays, which, unlike neutrinos, can also be produced by leptonic processes such as IC scattering of high-energy electrons with ambient radiation field. Typically, gamma-rays and neutrinos from pp and $p\gamma$ production channels receive about 10% and 5% of the energy from the parent proton, respectively, and the differential luminosities of generated neutrinos (for all flavors) and gamma-rays are comparable.

2.1 Non-jetted AGN

This Section presents different theoretical models for the production of high-energy neutrinos in non-jetted AGN, focusing on the case of NGC 1068. NGC 1068 is a nearby ($D=14.4$ Mpc) Seyfert galaxy that hosts a Compton-thick AGN, has vigorous starburst activity and AGN-driven outflows, and for these reasons has been discussed as a potential source of high-energy neutrinos. As it was mentioned in Section 1, the best-fit neutrino flux measured by IceCube exceeds the observed gamma-ray emission in the HE and VHE band, and this implies a neutrino production site opaque to GeV-TeV gamma-rays.

The cores of AGN are one of the best candidates as the source of the high-energy neutrinos, because the intense AGN radiation could act as the target photon field for both photo-hadronic neutrino emission and for gamma-ray absorption due to photon-photon pair production. In AGN core models, non-thermal particles are assumed to be accelerated either by the hot corona that surrounds AGN accretion disks or at the inner edge of the accretion disks, with X-ray photons from the corona, providing the conditions for the absorption of gamma rays. Figure 2 compares the IceCube neutrino flux measurement with the model predictions^{17, 18}). The latter include neutrinos produced by both pp and $p\gamma$ interactions in the corona, and are able to reproduce the observed neutrino flux if the CR luminosity is $\sim 10\%$ -100% of the X-ray luminosity. However, these models cannot at the same time reproduce the observed gamma-ray spectrum due to the strong gamma-ray attenuation in this region. In this scenario the gamma-ray emission is not related to the neutrino emission and could arise from a separate region, which may be the starburst ring¹⁹⁾ and/or AGN-driven outflows.

The latter have also been proposed as possible sites for particle acceleration and neutrino production in non-jetted AGN. AGN-driven winds, similar to stellar winds, are expected to develop a structure characterized by an inner

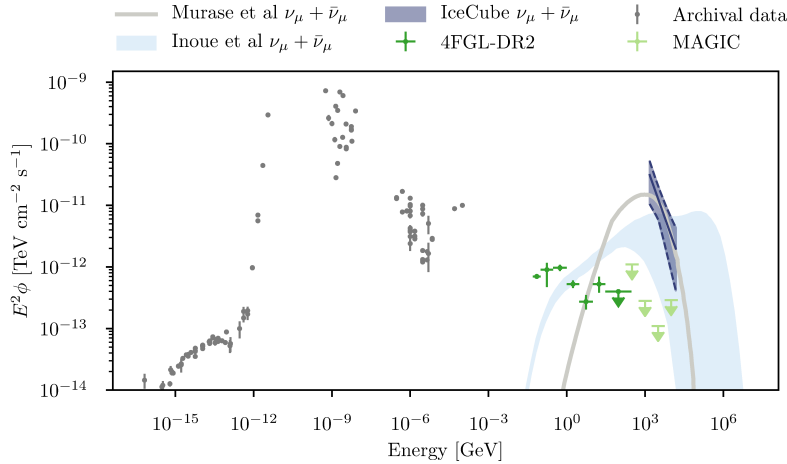


Figure 2: *Multi-messenger SED of NGC 1068. The best-fit neutrino spectrum (solid line, with the shaded region illustrating 95% confidence level) is compared with the neutrino emission models from ¹⁷ (shaded region) and ¹⁸ (solid line). Plot from ¹⁴.*

wind termination shock, a contact discontinuity, and an outer forward shock. The model that invoke particle acceleration and neutrino production at the forward shock of the AGN-driven molecular wind observed in NGC 1068 is strongly constrained by the upper limits on the gamma-ray flux in the VHE band obtained by the MAGIC telescopes ^{20, 16}). This model predicts a maximum neutrino event rate of 0.07 yr^{-1} from hadronuclear interactions in the galactic molecular disk which is much lower than that observed by IceCube.

An alternative AGN wind model assumes particle acceleration and neutrino production in the inner regions of a failed wind, which is a wind that never reach the local escape velocity ²¹). This model shares some similarities with the AGN core models including the spatial scale of the neutrino production site and the target AGN photon field. In this model neutrinos are mainly generated via photo-hadronic interactions with the AGN radiation, and the predicted neutrino flux can explain the level of neutrino flux observed by IceCube above 1 TeV. This system is optically thick for GeV-TeV gamma-rays,

to reproduce the observed gamma-ray spectrum in the *Fermi* band a separate external emission region is postulated, identified as the forward shock of a successful wind interacting with the gas and dust distributed in a torus-like structure surrounding the SMBH.

Finally, the multi-messenger emission produced by accelerated particles at the wind termination shock of the UFO that might be present in the core of NGC 1068 is presented ²²⁾. In this scenario the neutrino flux is dominated by the *pp* interactions taking place in the shocked ambient medium in the range from GeV up to 100 TeV. Photo-hadronic interactions take also place in the UFO environment, producing neutrinos with energies above 1 PeV. Overall the neutrino flux shows a remarkable flat spectrum from more than five orders of magnitude and the associated gamma-ray counterpart could dominate the gamma-ray flux observed in the Fermi band and gets absorbed above a few tens GeV from the strong photon field associated to the AGN and torus. In the TeV range the UFO could contribute from a few up to $\sim 10\%$ of the estimated flux by IceCube leaving room for other possible sources such as the corona, the molecular outflow, and/or the starburst ring.

2.2 Jetted AGN

This Section focuses on jetted AGNs, and in particular on models for neutrino production in the blazar TXS 0506+056. Figure 3 shows the multi-messenger spectral energy distribution (SED) of TXS 0506+056. The electromagnetic SED displays two bumps, one peaking in the UV-optical range and the second one in the GeV range, which is characteristic of the SED of blazars. In standard blazar emission models the low-energy component is associated to synchrotron radiation by relativistic electrons in the jet pointing close to our line of sight; while the origin of the high energy component is not fully understood yet. Two possible scenarios are proposed. In the leptonic scenario the high energy component is interpreted as IC scattering of soft photons by the relativistic electrons. Seed photons for IC scattering can be either synchrotron photons or photons from external radiation fields. In hadronic scenarios, protons co-accelerated in the jet could emit VHE emission through various processes, such as synchrotron radiation, photo-meson reactions or pion production.

Several research groups have been studying lepto-hadronic models for the blazar TXS 0506+056 and modelled the multi-messenger data set. Regardless

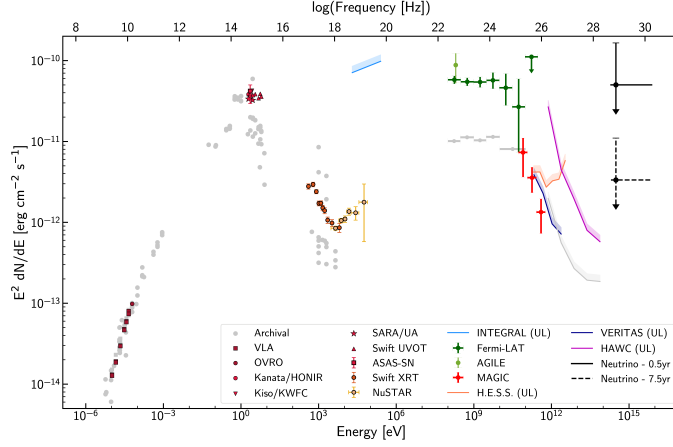


Figure 3: *Multi-messenger SED of TXS0506+056. The neutrino flux upper limits, that produce on average one detection like IceCube-170922A over a period of 0.5 and 7.5 yr, are shown as solid black and dashed black error lines, respectively. Plot from 11).*

of the details entering the theoretical calculation, what we learnt from TXS modelling is that lepto-hadronic blazar models, in which the neutrino emission is produced in $p\gamma$ interactions in the jet, are able to fit the electromagnetic SED and at the same time reproduce a neutrino rate consistent with the single event seen by IceCube in 2017. The electromagnetic emission is dominated by leptonic emission with a subdominant hadronic component, and the neutrino intensity is strongly constrained by the cascade flux in the X-ray band. While single-zone models face the disadvantage of requiring a large jet power (often super-Eddington) to fit the data ^{23, 24}, solutions that make use of external target photon fields seem more promising ^{25, 26}).

3 Summary

Observations with IceCube have revealed a diffuse flux of astrophysical neutrinos in the TeV-PeV energy range of unknown origin. Both galactic and extragalactic sources are candidate sources, but the isotropy of the neutrino

arrival directions favor an extragalactic origin. Recent studies with IceCube have shown that, like the blazar TXS 0506+056, the Seyfert galaxy NGC 1068 is a point source of high-energy neutrinos. The development of increasingly accurate theoretical models for neutrino production in jetted and non-jetted AGN, and future observations with new gamma-ray and neutrino facilities will allow us to shed more light on these recent observations, and establish high-energy neutrinos as an essential component for multi-messenger astronomy.

References

1. M.J. Aartsen *et al*, Science **342**, 6161 (2013).
2. R. Abbasi *et al*, Phys. Rev. D **104** 022002 (2021)
3. M. G. Aartsen *et al*, Astrophys. J. **833** 3 (2016)
4. M. G. Aartsen *et al*, Phys. Rev. Lett. **125** 121104 (2020)
5. R. Abbasi *et al*, Astrophys. J. **928** 50 (2022)
6. C. Haack *et al*, 35th International Cosmic Ray Conference. Proceedings of Science **1005** 1710.01191 (2018)
7. C. Kopper *et al*, 35th International Cosmic Ray Conference. Proceedings of Science **981** 1710.01191 (2018)
8. M. Ackermann *et al*, Astrophys. J. **799** 86 (2015)
9. I. Valino *et al*, 34th International Cosmic Ray Conference. Proceedings of Science **271** 1509.03732 (2016)
10. M Ahlers *et al*, Progress in Particle and Nuclear Physics **102** 73 (2018)
11. IceCube Collaboration *et al*, Science **361** eaat1378 (2018)
12. M. Aartsen *et al*, Science **361** 6398 (2018)
13. M. G. Aartsen *et al*, Phys. Rev. Lett. **124** 051103 (2020)
14. IceCube Collaboration *et al*, Science **378** 538 (2022)
15. S. Abdollahi *et al*, Astrophys. J.. Suppl. Ser **247** 33 (2020)

16. V. Acciari *et al*, *Astrophys. J.* **883** 135 (2019)
17. Y. Inoue *et al*, *Astrophys. J. Lett.* **891** L33 (2020)
18. K. Murase *et al*, *Phys. Rev. Lett.* **125** 011101 (2020)
19. B. Eichmann *et al*, *Astrophys. J.* **939** 43 (2022)
20. A. Lamastra *et al*, *Astron. Astrophys.* **596** A68 (2016)
21. S. Inoue *et al*, arXiv e-print 2207.02097 (2022)
22. E. Peretti *et al*, in prep. (2022)
23. S. Gao *et al*, *Nat. Astron.* **154** L10 (2018)
24. M. Cerruti *et al*, *Mon. Not. R. Astron. Soc.* **483** L12 (2018)
25. S. Ansoldi *et al*, *Astrophys. J. Lett.* **863** L10 (2018)
26. A. Keivani *et al*, *Astrophys. J.* **864** 84 (2018)

INTRIGUING HINTS FROM INDIRECT DARK MATTER SEARCHES

Manuela Vecchi

*Kapteyn Astronomical Institute, University of Groningen,
Landleven 12, 9747 AD Groningen, The Netherlands*

Abstract

The existence of dark matter (DM) is supported by a large body of evidence on local and cosmological scales collected over the past decades. However, we still need to gain more knowledge about its nature and interaction mechanisms. If Dark Matter is made of weakly interacting massive particles (WIMPs), indirect searches are an extremely promising method to probe annihilating and decaying dark matter particle models, with masses in the GeV to TeV region. Indirect searches can be carried out by looking for an excess of gamma rays or neutrinos from DM-dominated regions, like the galactic centre or dwarf galaxies. The search for DM with charged cosmic rays can be performed by searching for spectral features in the antimatter fluxes, where the DM signal would appear as excess with respect to the background from conventional astrophysical processes. This contribution will focus on a few intriguing and debated detection claims from indirect searches, namely the Galactic Centre excess and the cosmic-ray antiproton excess.

1 Introduction

There is clear evidence for dark matter (DM) in the universe, and this evidence has been built over several decades due to profound and diverse scientific work with many facets. However, it took about a century for the scientific community to reach the current recognition stage. A thorough overview of the historical perspective on this path is given in a recent work ¹⁾.

We know that only a tiny fraction of about 5% of the universe we have observed so far is made of ordinary matter, made by baryons. The remaining 95% is made of DM and dark energy. From astrophysical observations and cosmological simulations, we know that DM constitutes 85% of the mass content of the universe, and it drives the formation of all the structures that we can see. The field's current knowledge suggests that DM should be non-baryonic, electrically neutral, long-lived and non-relativistic (cold). These characteristics do not match any particle included in the Standard Model (SM). More or less plausible DM candidates span 90 orders of magnitude in mass, ranging from ultra-light bosons, to massive primordial black holes (PBH). Figure 1 displays the existing DM candidates. An excellent overview is given in ²⁾.

In the following, we will focus on the possibility of detecting DM from super-symmetric extensions of the Standard Model of particle physics ³⁾ ⁴⁾. These theories predict the existence of Weakly Interacting Massive Particles (WIMPs), whose mass lies in the GeV to TeV range, with interaction cross sections typical of weak interactions (order of fb). WIMPs are predicted to be stable Majorana particles, implying that they can self-annihilate to produce Standard Model particles like fermions or gauge bosons.

Dark matter annihilation plays a crucial role in the early Universe, as it provides a natural mechanism through which WIMPs have been produced ⁵⁾. DM particles are thought to be thermal relics from the Early Universe. They were as abundant as photons, in the beginning, being freely created and destroyed in pairs as long as the temperature of the hot plasma was higher than their mass. Their relative number density started then being suppressed as annihilation proceeded, but due to the Universe cooling, the temperature dropped below their mass. Finally, the annihilation process also froze out as the Universe expanded further. The remaining diluted abundance of stable particles constitutes the DM of today.

Three complementary strategies can be used to search for DM. Direct

searches ⁶⁾ can be conducted in underground laboratories for DM particles scattering off nuclei. DM particles could be produced at colliders ⁷⁾ and hunted by looking for a deviation from the Standard Model. An indirect search ⁹⁾ can

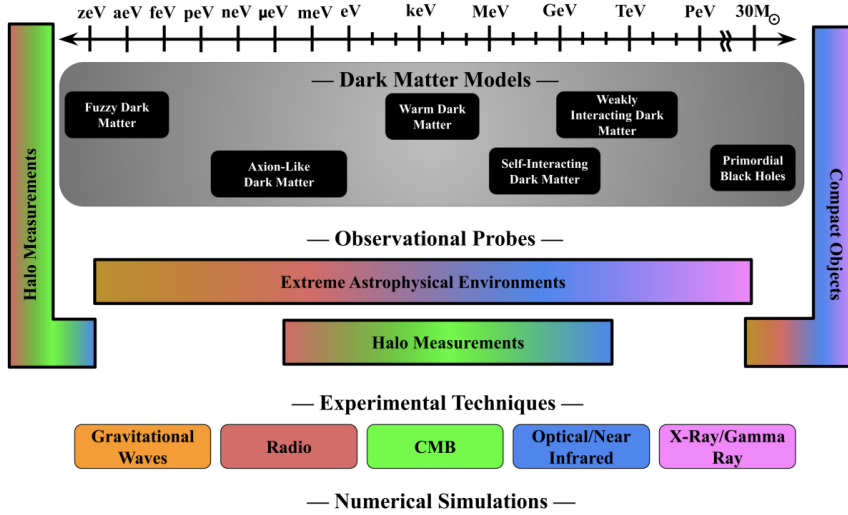


Figure 1: Dark matter candidates, together with their mass. Figure from ⁸⁾.

be performed by detecting gamma rays, cosmic rays or high-energy neutrinos produced in DM annihilation or decay in the universe. Several DM experiments have claimed excess signals above the background over the past years. However these hints do not provide yet a definitive proof of a DM discovery.

This review focuses on two puzzling hints from indirect searches: the GeV gamma-ray emission from Galactic Centre and the cosmic-ray antiproton flux. The reason for this (personal) choice is twofold: first, these two results point towards the very same range of DM candidates and thus have increased interest. Second, we believe that a robust understanding of these signals, leading to a conclusive word on their origin, is within reach for the coming decade. In section 2, we discuss the GeV gamma-ray emission from Galactic Centre, while in section 3 we review the cosmic-ray antiproton excess and its interpretations. The summary is provided in section 4.

2 The Galactic Centre excess

The Galactic Centre (GC) region is the richest environment of our Galaxy in terms of high-energy emitters. In addition to a large amount of non-thermal astrophysical sources ^{10) 11)}, the GC is also considered the strongest source of gamma rays from DM annihilation due to its large DM density and relative proximity to Earth.

The Large Area Telescope (LAT) onboard the Fermi mission ¹²⁾ has achieved a tremendous wealth of detailed observations of steady and transient astrophysical sources. The 4FGL catalog ¹³⁾ includes 5064 sources detected with high (4σ) significance, with the corresponding localisation and spectral properties. Besides the astrophysical emitters, LAT is essential to perform indirect DM searches ¹⁴⁾. A preliminary analysis ¹ of the first 11 months of

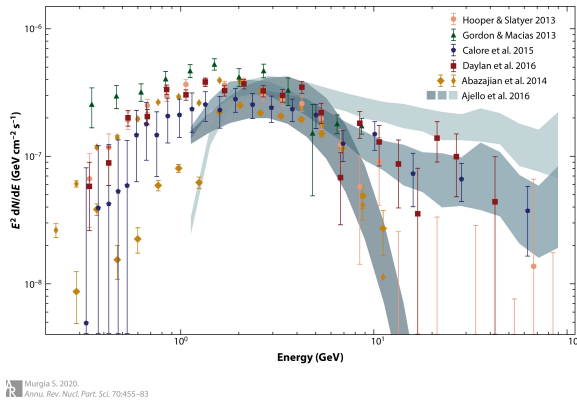


Figure 2: The GCE spectrum (re-scaled by the energy squared, E^2) as a function of energy, for different analyses. Figure taken from ¹⁵⁾.

LAT data ¹⁶⁾ pointed out a hint for a residual emission after subtraction of the relevant background components. An independent analysis ¹⁷⁾ ² reached similar conclusions and appeared very close in time. The statistical significance of the GC excess (GCE) is now well established, and the LAT collaboration has

¹carried out by members of the LAT collaboration

²carried out by non-LAT members

later confirmed its existence ¹⁸⁾ ³. Focusing on a $15^\circ \times 15^\circ$ region about the direction of the GC and on the energy range between 1 and 100 GeV, a residual was found after subtracting the contributions from both interstellar emission and point sources. A more “DM-focused” analysis of the GCE was published a few years later by the LAT collaboration ¹⁹⁾, where no DM detection was claimed, and annihilation cross-section upper limits are reported for different values of the DM particle mass.

A wealth of publications on the interpretation of the GCE has been produced. However, its origin is still controversial. Leading explanations are either WIMP DM or a new population of unresolved gamma-ray emitters, such as pulsars ¹⁵⁾. The interstellar emission generated by CRs interacting with the interstellar medium (gas and radiation field) represents the biggest challenge in determining the nature of the GCE.

Several aspects of the GCE are studied to discern its origin. Figure 2 shows a review of the GCE spectrum results as a function of energy ¹⁵⁾. A prominent peak emerges around 3 GeV, while extending the excess up to 10 GeV is still uncertain and dependent on the analysis technique.

The morphology of the excess is also a very important aspect. In particular, to determine whether the GCE originates from an unresolved population of point sources (mainly pulsars) or from the smooth emission expected if DM is the source of the observed excess.

The robustness of the GCE can be probed by comparing the result with those obtained by studying independent targets. Dwarf spheroidal galaxies ²⁰⁾ are known to be the most DM-dominated objects in the universe ⁴. They are low luminosity objects with no gamma-ray emission expected of astrophysical origin. These targets are less susceptible to the limitations in modelling the astrophysical background. DM searches from Dwarf spheroidal galaxies provide the most stringent limits (together with antiprotons). Figure 3 shows the velocity-averaged annihilation cross-section as a function of the DM particle mass for several analyses, targeting the GCE and the dwarf spheroidal galaxies. We can see that several groups claimed the detection of DM with masses around 10 GeV, but these results are in tension with the limits of dwarf

³based on the analysis of LAT data taken during the first 62 months of the mission

⁴see F. G. Saturni’s contribution at this workshop

spheroidal galaxies.

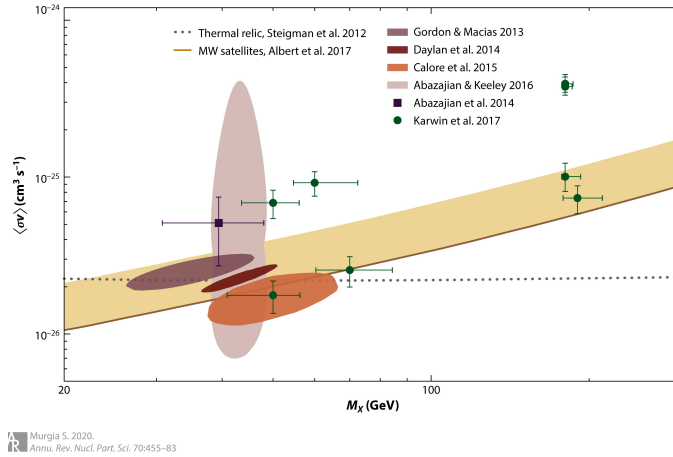


Figure 3: Velocity-averaged annihilation cross-section as a function of the DM particle mass for several analyses, targeting the GCE and the dwarf spheroidal galaxies. Figure from (15).

A multimessenger view of the GC with improved performance is the key to understand the GCE. The upcoming ground-based gamma-ray observatory Cherenkov Telescope Array (CTA) (21) will provide essential information, together with the future gamma-ray space missions such as e-Astrogam (22), in synergy with other upcoming facilities, such as the radio telescope Square Kilometer Array (SKA) (23).

3 The cosmic-ray antiproton excess

Every day our planet is hit by a large flux of high-energy particles, Cosmic Rays (CR). They are mainly made of matter particles and nuclei, such as electrons, protons, and heavier nuclei (including C, O and Fe). CR travel long distances through the interstellar medium (24). A tiny fraction of the total CR flux is made of antimatter. In particular about $5 \cdot 10^{-3}$ for positrons, 10^{-5} for antiprotons, $5 \cdot 10^{-7}$ for antideuterons and less than $5 \cdot 10^{-8}$ for antihelium and heavier antinuclei. Despite being rare, antimatter particles carry a great

wealth of information since their origin is closely connected to fundamental processes ²⁵⁾. To date, the most precise measurements of CR antimatter, in particular positrons and antiprotons, have been performed by the AMS-02 experiment ²⁶⁾, taking data on the International Space Station since 2011. The physics objectives of AMS-02 include the search for the origin of CR, DM and antimatter, as well as the search for new phenomena in the universe.

The AMS-02 collaboration has published high-precision data of the antiproton flux and the antiproton-to-proton ratio ²⁷⁾ ²⁶⁾.

An excess of antiprotons at about 10 GeV energy with respect to the astrophysical background of (secondary) antiprotons was first claimed by ²⁸⁾ and ²⁹⁾. Several other groups followed this claim (see ³⁰⁾ for a comprehensive review), reporting that the data can be well described by including a primary component due to DM annihilation in addition to the secondary antiprotons. Exciting and puzzling is the fact that due to DM, this excess can be explained in terms of the same parameters, namely mass, annihilation cross section and annihilation channels which describe the GCE. However, the existence of the antiproton excess is not firmly established. Several groups ³³⁾ ³⁴⁾ ³⁵⁾ ³¹⁾ carried out sophisticated statistical analyses and did not find any evidence of primary antiprotons, thus rejecting the need for a DM component to explain the antiproton data (see Figure 4).

Two aspects are of primary importance to firmly establish the robustness of this hint in the upcoming years. It is essential to better understand the systematic uncertainties of the measurement, given their high precision which often goes beyond the theoretical uncertainties. It is also important to improve the understanding on the secondary antiproton production. This aspect requires detailed measurements of the antiproton production cross-section, which can only be done using dedicated setups at colliders. Moreover, the upcoming GAPS (General Anti-Particle Spectrometer) ³⁶⁾ ³⁷⁾ will certainly improve the current understanding of cosmic-ray antiproton and this puzzling excess. GAPS is a balloon-borne experiment designed to measure low-energy ($E < 0.25$ GeV/n) cosmic antiparticles and antinuclei (i.e., antiprotons, antideuterons, and antihelium nuclei), in a low-energy region currently inaccessible to any experiment. Its first flight is expected to be performed in the austral summer of 2023-2024.

Antinuclei, such as antideuterons or antihelium, have never been detected

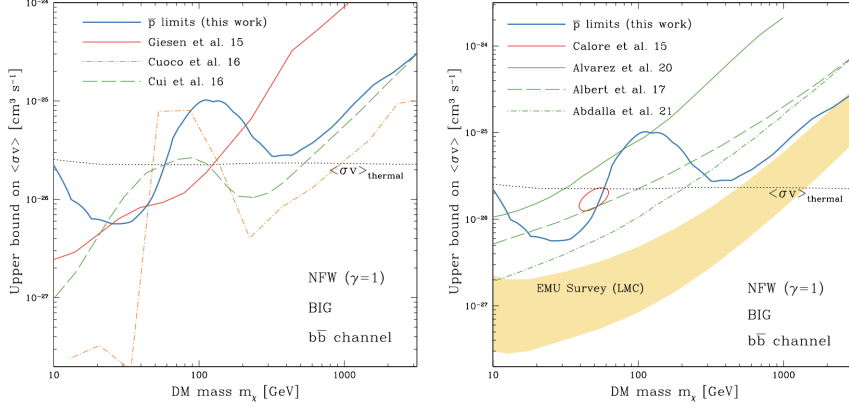


Figure 4: Left panel: The upper limit on the annihilation cross section for the $b\bar{b}$ channel (solid blue line), compared to other results involving antiproton analyses (see 31) for the full list of results and corresponding references). Right panel: The upper limit on the annihilation cross section derived in this work for the $b\bar{b}$ channel (solid blue line), compared to other probes. The thermal relic cross section reported in dotted black lines is computed in 32). Figure from 31).

in CRs. Their discovery would dramatically change our present knowledge of antimatter in the universe, with groundbreaking consequences for early-universe cosmology and high energy physics 38). The unique strength of a possible discovery of antinuclei lies in their very low level of astrophysical background, the flux of antinuclei generated when CR protons and antiprotons hit the interstellar medium, which is kinematically suppressed with respect to the primary signal that could be produced in the annihilation or decay of Dark Matter (DM) particles in the galaxy. In particular, the energy region around 1 GeV/n offers a nearly background-free search window. The detection of antinuclei is within the reach of AMS-02 ⁵, planning to continue operations

⁵A few antihelium candidates have been announced a few years ago by the AMS-02 collaboration, but this result is still being thoroughly investigated within the collaboration.

until 2030. Antideuterons and antihelium are also within the reach of the upcoming GAPS, which will explore a complementary low energy window.

4 Conclusions

The past decade has reported many intriguing claims about possible DM detection. This review focused on two of them: the gamma-ray excess from the Galactic Centre and the cosmic-ray antiproton excess. A GeV-scale excess has been detected by the Fermi Large Area Telescope (Fermi-LAT) in the galactic centre. The statistical significance of this excess is well-established; however, its origin is still debated within the community. The DM origin of this excess is a viable explanation, together with a new population of unresolved point sources. An accurate model for the Galactic diffuse gamma-ray foreground is the most significant limitation in understanding this region. The final word could come from the next generation of observatories, including the gamma-ray experiments CTA, e-Astrogam and the radio telescope SKA. Several groups have identified an excess of GeV cosmic-ray antiprotons in the AMS-02 data. A DM signal requires similar mass, cross-section and annihilation channels to those required to explain the GCE. The underlying correlations of the AMS-02 systematic errors, together with future antiproton production cross-section measurements from inelastic hadronic collisions are needed to establish the robustness of this excess. The future observation of antideuteron or antihelium nuclei by AMS-02 and future GAPS will be an unambiguous signal of new physics.

5 Acknowledgements

I am especially grateful to the organisers of the Vulcano workshop for their kind invitation to attend this fruitful event. This paper is written with a personal title and reflects my perspective on the field. I am immensely grateful to all the colleagues I have worked with in the past few years on indirect dark matter searches, from whom I have learned so much. Many thanks to Pierre Salati, Mathieu Boudaud, Fabio Iocco (just to name a few) and all my colleagues from the AMS-02, HESS and CTA collaborations.

References

1. G. Bertone and D. Hooper. History of dark matter. *Reviews of Modern Physics*, 90(4):045002, October 2018.
2. G. Bertone. History of dark matter. *Reviews of Modern Physics*, 90(4):045002, October 2018.
3. G. Bertone, D. Hooper, and J. Silk. Particle dark matter: Evidence, candidates and constraints. *Physics Reports*, 405(5-6):279–390, 2005.
4. J. Cooley et al. Report of the Topical Group on Particle Dark Matter for Snowmass 2021. *preprint arXiv:2209.07426*, 9 2022.
5. L. Bergstrom et al. New Positron Spectral Features from Supersymmetric Dark Matter - a Way to Explain the PAMELA Data? *Phys. Rev.*, D78:103520, 2008.
6. J. Billard and other. Direct detection of dark matter—appec committee report. *Reports on Progress in Physics*, 85(5):056201, apr 2022.
7. O. Buchmueller and other. Search for dark matter at colliders. *Nature Phys.*, 13(3):217–223, 2017.
8. A. Drlica-Wagner et al. Report of the Topical Group on Cosmic Probes of Dark Matter for Snowmass 2021. *e-prints arXiv:2209.08215*, page arXiv:2209.08215, September 2022.
9. M. Cirelli. Status of indirect (and direct) dark matter searches. *arXiv preprint arXiv:1511.02031*, 2015.
10. C. van Eldik. Gamma rays from the galactic centre region: A review. *Astroparticle Physics*, 71:45–70, 2015.
11. A. Viana et al. The Cherenkov Telescope Array view of the Galactic Center region. *PoS, ICRC2019:817*, 2021.
12. W. B. Atwood et al. The Large Area Telescope on the Fermi Gamma-ray Space Telescope Mission. *Astrophys. J.*, 697:1071–1102, 2009.
13. S. Abdollahi et al. Fermi large area telescope fourth source catalog. *The Astrophysical Journal Supplement Series*, 247(1):33, mar 2020.

14. E. A. Baltz et al. Pre-launch estimates for GLAST sensitivity to Dark Matter annihilation signals. *JCAP*, 07:013, 2008.
15. S. Murgia. The fermi–lat galactic center excess: Evidence of annihilating dark matter? *Annual Review of Nuclear and Particle Science*, 70(1):455–483, 2020.
16. V. Vitale and A. Morselli. Indirect Search for Dark Matter from the center of the Milky Way with the Fermi-Large Area Telescope. *arXiv e-prints*, page arXiv:0912.3828, December 2009.
17. L. Goodenough and D. Hooper. Possible Evidence For Dark Matter Annihilation In The Inner Milky Way From The Fermi Gamma Ray Space Telescope. *e-prints arXiv:0910.2998*, 10 2009.
18. M. Ajello et al. Fermi-LAT Observations of High-Energy γ -Ray Emission Toward the Galactic Center. *Astrophys. J.*, 819(1):44, 2016.
19. M. Ackermann et al. The Fermi Galactic Center GeV Excess and Implications for Dark Matter. *Astrophys. J.*, 840(1):43, 2017.
20. L. Strigari. Dark matter in dwarf spheroidal galaxies and indirect detection: a review. *Rept. Prog. Phys.*, 81(5):056901, 2018.
21. B. S. Acharya et al. *Science with the Cherenkov Telescope Array*. WSP, 11 2018.
22. M. Tavani et al. Science with e-ASTROGAM: A space mission for MeV–GeV gamma-ray astrophysics. *JHEAp*, 19:1–106, 2018.
23. F. Aharonian et al. Pathway to the Square Kilometre Array - The German White Paper -. *preprint arXiv:1301.4124*, 1 2013.
24. I. A. Grenier, J. H. Black, and A. W. Strong. The nine lives of cosmic rays in galaxies. *Annual Review of Astronomy and Astrophysics*, 53(1):199–246, 2015.
25. P. Salati. What charged cosmic rays tell us on dark matter? *preprint arXiv:2210.07166*, 10 2022.

26. M. Aguilar et al. The Alpha Magnetic Spectrometer (AMS) on the international space station: Part II - Results from the first seven years. *Physics Report*, 894:1–116, February 2021.
27. M. Aguilar et al. Antiproton Flux, Antiproton-to-Proton Flux Ratio, and Properties of Elementary Particle Fluxes in Primary Cosmic Rays Measured with the Alpha Magnetic Spectrometer on the International Space Station. *Phys. Rev. Lett.*, 117(9):091103, 2016.
28. A. Cuoco et al. Novel Dark Matter Constraints from Antiprotons in Light of AMS-02. *Phys. Rev. Lett.*, 118(19):191102, 2017.
29. M. Cui et al. Possible dark matter annihilation signal in the ams-02 antiproton data. *Phys. Rev. Lett.*, 118:191101, May 2017.
30. R. K. Leane et al. Snowmass2021 Cosmic Frontier White Paper: Puzzling Excesses in Dark Matter Searches and How to Resolve Them. page arXiv:2203.06859, March 2022.
31. F. Calore et al. AMS-02 antiprotons and dark matter: Trimmed hints and robust bounds. *SciPost Phys.*, 12:163, 2022.
32. G. Steigman et al. Precise Relic WIMP Abundance and its Impact on Searches for Dark Matter Annihilation. *Phys. Rev. D*, 86:023506, 2012.
33. G. Giesen et al. AMS-02 antiprotons, at last! Secondary astrophysical component and immediate implications for Dark Matter. *JCAP*, 09:023, 2015.
34. M. Boudaud et al. Ams-02 antiprotons' consistency with a secondary astrophysical origin. *Phys. Rev. Res.*, 2:023022, Apr 2020.
35. P. De La Torre Luque. Combined analyses of the antiproton production from cosmic-ray interactions and its possible dark matter origin. *JCAP*, 11:018, 2021.
36. T. Aramaki et al. Antideuteron sensitivity for the GAPS experiment. *Astroparticle Physics*, 74:6–13, February 2016.
37. F. Rogers et al. Sensitivity of the GAPS experiment to low-energy cosmic-ray antiprotons. *Astropart. Phys.*, 145:102791, 2023.

38. P. von Doetinchem et al. Cosmic-ray antinuclei as messengers of new physics: status and outlook for the new decade. *JCAP*, 08:035, 2020.

A COSMOGRAPHIC OUTLOOK ON DARK ENERGY AND MODIFIED GRAVITY

Salvatore Capozziello

*Dipartimento di Fisica “E. Pancini”, Università di Napoli “Federico II”,
Via Cinthia 9, 80126 Napoli, Italy.*

Rocco D’Agostino

Scuola Superiore Meridionale, Largo S. Marcellino 10, 80138 Napoli, Italy.

Abstract

The cosmographic technique is a powerful model-independent tool for distinguishing between competing cosmological scenarios. The key strengths and weaknesses of standard cosmography are discussed in view of healing the convergence problem endangering the high-redshift expansions of cosmological distances. We focus especially on rational cosmographic approximations to reconstruct the dark energy behaviour under the $f(R)$, $f(T)$ and $f(Q)$ gravity frameworks. Based on observational constraints over the cosmographic series, we investigate the origin of cosmic acceleration and the possibility of going beyond the standard cosmological model to explain the dark energy problem.

1 Introduction

Our understanding of the cosmos has significantly changed since the discovery of accelerated expansion shown by the light coming from most distant

Supernovae ^{1, 2}). Indeed, observations showed the presence of a cosmological constant with negative pressure that accelerates the cosmic expansion at recent times ³). The standard Λ CDM model is the most widely accepted theory that incorporates the cosmological constant effects and includes cold dark matter and baryons within a spatially flat geometry ⁴). In spite of its effectiveness, the Λ CDM paradigm is characterized by a number of flaws that are mostly related to the cosmological constant problem, arisen from the challenges of reconciling the standard model of particle physics with cosmological data ^{5, 6}). Because of the enigmatic feature of dark energy, some authors have looked for a different explanation for the cosmic speed-up. Possible alternatives include taking into account that the accelerated expansion may be due to dynamical scalar fields ⁷), or to the presence of a single cosmic fluid endowed with an equation of state that causes it to behave like dark matter and dark energy at high and low densities, respectively ⁸).

Furthermore, it has been explored the possibility to solve the dark energy problem without introducing exotic components into the energy-momentum tensor. Such scenarios refer to extensions or modifications of Einstein's gravity aimed at solving the Λ problems from first principles ^{10, 11}). In fact, corrections to the Einstein-Hilbert gravitational action have attracted a lot of attention due to their ability to provide, within a single picture, an alternative interpretation of vacuum energy and an explanation for dark matter by means of geometrical effects. The recent evidence supporting the Starobinsky model of inflation ⁹) has renewed interest for $f(R)$ models ^{12, 13}), whose action is described by a general function of the Ricci scalar, R . A different way to characterize the gravitational interaction is to consider spacetime twisted by torsion. The teleparallel description of gravity has lately attracted significant interest among all the ideas explored to explain the late-time cosmic expansion ¹⁴). Hence, theories in which the torsion scalar is replaced by a nonlinear function $f(T)$ ^{15, 16}) provide a workable framework inspired by $f(R)$ gravity. Even more recently, the possibility to consider non-metricity as the mediator for the gravitational interaction, while assuming vanishing curvature and torsion, has induced to investigate $f(Q)$ theories ^{17, 18}) to obtain new insights into the universe's acceleration resulting from the implication of a different geometric setup with respect to the more common Riemann geometry.

Distinguishing among different models invoked to explain the late evolu-

tion of the universe becomes therefore crucial. In this respect, model-independent approaches, such as cosmography, represent a powerful tool to discriminate between dark energy and modified gravity scenarios (19, 20). However, the difficulty of treating high-redshift data due to the scarcity of accurate measurements at $z > 1$ puzzles the use of the standard cosmographic method relying on Taylor series. Indeed, the convergence issues inherent to the short convergence radius of the Taylor series may limit the predictability of cosmography, requiring then to explore new techniques that could allow to extend the standard kinematic procedure to high redshifts. This is the case of rational approximations, based on Padé and Chebyshev polynomials (21).

In this paper, we provide an updated outlook on the most recent developments regarding the cosmographic method and its application under different theoretical frameworks to reconstruct the gravitational action and, thus, deduce the nature of the dark energy behaviour.

2 Modern cosmography

Cosmography is probably the most basic of all model-independent techniques. It uses the cosmological principle's observational premise and is based on Taylor expansions of observables that could be directly compared to data. In principle, cosmography is a strong tool for breaking the degeneracy among cosmological models. In the context of Friedmann-Lemaître-Robertson-Walker (FLRW) spacetime, the idea is to expand the cosmic scale factor, $a(t)$, in the Taylor series around the current time, t_0 . This method allows to study the kinematics of the universe by means of the $a(t)$ derivatives, which provides the so-called cosmographic series (22):

$$H(t) \equiv \frac{1}{a} \frac{da}{dt}, \quad q(t) \equiv -\frac{1}{aH^2} \frac{d^2a}{dt^2}, \quad j(t) \equiv \frac{1}{aH^3} \frac{d^3a}{dt^3}, \quad s(t) \equiv \frac{1}{aH^4} \frac{d^4a}{dt^4}, \quad (1)$$

known as the Hubble, deceleration, jerk and snap parameters, respectively. One can then use the above definitions to expand the luminosity distance in terms of the current values of the cosmographic parameters. In particular, for a spatially flat universe, we find

$$d_L(z) = H_0^{-1} \left[z + \frac{1}{2}(1 - q_0)z^2 - \frac{1}{6}(1 - q_0 - 3q_0^2 + j_0)z^3 + \frac{1}{24}(2 - 2q_0 - 15q_0^2 - 15q_0^3 + 5j_0 + 10q_0j_0s_0)z^4 + \mathcal{O}(z^5) \right], \quad (2)$$

leading to the Hubble expansion series

$$H(z) \simeq H_0 \left[1 + z(1 + q_0) + \frac{z^2}{2}(j_0 - q_0^2) - \frac{z^3}{6}(-3q_0^2 - 3q_0^3 + j_0(3 + 4q_0) + s_0) \right]. \quad (3)$$

Despite the simplicity and immediate applicability of the cosmographic technique, unfortunately, the absence of numerous and very accurate data at high redshifts prevents from univocally bound the higher-order terms of the cosmographic series, weakening severely the ability to disentangle modified gravity theories from effective dark energy models. In short, the standard formulation of cosmography is affected by two major problems: first, the presence of systematic errors caused by the chosen truncation order; second, the reduced predictive power when analyzing data beyond $z = 1$, exceeding the radius of convergence of the Taylor series ²³).

2.1 Padé polynomials

In order to overcome the aforementioned issues, a intriguing possibility is to take into account rational polynomials. One first relevant example consists in using Padé polynomials to approximate cosmological distance measures ²⁴). The (n, m) Padé approximation of a generic function $f(z)$ is defined as

$$P_{n,m}(z) = \frac{\sum_{i=0}^n a_i z^i}{1 + \sum_{j=1}^m b_j z^j}, \quad (4)$$

where the coefficients a_i and b_i can be found from the following system:

$$\begin{cases} a_i = \sum_{k=0}^i b_{i-k} c_k, \\ \sum_{j=1}^m b_j c_{n+k+j} = -b_0 c_{n+k}, \quad k = 1, \dots, m. \end{cases} \quad (5)$$

where c_k are the coefficients of the Taylor series expansion of $f(z)$.

2.2 Chebyshev polynomials

A second possible approach aimed at extending the convergence radius of the cosmographic series and, at the same time, at overcoming the degree of subjec-

tivity in truncating the expansion that may still be present in the Padé method, makes use of Chebyshev polynomials. The latter, in fact, are able to highly reduce the uncertainties on higher-order cosmographic coefficients and, thus, provide an accurate description of the late-time evolution of the universe ²¹⁾. Specifically, the Chebyshev polynomials of the first kind are given as

$$T_n(z) = \cos(n\theta), \quad \theta = \arccos(z), \quad n \in \mathbb{N} \quad (6)$$

obeying the recurrence relation $T_{n+1}(z) = 2zT_n(z) - T_{n-1}(z)$, such that

$$\int_{-1}^1 T_n(z) T_m(z) w(z) dz = \begin{cases} \pi, & n = m = 0 \\ \frac{\pi}{2} \delta_{nm}, & \text{otherwise} \end{cases}$$

Then, analogously to the Padé technique, one can build rational Chebyshev polynomials as ²¹⁾

$$R_{n,m}(z) = \frac{\sum_{i=0}^n a_i T_i(z)}{1 + \sum_{j=1}^m b_j T_j(z)}. \quad (7)$$

2.3 Rational approximations vs standard cosmography

The advantages of rational approximations based on Padé and Chebyshev cosmography with respect to the standard Taylor approach can be verified by testing the effective improvement in terms of stability at high-redshift domains. For instance, taking into account the reference values obtained for the Λ CDM model by assuming $\Omega_{m0} = 0.3$, namely $(q_0, j_0, s_0) = (-0.55, 1, -0.35)$, we show in Figure 1 the significant improvements resulting from the use of the Padé and Chebyshev polynomials as they are able to fairly approximate the Λ CDM luminosity distance at high z , while the accuracy of the Taylor approximation gets worse and worse as soon as $z > 1$ ²¹⁾.

3 Cosmographic parametrization of dark energy

In this section, we provide a first example of application of the cosmographic method. In particular, we shall study the dark energy features in an effective manner by combining kinematic reconstructions and thermodynamic requirements. The constraints coming from the entropy of the universe and the

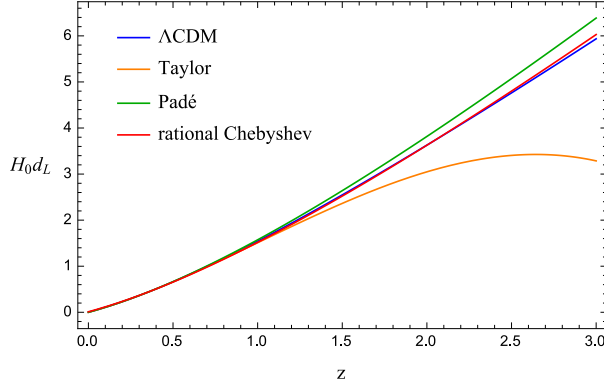


Figure 1: 4th-order Taylor, (2,2) Padé and (2,1) Chebyshev approximations of the luminosity distance compared with the predictions of the Λ CDM model.

properties of the deceleration parameter may allow, in fact, to investigate the cosmic history without assuming any specific underlying cosmology.

Let us consider the relation between the entropy of the apparent horizon and its area:

$$S_h \propto \mathcal{A}_h = 4\pi\tilde{r}_h^2, \quad \tilde{r}_h = (H^2 + ka^{-2})^{-1/2}, \quad (8)$$

and the constraints from the second law of thermodynamics:

$$\mathcal{A}'_h \geq 0, \quad \text{at any time} \quad (9)$$

$$\mathcal{A}''_h < 0, \quad \text{at late times} \quad (10)$$

Recalling the expression of the deceleration parameter, in the case of vanishing spatial curvature ($k = 0$), we have

$$\frac{\mathcal{A}'_h}{\mathcal{A}_h} = \frac{2}{a}(1+q) \geq 0 \implies q \geq -1, \quad \forall z \quad (11)$$

$$\frac{\mathcal{A}''_h}{\mathcal{A}_h} = \frac{2}{a} \left[q' + \frac{2q(1+q)}{a} \right] \underset{a \gg 1}{\sim} \frac{2q'}{a} < 0 \implies \frac{dq}{dz} > 0, \quad z \rightarrow -1 \quad (12)$$

Moreover, a further constraint could be obtained from the observational predictions of structure formation:

$$q \rightarrow \frac{1}{2}, \quad z \gg 1. \quad (13)$$

Now, we consider the (0,1) Padé parametrization of the deceleration parameter relative to the dark energy term,

$$q_{de}(z) = \frac{q_{de,0}}{1 + q_1 z}, \quad (14)$$

guaranteeing the sub-dominant behaviour of dark energy with respect to matter: $q_{de} \rightarrow 0$ as $z \rightarrow \infty$. Hence, imposing the constraints (11), (12) and (13) provides us with a model-independent parametrization of dark energy through the following form of the total deceleration parameter ²⁵⁾:

$$q(z) = \frac{2q_{de,0}(1 - \Omega_{m0})(1 + z + q_{de,0}z) + \Omega_{m0}(1 + z)^3}{2[(1 - \Omega_{m0})(1 + z + q_{de,0}z)^2 + \Omega_{m0}(1 + z)^3]}. \quad (15)$$

The latter leads to

$$H(z) = H_0 \sqrt{\Omega_{m0}(1 + z)^3 + (1 - \Omega_{m0})(1 + z + q_{de,0}z)^2}, \quad (16)$$

which represents a one-parameter extension of the Λ CDM paradigm, recovered in the limit $q_{de,0} \rightarrow -1$. Our model can be recast into dynamical dark energy:

$$\left(\frac{H}{H_0}\right)^2 = \Omega_{m0}(1 + z)^3 + (1 - \Omega_{m0}) \exp \left\{ 3 \int_0^z \frac{1 + w_{de}(z')}{1 + z'} dz' \right\}, \quad (17)$$

where the dark energy equation of state parameter is given by

$$w_{de}(z) = \frac{1}{3} \left[\frac{2q_{de,0}}{1 + z(1 + q_{de,0})} - 1 \right]. \quad (18)$$

The cosmological behaviour of the new dark energy scenario is shown in Figure 2, as a result of a joint analysis of recent observations ²⁵⁾.

4 Cosmographic reconstruction of modified gravity

The cosmographic setups presented above may be employed to reconstruct the gravitational Lagrangian under different modified gravity frameworks starting from first principles. This allows us to investigate the origin of dark energy free of possible biases induced by specific cosmological models. In the following, we use units of $c = 8\pi G = 1$.

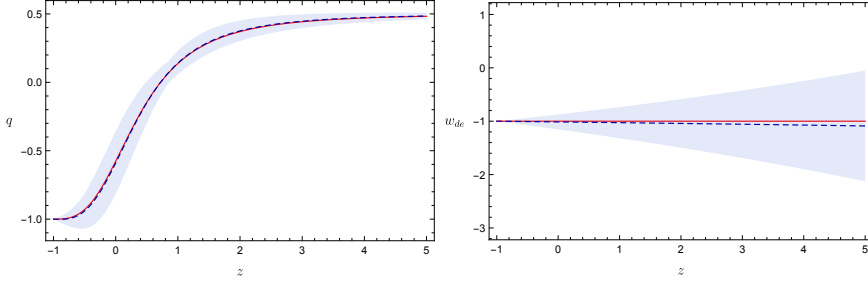


Figure 2: 1σ reconstruction of the deceleration and dark energy equation of state parameters compared to the Λ CDM predictions (red curves).

4.1 The $f(T)$ gravity case

As first application of the cosmographic method, we analyze the universe's dynamics when gravity is mediated by torsion. The geometry needed to describe spacetime makes use of vierbein fields, $e_A(x^\mu)$, which allow to define the metric tensor as $g_{\mu\nu} = \eta_{AB} e^A{}_\mu e^B{}_\nu$, being $\eta_{AB} = \text{diag}(+1, -1, -1, -1)$ the metric of tangent space. Thus, the Lagrangian density of teleparallel equivalent to general relativity (TEGR) can be written as

$$\mathcal{L}_{\text{TEGR}} = T = S_\rho{}^{\mu\nu} T^\rho{}_{\mu\nu}, \quad (19)$$

where T is the torsion scalar, while the torsion tensor is given by $T_{\mu\nu}^\lambda = \hat{\Gamma}_{\mu\nu}^\lambda - \hat{\Gamma}_{\nu\mu}^\lambda = e_A^\lambda (\partial_\mu e_\nu^A - \partial_\nu e_\mu^A)$, being $\hat{\Gamma}_{\mu\nu}^\lambda = e_A^\lambda \partial_\mu e_\nu^A$ the zero-curvature Weitzenböck connection. Here, we have introduced the tensor

$$S_\rho{}^{\mu\nu} = \frac{1}{2} (K^{\mu\nu}{}_\rho + \delta_\rho^\mu T^{\alpha\nu}{}_\alpha - \delta_\rho^\nu T^{\alpha\mu}{}_\alpha), \quad (20)$$

defined in terms of the contortion tensor, $K^{\mu\nu}{}_\rho = -\frac{1}{2} (T^{\mu\nu}{}_\rho - T^{\nu\mu}{}_\rho - T_\rho{}^{\mu\nu})$.

Lagrangian (19) can be also generalized to include a generic function of the torsion scalar, such that the gravitational action reads

$$S = \int d^4x e \left[\frac{f(T)}{2} + \mathcal{L}_m \right], \quad (21)$$

where $e = \sqrt{-g} = \det(e_\mu^A)$, \mathcal{L}_m is the matter field Lagrangian. From the above

action, one can derive the following field equations¹⁴⁾:

$$e_A^\rho S_\rho^{\mu\nu} (\partial_\mu T) f'' + \left[\frac{1}{e} \partial_\mu (e e_A^\rho S_\rho^{\mu\nu}) - e_A^\lambda T^\rho{}_{\mu\lambda} S_\rho{}^{\nu\mu} \right] f' + \frac{1}{4} e_A^\nu f = \frac{1}{2} e_A^\rho T^{(m)}{}_\rho{}^\nu. \quad (22)$$

Assuming the flat FLRW line element, such that $e_A^\mu = \text{diag}(1, a, a, a)$, we obtain the modified Friedmann equations in the form

$$H^2 = \frac{1}{3}(\rho_m + \rho_T), \quad (23)$$

$$2\dot{H} + 3H^2 = -\frac{1}{3}p_T, \quad (24)$$

where non-relativistic matter is assumed to have vanishing pressure and density $\rho_m = 3H_0^2 \Omega_{m0}(1+z)^3$, whereas the torsion contribution is accounted for in

$$\rho_T = T f'(T) - \frac{f(T)}{2} - \frac{T}{2}, \quad p_T = \frac{f - T f'(T) + 2T^2 f''(T)}{2[f'(T) + 2T f''(T)]}. \quad (25)$$

Thus, the combination of the Friedmann equations yields²⁶⁾

$$\left(\frac{df}{dz}\right)^{-1} \left[H(1+z) \frac{d^2 f}{dz^2} + 3f \frac{dH}{dz} \right] = \frac{1}{H} \left(\frac{dH}{dz}\right)^{-1} \left[3 \frac{dH}{dz} + (1+z) \frac{d^2 H}{dz^2} \right], \quad (26)$$

where we converted the derivatives with respect to T into the derivatives with respect to z through $d/dT = -12H(z)H'(z)d/dz$, following by the relation $T = -6H^2$. Combining the latter with the first Friedmann equation provides us with the initial condition $f(z=0) = 6H_0^2(\Omega_{m0} - 2)$. Moreover, we may assume no departures of the effective gravitational constant from Newton's value, leading to the second initial condition $df/dz|_{z=0} = 1$.

Pursuing a model-independent approach, we can adopt the 3rd-order Taylor approximation given by Eq. (3) and the best-fit results $(h, q_0, j_0, s_0) = (0.692, -0.545, 0.776, -0.192)$, where $h \equiv \frac{H_0}{\text{km/s/Mpc}}$, to find $f(z)$ from numerically integrating Eq. (26). Thus, after inverting $H(z)$ by means of $T = -6H^2$ to find $z(T)$, the latter can be inserted back into $f(z)$ to finally get the function $f(T)$ ²⁶⁾. We show the reconstructed behaviour of $f(T)$ in Figure 3.

4.2 The $f(R)$ gravity case

The second application of the cosmographic method we want to discuss concerns $f(R)$ theories, where gravity is induced by non-linear functions of the

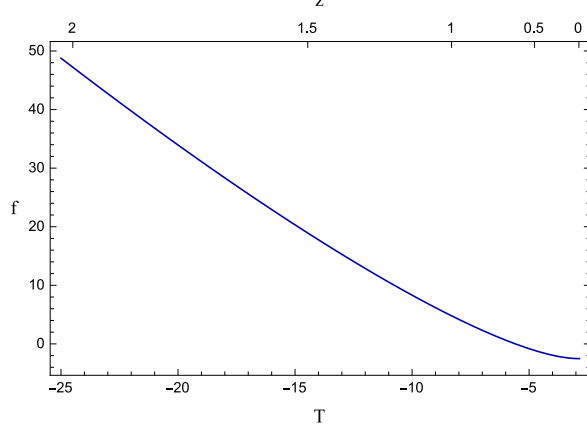


Figure 3: Cosmographic reconstruction of $f(T)$ as a function of the redshift based on the 3rd-order Taylor parametrization.

Ricci curvature, while torsion is vanishing:

$$S = \int d^4x \sqrt{-g} \left[\frac{f(R)}{2} + \mathcal{L}_m \right]. \quad (27)$$

In the metric formalism, the field equations take the form ²⁷⁾

$$R_{\mu\nu} - \frac{1}{2}g_{\mu\nu}R = T_{\mu\nu}^{(m)} + \frac{1}{f'} \left[\frac{1}{2}g_{\mu\nu}(f - Rf') + (\nabla_\mu \nabla_\nu - g_{\mu\nu} \square) f' \right]. \quad (28)$$

For a flat FLRW spacetime and non-relativistic matter fields, the Friedmann equations modify as

$$H^2 = \frac{1}{3} \left[\frac{1}{f'} \rho_m + \rho_{curv} \right], \quad (29)$$

$$2\dot{H} + 3H^2 = -p_{curv}, \quad (30)$$

where the effective curvature density and pressure are give by

$$\rho_{curv} = \frac{1}{f'} \left[\frac{1}{2}(f - Rf') - 3H\dot{R}f'' \right]. \quad (31)$$

$$p_{curv} = \frac{1}{f'} \left[2H\dot{R}f'' + \ddot{R}f'' + \dot{R}^2 f''' - \frac{1}{2}(f - Rf') \right]. \quad (32)$$

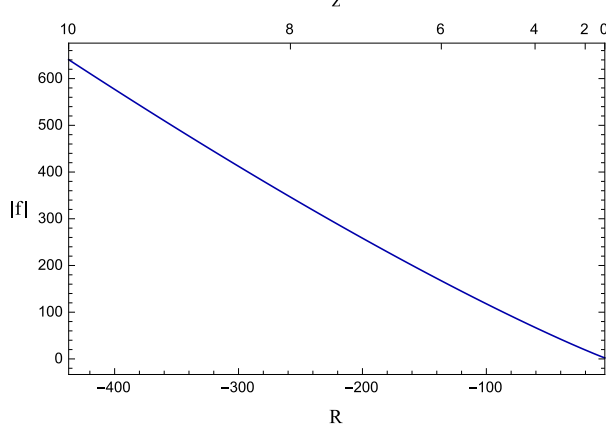


Figure 4: Cosmographic reconstruction of $f(R)$ as a function of the redshift based on the (2,1) Padé parametrization.

In this case, the Hubble parameter is related to the Ricci scalar through $R = -6(\dot{H} + 2H^2)$, which allows to recast the first Friedmann equation as ²⁸⁾

$$\begin{aligned}
H^2 f_z = & \left[-(1+z)H_z^2 + H(3H_z - (1+z)H_{zz}) \right] \times \left[-6H_0^2(1+z)^3\Omega_{m0} - f \right. \\
& - \frac{Hf_z(2H - (1+z)H_z)}{(1+z)H_z^2 + H(-3H_z + (1+z)H_{zz}^2)} - \frac{(1+z)H^2}{[(1+z)H_z^2 + H(-3H_z + (1+z)H_{zz})]^2} \\
& \times \left(f_{zz}((1+z)H_z^2 + H(-3H_z + (1+z)H_{zz})) + f_z(2H_z^2 - 3(1+z)H_zH_{zz} \right. \\
& \left. \left. + H(2H_{zz} - (1+z)H_{zzz})) \right) \right], \tag{33}
\end{aligned}$$

where we have converted the derivatives with respect to R into the derivatives with respect to z by means of $\frac{d}{dR} = \frac{1}{6} \left[(1+z)H_z^2 + H(-3H_z + (1+z)H_{zz}) \right]^{-1} \frac{d}{dz}$. Eq. (33) can be solved with the help of the initial conditions obtained from requiring no deviations from the Newton gravitational constant, i.e., $f_0 = R_0 + 6H_0^2(\Omega_{m0} - 1)$ and $f_z|_{z=0} = R_z|_{z=0}$.

Motivated by the good properties of Padé polynomials, we consider the

(2,1) Padé approximation of the luminosity distance,

$$d(z) \simeq \frac{1}{H_0} \left[\frac{z(6(-1+q_0) + (-5-2j_0+q_0(8+3q_0))z)}{-2(3+z+j_0z) + 2q_0(3+z+3q_0z)} \right], \quad (34)$$

from which we can derive $H(z)$ to be used in Eq. (33) and find $f(z)$ by means of the best-fit values $(h, q_0, j_0) = (0.706, -0.471, 0.593)$. Adopting a similar back-scattering procedure as for the $f(T)$ case, one finds that the analytical function that best-approximates the numerical results is ²⁸⁾ $f(z) = A+Bz^3e^{Cz}$, leading to the $f(R)$ function shown in Figure 4. The same procedure can be utilised to reconstruct the shape of $f(R)$ within the Palatini formalism ²⁹⁾.

4.3 The $f(Q)$ gravity case

A further possibility is to consider gravity as a result of non-metricity, while curvature and torsion are vanishing. In fact, the most general form of affine connections is ³⁰⁾ $\Gamma^\lambda_{\mu\nu} = \{\lambda_{\mu\nu}\} + K^\lambda_{\mu\nu} + L^\lambda_{\mu\nu}$, where $\{\lambda_{\mu\nu}\} \equiv \frac{1}{2} g^{\lambda\beta} (\partial_\mu g_{\beta\nu} + \partial_\nu g_{\beta\mu} - \partial_\beta g_{\mu\nu})$ are the Levi-Civita connections. Here, $K^\lambda_{\mu\nu}$ is the contortion tensor, $L^\lambda_{\mu\nu} \equiv \frac{1}{2} g^{\lambda\beta} (-Q_{\mu\beta\nu} - Q_{\nu\beta\mu} + Q_{\beta\mu\nu})$ is the disformation tensor, and $Q_{\rho\mu\nu} \equiv \nabla_\rho g_{\mu\nu} - \partial_\rho g_{\mu\nu} - \Gamma^\beta_{\rho\mu} g_{\beta\nu} - \Gamma^\beta_{\rho\nu} g_{\mu\beta}$ is the non-metricity tensor ¹⁸⁾. We can thus consider a gravitational action of the form

$$S = \int d^4x \sqrt{-g} \left[\frac{1}{2} f(Q) + \mathcal{L}_m \right], \quad (35)$$

where $f(Q)$ is a generic function of the non-metricity scalar:

$$Q = -\frac{1}{4} Q_{\alpha\beta\mu} Q^{\alpha\beta\mu} + \frac{1}{2} Q_{\alpha\beta\mu} Q^{\beta\mu\alpha} + \frac{1}{4} Q_\alpha Q^\alpha - \frac{1}{2} Q_\alpha \tilde{Q}^\alpha. \quad (36)$$

Hence, the field equations are given as

$$\begin{aligned} & \frac{2}{\sqrt{-g}} \nabla_\alpha \left\{ \sqrt{-g} g_{\beta\nu} f_Q \left[-\frac{1}{2} L^{\alpha\mu\beta} - \frac{1}{8} (g^{\alpha\mu} Q^\beta + g^{\alpha\beta} Q^\mu) + \frac{1}{4} g^{\mu\beta} (Q^\alpha - \tilde{Q}^\alpha) \right] \right\} \\ & + f_Q \left[-\frac{1}{2} L^{\mu\alpha\beta} - \frac{1}{8} (g^{\mu\alpha} Q^\beta + g^{\mu\beta} Q^\alpha) + \frac{1}{4} g^{\alpha\beta} (Q^\mu - \tilde{Q}^\mu) \right] Q_{\nu\alpha\beta} + \frac{1}{2} \delta^\mu_{\nu} f = T^\mu_{\nu}, \end{aligned} \quad (37)$$

where $f_Q \equiv \frac{\partial f}{\partial Q}$. For the line element $ds^2 = -dt^2 + a(t)^2 \delta_{ij} dx^i dx^j$, one finds the following modified Friedmann equations ³¹⁾:

$$6H^2 f_Q - \frac{1}{2} f = \rho, \quad (38)$$

$$(12H^2 f_{QQ} + f_Q) \dot{H} = -\frac{1}{2} (\rho + p). \quad (39)$$

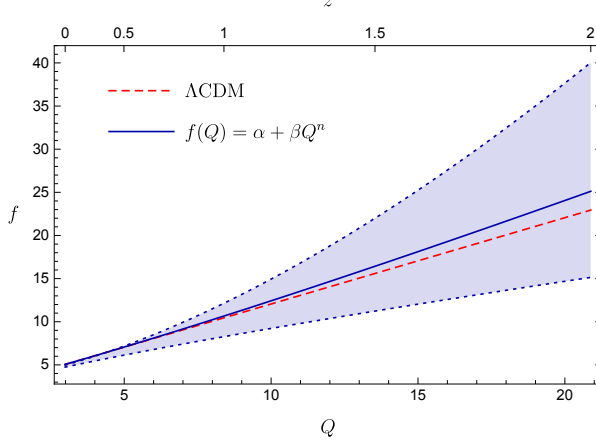


Figure 5: Cosmographic reconstruction of $f(Q)$ compared to the predictions of the concordance Λ CDM cosmology.

Neglecting the pressure of non-relativistic matter, we have $\rho = 3H_0^2\Omega_{m0}(1+z)^3$. In the coincident gauge, where general relativity is recovered in the case $f(Q) = Q$, the relation $Q = 6H^2$ holds true, implying $f_Q = \frac{f'(z)}{12H(z)H'(z)}$. Therefore, the first Friedmann equation can be written as ²⁵⁾

$$\frac{H'(z)}{H(z)} f'(z) - f(z) = 6H_0^2\Omega_{m0}(1+z)^3. \quad (40)$$

If one requires no deviations from Newton's gravitational constant, then $f_Q|_{z=0} = 1$, leading to the initial condition $f_0 = 6H_0^2(2 - \Omega_{m0})$.

Following the analogous strategy as above, we can use the (2,1) Padé parametrization for $H(z)$ along with the observational constraints $h = 0.693 \pm 0.002$, $q_0 = -0.73 \pm 0.13$ and $j_0 = 2.84^{+1.00}_{-1.23}$ to find $f(z)$. Then, we perform a numerical inversion by means of $Q = 6H^2$ to finally get $f(Q)$. In so doing, we find that the best analytical matching is provided by the function $f(Q) = \alpha + \beta Q^n$, with $(\alpha, \beta, n) = (2.492, 0.757, 1.118)$, which show small departures from the standard Λ CDM model ²⁵⁾. However, when taking into account the 1σ uncertainties on the free parameters, $\alpha \in [2.058, 3.162]$, $\beta \in [0.332, 1.076]$ and $n \in [0.821, 1.550]$, we find no statistically significant deviations with respect to the concordance scenario with $\Omega_{m0} = 0.3$ and $h = 0.70$ (see Figure 5).

5 Final remarks

The standard description of the universe based on the Λ CDM cosmology is challenged by long-standing theoretical drawbacks associated to physical interpretation of the cosmological constant and by recent tensions among observations. For this reason, the development of model-independent techniques able to feature the late-time acceleration of the universe becomes crucial in order to discriminate among the plethora of cosmological models proposed over the last years as possible solutions to the dark energy problem.

In this brief report, we provided an outlook on the current status of the cosmographic method. After reviewing the basic principles of cosmography, we focused on the issues limiting the standard approach in the era of precision cosmology. Thus, we discussed the role of rational parametrizations in view of healing the convergence problem related to Taylor series expansions of cosmological distances when dealing with high-redshift data. Specifically, reconstruction techniques relying on Padé and Chebyshev polynomials offer clear advantages in terms of stability and accuracy of cosmographic series including high-order coefficients. Rational cosmography can be used to address dark energy from a model-independent perspective. In particular, the combination of thermodynamic principles and Padé modeling of the deceleration parameter provides us with a cosmological scenario that reproduces the Λ CDM behaviour only under particular limits. This allows us to explore discrepancies with respect to the standard paradigm avoiding biases induced by setting a specific cosmic expansion.

On the other hand, we explored applications of the cosmographic approach to modified gravity scenarios. Under the hypothesis that the current cosmic speed-up may be due to extensions of general relativity, we considered the cosmological consequences of non-linear functions of the Ricci curvature, or gravitational interaction mediated by torsional effects and non-metricity. Thus, we described a back-scattering procedure to reconstruct the $f(R)$, $f(T)$ and $f(Q)$ actions by exploiting the most recent constraints on the cosmographic coefficients. Our results show that the cosmographic method is effective in suggesting the models that better fit to kinematics, although no substantial evidence for deviations from the standard Λ CDM model is highlighted. This is basically due to the elevated uncertainties affecting the cosmographic coefficients of high order that, currently, do not permit to draw any final conclusions.

Therefore, these methods will need to be improved in order to be completely predictive with more stringent observational bounds. This would enable cosmography to shed light on the dark energy nature in view of new and more precise data measurements at high redshifts from future cosmology surveys.

6 Acknowledgements

The authors are thankful to Istituto Nazionale di Fisica Nucleare (INFN), Sezione di Napoli, *iniziative specifiche* QGSKY and MOONLIGHT2 for financial support.

References

1. A. G. Riess *et al.*, *Astron. J.* **116**, 1009 (1998).
2. S. Perlmutter *et al.*, *Astrophys. J.* **517**, 565 (1999).
3. P. J. E. Peebles, B. Ratra, *Rev. Mod. Phys.* **75**, 559 (2003).
4. N. Aghanim *et al.* [Planck], *Astron. Astrophys.* **652**, C4 (2021).
5. S. Weinberg, *Rev. Mod. Phys.* **61**, 1 (1989).
6. S. M. Carroll, *Living Rev. Rel.* **4**, 1 (2001).
7. E. J. Copeland, M. Sami, S. Tsujikawa, *Int. J. Mod. Phys. D* **15**, 1936 (2006).
8. S. Capozziello, R. D'Agostino, O. Luongo, *Phys. Dark Univ.* **20**, 1 (2018).
9. Y. Akrami *et al.* [Planck], *Astron. Astrophys.* **641**, A10 (2020).
10. S. Capozziello, M. De Laurentis, *Phys. Rept.* **509**, 167 (2011).
11. S. Nojiri, S. D. Odintsov, *Phys. Rept.* **505**, 59 (2011).
12. A. A. Starobinsky, *JETP Lett.* **86**, 163 (2007).
13. T. P. Sotiriou, V. Faraoni, *Rev. Mod. Phys.* **82**, 451 (2010).
14. G. R. Bengochea, R. Ferraro, *Phys. Rev. D* **79**, 124019 (2009).
15. E. V. Linder, *Phys. Rev. D* **82**, 109902 (2010).

16. Y. F. Cai, S. Capozziello, M. De Laurentis, E. N. Saridakis, Rept. Prog. Phys. **79**, 106901 (2016).
17. J. Beltrán Jiménez, L. Heisenberg, T. Koivisto, Phys. Rev. D **98**, 044048 (2018).
18. L. Järv, M. Rünkla, M. Saal, O. Vilson, Phys. Rev. D **97**, 124025 (2018).
19. S. Capozziello, R. D'Agostino, O. Luongo, Int. J. Mod. Phys. D **28**, 1930016 (2019).
20. S. Capozziello, R. D'Agostino, O. Luongo, Acta Phys. Polon. Supp. **13**, 271 (2020).
21. S. Capozziello, R. D'Agostino, O. Luongo, MNRAS, **476**, 3924 (2018).
22. C. Cattoen, M. Visser, Class. Quant. Grav. **24**, 5985 (2007).
23. P. K. S. Dunsby, O. Luongo, Int. J. Geom. Meth. Mod. Phys. **13**, 1630002 (2016).
24. A. Aviles, A. Bravetti, S. Capozziello, O. Luongo, Phys. Rev. D **90**, 043531 (2014).
25. S. Capozziello, R. D'Agostino, O. Luongo, Phys. Dark Univ. **36**, 101045 (2022).
26. S. Capozziello, R. D'Agostino, O. Luongo, Gen. Rel. Grav. **49**, 141 (2017).
27. A. De Felice and S. Tsujikawa, Living Rev. Rel. **13**, 3 (2010).
28. S. Capozziello, R. D'Agostino, O. Luongo, JCAP **05**, 008 (2018).
29. S. Capozziello, R. D'Agostino, O. Luongo, Gen. Rel. Grav. **51**, 2 (2019).
30. F. W. Hehl, J. D. McCrea, E. W. Mielke, Y. Ne'eman, Phys. Rept. **258**, 1 (1995).
31. J. Beltrán Jiménez, L. Heisenberg, T. S. Koivisto, S. Pekar, Phys. Rev. D **101**, 103507 (2020).
32. S. Capozziello, R. D'Agostino, Phys. Lett. B **832**, 137229 (2022).

CONSTRAINTS ON DARK MATTER FROM REIONIZATION

Marco Castellano

INAF - Osservatorio Astronomico di Roma, via di Frascati 33, 00078 Monte Porzio Catone (RM), Italy

Nicola Menci

INAF - Osservatorio Astronomico di Roma, via di Frascati 33, 00078 Monte Porzio Catone (RM), Italy

Massimiliano Romanello

INAF - Osservatorio Astronomico di Roma, via di Frascati 33, 00078 Monte Porzio Catone (RM), Italy

Abstract

The abundance of galaxies in the epoch of reionization ($z > 6$) is dependent on fundamental cosmological parameters, most importantly on the properties of dark matter, such that it can be used as a powerful cosmological probe. Here we show how the number density of primordial galaxies allows to constrain the mass of thermal WDM candidates, and the constraints that will be made possible by future JWST observations. We then investigate how the Reionization process is affected by early galaxy formation in different cosmological scenarios. We use a semi-analytic model with suppressed initial power spectra to obtain the UV Luminosity Function in thermal Warm Dark Matter and sterile neutrino cosmologies. For each cosmology, we find an upper limit to fixed f_{esc} , which guarantees the completion of the process at $z < 6.7$. The analysis is tested with two limit hypothesis on high- z ionized hydrogen volume fraction, comparing our predictions with observational results.

1 Introduction

The Epoch of Reionization (EoR) marked a fundamental phase transition in the history of the Universe, during which the Intergalactic Medium (IGM) became transparent to UV photons. The most recent observations indicate a late-Reionization scenario [1–3], with the end of the EoR at $z \approx 6$, but the exact contribution from different ionizing sources and the exact timeline and topology of Reionization are still unknown.

From a theoretical point-of-view, cosmic Reionization depends on non-linear and non-local phenomena, in which the physics of galaxy formation couples with the physics of gravity and radiation transport. The first process is determined by both baryonic physics and poorly known feedback effects, but also by the initial power spectrum of density fluctuations: in fact, dark matter produces the potential wells in which baryonic perturbation undergo an accelerated growth. Therefore, the study of Reionization is strongly related to the comprehension of cosmological framework in which cosmic structures form and grow.

The currently most acknowledged cosmological model is the Λ CDM model. It is based on the contribution of the cosmological constant Λ ($\approx 69\%$) and Cold Dark Matter ($\approx 26\%$) and provides a coherent large-scale description of the Universe with respect to the available data. The Λ CDM model postulates the existence of Dark Matter in a “cold” version, i.e., composed by Weakly Interacting Massive Particles (WIMPs) with $m_X > 0.1$ GeV or condensates of light axions, with $m_X \approx 10^{-5}$ – 10^{-1} eV.

However, there are some possible tensions related to observations at galactic and sub-galactic scales, of the order of kpc. Furthermore, the lack of detection of CDM candidates has suggested the possibility to investigate on alternative cosmological scenarios, based on the existence of Warm Dark Matter particles, with mass of the order of keV. While in the Λ CDM model, due to the high mass particles, all the cosmological density perturbations can become gravitationally unstable, in a WDM scenario, depending on the value of m_X , only perturbations above the kpc scale can collapse, producing shallower density profiles and a smaller number of low-mass halos. This, in the context of the hierarchical growth of the cosmic structures, implies a reduction in the number of faint galaxies and a delay in their formation [4, 5].

In WDM cosmologies, the simplest approach is to consider particles that behave as “thermal relics”, resulting from the freeze-out of DM species initially in thermal equilibrium with the early Universe, e.g. [6, 7]. A possible alternative is offered by sterile neutrinos (SN) or right-handed neutrinos, which are particles predicted in the

context of Standard Model extensions. Since they are produced out-of-equilibrium, from the oscillations of active neutrinos, they are characterized by a non-thermal power spectrum, which depends both on mass and on $\sin(2\theta)$, where θ is the mixing angle [8].

In the present paper we first summarise the results presented in Menci et al. 2016,2017 [4, 9] where stringent constraints on DM models with suppressed power spectra by have been derived by comparing the maximum number density of DM halos $\bar{\phi}$ expected at redshift $z = 6$ to the observed number density ϕ_{obs} of galaxies at the same redshift in the HFF. We then summarise the results presented in [10] on how Reionization scenarios are affected by early galaxy formation in WDM cosmologies. We have used the theoretical model by Menci et al. (2018) [11], where the collapse history of dark matter halos is modelled through the Extended Press-Schechter (EPS) formalism and baryonic processes taking place in each halo are included through physically motivated analytical recipes.

2 Method

2.1 Warm Dark Matter thermal relics

The simplest alternative to CDM is provided by Warm Dark Matter models assuming DM to be the result from the freeze-out of particles with mass in the keV range initially in thermal equilibrium in the early Universe. In these models, the population of low-mass galaxies is characterized by lower abundances and shallower central density profiles compared to Cold Dark Matter (CDM) due to the dissipation of small-scale density perturbations produced by the free-streaming of the lighter and faster DM particles. In this case, the mass of the DM particle completely determines the suppression of the density power spectrum compared to the CDM case

The computation of the halo mass function for the WDM scenario is based on the standard procedure described and tested against N-body simulations. The differential halo mass function (per unit $\log M$) based on the extended Press & Schechter approach [e.g. 12] reads:

$$\frac{d\phi}{d\log M} = \frac{1}{6} \frac{\bar{\rho}}{M} f(\nu) \frac{d\log \sigma^2}{d\log r}. \quad (1)$$

Here $\nu \equiv \delta_c^2(t)/\sigma^2$ depends on the linearly extrapolated density for collapse in the spherical model $\delta_c = 1.686/D(t)$ and $D(t)$ is the growth factor of DM perturbations. A spherical collapse model for which $f(\nu) = \sqrt{2\nu/\pi} \exp(-\nu/2)$ is assumed.

The key quantity entering Eq. 1 is the variance of the linear power spectrum $P(k)$ of DM perturbations (in terms of the wave-number $k = 2\pi/r$). Its dependence on the spatial scale r of perturbations is:

$$\frac{d \log \sigma^2}{d \log r} = -\frac{1}{2\pi^2 \sigma^2(r)} \frac{P(1/r)}{r^3}. \quad (2)$$

In WDM scenarios the spectrum P_{WDM} is suppressed with respect to the CDM case P_{CDM} below a characteristic scale depending on the mass m_X of the WDM particles. In the case of relic thermalized particles, the suppression factor can be parametrized as in Bode et al. 2001 [13]:

$$T_{WDM}(k) = \frac{P_{WDM}(k)}{P_{CDM}(k)} = \left[1 + (\alpha k)^{2\mu}\right]^{-10/\mu}. \quad (3)$$

where $\mu = 1.12$ and the quantity α is linked to the WDM free-streaming scale:

$$\alpha = 0.049 \left[\frac{\Omega_X}{0.25}\right]^{0.11} \left[\frac{m_X}{\text{keV}}\right]^{-1.11} \left[\frac{h}{0.7}\right]^{1.22} \frac{h^{-1}}{\text{Mpc}}, \quad (4)$$

where m_X is the WDM particle mass, Ω_X is the WDM density parameter (Ω_X) and h the Hubble constant in units of 100 km/s/Mpc.

The mass function is computed through Eq. 1 after substituting Eq. 2, with a power spectrum $P(k) = P_{WDM}(k)$ determined by the WDM particle mass m_X after Eqs. 3 and 4. A half-mode wavenumber is defined, as the k_{hm} at which the transfer function $T_{WDM}(k)$ is equal to 1/2 [13, 14]. Correspondingly, a half-mode mass M_{hm} can also be defined:

$$M_{hm} = \frac{4\pi}{3} \rho_m \left[\pi \epsilon (2^{\mu/5} - 1)^{-1/2\mu}\right]^3. \quad (5)$$

2.2 Semi-Analytic Model

To investigate the interplay between WDM scenarios and reionization history, we use the semi-analytic model developed by Menci et al. (2018), to which we refer for further informations [11]. The model retraces the collapse of dark matter halos through a Monte Carlo procedure on the basis of the merging history given by EPS formalism, at $0 < z < 10$ [11]. In this framework, the DM structures formation is determined by the power spectrum: the WDM $P(k)$ is computed by the suppression of the CDM one, due to the particles free streaming at kpc scale, as described in the previous section.

Conversely, for sterile neutrino based cosmological scenarios, we refer to M_{hm} from Lovell et al. (2020), obtained comparing CDM and WDM simulations performed

within the same cosmic volume and in which the parameterization of the WDM halo mass function is given by R_{fit} [15]:

$$R_{fit} = \frac{n_{WDM}}{n_{CDM}} = \left(1 + \left(\alpha \frac{M_{hm}}{M_{halo}} \right)^\beta \right)^\gamma, \quad (6)$$

where n_{CDM} and n_{WDM} are the differential halo mass functions and M_{halo} is the halo-mass. The numerical value of α , β and γ coefficients changes if we consider central ($\alpha = 2.3, \beta = 0.8, \gamma = -1.0$) or satellite halos ($\alpha = 4.2, \beta = 2.5, \gamma = -0.2$) [15].

We perform our analysis with five different sterile neutrino models, with a mass of 7.0 keV, labelled according to the lepton asymmetry number (L_6), which is indicated in the last part of the name. For example, $L_6 = 120$ is named LA120, $L_6 = 8$ is named LA8 and so on. Among them, the models LA9, LA10 and LA11 are based on decaying-particles that are compatible with the X-ray 3.55 keV emission line observed in galaxy clusters [15].

The semi-analytic model associates a galactic luminosity to each halo, depending on cooling process and merging history. The gas in the halo, initially set to have a density given by the universal baryon fraction and to be at the virial temperature, cools due to atomic processes and settles into a rotationally supported disk. Then, the cooled gas is gradually converted into stars, with a SFR given by: $\dot{M}_* = \frac{M_{gas}}{\tau_*}$, according to the Schmidt-Kennicutt law with a gas conversion time scale $\tau_* = q\tau_d$, proportional to the dynamical time scale τ_d through the free parameter q [11]. Moreover, galaxy interactions occurring in the same host halo may induce the sudden conversion of a fraction f of cold gas into stars on a short time-scale given by the duration of the interaction [11]. Feedback phenomena due to supernovae, AGNs and photoionization are also included, as described by Menci et al. (2018) [11]. Finally, the luminosity produced by the stellar populations is computed by assuming a Salpeter IMF [11]. In our analysis, we integrate the rest-frame UV ($\sim 1400 \text{ \AA}$) dust-corrected LF between the limits $M_{UV}^{lim} = [-25, -12]$, in order to obtain the corresponding luminosity density:

$$\rho_{UV} = \int^{M_{UV}^{lim}} dM_{UV} \frac{dN}{dM_{UV}} R_{fit} L_{UV}, \quad (7)$$

which is dominated by the contribution of systems with $M_{UV} \geq -20$ (see Section 3.2).

The number density of UV photons that actively participate to hydrogen ionization process is obtained by multiplying for two quantities [16]:

$$\dot{N}_{ion} = f_{esc} \xi_{ion} \rho_{UV}. \quad (8)$$

The ionizing photon production efficiency (ξ_{ion}) is expressed in $H\text{z}/\text{erg}$ units and it describes how efficiently is possible to get UV ionizing photons from an UV continuum radiation field. Finally, the escape fraction f_{esc} converts the intrinsic ionizing emissivity $\dot{N}_{ion,intrinsic} = \xi_{ion}\rho_{UV}$ into an effective one. It is defined as the fraction of ionizing photons that can escape from the source galaxy instead of being reabsorbed inside it and which therefore actively participates in the ionization of the IGM.

In our study, we model the Reionization history with different values of f_{esc} . Fixed escape fraction is useful to broadly characterize the Reionization history, although a universal value for f_{esc} is highly unrealistic.

Nevertheless, the investigation of the degenerate quantities $f_{esc}\xi_{ion}$, which drive the Reionization process, can yield to interesting upper limits to the escape fraction.

Once obtained \dot{N}_{ion} , the equation that accounts for ionization and recombination, which regulates the evolution of the hydrogen filling fraction Q_{HII} is:

$$\dot{Q}_{HII} = \frac{\dot{N}_{ion}}{\bar{n}_H} - \frac{Q_{HII}}{t_{rec}}, \quad (9)$$

where the comoving hydrogen mean density is computed as $\bar{n}_H \approx 2 \times 10^{-7} (\Omega_b h^2 / 0.022) \text{ cm}^{-3}$ and the recombination time-scale is $t_{rec} \approx 3.2 \text{ Gyr} [(1+z)/7]^{-3} C_{HII}^{-1}$ [17]. We consider case B of recombination, in which electrons fall to the ground level generate ionizing photons that are re-absorbed by the optically thick IGM, having no consequences on the overall ionization balance. We treat the evolution of the clumping factor C_{HII} with redshift, due to the effect of UVB generated by Reionization, according to, e.g., Haardt et al. 2012 [18]:

$$C_{HII} = 1 + 43z^{-1.71}. \quad (10)$$

After the reconstruction of the Reionization history, we use the redshift evolution of the filling fraction to compute the integral:

$$\tau_{es}(z) = c\sigma_T \bar{n}_H \int_0^z Q_{HII}(z')(1+z')^2 \left(1 + \frac{\eta Y}{4X}\right) H^{-1}(z') dz', \quad (11)$$

in which helium is singly-ionized ($\eta = 1$) at $z > 4$ and doubly-ionized ($\eta = 2$) at $z < 4$. Then, the electron scattering optical depth has been compared with observational constraints on τ_{es} obtained, from CMB anisotropy, by Planck and WMAP.

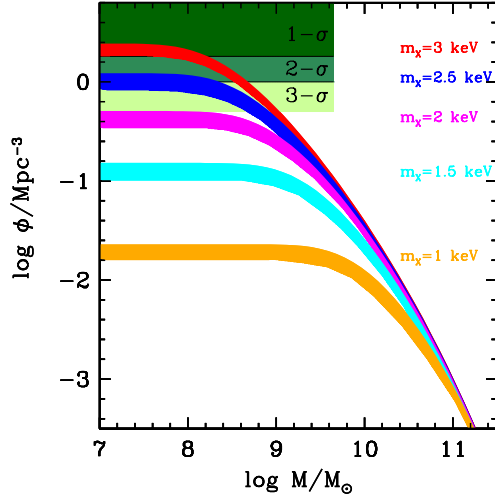


Figure 1: Adapted from Menci et al. 2016 [4]: the cumulative mass functions computed at $z = 6$ for different values of the WDM particle mass m_X from 1 to 3 keV (bottom to top). The shaded areas correspond to the observed number density of HFF galaxies within $1-\sigma$, $2-\sigma$, and $3-\sigma$ confidence levels.

3 Results

3.1 Constraints on thermal WDM from the abundance of high-redshift galaxies

We compare the halo number densities in WDM cosmologies to the observed number density ϕ_{obs} of galaxies derived by integrating the galaxy luminosity function (LF) at $z = 6$ by [19] down to the faintest bin $M_{UV} = -12.5$. Constraints on DM models are simply put by requiring that observed galaxies cannot outnumber their host DM halos ($\bar{\phi} \geq \phi_{obs}$). The reference luminosity function has been estimated from objects in the Abell 2744 and MACS 0416 cluster fields, selected on the basis of their photometric redshift.

In Fig. 1 we show the cumulative mass function $\phi(> M)$ at $z = 6$ for different assumed WDM particle masses. All the mass functions saturate to a maximum number density $\bar{\phi}_{m_X} \approx \phi(M_{hm})$. This is compared with the observed number density ϕ_{obs} of galaxies with $M_{UV} \leq -12.5$. The condition $\phi_{obs} \leq \bar{\phi}_{m_X}$ yields $m_X \gtrsim 2.9$ keV at $1-\sigma$ level, $m_X \gtrsim 2.4$ keV at $2-\sigma$ level, and $m_X \gtrsim 2.1$ keV at $3-\sigma$ level. In Fig. 2 we

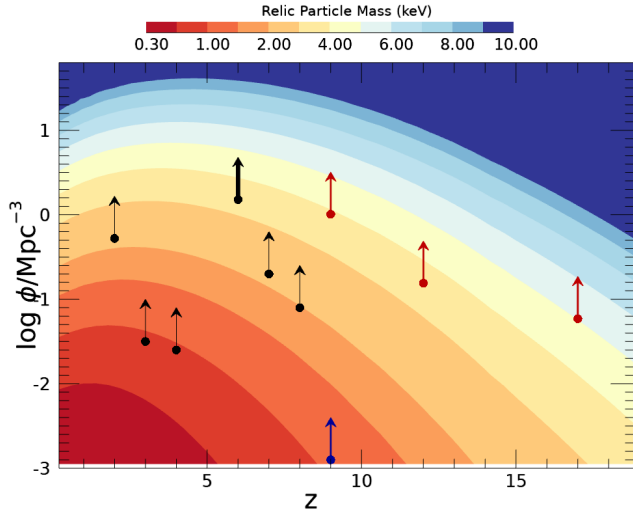


Figure 2: Constraints on the abundance of dark-matter halos derived from the galaxy LF at different redshifts (black arrows). The corresponding limits on the mass of WDM thermal relics are shown as colored contours. JWST measurements reaching $z > 9$ lensed galaxies down to $M_{UV} \leq -12.5$ (red arrows) can significantly strengthen current constraints if no cut-off of the LF will be found.

show the constraints on the thermal relic WDM particle mass from the abundance of galaxies in available observations at $z < 7$, including the quoted constraint from the HFF observations at $z \sim 6$, compared to what could be achieved by hypothetical JWST observations of strongly lensed galaxies at $z > 9$ (red arrows). We derive the estimate by extrapolating to $M_{UV} \leq -12.5$ the UV LF at $z = 9 - 16$ recently published by Harikane et al. 2022 [20]. If JWST will confirm a steep faint-end of the UV LF at extremely high-redshifts, thermal relic particles with masses $m_X < 5$ keV will be ruled out by galaxy abundance measurements alone.

3.2 The reionization history in WDM scenarios

Here we investigate the unfolding of the reionization epoch in WDM cosmologies, summarising the cited work by Romanello et al. 2021 [10].

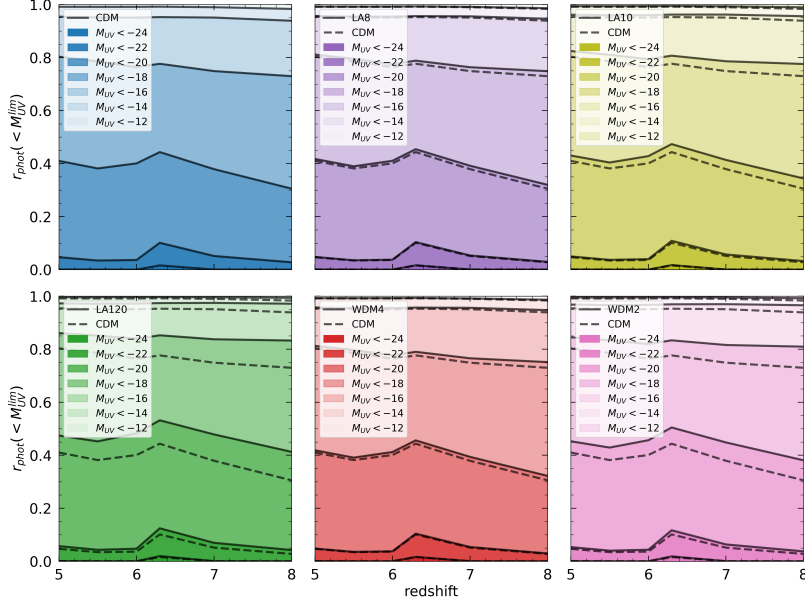


Figure 3: Adapted from Romanello et al. 2021 [10]. The multiple panels show the integrated photons ratio $r_{\text{phot}}(< M_{\text{UV}}^{\text{lim}})$, where $\dot{N}_{\text{ion,tot}}$ is computed by integrating Equation (7) between intrinsic $M_{\text{UV}}^{\text{sup}} = -12$ and $M_{\text{UV}}^{\text{inf}} = -25$. We compare with CDM two thermal WDM cosmologies (WDM3 is an intermediate case between WDM4 and WDM2), and three sterile neutrino cosmologies (here LA10 is the only representative scenario for radiatively decay Dark Matter, which is compatible with the 3.5 keV emission line observed in galaxy clusters).

In Figure 3 we plot the integrated ionizing photons ratio:

$$r_{\text{phot}}(< M_{\text{UV}}^{\text{lim}}) = \frac{\dot{N}_{\text{ion}}(M_{\text{UV}} < M_{\text{UV}}^{\text{lim}})}{\dot{N}_{\text{ion,tot}}} \quad (12)$$

in which we compute $\dot{N}_{\text{ion,tot}}$, using Equation (7) between intrinsic $M_{\text{UV}}^{\text{sup}} = -12$ and $M_{\text{UV}}^{\text{inf}} = -25$, while the numerator is obtained by varying the upper limit of the integral from -24 to -12 , including so the photons from progressively dimmer sources, until the unity is reached.

From Figure 3 we can identify two important features, through which we can understand the role and the different contribution of faint and bright galaxies during EoR. The first is the increasing of the relative contribution of the brightest systems

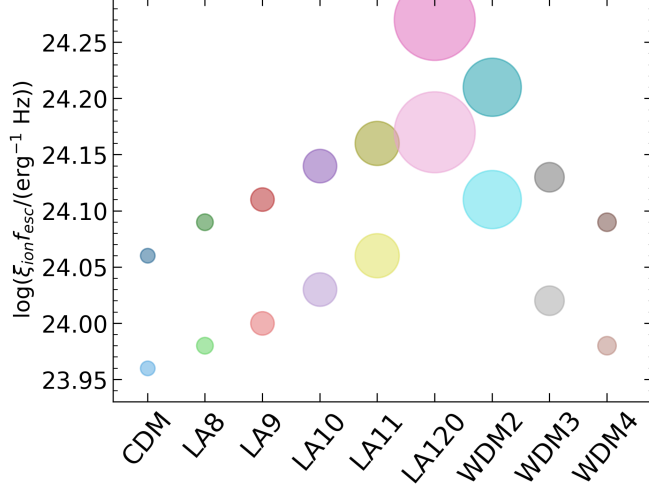


Figure 4: Adapted from Romanello et al. 2021 [10]. The product $\xi_{ion} f_{esc}$ required to ionize the IGM at $z = 6.7$, for a set of different cosmologies. The dot size increases with M_{hm} ; lighter colours refer to initial condition $Q_{HII}(z = 10) = 0.2$, while darker colours are for $Q_{HII}(z = 9) = 0.0$.

(respectively with intrinsic $M_{UV}^{sup} < -24$, $M_{UV}^{sup} < -22$ and $M_{UV}^{sup} < -20$) with the age of universe. In the Λ CDM model, $r_{phot}(< -22)$ passes from 2.8% at $z = 8$, to 10% at $z = 6.3$. In parallel, for $M_{UV}^{sup} = -20$ we have a raise from 31% at $z = 8$ to 44% at $z = 6.3$. We can interpret this trend in the light of the hierarchical growth of cosmic structures: merging phenomena between galaxies give origin to more massive and brighter structures, increasing their overall contribution. However, the role of faint galaxies in the Reionization process is still predominant.

The second issue to be highlighted derives from a comparison between different cosmological scenarios, which reveals that WDM models present a relative \dot{N}_{ion} higher than the CDM ones. Again, the reason resides in the effect of free-streaming, which determines a suppression in the number density of the faint-galaxies and so a decreasing in their relative contribution for each M_{UV}^{sup} . The difference between cosmologies is summarized in the half-mode mass and is not negligible: if we compare CDM with LA8 and WDM4, at $z = 8$ it values $\approx 1-2\%$, respectively for $M_{UV}^{sup} = -20$ and -18 , but it increases to 8 – 10% for WDM2 and LA120. Finally, we noted that the continue (WDM) and the dashed (CDM) lines in Figure 3 approach each other with

time; for example, at $z = 5$ the differences between CDM and WDM2-LA120 reduce respectively to 4–6%. Again, we can interpret this result by looking at the evolution of the UV LFs with z .

The current analysis is based on intrinsic UV luminosity and it is independent from the dust extinction, which is summarized in the escape fraction value: in fact f_{esc} appears only as a multiplicative constant, so it simplifies in the ratio between \dot{N}_{ion} . Conversely, if we consider other escape fraction dependencies (see below), we could expect a more various behaviour.

3.2.1 Implications on f_{esc}

The evolution of the filling fraction with cosmic time depends also on the initial condition for Equation (9). In particular, we choose two extreme possibilities, which are motivated both with model available in literature and with an observational point of view.

The first has $Q_{HII}(z = 10) = 0.2$. This assumption agrees with the 68% credibility interval modelled on the marginalized distribution of the neutral fraction ($1 - Q_{HII}$), from the SFR histories and the Planck constraints on τ_{es} , from Robertson et al. (2015) [26]. Similarly, it is coherent with the range of Q_{HII} allowed for the model by Bouwens et al. (2015), where Reionization is complete between $z = 5.9$ and $z = 6.5$ [27]. As a second possibility, we choose $Q_{HII}(z = 9) = 0.0$, which is preferred by the two hydrogen neutral fraction measurements performed by Mason et al. (2019) and Hoag et al. (2018)[1, 2]. All the others are intermediate cases.

For each of the two initial conditions we compute the number density of ionizing photons \dot{N}_{ion} with different combinations of $\xi_{ion}f_{esc}$, exploring the effect of the parameters degeneracy on the reheating of IGM. Particles free-streaming has consequences on galaxy formation, determining a lack of faint-galaxies which alters the UV LF, with a general reduction in the UV luminosity density in models with a high M_{hm} . Thus, we obtain a delay in the IGM ionizing process, with respect to CDM.

In Figure 4, we show $\log(\xi_{ion}f_{esc})$ in CDM, sterile neutrinos and thermal WDM cosmologies. Due to the great uncertainty on f_{esc} , we searched for the $\xi_{ion}f_{esc}$ values that ensure the completion of Reionization at $z = 6.7$. We note that $\log(\xi_{ion}f_{esc})$ increases with M_{hm} : a larger escape fraction and/or UV photons production efficiency are needed to complete the Reionization process in WDM scenarios. However, the quantity ξ_{ion} is better constrained than f_{esc} , so we assume from the literature a fiducial value of $\log(\xi_{ion}/(erg^{-1}Hz)) = 25.2$ [16, 27], as expected from a low metallicity

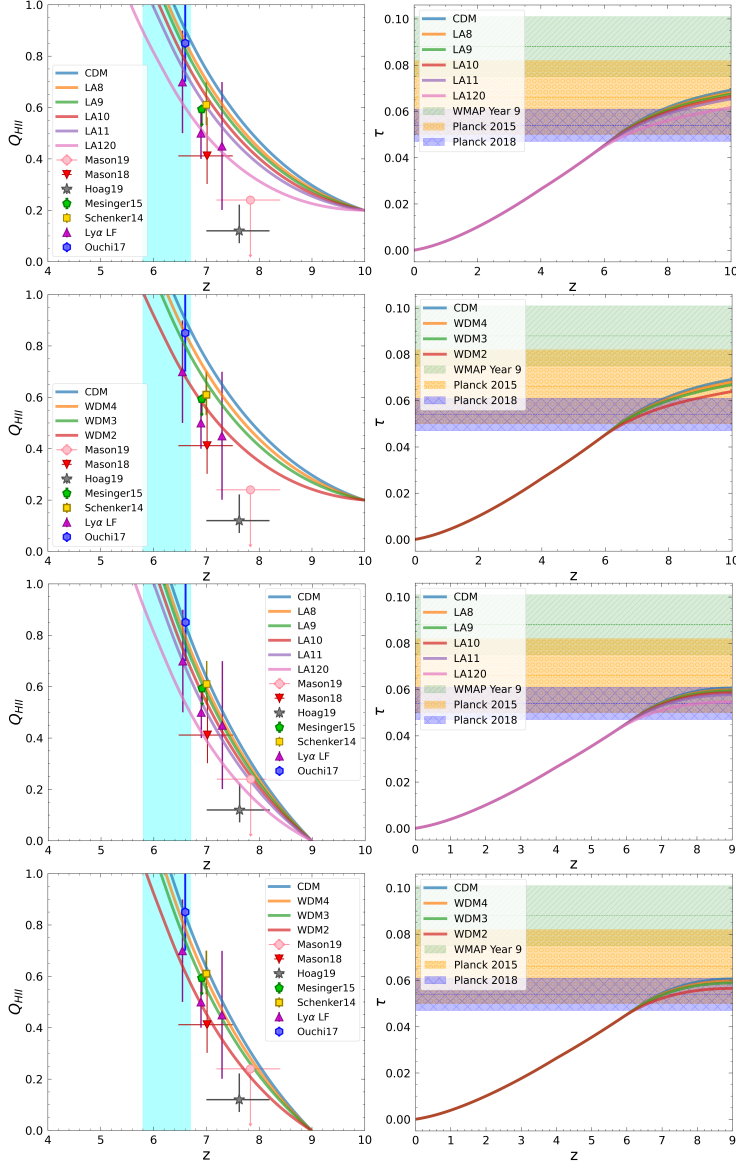


Figure 5: Adapted from [10]. **Left:** evolution of the filling fraction Q_{HII} , for sterile neutrino and thermal WDM models, with $\log(\xi_{\text{ion}}/(\text{erg}^{-1}\text{Hz})) = 25.2$. The two upper panels have initial condition $Q_{\text{HII}}(z = 10) = 0.2$ and $f_{\text{esc}} = 0.05$. The two lower panels are plotted with $Q_{\text{HII}}(z = 9) = 0.0$ and $f_{\text{esc}} = 0.06$. The cyan shaded region indicates our fiducial late-Reionization redshift interval, $5.8 < z < 6.7$. The upward triangle labelled Ly α LF includes results by Konno et al. (2014), Konno et al. (2017) and Zheng et al. (2017) [21–23]. **Right:** electron scattering optical depth for different models, compared with measurements from Planck and WMAP [3, 24, 25].

single-star population. This value is coherent with the Salpeter IMF assumed in the semi-analytic model [26]. We did not investigate the variation of ξ_{ion} with redshift and M_{UV} , which we have considered negligible with respect to changes in escape fraction. Similarly, we have neglected the variation with galaxy age. These hypotheses allow us to set an upper limit to f_{esc} for each different WDM particle and boundary condition. In general, models that start from $Q = 0$ need a higher f_{esc} value to ionize the IGM within the same z range. For this reason they are more inclusive and result in a weaker constraint to the admitted escape fraction. If $f_{esc} > f_{esc}^{sup}$, Reionization process is completed outside the fiducial redshift interval.

The evolution of the filling fraction Q_{HII} in the various cosmological models and for different assumptions is summarised in Fig. 5.

4 Conclusions

In this paper we have first summarised the results presented in Menci et al. 2016, 2017 [4, 9] putting stringent constraints on DM models with suppressed power spectrs. The comparison of the predicted maximum number density of DM halos $\bar{\phi}$ to the observed number density ϕ_{obs} provide robust constraints through the simple condition that observed galaxies cannot outnumber their host DM halos ($\bar{\phi} \geq \phi_{obs}$). Remarkably, these constraints are conservative, and independent of the modeling of baryonic physics in low-mass galaxies. The mass of WDM thermal relic candidates is constrained to be $m_X \geq 2.9$ keV at 1σ confidence level, and $m_X \geq 2.4$ keV at $2 - \sigma$ level. by have been derived by comparing the maximum number density of DM halos $\bar{\phi}$ expected at redshift $z = 6$ to the observed number density ϕ_{obs} of galaxies at the same redshift in the HFF.

We have then summarised the results presented in [10] on how Reionization scenarios are affected by early galaxy formation in WDM cosmologies. We have used the semi-analytic model described by Menci et al. (2018) [11], to produce the UV LF in a Λ CDM framework. We have tested some Λ WDM cosmologies, in which the contribution of the faint galaxies is suppressed: in particular, we have focused on five sterile neutrino models presented in Lovell et al. (2020) [15], and three thermal WDM models with $m_X = 2-3-4$ keV. In both cases, we have found that a higher M_{hm} leads to a general delay in the Reionization process. In CDM cosmology, merging between galaxies determines the rise of the intrinsic $M_{UV} < -20$ systems relative contribution to the ionizing photons budget, from $\approx 30\%$ to $\approx 45\%$ between $6.3 < z < 8$. In the WDM case, the particles free-streaming yields to a shift towards brighter sources and

$r_{phot}(M_{UV} < -20)$ undergoes a further 1–10% growth, depending on cosmology; We found that in WDM cosmologies a higher $f_{esc\xi_{ion}}$ is required, in order to complete the Reionization process at the same redshift.

The most important limits to our analysis are related to observational uncertainties. We expect significant advances thanks to improved constraints on the UV LF at very high-redshift made possible by forthcoming JWST surveys.

References

1. Hoag, A. *et al.* Constraining the Neutral Fraction of Hydrogen in the IGM at Redshift 7.5. *The Astrophysical Journal* **878**, 12. <https://doi.org/10.3847/1538-4357/ab1de7> (June 2019).
2. Mason, C. A. *et al.* Inferences on the timeline of reionization at $z \sim 8$ from the KMOS Lens-Amplified Spectroscopic Survey. *Monthly Notices of the Royal Astronomical Society* **485**, 3947–3969. ISSN: 0035-8711. <https://doi.org/10.1093/mnras/stz632> (Mar. 2019).
3. Planck Collaboration. Planck 2018 results - VI. Cosmological parameters. *A&A* **641**, A6. <https://doi.org/10.1051/0004-6361/201833910> (2020).
4. Menci, N., Grazian, A., Castellano, M. & Sanchez, N. G. A Stringent Limit on the Warm Dark Matter Particle Masses From the Abundance of $z=6$ Galaxies in the Hubble Frontier Fields. *The Astrophysical Journal* **825**, L1. <https://doi.org/10.3847/2041-8205/825/1/11> (June 2016).
5. Dayal, P., Mesinger, A. & Pacucci, F. Early Galaxy Formation in Warm Dark Matter Cosmologies. *The Astrophysical Journal* **806**, 67. <https://doi.org/10.1088/0004-637x/806/1/67> (June 2015).
6. Viel, M., Becker, G. D., Bolton, J. S. & Haehnelt, M. G. Warm dark matter as a solution to the small scale crisis: New constraints from high redshift Lyman- α forest data. *Phys. Rev. D* **88**, 043502. <https://link.aps.org/doi/10.1103/PhysRevD.88.043502> (4 Aug. 2013).
7. Corasaniti, P., Agarwal, S., Marsh, D. & Das, S. Constraints on dark matter scenarios from measurements of the galaxy luminosity function at high redshifts. *Physical Review D* **95**. ISSN: 2470-0029. <http://dx.doi.org/10.1103/PhysRevD.95.083512> (Apr. 2017).
8. Merle, A. *keV sterile neutrino Dark Matter* 2017. arXiv: 1702.08430 [hep-ph].
9. Menci, N. *et al.* Fundamental Physics with the Hubble Frontier Fields: Constraining Dark Matter Models with the Abundance of Extremely Faint and Distant Galaxies. *The Astrophysical Journal* **836**, 61. arXiv: 1701.01339 [astro-ph.CO] (Feb. 2017).

10. Romanello, M., Menci, N. & Castellano, M. The Epoch of Reionization in Warm Dark Matter Scenarios. *Universe* **7**, 365. arXiv: 2110.05262 [astro-ph.CO] (Sept. 2021).
11. Menci, N. *et al.* Galaxy Formation in Sterile Neutrino Dark Matter Models. *The Astrophysical Journal* **854**, 1. arXiv: 1801.03697 [astro-ph.CO] (Feb. 2018).
12. Bond, J. R., Cole, S., Efstathiou, G. & Kaiser, N. Excursion Set Mass Functions for Hierarchical Gaussian Fluctuations. *The Astrophysical Journal* **379**, 440 (Oct. 1991).
13. Bode, P., Ostriker, J. P. & Turok, N. Halo Formation in Warm Dark Matter Models. *The Astrophysical Journal* **556**, 93–107. <https://doi.org/10.1086/321541> (July 2001).
14. Schneider, A., Smith, R. E., Macciò, A. V. & Moore, B. Non-linear evolution of cosmological structures in warm dark matter models. *Monthly Notices of the Royal Astronomical Society* **424**, 684–698. ISSN: 0035-8711. <https://doi.org/10.1111/j.1365-2966.2012.21252.x> (July 2012).
15. Lovell, M. R. Toward a General Parameterization of the Warm Dark Matter Halo Mass Function. *The Astrophysical Journal* **897**, 147. <https://doi.org/10.3847/1538-4357/ab982a> (July 2020).
16. Finkelstein, S. L. *et al.* Conditions for Reionizing the Universe with a Low Galaxy Ionizing Photon Escape Fraction. *The Astrophysical Journal* **879**, 36. <https://doi.org/10.3847/1538-4357/ab1ea8> (July 2019).
17. Lapi, A. & Danese, L. Cold or warm? Constraining dark matter with primeval galaxies and cosmic reionization after Planck. *Journal of Cosmology and Astroparticle Physics* **2015**, 003–003. ISSN: 1475-7516. <http://dx.doi.org/10.1088/1475-7516/2015/09/003> (Sept. 2015).
18. Haardt, F. & Madau, P. Radiative Transfer in a Clumpy Universe. IV. New Synthesis Models of the Cosmic UV/X-Ray Background. *The Astrophysical Journal* **746**, 125. <https://doi.org/10.1088/0004-637x/746/2/125> (Feb. 2012).
19. Livermore, R. C., Finkelstein, S. L. & Lotz, J. M. Directly Observing the Galaxies Likely Responsible for Reionization. *The Astrophysical Journal* **835**, 113. <https://doi.org/10.3847/1538-4357/835/2/113> (Jan. 2017).
20. Harikane, Y. *et al.* A Comprehensive Study on Galaxies at $z=9-17$ Found in the Early JWST Data: UV Luminosity Functions and Cosmic Star-Formation History at the Pre-Reionization Epoch. *arXiv e-prints*, arXiv:2208.01612. arXiv: 2208.01612 [astro-ph.GA] (Aug. 2022).

21. Konno, A. *et al.* Accelerated Evolution of the Ly Luminosity Function at $z \gtrsim 7$ Revealed by the SUBARU Ultra-Deep Survey for Ly Emitters at $z = 7.3$. *The Astrophysical Journal* **797**, 16. <https://doi.org/10.1088/0004-637x/797/1/16> (Nov. 2014).
22. Konno, A. *et al.* SILVERRUSH. IV. Ly α luminosity functions at $z = 5.7$ and 6.6 studied with ≈ 1300 Ly α emitters on the $14\text{--}21$ deg 2 sky. *Publications of the Astronomical Society of Japan* **70**, S16. issn: 0004-6264. <https://doi.org/10.1093/pasj/psx131> (Dec. 2017).
23. Zheng, Z.-Y. *et al.* First Results from the Lyman Alpha Galaxies in the Epoch of Reionization (LAGER) Survey: Cosmological Reionization at $z \sim 7$. *The Astrophysical Journal* **842**, L22. <https://doi.org/10.3847/2041-8213/aa794f> (June 2017).
24. Planck Collaboration. Planck 2015 results - XIII. Cosmological parameters. *A&A* **594**, A13. <https://doi.org/10.1051/0004-6361/201525830> (2016).
25. Hinshaw, G. *et al.* Nine-Year Wilkinson Microwave Anisotropy Probe (WMAP) Observations: Cosmological Parameter Results. *The Astrophysical Journal Supplement Series* **208**, 19. <https://doi.org/10.1088/0067-0049/208/2/19> (Sept. 2013).
26. Robertson, B. E., Ellis, R. S., Furlanetto, S. R. & Dunlop, J. S. Cosmic Reionization and Early Star-Forming Galaxies: a Joint Analysis of New Constraints from Planck and the Hubble Space Telescope. *The Astrophysical Journal* **802**, L19. <https://doi.org/10.1088/2041-8205/802/2/119> (Apr. 2015).
27. Bouwens, R. J. *et al.* Reionization After Planck: the Derived Growth of the Cosmic Ionizing Emissivity now Matches the Growth of the Galaxy UV Luminosity Density. *The Astrophysical Journal* **811**, 140. <https://doi.org/10.1088/0004-637x/811/2/140> (Sept. 2015).

A review of multiple dark matter signatures: indirect searches and machine learning.

Viviana Gammaldi, Jaume Zuriaga-Puig

December 29, 2022

Abstract

What is Dark Matter (DM) and how it manifests besides the gravitational evidences? This is one of the most intriguing open question in cosmology and particle physics so far. In this invited contribution to the 2021 edition of the Vulcano Workshop, we briefly review the indirect searches for multiple DM signatures in astrophysical targets. We review the multi-messenger and multi-wavelength approach to the indirect detection of Weakly Interacting Massive Particles (WIMPs), with a particular focus on the log-parabola data-driven approach for ML application.

1 Introduction

For more than 50 years now, Dark Matter (DM) has been escaped researchers all around the world. DM represents more than 27% of the total content of the universe, yet no one has managed to find any trace of its existence beyond the well-known gravitational effects. One of the main problems is that we do not know what it is made of. Many candidates have been proposed during the years (see e.g. [1, 2]). Among other candidates, Weakly Interacting Massive Particles (WIMPs) represent an elegant way of explaining the existence of the cold DM (CDM) component of the Universe, by considering that any unknown elementary particle must exist beyond the Standard Model (SM) of particle physics. The CDM WIMP candidates would allow to solve open questions in both SM physics and cosmology [3]. The existence of such WIMPs may be proved through different types of experiments. A trace of the scattering of light WIMPs with atoms of the SM, is expected in direct searches with underground laboratories [4]. A missing energy is expected in the products of the collision e.g. of two protons in particle accelerators, as a signature of DM particle of masses up to a few TeV [5]. Among other WIMP candidates, the supersymmetric (SUSY) models benefits of strong approval for years. Nonetheless, null result of the Large Hadron Collider (LHC) below the TeV energy scale has - at least -

weakened the popularity of that models. Many other theoretical models could justify the existence of DM candidates at the TeV scale (see e.g. Brane world DM [6], Feebly Interacting Massive Particle [7] and superWIMP [8]). Indirect detection allows to search for WIMP candidates of a broad range of energy up to hundreds of TeV, by studying the flux of astrophysical targets [9]. Although, not all the DM candidates have an expected signature in the framework of indirect detection.

In these proceedings we focus on multiple signatures of WIMP candidates. In Section 2, we review the fundamental equations for both the multi-messenger and multi-wavelength approach to WIMP searches. In Section 3, we discuss a data-driven approach adopted to introduce the WIMP candidate as a theoretical data sample in machine learning analyses. We also show an example of the validity of such first-level approximation. Finally, we trace the conclusion of this proceedings in Section 4.

2 Multiple WIMP signatures

In the most general approach, the secondary emission expected by annihilation or decay events of WIMPs in any astrophysical source is given by:

$$\frac{d\Phi_{\text{DM}}}{dE}(E, \Delta\Omega, l.o.s.) = P(E) \times J_g(\Delta\Omega, l.o.s.). \quad (1)$$

The $P(E)$ and $J_g(\Delta\Omega, l.o.s.)$ are the particle physics factor (or source term) and the generalized astrophysical factor, respectively. The specific expression of each of those factors depends on the particular case of interest, as we explain in the following lines. In Fig. 1, we schematically show the WIMP annihilation process (i.e. the P-factor). By each annihilation event, WIMPs produce a couple of SM particle-antiparticle (i.e. leptons, quarks or bosons) which decay and hadronization processes generate fluxes of secondary particles, e.g. gamma rays, neutrinos, matter-antimatter (electron-positron, proton-antiproton, etc...). These fluxes may be observed by detectors on satellites [10, 11] or ground-based Cherenkov telescopes [12, 13, 14, 15]. Each of this particle is considered to be a *messenger* of the information on the nature of the WIMP candidate, i.e. its mass and interaction with the SM particles. In fact, given a WIMP mass and interaction (i.e. a specific DM candidate), the products of the annihilation process are well defined SM particles. SM hadronization and decay processes can produce fluxes of secondary particles, whose spectral shape depends on the first SM channel produced in the WIMP annihilation process. Therefore, the so-called *multi-messenger approach* refers to searching for multiple signatures

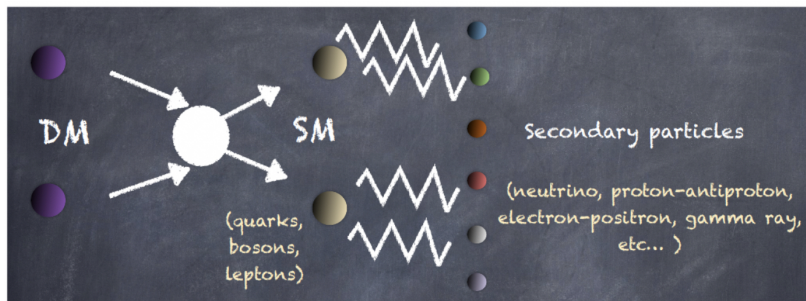


Figure 1: Illustrative schematization of the WIMP annihilation process happening in any astrophysical object dominated by a DM content, e.g. dwarf spheroidal galaxies [18, 19], dwarf irregular galaxies [20, 21], Galactic center [15, 22, 23], galaxy clusters [24]. See text for further details.

of DM candidates in several fluxes of secondary astroparticles. Furthermore, charged particles produced by WIMP annihilation events interact with the magnetic field in our Galaxy or in the emitting source, producing a broad spectra of electromagnetic emission, via e.g. synchrotron emission, inverse Compton, Bremsstrahlung, Coloumb interaction. In this case, the P-factor is indeed the source term of a diffusion equation, which final electromagnetic emission can be detected by several telescope, e.g. with interferometric technique of the Square Kilometer Array (SKA) [16, 17]. In this case, searching for multiple signatures of the same WIMP candidate through several electromagnetic emission is called *multi-wavelength approach*.

Finally, the J_g -factor is defined by the astrophysical target, i.e. the DM dominated astrophysical object where the WIMP annihilation/decay process is happening, e.g. dwarf galaxies [18, 19, 20, 21], the Galactic center [15, 22, 23], galaxy clusters [24]. Indeed, the J_g -factor is the normalization factor, which depends on the amount of DM in the astrophysical target. The calculation of this J_g -factor represents the highest source of uncertainty in indirect searches [25]. Nonetheless, in this proceeding, we focus on the P-factor and related uncertainty.

2.1 Multi-messenger approach

The multi-messenger nature of the indirect searches can be made explicit by rewriting the Eq. 1 as:

$$\frac{d\Phi_{\text{sp-DM}}}{dE} = \frac{\eta_{\text{sp}}}{4\pi} \sum_{a=1}^2 J_{\text{g-sp}}^{(a)} \cdot \sum_j^{\text{SM channels}} \frac{\zeta_j^{(a)}}{\delta m_{\text{DM}}^a} \frac{dN_{(\text{sp})}^j}{dE} \quad (2)$$

This equation describes the expected flux of secondary particles produced by DM annihilation and decay events. The η_{sp} parameter is related to both the propagation or deviation of the observed particle¹; a is related to the DM event: $a = 1$ is for DM decay and $a = 2$ is for DM annihilation. The astrophysical factor $J_{\text{g-sp}}^{(a)}$ is given by the integration along the line of sight of the DM density distribution in the target: in case of DM decay $J_{\text{g-sp}}^{(1)} \propto \rho_{DM}$ and for DM annihilation $J_{\text{g-sp}}^{(2)} \propto \rho_{DM}^2$. The SM channels (quarks, bosons or leptons) are the products of DM decay or annihilation: the branching ratios of production $Br_j = \zeta_j^{(a=2)} / \langle \sigma v \rangle$ or $Br_j = \zeta_j^{(a=1)} \tau_{\text{decay}}^{-1}$ is the probability of annihilation/decay in each SM channel. In the model independent approach for thermal WIMPs, the WIMP candidates annihilate (decay) into one SM channel with 100% of probability ($Br = 1$), i.e. $\zeta_j^{(a=2)} = \langle \sigma v \rangle$ ($\zeta_j^{(a=1)} = \tau_{\text{decay}}^{-1}$). Instead, in a model dependent approach, the combination of different SM channels and their branching ratios depends on the specific WIMP candidate. Finally, $\frac{dN_{\text{sp}}^j}{dE}$, is the differential flux of secondary particles expected by each DM annihilation or decay event. It depends on the SM channel and it is generally computed with Monte Carlo events generator software. More details on Eq. 2 can be found in [26], with a particular focus on the Galactic Very Inner Region (VIR) and the multi-TeV WIMP candidate.

2.2 Multi-wavelength approach

In this section we briefly introduce the reader to the connection between multi-messenger and multi-wavelength signals from WIMP annihilation events. During the transport of the secondary cosmic rays in the galactic environment, the deflection of charged particles by the galactic magnetic field would result in the emission of electromagnetic radiation. In the case of ultra-relativistic particles, the emission is produced through synchrotron radiation in a continuous frequency range. Indeed, ultra-relativistic e^+/e^- are responsible for a large number of signatures in the sky, being the synchrotron emission one of the main mechanisms of energy losses. Such an e^+/e^- propagation is dominated by the diffusion equation:

$$-\nabla \cdot [D(\mathbf{r}, E) \nabla \psi] - \frac{\partial}{\partial E} [b(\mathbf{r}, E) \psi] = Q_e(\mathbf{r}, E) \quad (3)$$

where $D(\mathbf{r}, E)$ is the diffusion coefficient, $\nabla \psi$ is the number density of charged particles after propagation, $b(\mathbf{r}, E)$ is the energy loss term, and $Q_e(\mathbf{r}, E)$ is the source term. If the primary source of injected electrons is the annihilation of WIMPs, the source term is given by:

¹E.g. $\eta_\gamma \approx 1$ for a gamma ray, which travels undeflected in the local Universe

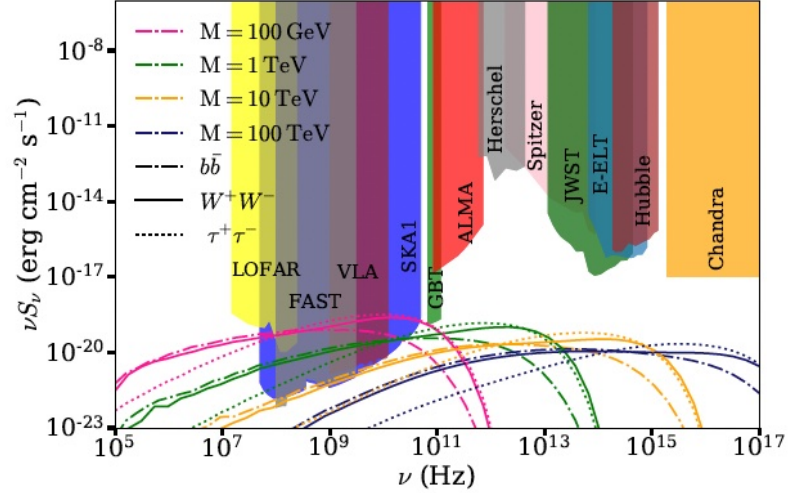


Figure 2: Flux density for a Draco-like dSph in the range of frequencies $10^5 - 10^{17}$ Hz as produced by the Synchrotron emission of secondary e^+e^- for different DM masses and annihilation channels. Colour bands represent the sensitivity regions of several detectors. Targets with a radio signal boost mechanism could improve the competitiveness of these detectors. Figure from [16].

$$Q_e(\mathbf{r}, E) = \frac{1}{2} \langle \sigma v \rangle \left(\frac{\rho_{\text{DM}}(\mathbf{r})}{M} \right)^2 \sum_j \beta_j \frac{dN_e^j}{dE}. \quad (4)$$

The diffusion Eq. 3 is a simplification of the Ginzburg-Syrovatsky transport equation. The latter takes into consideration some other mechanisms such as re-acceleration of cosmic rays (negligible in the case of ultra-relativistic e^+/e^-), spallation of cosmic rays, radioactive decay of nuclei of the interstellar medium as well as eventual interactions with the galactic wind [16, 17]. Indeed, the multi-wavelength approach is also affected by the uncertainty in the description of the galactic and extra-galactic magnetic field. In Fig. 2 [16], we show the multi-wavelength Synchrotron emission produced in the range of frequencies $10^5 - 10^{17}$ Hz by secondary e^+e^- produced by several WIMPs masses and annihilation channels. WIMP candidates at GeV energy scale are suitable to be detected in radio frequencies, yet TeV DM would be better detected at higher frequencies. Even though SKA1 exhibits a competitive sensitivity to measure signatures of WIMPs up to 10 TeV (yellow lines), for heavier TeV WIMPs, the maximum of emission shifts to frequencies higher than the SKA1 range.

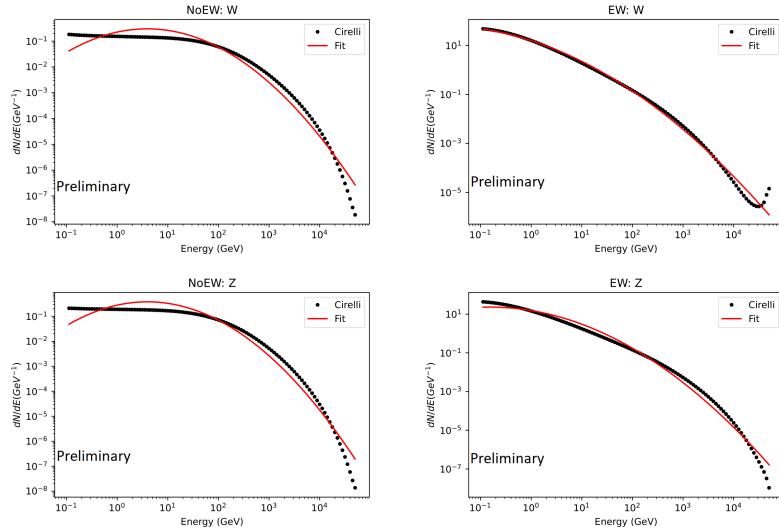


Figure 3: LP fits of the gamma-ray flux simulated with `PYTHIA 8` for a WIMP mass of 50 TeV, annihilating 100% in W^+W^- or ZZ with (EW) or without (NoEW) the electroweak contribution. The values of the parameters can be found in Tab. 1.

3 WIMP signatures and machine learning

In the benchmark data-fitting approach, any detected spectra of both astroparticles or electromagnetic emission is fitted via the differential flux expected by WIMP annihilation events. Indeed, the spectral shape is fixed by the WIMP mass while the amplitude of the signal is a degenerate case of both the astrophysical J-factor and e.g. the annihilation cross section (see Eq. 2). Moreover, an uncertainty on the amplitude is introduced by the multiplicity of secondary particles produced in each annihilation event, which changes with the Monte Carlo event generator software [27]. In [28] a new approach to search for WIMP signatures among a sample of detected but unidentified sources² is proposed. The latter is inspired by the data-driven Log Parabola (LP) first fit of any detected source of the Femi-LAT catalogues [29, 30, 31]:

$$\frac{dN}{dE} = N_0 \left(\frac{E}{E_0} \right)^{-\alpha - \beta \cdot \log(E/E_0)} \quad (5)$$

where N_0 is the gamma-ray flux normalization, E_0 the pivot energy, α the gamma-ray spectral index and β the curvature. Note this parametric form is reduced to a simple power law in the case of $\beta = 0$. From this expression we

²Indeed, those sources without any association with known astrophysical sources.

can extract a useful parameter: the peak energy, E_{peak} , i.e., the energy at which the energy spectrum ($E^2 dN/dE$) is maximum, by performing the consequent derivative, obtaining $E_{\text{peak}} = E_0 \cdot e^{\frac{2-\alpha}{2\beta}}$, which represents a signature of different kind of emitting sources.

Parameters	Z - EW	Z - NoEW	W - EW	W - NoEW
E_{Peak} (TeV)	0.8 ± 0.3	1.9 ± 0.5	5 ± 2	2.4 ± 0.7
α	0.44 ± 0.04	-0.45 ± 0.05	0.67 ± 0.03	-0.43 ± 0.05
β	0.116 ± 0.004	0.16 ± 0.08	0.078 ± 0.003	0.156 ± 0.005

Table 1: Value of the relevant parameters for the LP fits of the gamma-ray flux simulated with `PYTHIA 8` for a WIMP mass of 50 TeV, annihilating 100% in W^+W^- or ZZ with (EW) or without (NoEW) the electroweak contribution.

In [28, 32] the gamma-ray spectra obtained in the PPPC4DMID [33] for several DM masses and annihilation channels are fitted with a LP, obtaining the same characterization in the parameter space defined by the observational LP modelling. In Tab. 1 and Fig. 3 we show the gamma-ray flux produced by the PPPC4DMID for a WIMP mass of 50 TeV annihilating into W^+W^- (upper panels) and ZZ (lower panels) channels, without the ElectroWeak (EW) corrections (left panels) and by including the EW corrections (right panels). In the left upper panel of Fig. 4 we show the E_{peak} , β parameters resulting of the LP fitting of a combination of W^+W^- and ZZ annihilation channels:

$$\frac{dN}{dE} = B_r \left(\frac{dN}{dE} \right)_Z + (1 - B_r) \left(\frac{dN}{dE} \right)_W, \quad (6)$$

where the branching ratio B_r goes from 0 to 1 with a 0.1 step. In the right upper panel of Fig. 4 we show the relative uncertainty ϵ_β/β . In the lower left and right panels we show the same procedure by including the EW contribution.

This LP approach allows to search for DM candidates in a broad sample of sources, by applying Machine Learning (ML) algorithms, e.g. an artificial Neural Network (NN) [28]. Within this approach, E_{peak} and β are features for the ML algorithm. In [28] it is also shown that the overall classification accuracy can be improved by including systematic features, which allow to model instrumental systematic uncertainty for the expected DM class. Without entering into the details of that work, in this proceeding we have just introduced the LP data-driven approach for indirect searches of WIMPs by reproducing part of that procedure. Moreover, we also include new preliminary results: the black point in Fig. 4 is indicative of the E_{peak} and β parameters obtained by fitting the Galactic VIR with a LP (see the following section).

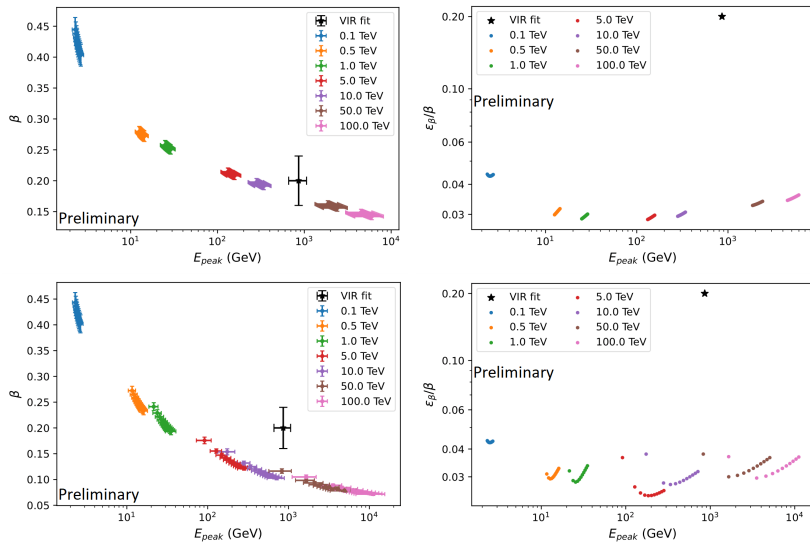


Figure 4: Upper panel: $E_{\text{peak}} - \beta$ plot for the LP parametrization of the PPPC4DMID code for several WIMP masses without EW corrections. For each mass in the range from 0.1 to 100 TeV (different colors), different fits have been performed with branching ratios B_r from 0 to 1 with a 0.1 step (as defined in Eq. 6). The relative uncertainty on the β parameter (ϵ_{β}/β) is showed in the right panel. Lower panels: Same as upper panels, applied to PPPC4DMID code with EW corrections. The black point is the fit of the gamma-ray cut-off detected by HESS in the Galactic VIR (left panel) and its relative error (right panel) (see Sec. 3.1). The relative uncertainty associated with the LP fit of the gamma-ray data dominates on the uncertainty associated with the LP fit of the PPPC4DMID code.

3.1 Example: the Galactic very inner region

In this section we generalize the LP data-drive approach [28, 32] based on Fermi-LAT catalogues to a different gamma-ray detected source, namely, the gamma-ray cut-off detected by HESS at the Galactic VIR [34]. The best fit of these data as DM is obtained by assuming that the total gamma-ray flux is given by a combination of a DM signature more an extra background component of unknown astrophysical origin [22, 23]. The latter is modeled as a power law, while the DM component is given by Eq. 1. The total fit is given by:

$$\frac{d\Phi_{\text{DM}}}{dE} = \sum_i^{\text{channels}} \frac{\langle\sigma v\rangle_i}{2} \frac{dN_i}{dE} \frac{\Delta\Omega\langle J\rangle_{\Delta\Omega}}{4\pi m_{\text{DM}}^2} + B^2 E^{-\gamma} \quad (7)$$

We use the HESS data as an example to cross check the validity of that general approach. In Fig. 5 we show the fit of the HESS data from the Galactic VIR [34] performed with two different Monte Carlo event generator software, namely PYTHIA 6 and PYTHIA 8. In the first case we use the analytical fitting

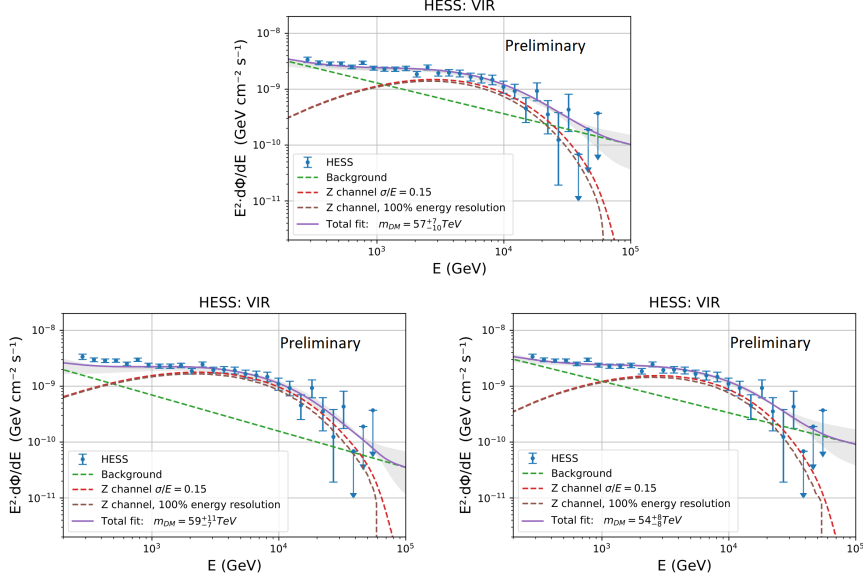


Figure 5: Fit of the gamma-ray flux observed by HESS in the Galactic VIR [34], by assuming a power-law background component and DM signature of WIMPs annihilating in in the Z channel. Upper panel: we adopted the analytic fitting functions of PYTHIA 6, [35]), with $\sigma/E = 0.15$ energy resolution. Lower left panel: same as upper panel, but computed with PYTHIA 8, including the EW. Lower right panel: Same as left lower panels, but now considering ZZ channel without including the EW corrections.

functions [35], in the second case we use the PPPC4DMID interpolation function [33] (with/out EW corrections). In Tab. 2 we show the parameters of these fits. We performed the fit by taking into account the HESS energy resolution of 15%. By introducing this effect the fitted DM mass is a 14% lower than the value obtained by fitting the data without the instrumental energy resolution. The results are in agreement with [22, 23]. For WIMP masses of $\sim 50\text{TeV}$ annihilating in to the ZZ channel, the uncertainty introduced by using a different version of PYTHIA is indeed negligible [27].

Finally, we perform the fit of the HESS Galactic VIR with a LP (Fig. 6). The fitted parameter are shown in Tab. 3. In Fig. 4 we compare the obtained E_{peak} and β with the LP parametrization of the PPPC4DMID code. E_{peak} is compatible with a WIMP candidate of $\sim 50\text{TeV}$ within the uncertainty showed in Tab. 2. The β parameter is compatible with the LP fit of the PPPC4DMID code without the EW correction, in agreement with the best fit value reported in Tab. 2. The relative uncertainty ϵ_{β}/β of the LP modelling of the PPPC4DMID code is negligible if compared to the relative uncertainty associated to the LP

Parameters	PYTHIA 6	PYTHIA 8 EW	PYHTIA 8 NoEW
m_{DM} (TeV)	57_{-10}^{+6}	59_{-7}^{+11}	54_{-8}^{+8}
$B^2(10^{-8} \text{ GeV cm}^{-2} \text{ s}^{-1})$	5_{-3}^{+8}	6_{-5}^{+18}	6_{-3}^{+9}
γ	$2.5_{-0.1}^{+0.2}$	$2.6_{-0.2}^{+0.2}$	$2.6_{-0.1}^{+0.2}$
$\langle J \rangle_{\Delta\Omega} (10^{28} \text{ GeV}^2 \text{ cm}^{-5})$	4_{-1}^{+1}	5_{-1}^{+1}	4_{-1}^{+1}
$\langle J \rangle_{\Delta\Omega} / J_{EVANS} (\times 10^3)$	$1.4_{-0.4}^{+0.3}$	$2.1_{-0.5}^{+0.4}$	$1.6_{-0.4}^{+0.3}$
χ^2 / dof	1.33	2.52	1.23
$\Delta\Omega$ (sr)	1.16×10^{-5}		

Table 2: Fitted parameters of the Galactic VIR ($\Delta\Omega$ is the solid angle of the region) as a combination of a WIMP signature and a power-law background (Eq. 7) within 1σ confidence level. We consider the ZZ annihilation channel. The secondary flux of gamma-ray has been simulated with both PYTHIA 6 and PYTHIA 8, with/without the EW effect. We also show the χ^2/dof of each fit.

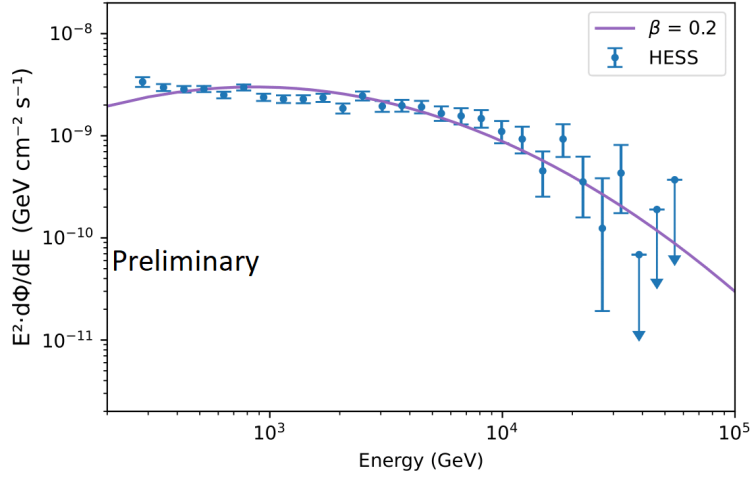


Figure 6: Fit GC with LP, the parameters can be found in Tab. 3.

E_{Peak} (TeV)	α	β	χ^2/dof
0.9 ± 0.2	2.1 ± 0.1	0.20 ± 0.04	3.03

Table 3: Fitted parameters of the HESS data of the Galactic VIR with the LP.

fit of the VIR gamma-ray spectra .

4 Conclusions

In this proceedings we reviewed both the benchmark approach to indirect detection of WIMP candidate and the Log Parabola (LP) data-driven approach for Machine Learning (ML) application. The multi-messenger and multi-wavelength detection of any WIMP signature would result in a competitive claim of the indirect detection of DM. The first term refers to the study of multiple fluxes of secondary particles, which could be emitted contemporaneously from a same DM candidate. In the second case, the same concept is extended to the study of any electromagnetic emission, produced by the interaction of the secondary flux of charged particles with a magnetic field. All that multiple signatures of WIMP candidates are predicted with Monte Carlo event generator software. Although the use of Monte Carlo software can introduce some uncertainty in the predicted flux of secondary particles, in the case of WIMPs annihilating into ZZ channel, the expected gamma-ray flux can be predicted with high precision. In Fig. 5 and Tab. 3 we show the result of the fit of the gamma-ray cut-off detected by HESS at the Galactic Very Inner Region (VIR) by using the gamma-ray flux simulated by PYTHIA 6 or PYTHIA 8 with/out electroweak corrections. All these results are in agreement within the uncertainty.

Moreover, we reviewed the LP data-driven framework developed for the application of ML algorithms to indirect searches for DM. The latter approach focuses on the LP fitting of the expected fluxes of secondary particles. Thus, bringing the theoretical expectation on the experimental parameter space, we can improve the possibility to disentangle prospective WIMP candidates in a vast sample of unidentified sources. In Figs 4, 6 and Tab. 3 we show as this approach has a first order validity, and the prospective DM candidate found out with ML algorithms need to be undergo to further analyses.

5 Acknowledgements

The work of VG and JZP was supported by the grants PID2021-125331NB-I00 and CEX2020-001007-S, both funded by MCIN/AEI/10.13039/501100011033 and by “ERDF A way of making Europe”. VG’s contribution to this work has been supported by *Juan de la Cierva-Incorporación* IJC2019-040315-I grants. JZP’s contribution to this work has been supported by *FPI Severo Ochoa* PRE2021-099137 grant.

References

- [1] Leszek Roszkowski, Enrico Maria Sessolo, and Sebastian Trojanowski. WIMP dark matter candidates and searches—current status and future prospects. *Rept. Prog. Phys.*, 81(6):066201, 2018.
- [2] Anne M Green and Bradley J Kavanagh. Primordial black holes as a dark matter candidate. *Journal of Physics G: Nuclear and Particle Physics*, 48(4):043001, feb 2021.
- [3] P. J. E. Peebles, D. N. Schramm, E. L. Turner, and R. G. Kron. The case for the relativistic hot Big Bang cosmology. , 352(6338):769–776, August 1991.
- [4] Marc Schumann. Direct Detection of WIMP Dark Matter: Concepts and Status. *J. Phys. G*, 46(10):103003, 2019.
- [5] Antonio Boveia and Caterina Doglioni. Dark Matter Searches at Colliders. *Ann. Rev. Nucl. Part. Sci.*, 68:429–459, 2018.
- [6] J. A. R. Cembranos, A. Dobado, and Antonio Lopez Maroto. Brane world dark matter. *Phys. Rev. Lett.*, 90:241301, 2003.
- [7] Lawrence J. Hall, Karsten Jedamzik, John March-Russell, and Stephen M. West. Freeze-In Production of FIMP Dark Matter. *JHEP*, 03:080, 2010.
- [8] Jonathan L. Feng, Arvind Rajaraman, and Fumihiko Takayama. Super-weakly interacting massive particles. *Phys. Rev. Lett.*, 91:011302, 2003.
- [9] Jennifer M. Gaskins. A review of indirect searches for particle dark matter. *Contemp. Phys.*, 57(4):496–525, 2016.
- [10] E. Charles et al. Sensitivity Projections for Dark Matter Searches with the Fermi Large Area Telescope. *Phys. Rept.*, 636:1–46, 2016.
- [11] Francesca Calore, Marco Cirelli, Laurent Derome, Yoann Genolini, David Maurin, Pierre Salati, and Pasquale Dario Serpico. AMS-02 antiprotons and dark matter: Trimmed hints and robust bounds. *SciPost Phys.*, 12(5):163, 2022.
- [12] Tolga Yapici and Andrew J. Smith. Dark Matter Searches with HAWC. *PoS, ICRC2017:891*, 2018.
- [13] Michele Doro. A review of the past and present MAGIC dark matter search program and a glimpse at the future. In *25th European Cosmic Ray Symposium*, 1 2017.

- [14] H. Abdalla et al. Search for Dark Matter Annihilation Signals in the H.E.S.S. Inner Galaxy Survey. *Phys. Rev. Lett.*, 129(11):111101, 2022.
- [15] A. Acharyya et al. Sensitivity of the Cherenkov Telescope Array to a dark matter signal from the Galactic centre. *JCAP*, 01:057, 2021.
- [16] J. A. R. Cembranos, Á De La Cruz-Dombriz, V. Gammaldi, and M. Méndez-Isla. SKA-Phase 1 sensitivity to synchrotron radio emission from multi-TeV Dark Matter candidates. *Phys. Dark Univ.*, 27:100448, 2020.
- [17] Sergio Colafrancesco, Marco Regis, Paolo Marchegiani, Geoff Beck, Rainer Beck, Hannes Zechlin, Andrei Lobanov, and Dieter Horns. Probing the nature of Dark Matter with the SKA. *PoS*, AASKA14:100, 2015.
- [18] M. Ackermann et al. Searching for Dark Matter Annihilation from Milky Way Dwarf Spheroidal Galaxies with Six Years of Fermi Large Area Telescope Data. *Phys. Rev. Lett.*, 115(23):231301, 2015.
- [19] Tjark Miener, Daniel Nieto, Viviana Gammaldi, Daniel Kerszberg, and Javier Rico. Constraining branon dark matter from observations of the Segue 1 dwarf spheroidal galaxy with the MAGIC telescopes. *JCAP*, 05(05):005, 2022.
- [20] V. Gammaldi, E. Karukes, and P. Salucci. Theoretical predictions for dark matter detection in dwarf irregular galaxies with gamma rays. *Phys. Rev. D*, 98(8):083008, 2018.
- [21] Viviana Gammaldi, Judit Pérez-Romero, Javier Coronado-Blázquez, Mattia Di Mauro, Ekaterina Karukes, Miguel Angel Sánchez-Conde, and Paolo Salucci. Dark Matter search in dwarf irregular galaxies with the Fermi Large Area Telescope. *PoS*, ICRC2021:509, 2021.
- [22] J. A. R. Cembranos, V. Gammaldi, and A. L. Maroto. Possible dark matter origin of the gamma ray emission from the galactic center observed by HESS. *Phys. Rev. D*, 86:103506, 2012.
- [23] J. A. R. Cembranos, V. Gammaldi, and A. L. Maroto. Spectral Study of the HESS J1745-290 Gamma-Ray Source as Dark Matter Signal. *JCAP*, 04:051, 2013.
- [24] Judit Pérez-Romero. Sensitivity of CTA to gamma-ray emission from the Perseus galaxy cluster. *PoS*, ICRC2021:546, 2021.

- [25] N. W. Evans, J. L. Sanders, and A. Geringer-Sameth. Simple J-Factors and D-Factors for Indirect Dark Matter Detection. *Phys. Rev. D*, 93(10):103512, 2016.
- [26] Viviana Gammaldi. Multimessenger Multi-TeV Dark Matter. *Front. Astron. Space Sci.*, 6:19, 2019.
- [27] J. A. R. Cembranos, A. de la Cruz-Dombriz, V. Gammaldi, R. A. Lineros, and A. L. Maroto. Reliability of Monte Carlo event generators for gamma ray dark matter searches. *JHEP*, 09:077, 2013.
- [28] V. Gammaldi, B. Zaldívar, M. A. Sánchez-Conde, and J. Coronado-Blázquez. A search for dark matter among Fermi-LAT unidentified sources with systematic features in Machine Learning. 7 2022.
- [29] S. Abdollahi et al. *Fermi* Large Area Telescope Fourth Source Catalog. *Astrophys. J. Suppl.*, 247(1):33, 2020.
- [30] The Fermi-LAT Collaboration. Fermi Large Area Telescope Third Source Catalog. *APJS*, 2015.
- [31] The Fermi-LAT Collaboration. 3FHL: The Third Catalog of Hard Fermi-LAT Sources. *APJS*, 232:18, October 2017.
- [32] Javier Coronado-Blázquez, Miguel A. Sánchez-Conde, Mattia Di Mauro, Alejandra Aguirre-Santaella, Ioana Ciucă, Alberto Domínguez, Daisuke Kawata, and Néstor Mirabal. Spectral and spatial analysis of the dark matter subhalo candidates among Fermi Large Area Telescope unidentified sources. *JCAP*, 11:045, 2019.
- [33] Marco Cirelli, Gennaro Corcella, Andi Hektor, Gert Hutsi, Mario Kadastik, Paolo Panci, Martti Raidal, Filippo Sala, and Alessandro Strumia. PPPC 4 DM ID: A Poor Particle Physicist Cookbook for Dark Matter Indirect Detection. *JCAP*, 03:051, 2011. [Erratum: *JCAP* 10, E01 (2012)].
- [34] F. Aharonian et al. Spectrum and variability of the Galactic center VHE γ -ray source HESS J1745-290. , 503(3):817–825, September 2009.
- [35] J. A. R. Cembranos, A. de la Cruz-Dombriz, A. Dobado, R. Lineros, and A. L. Maroto. Fitting formulae for photon spectra from WIMP annihilation. *J. Phys. Conf. Ser.*, 314:012063, 2011.

CONSTRAINTS ON DARK ENERGY FROM THE ABUNDANCE OF MASSIVE GALAXIES

Paola Santini

INAF - Osservatorio Astronomico di Roma, via di Frascati 33, 00078 Monte Porzio Catone (RM), Italy

Nicola Menci

INAF - Osservatorio Astronomico di Roma, via di Frascati 33, 00078 Monte Porzio Catone (RM), Italy

Marco Castellano

INAF - Osservatorio Astronomico di Roma, via di Frascati 33, 00078 Monte Porzio Catone (RM), Italy

Abstract

Dynamical dark energy (DDE) models have been proposed to address several observational tensions arising within the standard Λ cold dark matter (Λ CDM) scenario. Different DDE models, parameterized by different combinations of the local value of the equation-of-state parameter w_0 and its time derivative w_a , predict different maximal abundance of massive galaxies in the early Universe. We use the observed abundance of massive galaxies already in place at $z \gtrsim 4.5$ to constrain DDE models. To this aim, we consider four independent probes: (i) the observed stellar mass function at $z \sim 6$ from the CANDELS survey; (ii) the estimated volume density of massive haloes derived from the observation of massive, star-forming galaxies detected in the submillimeter range at $z \sim 5$; (iii) the rareness of the most massive system detected at $z \sim 7$ by the SPT survey; (iv) the abundance of massive ($M > 10^{10.5} M_\odot$) galaxies at $z \sim 10$ as inferred from early JWST observations. Our probes *exclude* a major fraction of the DDE parameter space that is allowed by other existing probes. In particular, early JWST results, if confirmed, are in tension with the standard Λ CDM scenario at a 2σ confidence level.

1 Introduction

The current theory of structure formation envisages all cosmic structures to form from the collapse and the growth of initially tiny density perturbations of the dark matter (DM) density field in a universe characterized by an accelerated expansion. Such an acceleration indicates that the dominant component (with density parameter $\Omega_\Lambda \simeq 0.7$) of the cosmic fluid must be composed of some form of dark energy (DE), with equation-of-state parameter $w = p/\rho \leq -1/3$. Although the nature of such a component remains unknown, the simplest model assumes DE to be connected with the vacuum energy, the so-called cosmological constant, with $w = -1$. When coupled with the assumption that DM is composed of nonrelativistic particles at decoupling, such a scenario leads to the Λ cold DM (Λ CDM) standard cosmological model [1].

While measurements of the Cosmic Microwave Background (CMB) have provided a first, strong confirmation of such a scenario, tensions have recently emerged ([2] and references therein) and have stimulated an extended effort toward the investigation of more complex cosmological models. One of the simplest physical alternatives is a DE with a time-dependent equation of state, also called dynamical dark energy (DDE) (see [3] for a review).

The abundance of massive galaxies at high redshift constitutes a powerful probe for cosmological models. In fact, in the standard CDM scenario, large-mass DM haloes become progressively rarer with increasing redshift. The exponential high-mass tail of the mass function of DM haloes is expected to shift toward progressively smaller masses for increasing redshift (see, e.g., [4] for a review) at a rate that depends on the assumed cosmology. Hence, the comparison of the predicted abundance of massive DM haloes at increasingly larger redshift with the observed abundance of galaxies with corresponding stellar mass M_* provides increasingly strong constraints on the assumed cosmological framework. Indeed, viable cosmological models must allow for an evolution of the initial density perturbations that is fast enough to match the abundance of massive galaxies observed to be in place at early epochs.

Under (extremely) conservative assumptions and considering different observables, we compare the maximal abundance of massive galaxies predicted in different DDE models at high redshifts with the measured abundance of the most massive systems observed to be already in place at the same redshifts. This conference proceeding summarizes the results that are presented and discussed in [2, 5].

2 Method

We compute the expected abundance of DM haloes, as a function of redshift z and DM mass M_h , in different DDE models adopting the most conservative assumptions.

We adopt the Sheth & Tormen [6] mass function, within the Press and Schechter formalism. Besides being physically motivated and tested against N-body simulations for a variety of cosmologies, it has the most extended high-mass tail among the different proposed forms, hence representing the most conservative choice.

The high-mass exponential cutoff in the Sheth & Tormen mass function is critically determined by the cosmic expansion rate and by the growth factor, which depend on the equation of state of DE. For the latter, we use the CPL parameterization [7, 8] in terms of the scale factor a :

$$w(a) = w_0 + w_a(1 - a) \quad (1)$$

where the parameter w_0 represents the value of w at the present epoch, while w_a is its look-back time variation $w_a = -dw/da$. In the above parameterization, the standard Λ CDM cosmology corresponds to $w_0 = -1$ and $w_a = 0$. For each combination (w_0, w_a) , we can compute the expected number of DM haloes of mass M_h as a function of redshift. We refer the reader to [2] for a full description of the methodology and assumptions on the various involved cosmological parameters.

To compare these cosmological predictions on abundance of DM haloes with the measured abundance of galaxies it is necessary to take into account the baryon physics. However, baryonic effects are degenerate with cosmology in determining the expected galaxy abundance. This can be bypassed by noticing that the ratio of galaxy baryonic components (stellar mass or gas mass) to DM halo mass has an absolute maximum at the cosmic baryon fraction f_b ($f_b \simeq 0.16$, [9]). In fact, the observed abundance of galaxies with large mass in the baryonic component M_b places a lower limit on the abundance of DM haloes with masses $M_h \geq M_b/f_b$. Such a constraint can be used to rule out cosmological models that do not allow for a sufficiently rapid growth of galactic DM haloes. In other words, since galaxies cannot outnumber their DM haloes, any (w_0, w_a) combinations for which $\phi_{w_0, w_a}(M_h \geq M_b/f_b, z) \leq \phi_{obs}(M_b, z)$ can be excluded.

Due to the exponential cutoff of the DM halo mass function and to its rapid redshift evolution, the highest masses at the highest redshifts put the most stringent limits. To adopt the most conservative assumptions, all our choices aim at maximizing $\phi_{w_0, w_a}(M_h, z)$ and minimizing $\phi_{obs}(M_b, z)$.

3 Results

We describe here the various observables considered to constrain the w_0-w_a parameter space and the relevant regions excluded.

3.1 Stellar mass function at $z = 6$ from the CANDELS survey

We first compare with the observed stellar mass distribution of massive, distant galaxies. Since stellar mass is a time-integrated quantity, it is not much sensitive to the details of the star formation history [10] and can be easily related to the DM mass of the host halo. An extended wavelength coverage is essential for estimating stellar masses from spectral energy distribution (SED) fitting, while a combination of survey volume and depth is required to measure the abundance of distant, massive and rare galaxies. The CANDELS project [11, 12], taking advantage of the optical/near-infrared/mid-infrared imaging provided by HST, Spitzer, and VLT on almost 1000 arcmin² down to faint fluxes, provides an ideal data set to base such a measurement. Here, we use the mass function derived by Grazian et al. [13], who used a spectral-fitting technique to derive stellar masses for a galaxy sample with high-quality photometric redshifts based on the CANDELS GOODS-South and UDS fields.

We focus on their largest stellar mass bin (centered on $M_* = 8 \times 10^{10} M_\odot$, assuming a Salpeter initial mass function [14]) at $z = 5.5 - 6.5$. These high redshifts and large masses ensure that the mass functions predicted by the different DDE models are in the full exponential regime, and are steep enough to make the comparison with the observed number density discriminant for the different DDE models.

We associate the stellar mass M_* to the host halo DM mass M_h using the relation $M_* = F f_b M_h$, where F describes the efficiency of baryon conversion into stars. We consider three cases: (a) the extremely unrealistic case $F = 1$, corresponding to a complete conversion; (b) the more realistic case $F = 0.25$, as obtained from abundance matching techniques (e.g., [16]) - this value however is derived assuming a Λ CDM halo mass function; and (c) the conservative value $F = 0.5$, derived as a conservative upper limit on the star formation efficiency from hydrodynamical N-body simulations.

Before comparing the predicted number density of DM haloes with observations, we rescale the observed volumes and luminosities from a Λ CDM assumption to a generic cosmology through the factors $f_{vol} = V_\Lambda / V_{w_0, w_a}$ and $f_{lum} = D_{L, w_0, w_a}^2 / D_{L, \Lambda}^2$, respectively, where V is the cosmological volume and D_L^2 is the square luminosity distance used to convert observed fluxed into luminosities, hence stellar masses. In

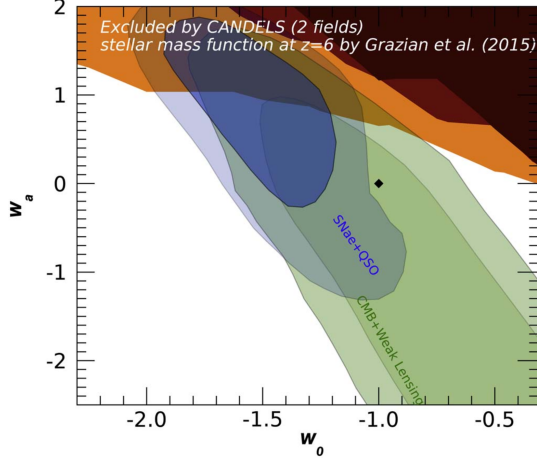


Figure 1: Exclusion regions at a 2σ confidence level in the $w_0 - w_a$ plane derived from the observed CANDELS stellar mass function at $z \sim 6$ [13]. The brown, red, and orange regions correspond to the assumption of $F = 1$, $F = 0.5$ and $F = 0.25$, respectively (see text). Our exclusion region is compared with the 2σ and 3σ contours allowed by CMB+weak lensing (green regions) and by the combination of the same data with the Hubble diagram of supernovae and quasars (blue region), derived from Figure 4 of [15]. The black dot corresponds to the Λ CDM case ($w_0 = -1$, $w_a = 0$).

summary, for each combination (w_0, w_a) , we compare the volume-corrected, observed abundance of galaxies $\tilde{\phi} = \phi_{obs} f_{Vol}$ with stellar mass $M_* = 8 f_{lum} 10^{10} M_\odot$ at $z \sim 6$ with the predicted number density of DM haloes with DM masses larger than $M_*/(F f_b)$, i.e. $\phi_{w_0, w_a}(M_h \geq M_*/(F f_b))$. The confidence for the exclusion P_{excl} of each considered DDE model is obtained from the probability distribution function $p(\tilde{\phi})$ as the probability that the measured abundance $\tilde{\phi}$ is larger than number density predicted by the model, i.e., $P_{excl}(w_0, w_a) = \int_{\tilde{\phi}_{w_0, w_a}}^{\infty} p(\tilde{\phi}) d\tilde{\phi}$.

We show in Figure 1 the region of the $w_0 - w_a$ parameter space excluded at a 2σ confidence level (i.e., $P_{excl} \geq 0.95$) for $F = 1$, $F = 0.5$ and $F = 0.25$. The exclusion region is overplotted on the regions allowed by CMB and weak lensing observations, and on the one derived by the combination of the same data with the Hubble diagram of supernovae and distant quasars [15]. Our probe significantly restricts the region in the DDE parameter space allowed by other methods. In particular, we exclude an ap-

preciable part of the region favored by the distant quasar method. Very similar results are obtained by comparing DDE predictions to the [17] mass function of CANDELS galaxies.

3.2 Submillimeter detected massive galaxies at $z \sim 5$

The population of galaxies identified in rest-frame optical and ultraviolet is known to under represent the most massive galaxies, which have rich dust content and/or old stellar populations. These are, however, detectable at submillimeter (sub-mm) wavelengths. Wang et al. [18] performed detailed sub-mm (870 μm) observations with ALMA of a sample of IRAC–bright galaxies. They detected 39 star-forming objects at $z > 3$, which are unseen in even the deepest near-infrared (H -band) imaging with the HST (“ H -dropouts”) and proved to be massive galaxies with stellar mass extending up to $M_* \simeq 3 \times 10^{11} M_\odot$, with a median mass $M_* \simeq 4 \times 10^{10} M_\odot$.

For such objects, we follow a procedure similar to that explained in the previous section. We compute the number density of galaxies with stellar masses in the bin $10.25 \leq \log(M_*/M_\odot) \leq 10.75$ (dominating the statistics of observed objects) at redshifts $z = 4.5\text{--}5.5$, and derive the corresponding 2σ lower limit $\phi_{low}(M_*) = 1.8 \times 10^{-5} \text{Mpc}^{-3}$. To relate the observed stellar mass M_* to the DM mass M_h , we first adopt the highly conservative assumption $M_h = M_*/f_b$ (i.e., $F = 1$). The comparison allows us to exclude (at a 2σ confidence level) the combinations (w_0, w_a) for which $\phi_{w_0, w_a} < \phi_{low}$. The result is shown as a brown exclusion region in Figure 2.

Of course, the above approach is very conservative, since we assume that the whole baryonic mass is in stars, and that the baryon mass of DM haloes is related to the DM mass through the universal baryon fraction (no loss of baryons). However, the very fact that the objects are characterized by high star formation rates ($\gtrsim 200 M_\odot \text{yr}^{-1}$, [18]) indicates that a sizable fraction of baryons is in the form of gas. Properly accounting for such a gas fraction would yield larger values of M_h associated with the observed M_* and, hence, tighter constraints. However, gas mass estimates for these objects are affected by extremely large uncertainties (\sim a factor of 10) related to the uncertainties affecting the photometric redshifts and to all the assumptions required to convert the sub-mm continuum flux into a gas mass. To bypass this and to derive more realistic constraints for DDE models, we analyze the clustering properties of the H -dropouts. We base our analysis on the procedure adopted by [18], who estimated the halo mass function from the measured correlation function, modified as described in [2] to be adapted to a generic cosmology. We find that $M_h = 10^{13} M_\odot$ constitutes

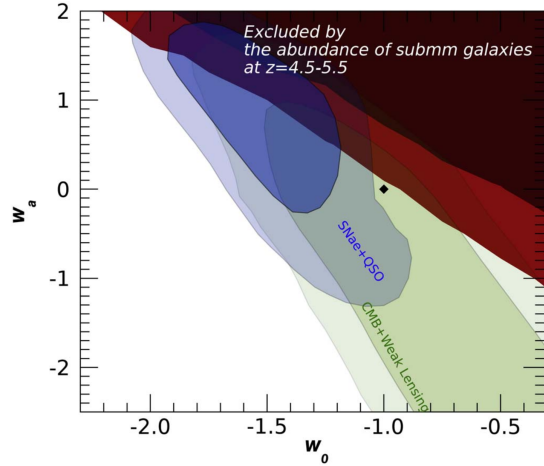


Figure 2: Exclusion regions at a 2σ confidence level in the $w_0 - w_a$ plane derived from the observed abundance of luminous sub-mm galaxies at $z = 4.5 - 5.5$ [18]. The brown region corresponds to the assumption that the observed stellar masses are related to the DM mass through the baryon fraction f_b ($M_* = f_b M_h$). The red region corresponds to adoption of the DM mass derived from the measured cross-correlation function of H-dropouts (see text).

a 2σ lower limit for the value of the DM mass for any DDE model. The resulting exclusion region in the $w_0 - w_a$ plane is shown in red in Figure 2. While the Λ CDM model remains marginally consistent with the observations, a much larger fraction of the $w_0 - w_a$ parameter space is excluded by the abundance of optically invisible, sub-mm galaxies at $z \sim 5$.

3.3 SPT0311-58 at $z = 6.9$

The most massive system detected at $z \geq 6$ is a far-infrared luminous object at redshift $z = 6.9$ identified in the 2500 deg² South Pole Telescope (SPT) survey [19]. High-resolution imaging revealed this source (denoted SPT0311-58) to be a pair of extremely massive star-forming galaxies, with the larger galaxy (SPT0311-58W) forming stars at a rate of 2900 M_\odot/yr and largely dominating over the companion. An elongated faint object seen at optical and near-infrared wavelengths is consistent with

a nearly edge-on spiral galaxy at $z \simeq 1.4$ acting as a gravitational lens for the source, with an estimated magnification $\mu = 2$.

The molecular gas mass was estimated from ALMA observations, both based on the CO luminosity and from a radiative transfer model [20]. We adopt the latter value of $M_{H_2} \simeq (3.1 \pm 1.9) \times 10^{11} M_\odot$ as a baseline, since it is based on a detailed fit with a model built ad-hoc to study the interstellar medium properties of this object and does not require assumptions on the conversion factor from the CO line to the H_2 mass [19]. To estimate the DM mass of the host halo of this galaxy, we assume that $M_h = (M_* + M_{gas})/f_b$, where M_{gas} is the total gas mass. Since the stellar mass cannot be directly measured due to the extremely faint optical emission of the galaxy (likely due to the large dust extinction), we can infer a lower limit on the stellar content from existing measurements of the molecular gas fraction $f_{H_2} = M_{H_2}/(M_* + M_{H_2})$. We consider the most conservative value $f_{H_2} = 0.8$ measured on high- z star-forming galaxies (see references in [2]) and a more realistic value $f_{H_2} = 0.4$ suggested by both theoretical models [21] and observations [22]. Assuming that H_2 constitutes 80% of the gas mass at high redshifts (an upper limit according to [23, 24]) leads to a DM mass ranging from $\simeq 2 \times 10^{12} M_\odot$ to $\simeq 6 \times 10^{12} M_\odot$. An even larger DM mass would be consistent with the observations if the object lost the majority of its molecular gas content.

To estimate the rareness of such a system in all the considered DDE cosmologies, we compute the Poisson probability of finding such a massive object within the volume probed by the SPT survey, for different combinations (w_0, w_a) . We follow the method in [25] adapted to a generic cosmology and take into account the uncertainties in the measured value of M_{H_2} as described in [2]. We consider the total area of the SPT survey, although the effective area is potentially much smaller. In fact, most of the objects in the survey are strongly lensed, indicating that a source must be gravitationally lensed to exceed the flux threshold for inclusion in the observations. For this reason, in the following we also consider the case of an effective area reduced by 1/10. From the rareness, we compute the associated 2σ exclusion regions in the $w_0 - w_a$ plane. The result is shown in Figure 3.

In the case $M_h = 6 \times 10^{11} M_\odot$, corresponding to the assumption of $f_{H_2} = 0.4$ for the H_2 gas fraction, a major portion of the $w_0 - w_a$ plane is excluded, although the Λ CDM case ($w_0 = -1, w_a = 0$) remains allowed. The excluded region includes both the larger w_a cases allowed by the quasar method (blue region) and the cases $w_0 \geq -0.6$ allowed by the CMB + weak lensing results, which shows the potential

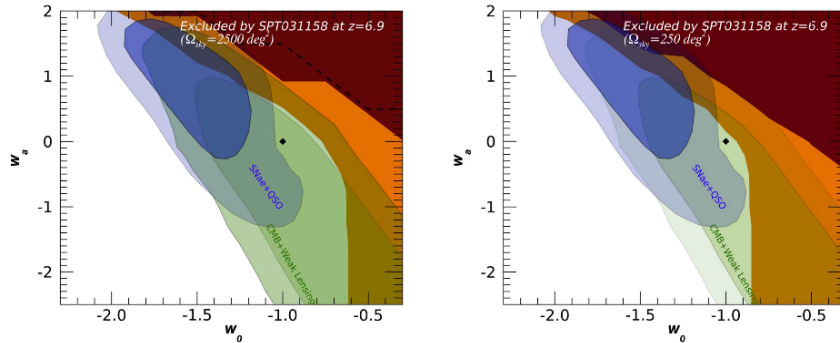


Figure 3: *Exclusion regions at a 2σ confidence level in the $w_0 - w_a$ plane for two different inferred DM masses of SPT0311–58: $2 \times 10^{12} M_\odot$ (red area) and $2 \times 10^{12} M_\odot$ (yellow area). The left panel assumes the full SPT survey area of 2500 deg^2 while the right one assumes 250 deg^2 .*

impact of our results. Tighter constraints are obtained assuming an area of 250 deg^2 , shown in the right panel of Figure 3.

3.4 High- z galaxies from early JWST results

We finally exploit the very recent, early JWST results to derive even tighter constraints on DDE models. We compare the maximum stellar mass density $\rho_{max, w_0, w_a}(> M_*)$ allowed by different cosmologies with the unexpected large stellar mass density measured by Labbé et al. [26], who observed seven galaxies with $M_* \geq 10^{10} M_\odot$ at $7 < z < 11$. To derive the most stringent limits on cosmological models, we focus on their most massive bin, i.e. $M_* \geq 10^{10.5} M_\odot$ (derived assuming a conservative Chabrier initial mass function [27]), in the redshift range $9 < z < 11$, yielding a stellar mass density of $\rho_{obs} \approx 10^6 M_\odot/\text{Mpc}^3$.

We compute the predicted maximal stellar mass density for different (w_0, w_a) combinations. We assume $M_h = M_*/f_b$ and adopt an even more conservative value for the baryon fraction of $f_b = 0.18$ [28]. We rescale the observed stellar mass density for the volume and luminosity correction factors to convert from ΛCDM to a generic DDE model as explained in Sect. 3.1. We derive the proper confidence level for exclusion for each considered cosmology by calculating the probability that $\rho_{max, w_0, w_a}(> \tilde{M}_*) <$

$\rho_{obs}(> \bar{M}_*)$, where $\bar{M}_* = 10^{10.5} M_{\odot}$. We run a Monte Carlo simulation to account for the observational uncertainties, assigning an errorbar of 0.5 dex to the stellar mass to account for systematics related with the SED fitting procedure [10].

The resulting exclusion regions in the $w_0 - w_a$ parameter space is shown in Figure 4 for different confidence levels, and compared with regions allowed by existing probes. The Λ CDM case is excluded at almost 2σ level, while a major fraction of the parameter space is excluded with high confidence level. Our probe severely restricts the region in the DDE parameter space allowed by other methods, and exclude almost all the region favored by the distant quasar method.

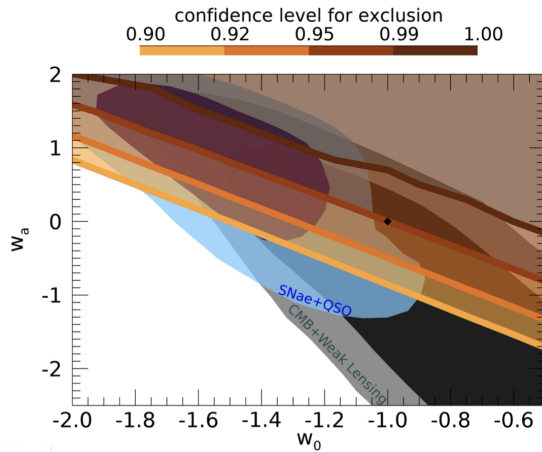


Figure 4: *Exclusion regions in the $w_0 - w_a$ plane derived from the observed stellar mass density at $z = 10$ [26]. The excluded regions above each coloured line correspond to different confidence levels shown in the upper bar. Our exclusion regions are compared with the 2σ and 3σ contours allowed by CMB+weak lensing (grey and dark-grey regions) and by the combination of the same data with the Hubble diagram of supernovae and quasars (blue regions), derived from Fig. 4 of [15].*

4 Discussion and Conclusions

We have determined exclusion regions in the $w_0 - w_a$ parameter space of DDE models from the abundance of massive galaxies at early ($z > 4.5$) epochs. Adopting the most conservative assumptions for the ratio between the observed baryonic component and

the DM mass, as well as conservative choices for the cosmological parameters, we have derived robust constraints that do not depend on the details of the baryon physics involved in galaxy formation. In addition, our results do not depend on the nature of the DM component [5].

All our probes exclude a major fraction of the parameter space favored by the quasar distances [15], including their best-fit combination $w_0 \simeq -0.8$ and $w_a \simeq -1.5$. If confirmed, recent JWST observations are in tension with a Λ CDM scenario at a 2σ confidence level. Our results leave open the possibility that the present tension in the value of H_0 between the values derived from Planck and those obtained from local luminosity distance measurements [29] may be solved in DDE models, since the combinations (w_0, w_a) that allow for the reconciliation of the different observations [30, 31] include values outside our exclusion region.

Our constraints will be greatly tightened when improved, reliable measurements of the actual baryon fraction in galaxies, and of the relative weight of each baryonic component, will be available. Increasing the statistics of high-redshift massive objects will also greatly tighten present constraints by reducing the uncertainties associated with the low abundance of these galaxies.

A critical issue is associated with the systematics dominating the error budget in the mass estimates, especially at high redshift. The advent of JWST has for the first time opened the possibility to measure the rest-frame optical emission at high redshift [32], which was previously possible, despite being subject to a high noise level, only for very few bright and isolated sources detected with the Spitzer telescope. Early JWST observations have revealed their potential impressive impact in constraining cosmological models, as also shown by independent analyses [33, 34]. However, JWST observations are extremely new and may still be subject to revision. In particular, the results of [26] were derived on the basis of the first set of calibrations released by STScI. A 10-20% level revision in the NIRCcam calibrations [35] is not expected to yield to revisions of the stellar mass-to-light ratios of the targets large enough to affect significantly mass estimates and our conclusions. Nevertheless, we caution that the effect on the overall shape of the galaxy SED (as well as the assumptions on the star formation histories adopted in the SED-fitting procedure [36]) may reflect in a non-linear way on the estimated physical parameters of some objects. Finally, we have just started studying in detail the physics of $z \sim 10$ galaxies, and cannot exclude that the star formation process can be significantly different from the lower redshift Universe, where our models and estimate procedures are calibrated. In particular, as discussed

by [37], the increase of gas temperatures in star-forming, high-redshift galaxies could result in an increasing contribution of massive stars to the galactic light, which would yield significantly lower values for the stellar masses compared to those measured by [26].

References

1. Peebles, P. J. E. *Principles of Physical Cosmology* (1993).
2. Menci, N. *et al.* Constraints on Dynamical Dark Energy Models from the Abundance of Massive Galaxies at High Redshifts. *The Astrophysical Journal* **900**, 108 (2020).
3. Huterer, D. & Shafer, D. L. Dark energy two decades after: observables, probes, consistency tests. *Reports on Progress in Physics* **81**, 016901 (2018).
4. Del Popolo, A. & Yesilyurt, I. S. The cosmological mass function. *Astronomy Reports* **51**, 709–734 (2007).
5. Menci, N. *et al.* High-redshift Galaxies from Early JWST Observations: Constraints on Dark Energy Models. *The Astrophysical Journal Letters* **938**, L5 (2022).
6. Sheth, R. K., Mo, H. J. & Tormen, G. Ellipsoidal collapse and an improved model for the number and spatial distribution of dark matter haloes. *Royal Astronomical Society, Monthly Notices* **323**, 1–12 (2001).
7. Chevallier, M. & Polarski, D. Accelerating Universes with Scaling Dark Matter. *International Journal of Modern Physics D* **10**, 213–223 (2001).
8. Linder, E. V. Exploring the Expansion History of the Universe. *Physical Review Letters* **90**, 091301 (2003).
9. Planck Collaboration *et al.* Planck 2018 results. V. CMB power spectra and likelihoods. *Astronomy & Astrophysics* **641**, A5 (2020).
10. Santini, P. *et al.* Stellar Masses from the CANDELS Survey: The GOODS-South and UDS Fields. *The Astrophysical Journal* **801**, 97 (2015).
11. Grogin, N. A. *et al.* CANDELS: The Cosmic Assembly Near-infrared Deep Extragalactic Legacy Survey. *The Astrophysical Journal Supplement Series* **197**, 35–+ (2011).
12. Koekemoer, A. M. *et al.* CANDELS: The Cosmic Assembly Near-infrared Deep Extragalactic Legacy Survey - The Hubble Space Telescope Observations, Imaging Data Products and Mosaics. *The Astrophysical Journal Supplement Series* **197**, 36–+ (May 2011).

13. Grazian, A. *et al.* The galaxy stellar mass function at $3.5 \leq z \leq 7.5$ in the CANDELS/UDS, GOODS-South, and HUDF fields. *Astronomy & Astrophysics* **575**, A96 (2015).
14. Salpeter, E. E. The Luminosity Function and Stellar Evolution. *The Astrophysical Journal* **121**, 161–+ (1955).
15. Risaliti, G. & Lusso, E. Cosmological Constraints from the Hubble Diagram of Quasars at High Redshifts. *Nature Astronomy* **3**, 272–277 (2019).
16. Behroozi, P. & Silk, J. The most massive galaxies and black holes allowed by Λ CDM. *Royal Astronomical Society, Monthly Notices* **477**, 5382–5387 (2018).
17. Duncan, K. *et al.* The mass evolution of the first galaxies: stellar mass functions and star formation rates at $4 < z < 7$ in the CANDELS GOODS-South field. *Royal Astronomical Society, Monthly Notices* **444**, 2960–2984 (2014).
18. Wang, T. *et al.* A dominant population of optically invisible massive galaxies in the early Universe. *Nature* **572**, 211–214 (2019).
19. Marrone, D. P. *et al.* Galaxy growth in a massive halo in the first billion years of cosmic history. *Nature* **553**, 51–54 (2018).
20. Strandet, M. L. *et al.* ISM Properties of a Massive Dusty Star-forming Galaxy Discovered at $z \sim 7$. *The Astrophysical Journal Letters* **842**, L15 (2017).
21. Narayanan, D., Bothwell, M. & Davé, R. Galaxy gas fractions at high redshift: the tension between observations and cosmological simulations. *Royal Astronomical Society, Monthly Notices* **426**, 1178–1184 (2012).
22. Tacconi, L. J. *et al.* Phibss: Molecular Gas Content and Scaling Relations in $z \sim 1$ –3 Massive, Main-sequence Star-forming Galaxies. *The Astrophysical Journal* **768**, 74 (2013).
23. Lagos, C. D. P. *et al.* Cosmic evolution of the atomic and molecular gas contents of galaxies. *Royal Astronomical Society, Monthly Notices* **418**, 1649–1667 (2011).
24. Lagos, C. D. P. *et al.* Which galaxies dominate the neutral gas content of the Universe? *Royal Astronomical Society, Monthly Notices* **440**, 920–941 (2014).
25. Harrison, I. & Hotchkiss, S. A consistent approach to falsifying Λ CDM with rare galaxy clusters. *Journal of Cosmology and Astroparticle Physics* **2013**, 022 (2013).
26. Labbe, I. *et al.* A very early onset of massive galaxy formation. arXiv: 2207.12446 (2022).

27. Chabrier, G. The Galactic Disk Mass Function: Reconciliation of the Hubble Space Telescope and Nearby Determinations. *The Astrophysical Journal Letters* **586**, L133–L136 (2003).
28. Planck Collaboration *et al.* Planck 2015 results. XIV. Dark energy and modified gravity. *Astronomy & Astrophysics* **594**, A14 (2016).
29. Kamionkowski, M. & Riess, A. G. The Hubble Tension and Early Dark Energy. *Invited Review for Ann. Rev. Nucl. Part. Sci.* arXiv: 2211.04492 (2022).
30. Di Valentino, E., Melchiorri, A., Linder, E. V. & Silk, J. Constraining dark energy dynamics in extended parameter space. *Physical Review D* **96**, 023523 (2017).
31. Zhao, G.-B. *et al.* Dynamical dark energy in light of the latest observations. *Nature Astronomy* **1**, 627–632 (2017).
32. Santini, P. *et al.* Early results from GLASS-JWST. XI: Stellar masses and mass-to-light ratio of $z > 7$ galaxies. *The Astrophysical Journal Letters*, in press. arXiv: 2207.11379 (2022).
33. Boylan-Kolchin, M. Stress Testing Λ CDM with High-redshift Galaxy Candidates. arXiv: 2208.01611 (2022).
34. Lovell, C. C., Harrison, I., Harikane, Y., Tacchella, S. & Wilkins, S. M. Extreme value statistics of the halo and stellar mass distributions at high redshift: are JWST results in tension with Λ CDM? *Royal Astronomical Society, Monthly Notices* **518**, 2511–2520 (2023).
35. Boyer, M. L. *et al.* The JWST Resolved Stellar Populations Early Release Science Program. I. NIRCcam Flux Calibration. *Research Notes of the American Astronomical Society* **6**, 191 (2022).
36. Endsley, R. *et al.* A JWST/NIRCcam Study of Key Contributors to Reionization: The Star-forming and Ionizing Properties of UV-faint $z \sim 7 - 8$ Galaxies. arXiv: 2208.14999 (2022).
37. Steinhardt, C. L., Kokorev, V., Rusakov, V., Garcia, E. & Sneppen, A. Templates for Fitting Photometry of Ultra-High-Redshift Galaxies. arXiv: 2208.07879 (2022).

**MEASURING THE DARK MATTER CONTENT
OF DWARF SPHEROIDAL GALAXIES**

Francesco G. Saturni

INAF – Osservatorio Astronomico di Roma

ASI – Space Science Data Center

Michele Doro

Università di Padova – Dip. di Fisica ed Astronomia “G. Galilei”

INFN – Sezione di Padova

Kaori D. Nakashima

FAU Erlangen-Nürnberg – Naturwissenschaftliche Fakultät

Aldo Morselli

Università di Roma “Tor Vergata” – Dip. di Fisica

INFN – Sezione di Roma 2

Gonzalo Rodríguez-Fernández

Università di Roma “Tor Vergata” – Dip. di Fisica

INFN – Sezione di Roma 2

for the CTA Consortium

www.cta-observatory.org/consortium_authors/

Abstract

Dark matter, a large ($\sim 85\%$) non-baryonic and non-relativistic component of the matter density of the Universe, likely consists of one or several so-far undetected particles hypothesized in theories beyond the Standard Model. One of the most promising approaches to shed light on the nature of dark matter particles is to search for signatures of their annihilation or decay into Standard Model particles from regions of the sky believed to be highly dark-matter dominated, such as the Galactic Center, the clusters of galaxies and the dwarf spheroidal galaxies around the Milky Way. In this context, dwarf spheroidal galaxies are among the most promising observational targets due to their relative proximity and lack of astrophysical background sources. In this contribution, we present new determinations of the dark matter amount (i.e. the astrophysical factors for dark matter annihilation and decay) in dwarf spheroidal galaxies halos obtained through a Monte-Carlo Jeans analysis of their brightness and kinematic data. We also discuss the systematic uncertainties affecting the calculation of such quantities.

1 Introduction

The concordance cosmological model (Λ -CDM, where “CDM” stands for Cold Dark Matter) predicts that the formation of visible astrophysical structures has been guided by gravitational accretion of baryons onto previously formed dark matter (DM) overdensities, which can be found in the present-day Universe as halos surrounding the baryonic structures (galaxies and clusters of galaxies). The cosmic evolution of these DM halos depends on initial halo parameters such as its mass and distribution – i.e. its DM density profile.

Cosmological simulations of DM segregation show that, inside DM halos at least the size of the Milky Way (MW) one, gravitationally bound DM substructures could have formed. Some of such resulting objects could have been sufficiently massive for accreting enough baryons to initiate star formation, and thus give origin to the variety of dwarf satellite galaxies that we actually observe in the MW halo. In particular, the modern dwarf spheroidal galaxies (dSphs) ¹⁾ are highly DM-dominated and relatively nearby with respect to other cosmological DM reservoirs ^{2, 3)}, and configure therefore as one of the primary targets for observations aimed at detecting potential observable signals from particle DM.

Nearby dSphs have already been the subject of extensive studies with currently operating Imaging Air Cherenkov Telescopes (IACTs) ^{4, 5)}, and are the targets for next-generation IACTs such as the Cherenkov Telescope Array (CTA) ⁶⁾ that provide the easiest separation of signal and background with respect to e.g. the MW center ⁷⁾; on the other hand, the expected DM signal from dSph halos is of low intensity, due to their larger distance and smaller halo mass.

In this contribution, we present a novel derivation of the expected DM content of dSph halos based on the Monte-Carlo (MC) Jeans analysis of the distribution and kinematics of the baryonic matter gravitationally bound inside the potential well. Such an analysis is performed by using the CLUMPY software ⁸⁾, and takes advantage of a common treatment of the input data for the considered dSphs. Its products are the estimated DM density profiles of the dSph halos, that can be in turn used to compute the expected DM γ -ray signal intensity and to rank such targets in view of their observation.

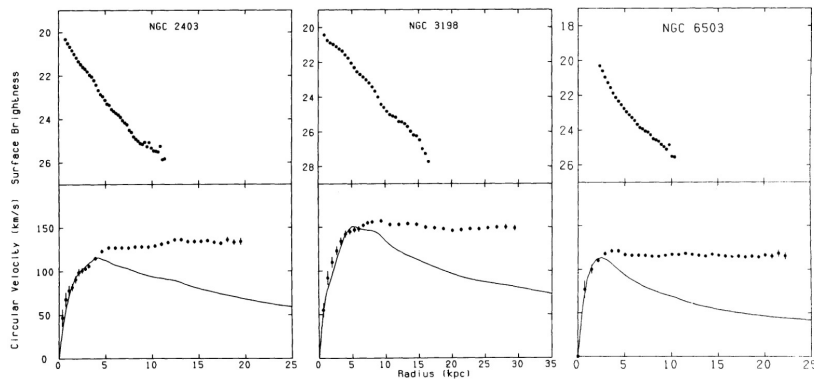


Figure 1: *Upper panel: the distribution of luminous matter in nearby spiral galaxies. Lower panel: the measured circular velocities (dots) of the same targets compared to the theoretical predictions (solid lines) in absence of DM ⁹⁾ (adapted).*

2 The quest for dark matter in the local Universe

DM was first introduced to explain the velocity distribution of galaxies in the Coma cluster, and later adopted to successfully describe the flattening of rotation curves in spiral galaxies ¹⁰⁾. Today, its importance in the energy budget of the Universe – $\sim 85\%$ of the Universe matter content, corresponding to $\sim 23\%$ of the total energy – is paramount to explain at once several astronomical and cosmological observations ^{11, 12, 13)}. The lack of any DM-related electromagnetic (EM) emission implies that we can infer the presence of DM only by looking at its gravitational effects on the baryonic matter ¹⁴⁾ (see Fig. 1) and radiation ¹⁵⁾. Such observations are however unable to provide information on the nature of DM components; as a result, the DM parameter space is still widely unconstrained ¹⁶⁾ (see Fig. 2).

Among the various possibilities, a particularly well motivated family of potential DM components naturally arises from quantum gravity (QG) theories ¹⁷⁾. Such theories predict that modifications of the general relativity at high energies naturally produce a family of weakly-interacting massive particles (WIMPs) that fall outside the Standard Model (SM) paradigm, and therefore

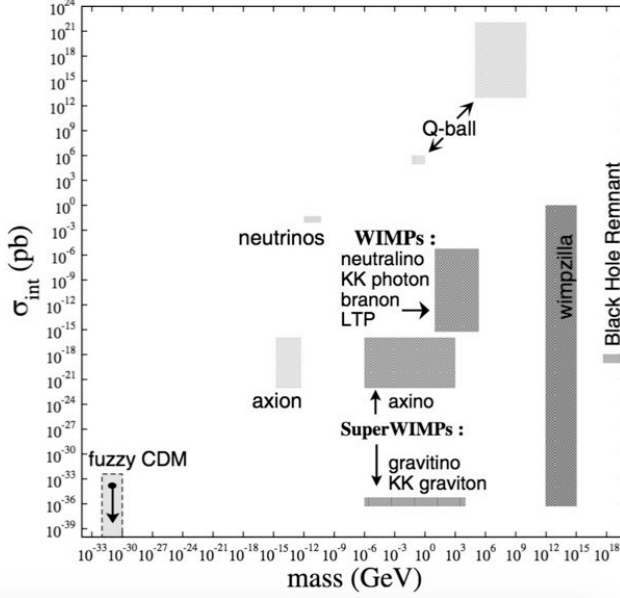


Figure 2: *The zoo of DM candidates, ranked according to their interaction cross section as a function of their mass.*

have no or negligible interactions with SM particles; nevertheless, WIMPs produced in this way can self-interact by either annihilating¹⁸⁾ or decaying¹⁹⁾ into final-state SM particles – among which γ -ray photons that can be detected with appropriate facilities²⁰⁾.

The differential γ -ray flux $d\Phi/dE_\gamma$ expected from annihilation or decay of WIMPs with mass m_χ can be computed as, respectively:

$$\frac{d\Phi_{\text{ann}}}{dE_\gamma} = \frac{\langle\sigma_{\text{int}}v\rangle}{8\pi m_\chi^2} \sum_i \text{BR}_i \frac{dN_\gamma^{(i)}}{dE_\gamma} \int_{\Delta\Omega} d\Omega \int_{\text{l.o.s.}} \rho_{\text{DM}}^2(\ell, \Omega) d\ell \quad (1)$$

$$\frac{d\Phi_{\text{dec}}}{dE_\gamma} = \frac{1}{4\pi m_\chi} \sum_i \Gamma_i \frac{dN_\gamma^{(i)}}{dE_\gamma} \int_{\Delta\Omega} d\Omega \int_{\text{l.o.s.}} \rho_{\text{DM}}(\ell, \Omega) d\ell \quad (2)$$

Inside such equations, the intensity of the final signal is mostly determined

by the amount of DM along the line of sight to the object, that is usually summarized into the so-called astrophysical factors ²⁾ $J(\Delta\Omega)$ (for annihilation) and $D(\Delta\Omega)$ (for decay). Since the astrophysical factors scale with powers of the target distance d ²¹⁾, the best strategy to look for such γ -rays is to target astrophysical DM reservoirs that are large and close enough to provide a significant signal; hence, the dSphs are among the most promising objects along with the Galactic Center (GC) and the most nearby galaxy clusters.

2.1 The dwarf spheroidal galaxies

The dSphs are a subclass of satellites of the Milky Way (MW) and other large Local Group galaxies. They possess a spherical or elliptical appearance, and contain $\mathcal{O}(10^2)$ to $\mathcal{O}(10^7)$ stars ²²⁾. The most striking property of the dSphs is related to their matter content, which appears not to be dominated by the baryonic component. If in fact such systems are old enough to have reached the gravitational equilibrium, owing to the virial theorem one gets a total gravitational mass M_{tot} that is proportional to both the system size R_{vir} and the measured radial velocity dispersion¹ of their components σ_r :

$$M_{\text{tot}} = 3 \frac{R_{\text{vir}} \sigma_r^2}{G} \quad (3)$$

The mass derived in this way is ~ 10 to >1000 times larger than that obtainable from the integrated dSph luminosity, which implies mass-to-light ratios $10 M_{\odot}/L_{\odot} \lesssim M/L \lesssim 10^4 M_{\odot}/L_{\odot}$. In contrast, a baryon-dominated system would exhibit $M/L \sim 1 M_{\odot}/L_{\odot}$.

This places the dSphs among the most DM-dominated objects in the local Universe; however, they are rather light in terms of absolute amount of DM hosted in their halos ($M_{\text{tot}} \lesssim 10^8 M_{\odot}$) if compared to e.g. the GC ($\sim 10^{12} M_{\odot}$) ²⁴⁾ and their distance is at least double than that of the GC (~ 10 kpc) – Segue I, the closest dSph, is located at ~ 23 kpc ²⁵⁾. Nevertheless, due to hosting no emission processes of very-high energy (VHE) radiation, dSphs are free of any significant γ -ray background, making any VHE signal that could be detected from their sky direction a highly compelling signature of DM self-interaction.

To date, there are >50 MW satellites classified as dSphs². Thanks to the

¹Assuming a perfectly spherical symmetry, one gets $\sigma_{\text{tot}}^2 = 3\sigma_r^2$.

²For some of them, the dSph classification is not fully confirmed yet ²⁶⁾.

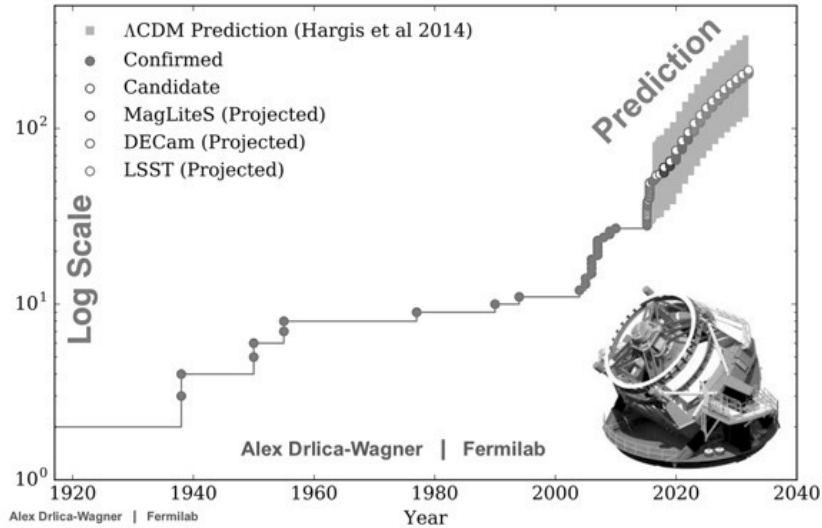


Figure 3: *History of the number increase of known dSphs, and prospects for discoveries of new objects with future optical facilities (courtesy of A. Drlica-Wagner, Fermilab).*

availability of data from recently concluded ²⁷⁾ and current survey projects ²⁸⁾, the number of known confirmed dSphs and candidates is expected to increase with time up to $\mathcal{O}(10^2)$ objects in the next years (see Fig. 3); in addition, the start of operations at facilities like the Vera Rubin Observatory ²⁹⁾ is expected to double such numbers within the next two decades.

2.2 Selection of optimal dwarf galaxies for indirect dark matter searches

The work for deriving the expected DM densities in dSph halos is tightly connected to the CTA science project of indirect DM searches in nearby astrophysical targets, for which the optimal observing strategy relies on selecting those among them with the highest chances of detection. We therefore perform a first selection according to the target distance $d_{\odot} \lesssim 100$ kpc and culmination zenith angle $ZA_{\text{culm}} \lesssim 30^\circ$ with respect to each of the CTA observing sites. The former criterion is adopted due to the decrease of J and D with the distance

Table 1: *Basic properties of the optimal dSphs, ranked in alphabetical order.*

Name	R.A. (hh mm ss)	dec. (dd mm ss)	Distance (kpc)	$ZA_{\text{culm N}}$ (deg)	$ZA_{\text{culm S}}$ (deg)	Ref.
BoöI	14 00 06.0	+14 30 00	65 ± 3	14.3	39.1	30)
CBe	12 26 59.0	+23 54 15	42 ± 2	4.9	48.5	31)
DraI	17 20 12.4	+57 54 55	75 ± 4	29.2	82.5	32)
GruII	22 04 04.8	-46 26 24	53 ± 5	75.2	21.8	33)
RetII	03 35 40.9	-54 03 00	32 ± 2	82.8	29.4	34)
SgrI	18 55 19.5	-30 32 43	31 ± 1	59.3	5.9	35)
SgrII	19 52 40.5	-22 04 05	67 ± 5	50.8	2.6	36)
ScI	01 00 09.4	-33 42 33	84 ± 2	62.5	9.1	37)
Seg1	10 07 04.0	+16 04 55	23 ± 2	12.7	40.7	25)
Sex	10 13 03.0	-01 36 53	84 ± 3	30.4	23.0	38)
TriII	02 13 17.4	+36 10 42	30 ± 2	7.4	60.8	39)
Wil1	10 49 21.0	+51 03 00	38 ± 7	22.3	75.7	25)

(see Sect. 2), the latter is applied since a higher target culmination guarantees to gather the lower energy photons thanks to the minimum atmospheric width.

Then, we remove from the analysis those candidates that do not have adequately populated stellar samples; this is needed since our intent is to use the dSph member stars to trace the density and extension of the DM halo. As a result, our sample is composed by:

- Boötes I (BoöI), Coma Berenices (CBe), Draco I (DraI), Segue 1 (Seg1), Triangulum II (TriII) and Willman 1 (Wil1) in the Northern hemisphere;
- Grus II (GruII), Reticulum II (RetII), Sculptor (ScI), Sextans (Sex), Sagittarius I (SgrI) and Sagittarius II (SgrII) in the Southern hemisphere.

We summarize in Tab. 1 the basic properties of these objects.

3 Jeans analysis of the optimal dwarf spheroidal galaxies

The procedure for evaluating the DM distribution in dSph halos is long debated, with an ample literature in methods and assumptions ^{3, 40, 41, 42, 43}) which sometimes lead to incompatibilities. Moreover, such analyses are in general

performed on a case-by-case basis. We thus provide our own estimation based on a common framework of settings, using the publicly available CLUMPY code.

CLUMPY allows to perform a Markov-Chain Monte Carlo (MCMC) dynamical analysis of the DM halo around a dSph. In detail, the galaxy is treated as a steady-state, collisionless system with spherical symmetry and negligible rotational support, in which the contribution of the stellar component to the total mass can be also neglected. Under such assumptions, the MCMC analysis relies on the solution of the second-order spherical Jeans equation ⁴⁴):

$$\frac{1}{n^*(r)} \left\{ \frac{d}{dr} \left[n^*(r) \overline{v_r^2} \right] \right\} + 2\beta_{\text{ani}}(r) \frac{\overline{v_r^2}}{r} = -\frac{GM_{\text{DM}}(r)}{r} \quad (4)$$

where $n^*(r)$ is the stellar number density, $\overline{v_r^2}$ is the velocity dispersion and $\beta_{\text{ani}}(r)$ is the velocity anisotropy of the dSph. Feeding CLUMPY with a parametric fixed input describing $n^*(r)$ and a set of discrete stellar velocities over which performing the MCMC to determine $\overline{v_r^2}$, Eq. 4 can be solved to obtain $\rho_{\text{DM}}(r)$ as a set of free parameters that characterize the adopted profile.

3.1 MC simulation set-up

First, we fit the brightness density $n^*(r)$ of each galaxy with a 3D Zhao-Hernquist profile ^{45, 46}):

$$n^*(r) = \frac{n_s^*}{\left(\frac{r}{r_s^*}\right)^{\gamma^*} \left[1 + \left(\frac{r}{r_s^*}\right)^{\alpha^*} \right]^{\frac{\beta^* - \gamma^*}{\alpha^*}}} \quad (5)$$

projected onto the corresponding circularized surface brightness profile (see Fig. 4). Then, we collect the most updated data sets of stellar member candidates for each dSph, provided that they contain an adequate number of stars to obtain a significant MCMC fit (see Fig. 5). For those targets with large stellar samples (the so-called “classical” dSphs, plus Seg1 and SgrI), we process the corresponding data sets through an expectation-maximization (EM) algorithm ⁴⁷); for the remaining sources (the “ultra-faint” dSphs), we adopt binary (0/1) memberships already available in the literature.

Finally, we adopt the most conservative priors ⁴⁸) for the treatment of the velocity anisotropy, using the Baes & van Hese profile ⁴⁹):

$$\beta_{\text{ani}}(r) = \frac{\beta_0 + \beta_\infty (r/r_a)^\eta}{1 + (r/r_a)^\eta} \quad (6)$$

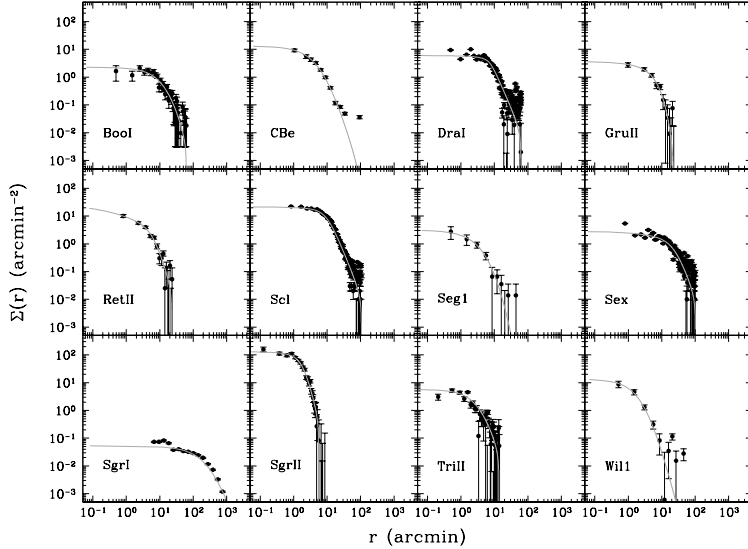


Figure 4: *Best-fit brightness profiles of the analyzed dSphs as a function of the projected radial coordinate from the dSph centroid. In each panel, the projection of the 3D profile resulting from the fit (solid line) is shown superimposed to the corresponding background-subtracted data set (filled dots).*

with 4 free parameters (central anisotropy β_0 , asymptotic anisotropy β_∞ , anisotropy scale radius r_a and sharpness index η). For the DM density, we choose both a cuspy Einasto profile ⁵⁰⁾ with 3 free parameters (DM scale density ρ_s , DM scale radius r_s and DM sharpness index α), and a cored Burkert profile ⁵¹⁾ with only scale density and radius as free parameters:

$$\rho_{\text{DM}}(r) = \begin{cases} \rho_s e^{-\frac{2}{\alpha}[(r/r_s)^\alpha - 1]} & \text{Einasto} \\ \frac{\rho_s}{(1 + \frac{r}{r_s})[1 + (\frac{r}{r_s})^2]} & \text{Burkert} \end{cases} \quad (7)$$

Such choices imply MC fits with a total of 7 and 6 free parameters, respectively. To estimate them through the analysis of their posterior distributions, we run 10 MC chains of 10,000 realizations each for every target. We then derive the distribution of virial radii R_{vir} for each dSph from the output profiles,

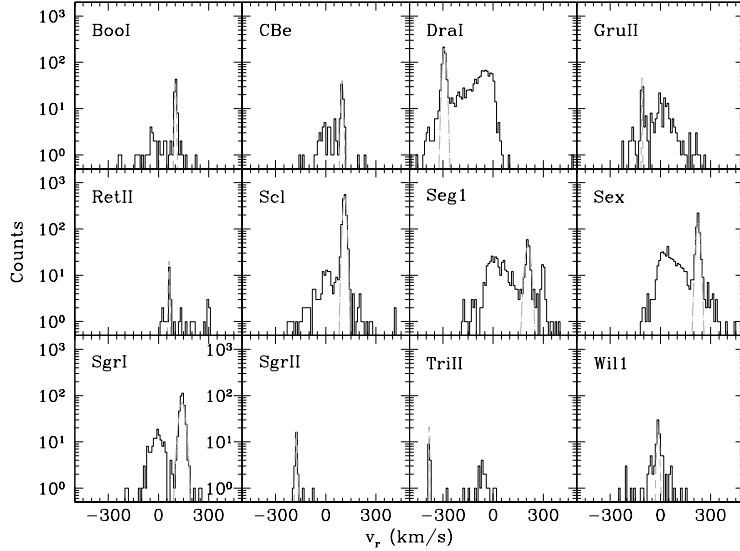


Figure 5: *Distributions of radial velocities for the most updated stellar samples available for each analyzed dSph. For each target, a Gaussian representing the velocity distribution of confirmed member stars obtained either from the application of the EM algorithm (dot-dashed lines) or from the binary classification extracted from the relevant literature (dashed lines) is shown.*

iteratively solving the tidal equation 44):

$$R_{\text{vir}} = d_{\text{GC}} \times \left[\frac{M_{\text{DM}}(d_{\text{GC}})}{\left(2 - \left. \frac{d \ln M_{\text{MW}}}{d \ln r} \right|_{d_{\text{GC}}} \right) \cdot M_{\text{MW}}(d_{\text{GC}})} \right]^{1/3} \quad (8)$$

where M_{DM} is the dSph DM mass enclosed within a certain radius, M_{MW} is the MW mass and d_{GC} is the dSph Galactocentric distance. The properties of the DM halos around dSphs derived in this way are summarized in Tab. 2, and the DM density profiles obtained with such parameters for the six most optimal CTA targets are shown in Fig. 6.

Table 2: *Brightness, kinematic and DM halo properties (both for cuspy and cored profiles) for the analyzed dSphs.*

Name	M_V (mag)	$\langle v_r \rangle$ (km s $^{-1}$)	Ref.	Einasto				Burkert		
				ρ_s ($10^8 M_\odot \text{ kpc}^{-3}$)	r_s (kpc)	α	R_{vir} (kpc)	ρ_s ($10^8 M_\odot \text{ kpc}^{-3}$)	r_s (kpc)	R_{vir} (kpc)
BoöI	-6.3 ± 0.2	100.6 ± 4.3	22, 52)	$0.09^{+0.10}_{-0.07}$	$1.7^{+4.2}_{-1.0}$	$0.51^{+0.33}_{-0.29}$	$5.1^{+10.7}_{-2.2}$	$1.42^{+0.69}_{-0.81}$	$2.2^{+4.2}_{-1.6}$	$15.1^{+30.4}_{-9.6}$
CBe	-4.1 ± 0.5	97.8 ± 5.8	22, 53)	$0.29^{+0.83}_{-0.21}$	$1.2^{+2.9}_{-1.0}$	$0.56^{+0.28}_{-0.28}$	$4.5^{+9.6}_{-3.2}$	$4.7^{+4.1}_{-1.9}$	$0.86^{+3.73}_{-0.65}$	$8.0^{+34.1}_{-5.8}$
DraI	-8.8 ± 0.3	-292.4 ± 9.5	22, 54)	$0.30^{+0.48}_{-0.11}$	$0.58^{+0.14}_{-0.29}$	$0.16^{+0.19}_{-0.02}$	$-4.12^{+0.65}_{-0.55}$	$4.25^{+0.95}_{-1.98}$	$0.283^{+0.056}_{-0.037}$	$4.01^{+0.51}_{-0.11}$
GruII	-3.9 ± 0.2	-109.8 ± 1.8	33, 55)	$0.0039^{+0.0119}_{-0.0024}$	$0.83^{+0.54}_{-0.55}$	$0.65^{+0.25}_{-0.34}$	$0.35^{+1.03}_{-0.32}$	$0.017^{+0.086}_{-0.015}$	$1.12^{+3.91}_{-0.82}$	≤ 9.5
RetII	-3.6 ± 0.2	64.0 ± 3.6	34, 56)	$0.26^{+0.84}_{-0.29}$	$0.61^{+3.35}_{-0.50}$	$0.54^{+0.32}_{-0.28}$	$1.7^{+6.4}_{-1.1}$	$4.4^{+5.9}_{-2.1}$	$0.40^{+3.15}_{-0.32}$	$2.7^{+19.7}_{-1.9}$
SgrI	-11.1 ± 0.5	140 ± 17	22, 57)	$0.0105^{+0.0182}_{-0.0064}$	$6.1^{+1.7}_{-2.0}$	$0.23^{+0.36}_{-0.10}$	$1.56^{+0.34}_{-0.73}$	$0.093^{+0.072}_{-0.051}$	$3.7^{+2.6}_{-1.3}$	≤ 1.7
SgrII	-1.5 ± 0.8	-175.7 ± 5.0	36, 58)	$1.2^{+2.7}_{-1.1}$	$0.35^{+3.12}_{-0.27}$	$0.51^{+0.31}_{-0.28}$	$2.7^{+13.8}_{-1.7}$	$20.1^{+16.3}_{-9.0}$	$0.38^{+3.04}_{-0.32}$	$7.6^{+60.6}_{-6.1}$
Scl	-9.3 ± 0.5	111.5 ± 9.1	22, 59)	$0.29^{+0.55}_{-0.12}$	$0.55^{+0.01}_{-0.30}$	$0.26^{+0.26}_{-0.10}$	$3.56^{+0.44}_{-0.57}$	$3.82^{+0.72}_{-0.79}$	$0.256^{+0.065}_{-0.023}$	$3.95^{+0.17}_{-0.25}$
SegI	-13.5 ± 0.3	206 ± 15	22, 60)	$0.022^{+0.220}_{-0.020}$	$0.59^{+2.76}_{-0.46}$	$0.59^{+0.27}_{-0.33}$	$2.3^{+1.3}_{-2.2}$	$0.065^{+1.72}_{-0.061}$	$0.78^{+3.13}_{-0.63}$	≤ 28
Sex	-5.2 ± 0.4	224 ± 11	22, 59)	$0.026^{+0.078}_{-0.017}$	$3.4^{+3.5}_{-2.4}$	$0.42^{+0.30}_{-0.23}$	$7.8^{+4.4}_{-2.9}$	$0.228^{+0.291}_{-0.084}$	$2.1^{+1.8}_{-1.1}$	$9.9^{+5.7}_{-3.4}$
TriII	-1.8 ± 0.5	-381.7 ± 2.5	39, 61)	$0.022^{+0.230}_{-0.019}$	$0.48^{+3.88}_{-0.41}$	$0.65^{+0.27}_{-0.34}$	$0.37^{+3.20}_{-0.35}$	$0.21^{+4.46}_{-0.20}$	$0.55^{+3.73}_{-0.46}$	≤ 56
Will	-2.7 ± 0.8	-13.6 ± 6.3	22, 62)	$2.6^{+5.0}_{-2.2}$	$0.093^{+0.362}_{-0.045}$	$0.43^{+0.39}_{-0.24}$	$1.05^{+1.16}_{-0.34}$	24^{+61}_{-18}	$0.079^{+1.470}_{-0.049}$	$1.41^{+12.67}_{-0.53}$

3.2 Discussion of analysis caveats

In general, the determination of the DM distribution in dSph halos is affected by several uncertainties and systematics. If not recognized and appropriately removed or mitigated, such spurious contributions may significantly alter the analysis of the dSph stellar kinematics, leading to a wrong estimate of the DM content. The major sources of error are:

- **Difficulty/impossibility to obtain tangential components of the member star velocities** – The possibility to neglect the rotational support in dSph dynamics, quantified by the dispersion of stellar proper motions, is key to consider such objects as DM dominated; in fact, the presence of a non-negligible stellar-velocity tangential component may significantly alter the distribution of measured radial velocities, thus artificially increasing an intrinsically low DM amount. However, since the typical proper motion of a dSph is roughly of $0.2 \div 0.5 \text{ mas yr}^{-1}$ and the inner radial velocity dispersion is of the order of 10 km s^{-1} , the proper-motion dispersion of the dSph member stars is of the order of 0.01 mas yr^{-1} ; for bright stars ($G < 15$), this amount is already at the limit of current and future stellar surveys, such as the *Gaia* data releases (63).
- **Stellar velocity dispersion dominated by tidal forces** – Another source of alteration of the dSph stellar velocity dispersion comes from the risk that the analyzed dwarf galaxy does not reside inside a gravitationally undisturbed DM mini-halo of primordial origin, but is rather a remnant

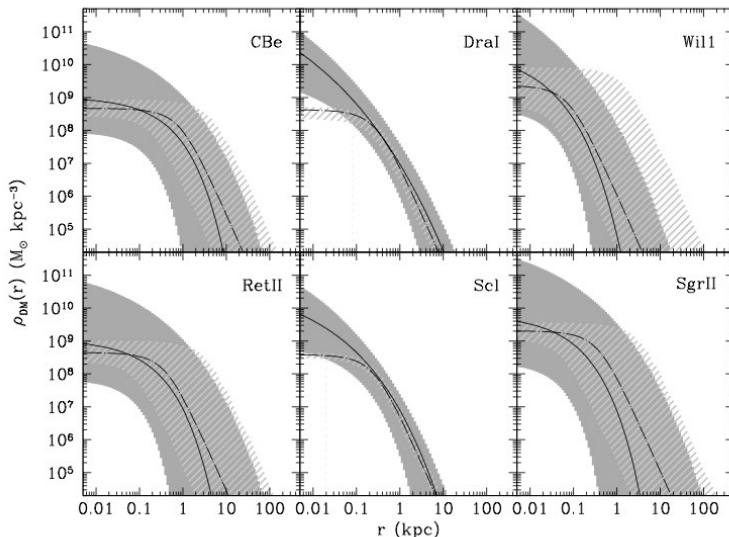


Figure 6: *Cored (shaded area) and cuspy (filled area) density profiles around the six most optimal dSphs (CBe, DraI, Wil1, RetII, Scl, and SgrII).*

of a bigger object that has been tidally disrupted by close encounters with the MW. In the first case, the measured radial velocity dispersion σ_r is ⁴⁴):

$$\sigma_r^{(\text{DM})} = \sqrt{\frac{GM_{\text{DM}}}{3R_{\text{vir}}}} \quad (9)$$

whereas in the second case one gets:

$$\sigma_r^{(\text{tid})} = \sqrt{\frac{2GM_{\text{MW}}R_{\text{vir}}}{3d_{\text{GC}}^2}} \quad (10)$$

It is therefore clear that, lacking hints of ongoing tidal interaction in the target, a large σ_r can potentially lead to its wrong attribution to an extreme DM domination. The current deep stellar surveys may help to identify tidally disrupted sources by detecting the stellar streams produced by the gravitational encounters of the dSph with the MW ⁶⁴), thus

allowing to reanalyze (or exclude) targets located within such features; this might likely be the case of Sgr II, that presumably lies inside the trailing arm of the Sagittarius stream ³⁶).

- **Contamination of member samples by foreground stars** – Since the dSphs are often viewed in projection only, with no or very few hints about surrounding stellar structures, foreground population of stars with age and metallicity that balance the distance difference with respect to the dSph cannot be distinguished through photometric measurements. Therefore, the measurement of spectroscopic velocities is crucial in order to fully disentangle the dSph stellar population by foreground contamination. The erroneous inclusion of such spurious populations may deeply alter the calculation of correct dSph astrophysical factors: this is the case of Seg 1, which has a population of high-velocity foreground stars ($v \sim 300 \text{ km s}^{-1}$) superimposed to the dSph structure ⁶⁵).

4 Summary

In this contribution, we have presented novel data-driven determinations of the DM distribution in dSph halos, based on MC Jeans analysis adopting a common framework for the treatment of input quantities. This effort is ultimately aimed at computing the prospects for the detectability of DM signals in the γ -ray domain with CTA, and the relevance of the limits on average WIMP parameters. To this end, we have down-selected the best candidates of the several tens of known dSphs, based on spectroscopic and photometric measurements.

Then, we have made use of the public CLUMPY code to estimate the DM content of dSph halos, obtaining DM density profiles that can be used for diverse purposes – e.g., the computation of realistic astrophysical factors J and D (see Sect. 2), the ranking of optimal dSph halos in terms of DM content, the study of the different impact of cuspy and cored profiles in the dSph evolution and expected strength of the DM signal, and the construction of scaling relations of J and D with distance and other dSph parameters ²¹) in order to easily estimate the DM amount in newly discovered halos.

Acknowledgements

This work was conducted in the context of the CTA DMEP Working Group. We

gratefully acknowledge financial support from the agencies and organizations listed here: http://www.cta-observatory.org/consortium_acknowledgments. FGS acknowledges financial support from the PRIN MIUR project “ASTRI/CTA Data Challenge” (PI: P. Caraveo), contract 298/2017. CLUMPY is licensed under the GNU General Public License (GPLv2).

References

1. L. Mayer, *Adv. Astron.* **2010**, 278434 (2010).
2. N. W. Evans *et al.*, *Phys. Rev. D* **69**, 123501 (2004).
3. L. E. Strigari *et al.*, *ApJ* **678**, 614 (2008).
4. VERITAS Coll., *PoS* **301**, 904 (2018).
5. MAGIC Coll., *PDU* **35**, 100912 (2022).
6. M. Doro *et al.*, *Astropart. Phys.* **43**, 189 (2013).
7. CTA Cons., *JCAP* **01**, 057 (2021).
8. M. Hütten *et al.*, *Comp. Phys. Comm.* **235**, 336 (2019).
9. T. S. van Albada & R. Sancisi, *Phil. Trans. Roy. Soc. A* **320**, 447 (1986).
10. F. Zwicky, *Helv. Phys. Acta* **6**, 110 (1933).
11. G. Bertone & D. Hooper, *Rev. of Mod. Phys.* **90**, 045002 (2018).
12. D. Clowe *et al.*, *ApJ* **604**, 596 (2004).
13. Planck Coll., *A&A* **641**, A5 (2020).
14. E. Corbelli & P. Salucci, *MNRAS* **311**, 441 (2000).
15. R. S. Ellis, *Phil. Trans. Roy. Soc. A* **368**, 967 (2010).
16. L. Roszkowski, *Pramana* **62**, 389 (2004).
17. J. A. R. Cembranos, *Phys. Rev. Lett.* **102**, 141301 (2009).
18. M. Reichert & J. Smirnov, *Phys. Rev. D* **101**, 063015 (2020).

19. X. Calmet & B. Latosh, *Eur. Phys. J. C* **78**, 520 (2018).
20. L. Bergström *et al.*, *Astropart. Phys.* **9**, 137 (1998).
21. A. B. Pace & L. E. Strigari, *MNRAS* **482**, 3480 (2019).
22. A. W. McConnachie, *AJ* **144**, 4 (2012).
23. M. Fabrizio *et al.*, *A&A* **580**, A18 (2015).
24. M. Merafina *et al.*, *Phys. Rev. D* **102**, 083015 (2020).
25. J. T. A. de Jong *et al.*, *AJ* **135**, 1361 (2008).
26. B. Willman *et al.*, *AJ* **129**, 2692 (2011).
27. DES Coll., *Nucl. and Part. Phys. Proc.* **273**, 302 (2016).
28. A. Drlica-Wagner *et al.*, *ApJL* **833**, L5 (2016).
29. J. A. Tyson, *Proc. SPIE* **4836**, 10 (2002).
30. S. Okamoto *et al.*, *ApJ* **744**, 96 (2012).
31. I. Musella *et al.*, *ApJL* **695**, L83 (2009).
32. N. Hernitschek *et al.*, *ApJ* **817**, 73 (2016).
33. A. Drlica-Wagner *et al.*, *ApJ* **813**, 109 (2015).
34. K. Bechtol *et al.*, *ApJ* **807**, 50 (2015).
35. A. T. Valcheva *et al.*, *MNRAS* **446**, 730 (2015).
36. B. P. M. Laevens *et al.*, *ApJ* **813**, 44 (2015).
37. C. E. Martínez-Vázquez *et al.*, *MNRAS* **454**, 1509 (2015).
38. G. E. Medina *et al.*, *ApJ* **855**, 43 (2018).
39. B. P. M. Laevens *et al.*, *ApJL* **802**, L18 (2015).
40. V. Bonnivard *et al.*, *MNRAS* **453**, 849 (2015).
41. A. Geringer-Sameth *et al.*, *ApJ* **801**, 74 (2015).

42. G. D. Martinez *et al.*, MNRAS **451**, 2524 (2015).
43. K. Hayashi *et al.*, MNRAS **461**, 2914 (2016).
44. J. Binney & S. Tremaine, Galactic Dynamics: Second Edition (2008).
45. L. Hernquist, ApJ **356**, 359 (1990).
46. H. Zhao, MNRAS **278**, 488 (1996).
47. M. G. Walker *et al.*, AJ **137**, 3109 (2009).
48. V. Bonnivard *et al.*, MNRAS **446**, 3002 (2015).
49. M. Baes & E. van Hese, A&A **471**, 419 (2007).
50. J. Einasto, Tr. Astrof. Inst. Alma-Ata **5**, 87 (1965).
51. A. Burkert, ApJL **447**, L25 (1995).
52. S. E. Koposov *et al.*, ApJ **736**, 146 (2011).
53. J. D. Simon & M. Geha, ApJ **670**, 313 (2007).
54. M. G. Walker *et al.*, MNRAS **448**, 2717 (2015).
55. J. D. Simon *et al.*, ApJ **892**, 137 (2020).
56. M. G. Walker *et al.*, ApJ **808**, 108 (2015).
57. R. A. Ibata *et al.*, AJ **113**, 634 (1997).
58. N. Longeard *et al.*, MNRAS **491**, 356 (2020).
59. M. G. Walker *et al.*, AJ **137**, 3100 (2009).
60. J. D. Simon *et al.*, ApJ **733**, 46 (2011).
61. E. N. Kirby *et al.*, ApJ **838**, 83 (2017).
62. B. Willman *et al.*, AJ **142**, 128 (2011).
63. Gaia Coll., A&A **616**, A12 (2018).
64. B. Mutlu-Pakdil *et al.*, ApJ **863**, 25 (2018).
65. V. Bonnivard *et al.*, MNRAS **462**, 223 (2016).

NA62 results on Dark Sector searches

Jan Jerhot*

*Center for Cosmology, Particle Physics and Phenomenology
Université Catholique de Louvain
Chemin du Cyclotron 2, B-1348 Louvain-la-Neuve, Belgium*

*for the NA62 Collaboration: A. Akmete, R. Aliberti, F. Ambrosino, R. Amendola, B. Angelucci, A. Antonelli, G. Anzivino, R. Arcidiacono, T. Bache, A. Baeva, D. Baigarashev, L. Bandiera, M. Barbanera, J. Bernhard, A. Biagioni, L. Bician, C. Biino, A. Bizzeti, T. Blazek, B. Bloch-Devaux, P. Boboc, V. Bonaiuto, M. Boretto, M. Bragadireanu, A. Briano Olvera, D. Britton, F. Brizioli, M.B. Brunetti, D. Bryman, F. Bucci, T. Capussela, J. Carmignani, A. Ceccucci, P. Cenci, V. Cerny, C. Cerri, B. Checcucci, A. Conovaloff, P. Cooper, E. Cortina Gil, M. Corvino, F. Costantini, A. Cotta Ramusino, D. Coward, P. Cretaro, G. D'Agostini, J. Dainton, P. Dalpiaz, H. Danielsson, M. D'Errico, N. De Simone, D. Di Filippo, L. Di Lella, N. Doble, B. Dობрич, F. Duval, V. Duk, D. Emelyanov, J. Engelfried, T. Enik, N. Estrada-Tristan, V. Falaleev, R. Fantechi, V. Fascianelli, L. Federici, S. Fedotov, A. Filippi, R. Fiorenza, M. Fiorini, O. Frezza, J. Fry, J. Fu, A. Fucci, L. Fulton, E. Gamberini, L. Gatignon, G. Georgiev, S. Ghinescu, A. Gianoli, M. Giorgi, S. Giudici, F. Gonnella, K. Gorshanov, E. Goudzovski, C. Graham, R. Guida, E. Gushchin, F. Hahn, H. Heath, J. Henshaw, Z. Hives, E.B. Holzer, T. Husek,

Abstract

NA62 is a precision physics experiment studying charged kaons and their decay products with an unprecedented accuracy (measurement of the $K^+ \rightarrow \pi^+ \nu \bar{\nu}$ branching ratio of the order of 10^{-11}), allowing indirect probes of new physics scales up to $\mathcal{O}(100)$ TeV. NA62 experiment also searches directly for weakly interacting particles of up to $\mathcal{O}(100)$ MeV masses in kaon decays and up to $\mathcal{O}(1)$ GeV masses when running in the beam dump mode. For both modes of direct searches, NA62 has been collecting data since 2021 after a successful 2016-18 run 1. Past results and future prospects are presented in this talk.

O. Hutanu, D. Hutchcroft, L. Iacobuzio, E. Iacopini, E. Imbergamo, B. Jenninger, J. Jerhot, R.W. Jones, K. Kampf, V. Kekelidze, D. Kereibay, S. Kholodenko, G. Khoriauli, A. Khotyantsev, A. Kleimenova, A. Korotkova, M. Koval, V. Kozhuharov, Z. Kucerova, Y. Kudenko, J. Kunze, V. Kurochka, V. Kurshetsov, G. Lanfranchi, G. Lamanna, E. Lari, G. Latino, P. Laycock, C. Lazzeroni, M. Lenti, G. Lehmann Miotto, E. Leonardi, P. Lichard, L. Litov, P. Lo Chiatto, R. Lollini, D. Lomidze, A. Lonardo, P. Lubrano, M. Lupi, N. Lurkin, D. Madigozhin, I. Mannelli, A. Mapelli, F. Marchetto, R. Marchevski, S. Martellotti, P. Massarotti, K. Massri, E. Maurice, A. Mazzolari, M. Medvedeva, A. Mefodev, E. Menichetti, E. Migliore, E. Minucci, M. Mirra, M. Misheva, N. Molokanova, M. Moulson, S. Movchan, M. Napolitano, I. Neri, F. Newson, A. Norton, M. Noy, T. Numao, V. Obraztsov, A. Okhotnikov, A. Ostankov, S. Padolski, R. Page, V. Palladino, I. Panichi, A. Parenti, C. Parkinson, E. Pedreschi, M. Pepe, M. Perrin-Terrin, L. Peruzzo, P. Petrov, Y. Petrov, F. Petrucci, R. Piandani, M. Piccini, J. Pinzino, I. Polenkevich, L. Pontisso, Yu. Potrebenikov, D. Protopopescu, M. Raggi, M. Reyes Santos, M. Romagnoni, A. Romano, P. Rubin, G. Ruggiero, V. Ryjov, A. Sadosky, A. Salamon, C. Santoni, G. Saracino, F. Sargeni, S. Schuchmann, V. Semenov, A. Sergi, A. Shaikhiev, S. Shkarovskiy, M. Soldani, D. Soldi, M. Sozzi, T. Spadaro, F. Spinella, A. Sturgess, V. Sugonyaev, J. Swallow, A. Sytov, G. Tinti, A. Tomczak, S. Trilov, M. Turisini, P. Valente, B. Velghe, S. Venditti, P. Vicini, R. Volpe, M. Vormstein, H. Wahl, R. Wanke, V. Wong, B. Wrona, O. Yushchenko, M. Zamkovsky, A. Zinchenko.

1 Introduction

Fixed-target experiments can probe regions in the parameter space (m_X, C_X) of New Physics (NP) particle mass m_X and coupling C_X to the Standard Model (SM) particles complementary to those probed by the collider experiments operating at the so-called energy frontier that directly probe mass scales of $\mathcal{O}(1)$ TeV. Fixed-target experiments operate at smaller centre of mass energies but can collect very large statistics while keeping the backgrounds under control, the so-called intensity frontier. At the intensity frontier, very large mass scales ($\gtrsim 100$ TeV) can be probed indirectly, through precision measurements of the SM processes and searches for SM-forbidden decays, and smaller mass scales ($\mathcal{O}(1)$ MeV to $\mathcal{O}(1)$ GeV) can be probed directly¹ for very small NP-SM couplings C_X . This summary will discuss the *direct* searches for NP particles for m_X and C_X values particularly interesting for models describing hypothetical mediators between Dark Matter and Standard Model particles, collectively called the Dark Sector portals. As well as providing an interaction between the SM and the DM sector, these mediators can often provide an explanation of some observations not described by the SM (e.g. neutrino masses, SM mass hierarchy, etc.).

The following table summarizes four portals that appear frequently in the literature and that are targeted as the main benchmark scenarios by the Physics Beyond Colliders initiative¹). Details of the fields and coupling constants involved will be given in dedicated sections.

Table 1: *Dark Sector portals.*

NP Particle	type	Dark Sector portal (dim ≤ 5)
HNL ² (N_I)	fermion	$F_{\alpha I}(\bar{L}_\alpha H)N_I$
dark photon (A'_μ)	vector	$-\frac{\varepsilon}{2 \cos \theta_W} F'_{\mu\nu} B^{\mu\nu}$
dark Higgs (S)	scalar	$(\mu S + \lambda S^2)H^\dagger H$
axion/ALP ³ (a)	pseudoscalar	$\frac{C_{aX}}{\Lambda} a X_{\mu\nu} \tilde{X}^{\mu\nu}, \frac{C_{af}}{\Lambda} \partial_\mu a \bar{f} \gamma^\mu \gamma^5 f$

¹By direct searches we mean the search for the production of NP particles in SM decays or NP particle decays into SM particles.

These new states can be searched for directly at fixed-target facilities in two types of processes:

- Search for the decay of a NP particle into SM final states seen by the detector, which allows the reconstruction of the original NP particle;
- Search for the decay of a SM particle into SM and NP particles where the NP particles can be reconstructed from the knowledge of the SM initial and final states even if the NP particle does not decay back to SM final states and escapes detection.

The following sections will describe the search for the four Dark Sector portal particles in both types of searches at the NA62 experiment.

2 NA62 experiment

The NA62 experiment is a fixed-target experiment at the CERN North Area and is served with a 400 GeV/ c proton beam from the SPS. NA62 is a multi-purpose experiment covering a broad kaon and beam-dump physics programme with the main goal of the measurement of the branching ratio of the very rare $K^+ \rightarrow \pi^+ \nu \bar{\nu}$ decay with 10% precision. About 4×10^{12} kaon decays have been collected during the data-taking period 2016-2018 (Run 1) and the result of the corresponding $\mathcal{B}_{K^+ \rightarrow \pi^+ \nu \bar{\nu}}$ measurement is $\mathcal{B}_{K^+ \rightarrow \pi^+ \nu \bar{\nu}} = (10.6 \pm 4.0) \times 10^{-11}$ ²). Data-taking resumed in 2021 (Run 2) after the CERN Long Shutdown 2 (LS2).

2.1 Kaon mode

In standard data-taking mode, called the *kaon mode*, the 400 GeV/ c proton beam impinges on a beryllium target, producing a secondary beam from which a 75 GeV/ c component is selected using movable copper-iron collimators called TAXes, located about 23 m from the target. The 75 GeV/ c secondary beam has a ~ 750 MHz particle rate and consists of about 6% K^+ . The kaons in the beam are selected using a Cherenkov counter detector (KTAG), which also provides the timing for the kaon tracks, while their momenta are measured by a silicon pixel spectrometer (GTK). The particle beam then enters a 117 m

²Heavy neutral lepton.

³Axion-like particle.

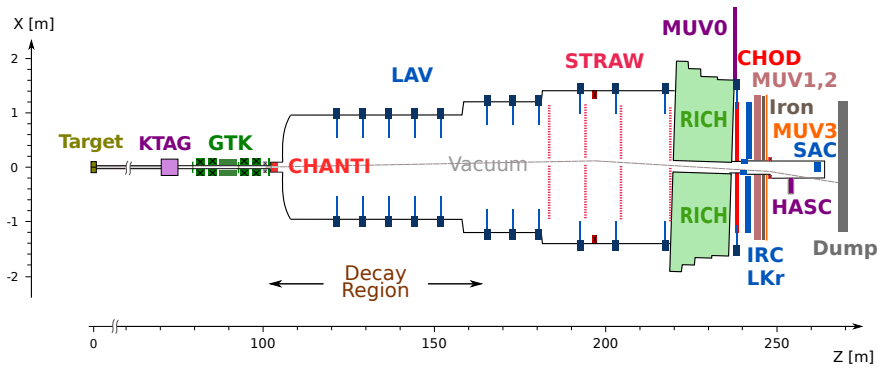


Figure 1: Schematic layout of the NA62 experiment in the X - Z plane in 2018 2).

long vacuum vessel where about 14% of the beam kaons decay in the fiducial volume (FV) that occupies the first about 75 m of the vacuum vessel. The momenta of the kaon decay products are measured using the STRAW spectrometer, consisting of 4 straw stations and a 0.9 Tm magnet. The vacuum vessel is followed by a ring-imaging Cherenkov counter (RICH) optimized for the momentum range 15-35 GeV/ c , to separate the final state π^+ and μ^+ 5). Further particle identification (PID) is by a sequence of calorimeters: the electromagnetic calorimeter (LKr) and hadronic calorimeters (MUV1 and MUV2). Muon identification is provided by a scintillating-tile muon detector (MUV3), located behind an 80 cm thick iron wall. The RICH and the charged hodoscope (CHOD) also provide the timing for the tracks of the final state particles.

2.2 Beam-dump mode

The experiment can also operate in a so-called *beam-dump mode* to search for NP particles too heavy to be produced in the kaon decays. In the beam-dump mode, the beryllium target is lifted from the beam line and the TAX collimators are closed, effectively dumping the 400 GeV/ c beam. Only neutrinos, muons and hypothetical NP particles produced in the interaction of the beam with the material of the TAX and in secondary particle decays can penetrate the TAX

and reach the NA62 decay volume. The currents of a set of dipole magnets, used for the modulation of the beam selected by TAX in the kaon mode, are set to produce magnetic fields in the same direction in the beam-dump mode in order to sweep the muons from the decay volume acceptance since the halo muon flux is the dominant background in the beam-dump mode³). The detectors preceding the decay volume are not used in the beam-dump data analyses except for an upstream veto (ANTI0), which allows further reduction of the muon halo background at the analysis level.

Three trigger lines are implemented in beam-dump mode:

1. Control, triggered by total deposited energy in the LKr of above 1 GeV and at least one reconstructed LKr cluster;
2. Q1/20, triggered by at least one signal in CHOD and downscaled by 20;
3. H2, triggered by two in-time signals in different CHOD tiles.

The low particle rate in beam-dump mode allows data to be collected at an increased proton beam intensity (about a factor 1.5 higher than in the kaon mode) resulting in rates of Control, Q1/20 and H2 triggers for the 4, 14 and 16 kHz respectively.

In 2021, data from about 1.4×10^{17} protons dumped on TAX (POT) were collected at NA62 during a period of 10 days of operation in the beam-dump mode. During the whole of Run 2 a total of about $N_{\text{POT}} = 10^{18}$ POT is expected.

3 Search for heavy neutral leptons

The general form of the HNL portal is

$$\mathcal{L} \supset F_{\alpha I} (\bar{L}_\alpha H) N_I, \quad (1)$$

where H is the Higgs doublet, L_α is the left-handed doublet of the SM neutrino of flavour α , N_I is the I -th HNL field and we sum over the flavour indices. Upon breaking the electroweak symmetry and diagonalizing the neutrino mass terms one obtains mixing terms between the neutrinos ν and HNLs L , typically parametrized by elements of matrix U for the respective flavours. Processes involving HNLs can then be obtained from the neutrino processes by an exchange $\nu_\alpha \rightarrow U_{\alpha I} L_I$. In the minimal scenario with one HNL, one can express

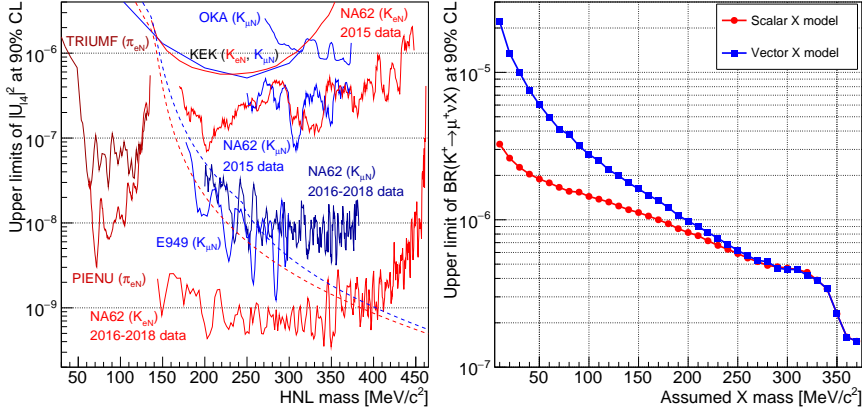


Figure 2: *Left*: UL at 90% CL on $|U_{\ell 4}|^2$ from production searches, red: $|U_{e4}|^2$, blue: $|U_{\mu 4}|^2$. *Right* UL on $\mathcal{B}(K^+ \rightarrow \mu^+ \nu X)$, where X is scalar or vector.

the branching ratio of the HNL production in a decay of a kaon K^+ to a charged lepton l^+ as

$$\mathcal{B}(K^+ \rightarrow \ell^+ N) = \mathcal{B}(K^+ \rightarrow \ell^+ \nu) \cdot \rho_\ell(m_N) \cdot |U_{l4}|^2, \quad (2)$$

where ρ_ℓ is a kinematic factor.

A search for HNL production in K^+ decays has been performed at NA62 in the Run 1 dataset in two independent analyses: with a muon⁶⁾ and with a positron⁷⁾ in the final state and with the HNL escaping detection.

The strategy of these analyses is to search for a spike in the missing mass spectrum $m_{\text{miss}}^2 = (P_K - P_\ell)^2$ that would correspond to the HNL mass m_N . The scan in m_N is performed in steps of $\mathcal{O}(1)$ MeV/ c^2 in mass ranges: 144–462 MeV/ c^2 for the $K^+ \rightarrow e^+ N$ decay and 200–384 MeV/ c^2 for the $K^+ \rightarrow \mu^+ N$ decay. The upper limits on $|U_{e4}|^2$ and $|U_{\mu 4}|^2$ obtained are plotted in Fig.2, left.

The analysis is also re-interpreted as a search for decay $K^+ \rightarrow \mu^+ \nu X$, where X is a scalar or vector. The corresponding upper limits on the branching ratios of these two cases, given the mass of particle X , are plotted in Fig.2, right. Another re-interpretation is a search for decay $K^+ \rightarrow \mu^+ \nu \nu \bar{\nu}$, where the upper limit obtained on the branching ratio⁴ is $\mathcal{B}(K^+ \rightarrow \mu^+ \nu \nu \bar{\nu}) < 1.0 \times 10^{-6}$.

⁴The predicted SM branching ratio is of the order 10^{-16} .

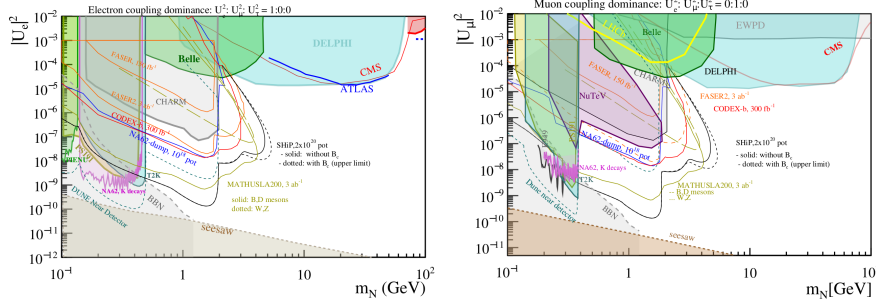


Figure 3: UL at 90% CL on $|U_{\ell 4}|^2$ (left: $|U_{e4}|^2$, right: $|U_{\mu 4}|^2$) comparison with beam-dump searches. Blue contour: projected NA62 sensitivities at $N_{\text{POT}} = 10^{18}$ combining searches for all kinematically allowed decay channels, including channels with open kinematics.

NA62 is also competitive in searches for HNL with masses ~ 1 GeV with the full statistics that will be collected in Run 2 in the beam-dump mode, see Fig. 3 8).

4 Search for dark photons

The Dark photon A' is a vector particle corresponding to a new $U(1)$ gauge symmetry. In the “minimal scenario” the dark photon interacts with the SM hypercharge through kinetic mixing term

$$\mathcal{L} \supset -\frac{\varepsilon}{2 \cos \theta_W} F'_{\mu\nu} B^{\mu\nu}, \quad (3)$$

where $F'_{\mu\nu} = \partial_\mu A'_\nu - \partial_\nu A'_\mu$, $B_{\mu\nu}$ is the SM hypercharge field strength tensor, θ_W is the Weinberg angle and ε is the coupling constant.

Dark photons can be produced through two mechanisms in the beam-dump mode at NA62 in proton-nucleus interactions:

- Bremsstrahlung production: $p + N \rightarrow X + A'$;
- meson-mediated production: $p + N \rightarrow X + M$, $M \rightarrow A' + \gamma(\pi^0)$, where $M \in \{\pi^0, \eta, \rho, \omega, \dots\}$.

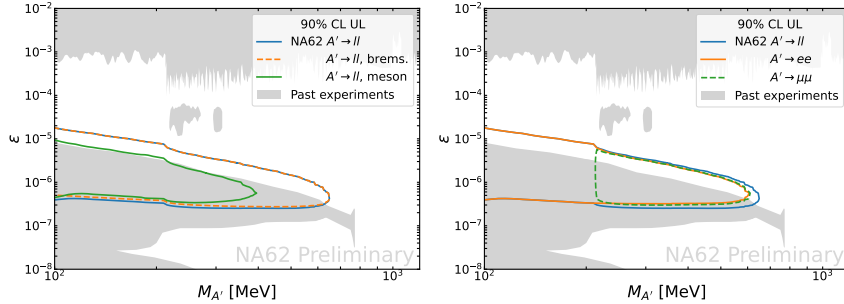


Figure 4: *NA62 sensitivity for dark photons, assuming 0 observed events in 1.4×10^{17} POT, per production mechanism (left) and per decay mode (right).*

The two mechanisms differ cross-sections and the angle-momentum distribution of the radiated dark photons, see NA62 sensitivity in Fig. 4 left. For dark photon masses $M_{A'} < 700$ MeV, the decay width is dominated by the lepton-antilepton decays, see Fig. 4 right. The expected dark photon yield N_{exp} is given by

$$N_{\text{exp}} = N_{\text{POT}} \times \chi(pp \rightarrow A') \times \mathcal{B}(A' \rightarrow \ell^+ \ell^-) \times P_{RD}(\varepsilon) \times A_{\text{acc}} \times A_{\text{trig}}, \quad (4)$$

where $\chi(pp \rightarrow A')$ is the dark photon emission probability, $\mathcal{B}(A' \rightarrow \ell^+ \ell^-)$ is the branching ratio, P_{RD} is the probability to decay in the NA62 decay volume and A_{acc} (A_{trig}) is the signal selection (trigger) efficiency.

A search for dark photon decays to a $\mu^+ \mu^-$ pair has been performed at NA62 with a sample with $N_{\text{POT}} = 1.4 \times 10^{17}$ selected using the H2 trigger in the beam-dump mode. The strategy of this analysis is to find the secondary $\mu^+ \mu^-$ vertex in the decay volume and reconstruct the primary vertex as a point of closest distance of approach of the reconstructed A' track to the proton beam. The primary vertex is expected to lie near the beam impact point on the TAX, see Fig. 5 left. Signal and control regions (SR, CR) are selected as $\pm 3\sigma$ in each axis of the expected signal distribution and are kept blinded in the data until the analysis is finalized.

The selection criteria are 2 tracks of opposite charge in coincidence in time with the trigger and with each other. The particle identification requires

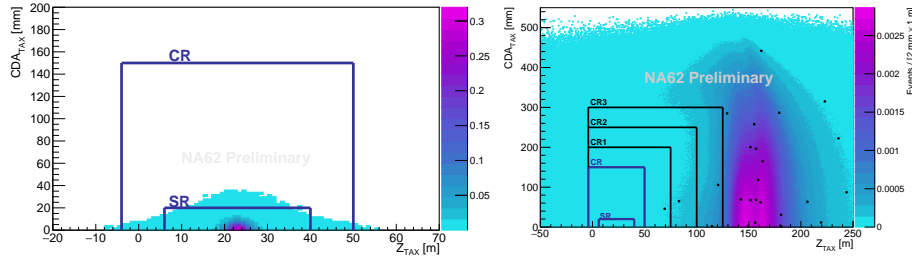


Figure 5: *Left: Signal MC and definition of control (CR) and signal regions (SR). Right: Data-MC comparison, SR closed.*

a single hit in MUV3 for each track and a ratio of energy deposited in the LKr and momentum $E/p < 0.2$. Additionally, no in-time activity in the LAV is allowed to reduce the background from secondary interaction of halo muons.

After applying the LAV veto, the dominant source of background is due to a random pairing of two halo muons from interactions of uncorrelated protons. To evaluate this background a control sample selected with the Q1 trigger in the absence of H2 has been used. See Fig.5 right and Tab. 2 for the comparison of the number of expected and observed background events.

Table 2: *Summary of expected $\mu^+\mu^-$ events from combinatorial background (N_{exp}), the related uncertainty (δN_{exp}), the observed events in data (N_{obs}) and the probability to obtain a likelihood L for data-MC compatibility equal or worse than that corresponding to N_{obs} ($P_{L \leq L_{\text{obs}}}$).*

	$N_{\text{exp}} \pm \delta N_{\text{exp}}$	N_{obs}	$p_{N \geq N_{\text{obs}}}$	$p_{L \leq L_{\text{obs}}}$
outside CR	26.3 ± 3.4	28	0.41	0.74
CR3	1.70 ± 0.22	2	0.25	0.25
CR2	0.58 ± 0.07	1	0.44	0.44
CR1	0.29 ± 0.04	1	0.50	0.68
CR1+2+3	2.57 ± 0.33	4	0.26	0.24
CR	0.17 ± 0.02	0	1.0	1.0
SR	0.016 ± 0.002	-	-	-

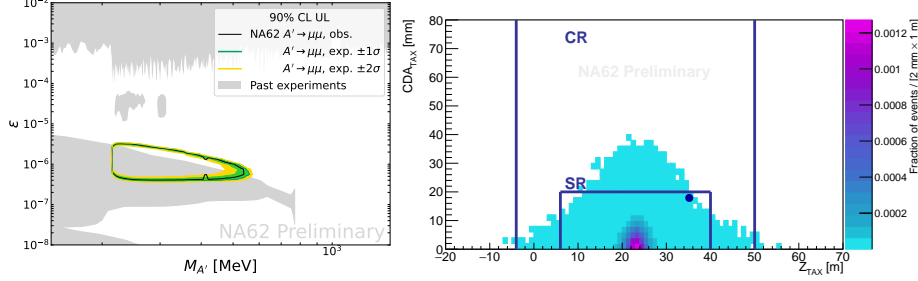


Figure 6: *Left: Final result with upper limit at 90% CL. Right: Signal MC - data, 1 event observed - counting experiment with 2.4σ significance. Signal shape not taken into account for the significance.*

No events have been observed in the CR. After opening the SR, one event with invariant mass ~ 411 MeV has been found. The corresponding upper limit at 90% CL is the region enclosed by black contour in Fig. 6 right. As a counting experiment, the global significance of the event observed is 2.4σ . Note, however, that the track time difference is about two standard deviations from the value of zero expected for in time tracks and that the extrapolation of the corresponding track to the impact point is barely in the SR, see Fig. 6 right, suggesting that the event found could be a combinatorial background event.

5 Search for axion-like particles

Axions were originally predicted as a possible explanation of the CP conservation in strong interactions, called the Strong CP problem. A more general case with various possible couplings to the SM not necessarily addressing the strong CP problem (axion-like particle/ALP) is usually considered:

- SM gauge boson coupling: $\mathcal{L} \supset \frac{C_{XX}}{\Lambda} a X_{\mu\nu} \tilde{X}^{\mu\nu}$, $X \in \{B, W, G\}$;
- SM fermion coupling: $\mathcal{L} \supset \frac{C_{ff}}{\Lambda} \partial_\mu a \bar{f} \gamma^\mu \gamma^5 f$, $f \in \{q, \ell\}$.

If one of the ALP-SM couplings, C_{qq} , C_{gg} , C_{WW} is non-zero ALPs can be produced in flavour-changing neutral current decays, such as $B \rightarrow K^{(*)} a$ and

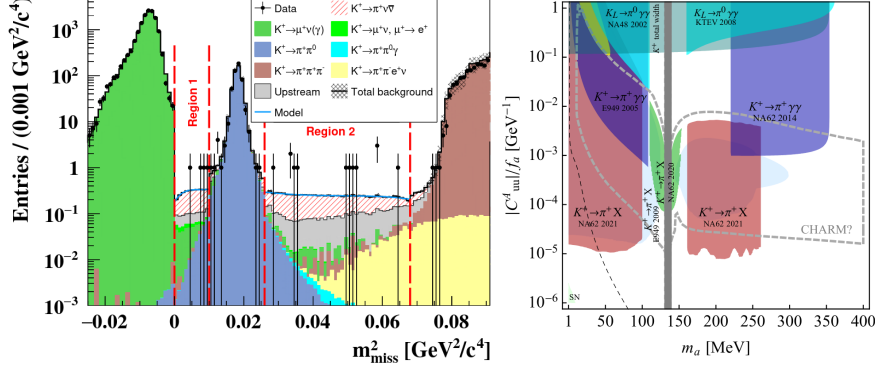


Figure 7: *Left: Expected and observed number of $K^+ \rightarrow \pi^+ \nu \bar{\nu}$ events as a function of the reconstructed m_{miss}^2 for the 2018 data set ⁴⁾. Right: Bounds on flavor-diagonal pseudoscalar quark couplings: coupling of ALP to up quarks ⁹⁾.*

$K \rightarrow \pi a$. Since the decay $K^+ \rightarrow \pi^+ a$ would have the same signature as the $K^+ \rightarrow \pi^+ \nu \bar{\nu}$ decay, it would appear as a peak above the continuous missing invariant mass spectrum of the $K^+ \rightarrow \pi^+ \nu \bar{\nu}$ decay, see the $K^+ \rightarrow \pi^+ \nu \bar{\nu}$ spectrum in 2018 NA62 data in Fig. 7 left. See Fig. 7 right for the upper limit obtained on the exclusion in the parametric space (m_a, C_{uu}) for the case of an ALP coupling to SM up-quarks based on the NA62 Run 1 data.

Depending on the coupling of ALPs to the SM, ALPs can be produced in the TAX in the beam-dump mode in various ways:

- photon-mediated (Primakoff) production from both off- and on-shell photons ^{10, 11)};
- flavour-changing neutral current B meson decays ¹²⁾;
- through mixing with other neutral pseudoscalars (π^0, η, η') ¹³⁾;
- interaction of secondary muons with the TAX nuclei ¹⁴⁾.

NA62 is sensitive to various decay channels (di-photon, di-lepton, hadronic) of ALPs of masses and couplings that have not yet been probed by other experiments, see Fig. 8 left for photonic coupling and right for gluonic coupling.

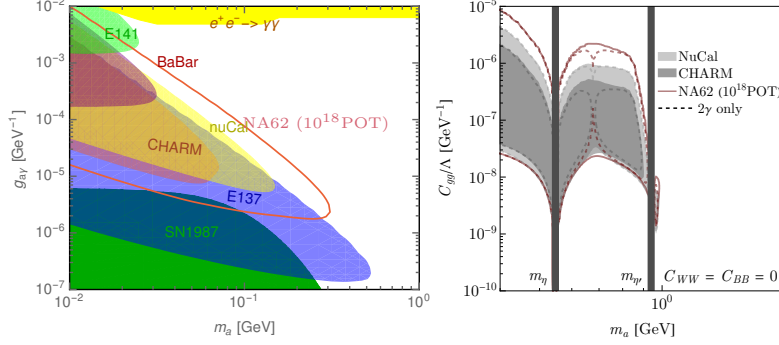


Figure 8: *NA62 Run 2 sensitivity with respect to past exclusions. Left: $a \rightarrow 2\gamma$ search for $g_{a\gamma} = C_{\gamma\gamma}/\Lambda$ coupling scenario ¹¹⁾. Right: $a \rightarrow$ hadrons and $a \rightarrow 2\gamma$ search for C_{gg} coupling-only ¹³⁾.*

6 Search for dark scalars

In the minimal model, a dark scalar S is coupled to the SM Higgs boson through the $H^\dagger H$ operator as

$$\mathcal{L} \supset -(\mu S + \lambda S^2)H^\dagger H. \quad (5)$$

Below the electroweak symmetry breaking scale H is substituted by $(v + h)\sqrt{2}$ and non-zero coupling μ would lead to mixing between S and h , which can be parametrized for small μ as

$$\theta \simeq \theta = \frac{\mu v}{m_h^2 - m_S^2}, \quad (6)$$

where $v = 246$ GeV.

At loop level, the dark scalar can be produced in flavour-changing neutral current processes and therefore, as in the case of ALPs, would appear at NA62 in the kaon mode as a bump above the $K^+ \rightarrow \pi^+ \nu \bar{\nu}$ spectrum. See Fig. 9 left for the exclusion in the $(m_S, \sin \theta)$ parametric space, corresponding to the full Run 1 statistics.

In the NA62 beam-dump mode, dark scalars can be produced in decays of secondary B mesons produced in the TAX. With the full Run 2 beam-dump

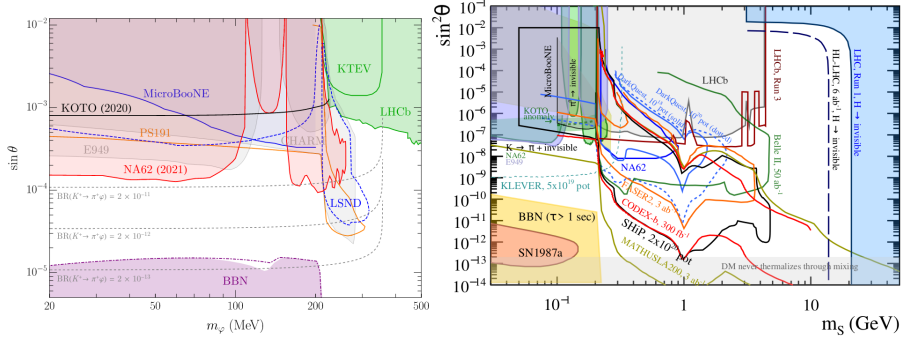


Figure 9: Excluded regions of $(m_S, \sin\theta)$ parameter space for S decaying only to visible SM particles. Left: exclusion from $K^+ \rightarrow \pi^+ + \text{inv.}$ and $\pi^0 \rightarrow \text{inv.}$ decays ⁹⁾ (red). Right: Projection for NA62 in the beam-dump mode 10^{18} POT $S \rightarrow \mu\mu$ (blue) ⁸⁾.

data sample, NA62 is sensitive in yet unexplored regions of the dark scalar parameter space, see Fig. 9 right, with the dark scalar decays to ee , $\mu\mu$ and $\pi\pi$ pairs.

7 Conclusion

NA62 is a multipurpose experiment that as well as the main goal of $K_{\pi\nu\bar{\nu}}$ and precision measurements, covers a wide program of direct searches for NP particles in both the kaon and beam-dump modes. NA62 results for various Dark Sector benchmark scenarios have been presented, including the first result using the 2021 beam-dump dataset.

NA62 can probe new regions in Dark Sector mass-coupling parameter spaces many years before dedicated facilities are built. Data-taking has been ongoing since since 2021 as a Run 2 with various software and hardware updates and increased beam intensity.

Acknowledgements

I would like to thank the organizers of the Volcano Workshop 2022 for the invitation to present this summary and I want to acknowledge the support

by the F.R.S.-FNRS (Fonds de la Recherche Scientifique - FNRS), Belgium, through grant FRIA/FC-36305.

References

1. J. Beacham, C. Burrage, D. Curtin, A. De Roeck, J. Evans, J. L. Feng, C. Gatto, S. Gninenko, A. Hartin and I. Irastorza, *et al.* *J. Phys. G* **47** (2020) no.1, 010501 doi:10.1088/1361-6471/ab4cd2 [arXiv:1901.09966 [hep-ex]].
2. E. Cortina Gil *et al.* [NA62], *JINST* **12** (2017) no.05, P05025 doi:10.1088/1748-0221/12/05/P05025 [arXiv:1703.08501 [physics.ins-det]].
3. M. Rosenthal, D. Banerjee, J. Bernhard, M. Brugger, N. Charitonidis, M. van Dijk, B. Döbrich, L. Gatignon, A. Gerbershagen and E. Montbarbon, *et al.* *Int. J. Mod. Phys. A* **34** (2019) no.36, 1942026 doi:10.1142/S0217751X19420260
4. E. Cortina Gil *et al.* [NA62], *JHEP* **06** (2021), 093 doi:10.1007/JHEP06(2021)093 [arXiv:2103.15389 [hep-ex]].
5. G. Anzivino, M. Barbanera, A. Bizzeti, F. Brizioli, F. Bucci, A. Cassese, P. Cenci, B. Checcucci, R. Ciaranfi and V. Duk, *et al.* *JINST* **13** (2018) no.07, P07012 doi:10.1088/1748-0221/13/07/P07012 [arXiv:1809.04026 [physics.ins-det]].
6. E. Cortina Gil *et al.* [NA62], *Phys. Lett. B* **816** (2021), 136259 doi:10.1016/j.physletb.2021.136259 [arXiv:2101.12304 [hep-ex]].
7. E. Cortina Gil *et al.* [NA62], *Phys. Lett. B* **807** (2020), 135599 doi:10.1016/j.physletb.2020.135599 [arXiv:2005.09575 [hep-ex]].
8. P. Agrawal, M. Bauer, J. Beacham, A. Berlin, A. Boyarsky, S. Cebrian, X. Cid-Vidal, D. d'Enterria, A. De Roeck and M. Drewes, *et al.* *Eur. Phys. J. C* **81** (2021) no.11, 1015 doi:10.1140/epjc/s10052-021-09703-7 [arXiv:2102.12143 [hep-ph]].
9. E. Goudzovski, D. Redigolo, K. Tobioka, J. Zupan, G. Alonso-Álvarez, D. S. M. Alves, S. Bansal, M. Bauer, J. Brod and V. Chobanova, *et al.* doi:10.1088/1361-6633/ac9cee [arXiv:2201.07805 [hep-ph]].

10. B. Döbrich, J. Jaeckel, F. Kahlhoefer, A. Ringwald and K. Schmidt-Hoberg, *JHEP* **02** (2016), 018 doi:10.1007/JHEP02(2016)018 [arXiv:1512.03069 [hep-ph]].
11. B. Döbrich, J. Jaeckel and T. Spadaro, *JHEP* **05** (2019), 213 [erratum: *JHEP* **10** (2020), 046] doi:10.1007/JHEP05(2019)213 [arXiv:1904.02091 [hep-ph]].
12. B. Döbrich, F. Ertas, F. Kahlhoefer and T. Spadaro, *Phys. Lett. B* **790** (2019), 537-544 doi:10.1016/j.physletb.2019.01.064 [arXiv:1810.11336 [hep-ph]].
13. J. Jerhot, B. Döbrich, F. Ertas, F. Kahlhoefer and T. Spadaro, *JHEP* **07** (2022), 094 doi:10.1007/JHEP07(2022)094 [arXiv:2201.05170 [hep-ph]].
14. C. Rella, B. Döbrich and T. T. Yu, *Phys. Rev. D* **106** (2022) no.3, 3 doi:10.1103/PhysRevD.106.035023 [arXiv:2205.09870 [hep-ph]].

PADME results and perspectives

Paolo Valente on behalf of the PADME collaboration*
INFN Sezione di Roma, P.le Aldo Moro 2, I-00185 Rome, Italy

Abstract

The dark matter nature, its origin, and the way it interacts with ordinary matter, although playing a crucial role in fundamental science is still not understood. Recently, models introducing an hidden sector with at least one particle with a very weak interaction with ordinary matter have been introduced, the simplest ones introducing a new vector boson kinetically mixed with the ordinary photon. Several experimental particle physics efforts are ongoing searching for hidden particles signals or trying to set more stringent limits on such theoretical models. The Positron Annihilation into Dark Matter Experiment (PADME) at LNF (Laboratori Nazionali di Frascati of INFN), has been designed for looking for hidden particles produced in association with a photon, by studying the missing-mass spectrum of single γ , resulting from the annihilation of a positron beam on the electrons of a fixed target. It is expected to reach a sensitivity of $\sim 10^{-6}$ on the kinetic mixing parameter ϵ^2 , which represents the coupling of a low-mass dark photon with ordinary photons. Due to the maximum positron beam energy of 550 MeV, a mass range up to $23.7 \text{ MeV}/c^2$

can be explored. In addition the experiment can perform a precise measurement of the cross-section of the $e^+ e^- \rightarrow \gamma\gamma$ process at $\sqrt{s} = 21 \text{ MeV}/c^2$ that can be compared with the Standard Model expectation in order to set limits on hidden particles decays to photon pairs.

1 Dark sector and the PADME experiment

One of the most important open issues of physics is the dark matter problem: its nature, origin, and the way it interacts with ordinary matter, although playing a crucial role in fundamental science, is still not understood. Several extensions of the Standard Model (SM) of particle physics have been proposed in order to account for the relic density of dark matter after the freeze-out induced by the expansion of the Universe. Weakly interacting massive particles (WIMP) are the favored scenario, but extensive searches at LHC have strongly reduced the allowed parameter space, so that in the recent years a growing attention has been given to alternative models.

In particular, a number of those models introduce a new dark sector, in which a “portal” particle couples both to dark matter heavy particles and – very feebly – to the SM. These models are classified in terms of the mediator, which can be a vector (a “dark photon”, A'), a pseudo-scalar (an axion-like particle), a scalar (a “dark Higgs”) or a fermion. In particular, if a vector gauge boson associated to a new $U(1)$ symmetry is introduced, it can kinetically mix the ordinary photon, so that such models are characterized by just two parameters: the dark photon mass, $m'_{A'}$, and its coupling to SM particles, ϵ .

The PADME experiment has been originally designed ¹⁾ for searching “invisible” decays of A' , i.e. in case it is heavy enough to decay to dark matter particles, $A' \rightarrow \chi\bar{\chi}$, thus escaping detection. PADME is located at INFN Frascati National Laboratories (LNF), and it makes use of the positron beam accelerated by the DAFNE complex LINAC, extracted to one of the two beam-lines of the BTF (Beam-Test Facility), BTF-1. The momentum of positron pulses, as well as their intensity and duration, can be adjusted in a wide range ²⁾ in order to optimize the luminosity vs. background and pile-up in the detectors.

The experiment can detect the production of dark particles in the in-flight annihilation of the positrons of the beam onto the atomic electrons of a thin target, either in associated production with a ordinary photon, $e^+e^- \rightarrow \gamma X$,

or in resonant direct production, $e^+e^- \rightarrow X$.

The maximum nominal energy of the LINAC beam in positron mode is 550 MeV, thus limiting the search in fixed-target annihilation events to masses $m_{A'} < 23.7 \text{ MeV}/c^2$. The production of a massive particle, like a dark photon, in $e^+e^- \rightarrow \gamma A'$ is signaled by a non-vanishing missing mass closing the kinematics, since the beam energy is known, by measuring the momentum of the photon (electrons are assumed to be practically at rest).

The position and energy of photons are measured by a finely segmented BGO electromagnetic calorimeter (ECal) ³⁾, made by 616 crystals arranged in a cylindrical shape, of $\sim 60 \text{ cm}$ diameter, as shown in Fig. 1, placed approximately 3.4 m downstream of the annihilation target. The dimensions of each crystal of $21 \times 21 \times 230 \text{ mm}^3$ allow the electromagnetic shower to be fully contained longitudinally, and $\approx 70\%$ of it in the transverse direction, and is readout by HZC XP1911 19 mm diameter photomultipliers.

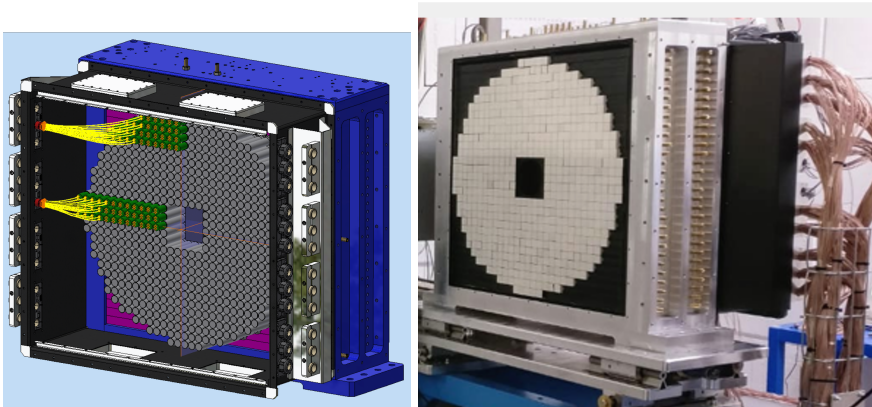


Figure 1: Left: technical drawing of the ECal structure (without the light-tight back cover), showing the mechanical structure, the BGO crystals and part of the photomultiplier tubes and attached power and readout cables. Right: ECal photograph (without the light-tight front cover).

Other detectors are used to reject the two main backgrounds, i.e. the Bremsstrahlung emission of a photon on a 0.1 mm thick CVD diamond target, and the annihilation in two or three photons. The diamond target not only provides the target for the annihilation process, but also measures the x and

y profile of the beam and the beam multiplicity, i.e. the number of positrons contained in each bunch, thanks 1 mm wide graphite strips, directly burnt by an intense laser beam directly on the sensor faces ⁴).

Being the angular distribution of the Bremsstrahlung radiation sharply peaked in the forward direction, the ECal has been realized with a central hole, behind which is placed a faster, Cherenkov detector, made of a square matrix of 25 PbF₂ crystals ⁵). This small angle calorimeter (SAC) is used in conjunction with plastic scintillator bars read out by means of green-shifting fibers and SiPM ⁶), placed in a vertical magnetic field, which allows tagging the positrons having irradiated a photon.

Any positron that does not interact in the target is directed towards a beam monitor and the beam dump by a magnetic field, which also deflects secondary charged particles towards a set of dedicated detectors. These detectors act both as vetoes for background reactions and as spectrometers for forward emitted charged particles (positrons on the bending side, electrons on the opposite one). The magnetic field of about 0.5 T is provided by a wide gap (23 cm), 1 m long dipole, inside which a a-magnetic steel vessel provides a $\sim 10^{-6}$ vacuum.

At the exit from the vacuum vessel, and before being dumped onto the concrete of the BTF hall, the beam can be imaged by a hybrid Silicon pixel detector, consisting of TimePix sensors, each made of a 256×256 square pixels of 0.055 mm side, arranged in a 6×2 matrix. This allows monitoring the beam spot position and size, and from the latter, reconstruct the beam divergence and momentum spread.

This setup has been optimized for the search of dark photons decaying invisibly in associated production, i.e. by looking for a bump in the missing mass distribution of single photon events. However, the scintillating bar detectors have been placed on both sides of the dipole magnet axis, so to allow reconstructing events with a pair of charged particles, coming from the $A' \rightarrow e^+e^-$ visible decays or from the SM processes, in particular the Bhabha scattering.

The flight path up to a polar angle of ~ 100 mrad, including the scintillating bar detectors between the dipole magnet poles, is inside a vacuum vessel connected to the BTF-1 beam-line on the upstream side and separated from the ECal by a large, 3 mm thick, carbon fiber window. A schematic view of the overall experiment setup is shown in Fig. 2.

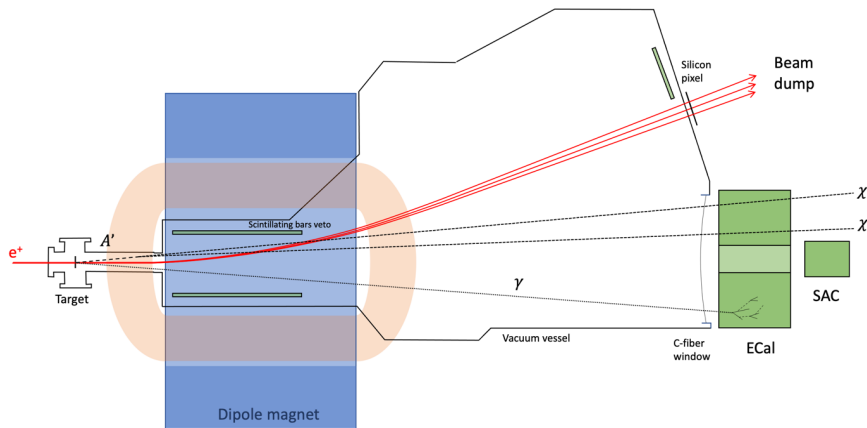


Figure 2: Schematic view of the PADME experiment (not to scale).

2 PADME experiment status

PADME has taken data in two periods, in fall 2019 (Run I) and fall 2020 (Run II) – see Fig. 3– collecting a similar statistics of $\approx 5 \times 10^{12}$ positrons on target (pot) but with different beam configurations: with a secondary beam of 490 MeV positrons, produced onto the attenuating target of the BTF yielding a high beam-induced background, in Run I, and by using the “primary” beam produced at the positron converter of the Frascati LINAC and accelerated to 430 MeV, in Run II. In order to reduce the pile-up, the density of positrons in a single beam pulse was limited to $\sim 10^2$ particles/ns, trying to produce the maximum length of the macro-bunches, up to ~ 300 ns ⁷⁾.

Between Run I and Run II the thin window separating the machine and experiment vacuum systems was also replaced and moved upstream, thus greatly reducing the amount of off-momentum beam particles entering the final dipole of the BTF beam-line and hitting the ECal. Further details on the beam, on the experiment commissioning and on the background studies can be found in ^{8, 9)}.

A small fraction of Run II data, about 10%, was used to measure the inclusive in-flight cross section $\sigma(e^+e^- \rightarrow \gamma\gamma(\gamma))$ with a precision of $\sim 5\%$ ¹⁰⁾, with two different analysis methods: a tag-and-probe two clusters selection,

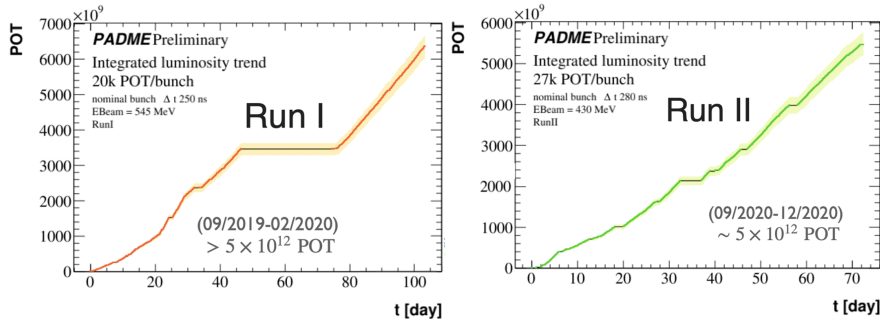


Figure 3: Integrated luminosity collected in the PADME Run I and Run II.

and a single photon selection exploiting the energy-angle correlation in two photons events. The result for the cross-section measurement $\sigma_{e^+e^- \rightarrow \gamma\gamma(\gamma)} = (1.977 \pm 0.018_{stat} \pm 0.119_{syst})$ mb not only is the best determination in the sub-GeV regime, as shown in Fig. 4, but also opens the possibility of setting limits to dark sector models, for instance for a pseudo-scalar decaying into photons. Moreover, such a measurement allowed to assess the performance of the PADME calorimeter and is an important intermediate step towards the single photon analysis looking for the associated production of a dark photon.

3 PADME perspectives

Since 2016 the observation of an anomaly in a nuclear physics experiment, known as “Beryllium anomaly”, has gained stronger and stronger evidence: a unexpected bump in the angular distribution of the e^+e^- produced by internal pair conversion in the decay of excited ^8Be nuclei ¹¹⁾, has been also seen, by the same collaboration, also in the de-excitation of ^4He ¹²⁾ and ^{12}C nuclei ¹³⁾. In all three cases, with large significances of more than 5σ , the production of a neutral boson with mass of around $17 \text{ MeV}/c^2$ has been advocated (the so-called X17 particle).

The PADME experiment, with a slightly modified setup, can address this anomaly by looking for the production of such a boson in e^+e^- annihilations into X17, by exploiting the increase of several orders of magnitude of the production cross-section expected when the positron beam energy is such that $\sqrt{s} \simeq m_{X17}$ ¹⁵⁾. Previous attempt of constraining the X17 parameter

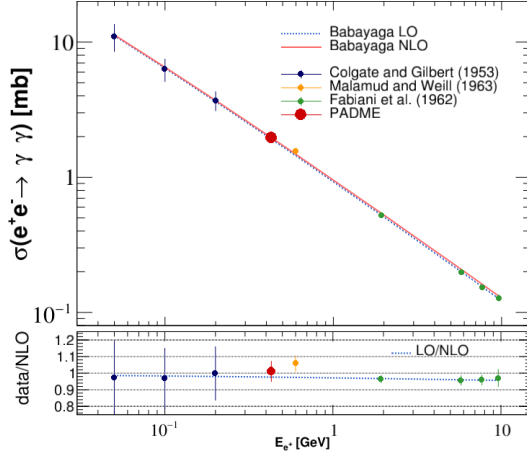


Figure 4: Theory predictions, at the leading order and next-to-leading order approximation, for the positron annihilation cross-section in flight as a function of the positron energy. The PADME measurement is compared to earlier measurements. Data to theory ratios are shown in the bottom pad.

space, both in the vector and scalar scenario, have provided significant but not yet final results¹⁴). Exploring the remaining allowed parameter space is very important to provide on the particle nature of the ATOMKI anomaly, although experimentally this is challengin: beam dump experiments, like NA64, are limited by the very short lifetime of the putative X17 particle, while the bump hunting in thin target experiments is limited by the overwhelming SM background. PADME, on the contrary, can exploit the highly efficient resonant production mechanism in e^+e^- annihilation to improve the signal to background ratio.

The main background to the $X17 \rightarrow e^+e^-$ signal is the elastic (Bhabha) electron-positron scattering. While the t -channel is peaked at high energies for the scattered positron, the s -channel has an identical kinematics with respect to the signal. In addition, two clusters from $\gamma\gamma$ events have to be rejected. Since the PADME veto spectrometer cannot be used to constrain e^+e^- vertices which do not come from the production target, the basic idea is to identify decays of a massive particle into electron-positron pairs using the ECal, as for the $\gamma\gamma$

events.

In order to allow low-momentum charged particles to reach the calorimeter the magnetic field has to be switched off. Provided that the beam intensity is kept low enough to have a negligible pile-up probability, the ECal can reconstruct precisely the e^+e^- invariant mass from the energy and angle of the clusters.

This technique requires however to disentangle charged particles and photon clusters. For this purpose an additional detector (the electron tagger, ETag) has been realized and installed in front of ECal. The ETag is made of 5 mm thick scintillating bars, each read out by 4 SiPM: the vertical segmentation of 4 cm allows to have a sustainable rate while covering the fiducial region of the calorimeter with a reasonable number of channels.

Phenomenological studies have been performed to establish the PADME Run III sensitivity based on two different scenarios for the total number of collected pot per point and beam energy resolution¹⁵):

- Conservative: 12 points summing up to 2×10^{11} total pot, with a 0.5% beam energy spread, in the energy range [265, 297] MeV.
- Aggressive: 14 points summing up to 4×10^{11} total pot, with 0.25% beam spread, in the narrower energy range [273, 291] MeV.

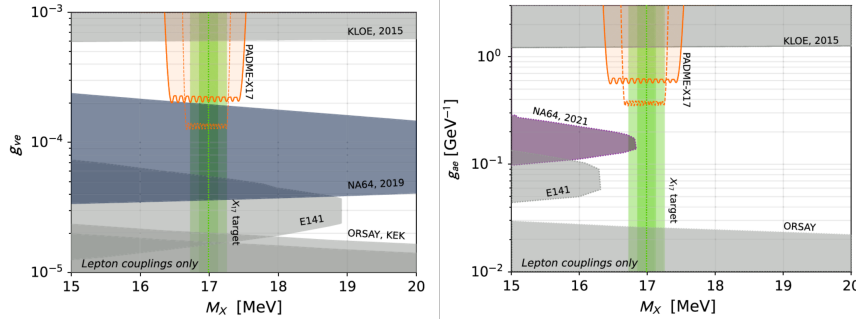


Figure 5: PADME expected sensitivity to a vector (left) and pseudo-scalar (right) boson.

Fig. 5 shows the projected 90% confidence level sensitivity of PADME Run-III on the couplings g_{ve} (vector–electron) and g_{ae} (pseudo-scalar–electron)

couplings of a X_{17} boson for the conservative (solid orange line) and aggressive (dashed orange line) setups.

Data collected during PADME Run III from October to December 2022 should allow to cover the entire scan range over a $1 \text{ MeV}/c^2$ mass range.

Acknowledgements

This work has been mainly funded by Istituto Nazionale di Fisica Nucleare. Other funds have been also granted by: BG-NSF KP-06-DO02/4 from 15.12.2020 as part of MUCCA, CHIST-ERA-19-XAI-009, and TA-LNF as part of STRONG-2020 EU Grant Agreement 824093.

References

1. M. Raggi, V. Kozhuharov and P. Valente, EPJ Web Conf. **96** (2015), 01025.
2. P. Valente *et al.*, [arXiv:1603.05651 [physics.acc-ph]] (2016).
3. P. Albicocco, *et al.* JINST **15** (2020) no.10, T10003.
4. I. Oceano [PADME], JINST **15** (2020) no.04, C04045.
5. A. Frankenthal, *et al.* Nucl. Instrum. Meth. A **919** (2019), 89-97.
6. F. Oliva [PADME], JINST **15** (2020) no.06, C06017.
7. P. Valente, *et al.* J. Phys. Conf. Ser. **874** (2017) no.1, 012017.
8. P. Albicocco, *et al.* JINST **17** (2022) no.08, P08032.
9. F. Bossi *et al.*, JHEP **09** (2022), 233.
10. F. Bossi *et al.* [PADME], [arXiv:2210.14603 [hep-ex]].
11. A. J. Krasznahorkay, *et al.* Phys. Rev. Lett. **116** (2016) no.4, 042501.
12. A. J. Krasznahorkay, *et al.* Phys. Rev. C **104** (2021) no.4, 044003.
13. A. J. Krasznahorkay, *et al.* [arXiv:2209.10795 [nucl-ex]].
14. M. Raggi, *et al.* FIP 2022 Proceedings (2023), in preparation.
15. L. Darmé, M. Mancini, E. Nardi and M. Raggi, Phys. Rev. D **106** (2022) no.11, 115036

SEARCH FOR AXION DARK MATTER

Alessandro D'Elia
Claudio Gatti

INFN, Laboratori Nazionali di Frascati, via Enrico Fermi 54, Frascati, 00044, Italy

Abstract

Dark matter is one of the greatest open problems in modern physics. The axion is an ideal cold dark matter candidate and its discovery would, at the same time, solve the strong CP problem. In this work we briefly review the status and discuss future developments for the axion search carried on by INFN.

1 Introduction

The Axion is an hypothetical particle first proposed by Wilczek and Weinberg in 1978 ^{1, 2)} as an extension of the standard model aimed to solve the strong CP problem. The Lagrangian of quantum chromodynamics (QCD) is supposed to violate the CP symmetry through the θ term:

$$\mathcal{L} = \theta \frac{\alpha_s}{8\pi} G_{\mu\nu}^a \tilde{G}_a^{\mu\nu} \quad (1)$$

where α_s is the QCD coupling constant and $G_{\mu\nu}^a$ and $\tilde{G}_a^{\mu\nu}$ are the gluon field-strength tensor and its dual, respectively. This Lagrangian predicts a θ dependent electric dipole moment (EDM) for hadrons. The latest experimental results on the neutron EDM impose $\theta < 10^{-10}$ ³⁾ suggesting that if CP violations are present they are extremely small. The reason behind the small value of θ is the heart of the strong CP problem. The most compelling solution of this problem was proposed by Peccei and Quinn ⁴⁾ that introduced a new U(1) symmetry spontaneously broken at high energy scale f_a . Wilczek and Weinberg realized that this spontaneous symmetry break implied the existence of a new pseudoscalar boson that they named axion.

The properties predicted for this particle, spin 0, charge neutrality, small mass and negligible interaction with the ordinary matter, and its production mechanism in the early universe make it also a strong candidate for the dark matter ⁵⁾. The discovery of the axion would therefore solve two of the greatest open problems in modern physics making the hunt for axion of paramount importance. Cosmology and astrophysical considerations, suggest an axion mass range $1 \mu eV < m_a < 10 meV$ ⁶⁾. Latest models that take into account dark matter density evolution in a post-inflationary scenario set the axion mass boundary to be $m_a \in [40 - 180]\mu eV$ ⁷⁾.

The search for axion spread all over the world and different experimental approaches have been adopted in the attempt to detect an axion signal. Most of them rely on the axion-electromagnetic field coupling that allows in presence of a strong magnetic field, through the inverse Primakoff effect, the conversion of an axion into observable photons. Light shining through the wall experiments like ALPS ⁸⁾, consist in sending a photon beam onto an opaque wall. Turning on the magnetic field, the photons can be converted into axions, that, interacting weakly with the ordinary matter can cross the wall, be converted again into photons and finally be detected. Polarization experiments, like PVLAS ⁹⁾ aim to observe a change into laser polarization induced by the axion-photon conversion. In this work we will focus on the haloscope detection scheme proposed by Sikivie ^{10, 11)}.

The haloscope design is based on a resonant cavity immersed in a strong magnetic field. The axions are converted into observable cavity modes ¹²⁾. The power expected by an axion conversion event is given by:

$$P_a = \left(\frac{g_{a\gamma\gamma}^2}{m_a^2} \hbar^3 c^3 \rho_a \right) \left(\frac{\beta}{1+\beta} \omega_c \frac{1}{\mu_0} B_0^2 V C_{mnl} Q_L \right) \left(\frac{1}{1 + (2Q_L \Delta_\omega / \omega_c)^2} \right) \quad (2)$$

In the first set of parenthesis, $g_{a\gamma\gamma}$ is the coupling constant of the axion-photon interaction, m_a is the axion mass and $\rho_a \sim 0.45 \text{ GeV}/\text{cm}^3$ [13] is the local dark matter density. In the second set of parenthesis there are β and Q_L that represent the antenna coupling and loaded quality factor of the cavity, the vacuum permeability μ_0 , the magnetic field B_0 , the cavity's volume V , C_{mnl} that is a geometrical factor and $\omega_c = 2\pi\nu_c$ is the resonance angular frequency of the cavity. In the third brackets, $\Delta_\omega = \omega_c - \omega_a$ is the detuning between the cavity resonance and the photon generated by the axion conversion with angular frequency ω_a .

The maximisation of the converted axion power, requires an high quality-factor (Q) and to work in resonant conditions, i.e. tune the resonance frequency to match the axion frequency. Different approaches have been used to optimize the signal-to-noise ratio. For example resonant cavities of superconductive and dielectric materials are becoming increasingly popular because of their high Q [14, 15, 16, 17, 18]. The haloscope approach, bounds the axion masses range observable to the resonant frequency of the cavity and in last analysis to the cavity's dimensions. A limited mass window can therefore be explored with a single cavity. The axion mass range of interest sets therefore the dimension of the experiment and the sensitivity necessary to observe a QCD axion. Among the haloscope based experiment we report ADMX [19, 20, 21, 22], HAYSTAC [23, 24], ORGAN [25], CAPP-8T [26, 27], CAPP-9T [28], CAPP-PACE [29], CAPP-18T [30], GrAHal [31], RADES [32, 33, 34], TASEH [35], QUAX [36, 37, 38, 39, 40]. We will focus our attention on QUAX and its future developments inside the Laboratori Nazionali di Frascati (LNF) and Laboratori Nazionali di Legnaro (LNL).

2 QUAX

The QUAX experiment is a cooperation between LNF and LNL looking for axion dark-matter with a mass around $40 \mu\text{eV}$ within the range of masses predicted by post-inflationary scenarios [7]. The frequency of operation, about 10 GHz, is experimentally very challenging since it involves a small volume of

the resonant cavity (fraction of liter) and large quantum-fluctuations limiting linear amplifiers.

In 2021 QUAX reached the sensitivity to QCD-axions (Fig. 1) ³⁷.

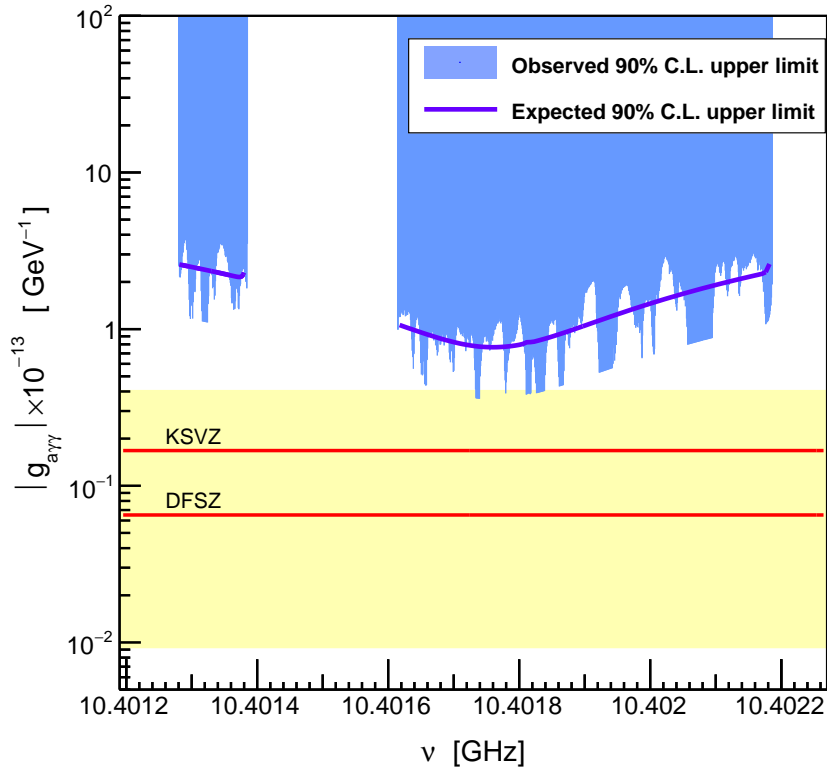


Figure 1: *90% single-sided C.L. upper limit for the axion coupling constant $g_{a\gamma\gamma}$. Each point corresponds to a test axion mass in the analysis window. The solid curve represents the expected limit in case of no signal. The yellow region indicates the QCD axions model band. We assume $\rho_a \sim 0.45 \text{ GeV}/\text{cm}^3$.*

The haloscope, assembled at LNL, was composed by a cylindrical OFHC-Cu cavity, with inner radius of 11.05 mm and length 210 mm, inserted inside

the 150 mm diameter bore of an 8 T superconducting (SC) magnet of length 450 mm. The whole system was hosted in a dilution refrigerator with base temperature of 90 mK. The first amplification stage was done with a JPA ⁴¹⁾ with noise temperature at the quantum-limit of about 0.5 K.

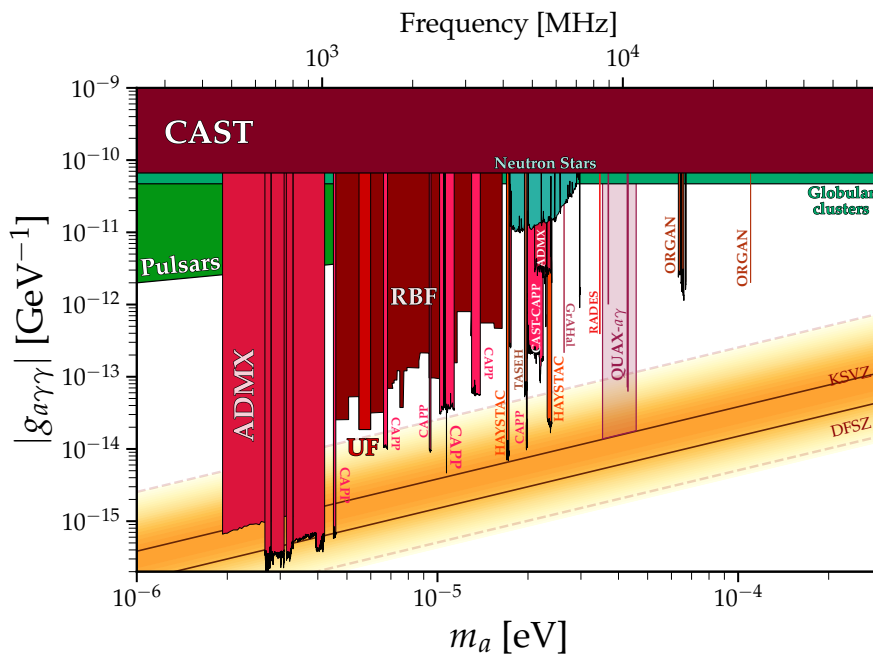


Figure 2: *Projections for axion searches by the QUAX haloscopes in the next few years are shown by the shaded area. The image is realized with ⁴²⁾*

In the next few years, the QUAX collaboration will probe the frequency region between 8 and 11 GHz with two complementary Sikivie haloscopes, one located at LNL and the other at LNF. The two haloscopes will be working at two different frequency ranges, implementing two different types of microwave cavities, dielectric and superconducting, and Travelling Wave Josephson Parametric Amplifiers (TWJPA) ^{43, 44)}. High quality-factor cavities able to operate in a strong magnetic field have been already fabricated and tested by the

QUAX collaboration (14, 16, 17) and used in axion searches (36, 45). Different geometries, including a multicavity approach, are foreseen. The expected limits within 2025 are shown in Fig. 2.

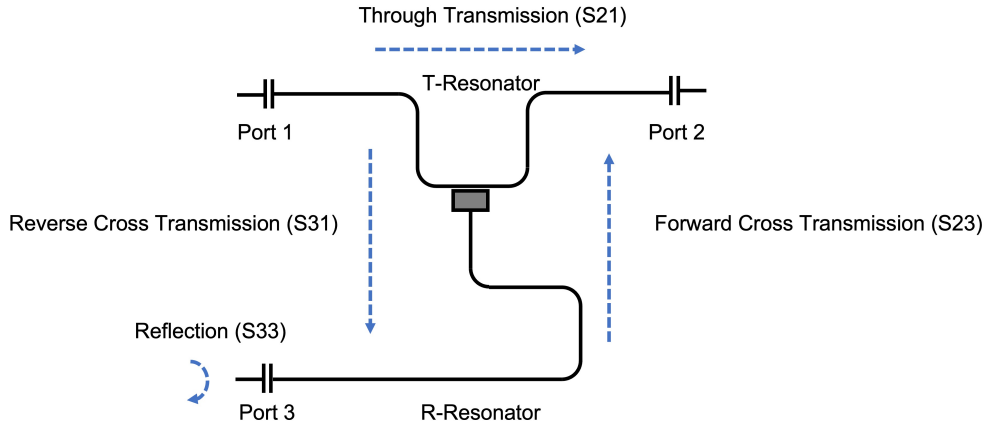


Figure 3: *Scheme of the T-type device composed of two resonators T and R coupled by a SQN (gray box).*

Due to the large quantum-fluctuations at this frequency, linear amplifiers are not suited to reach the sensitivity to axions predicted by the DFSZ model, and new counters sensitive to single microwave-photons with low dark-counts must be used (46, 47, 48). In particular, a Superconducting Qubit Network (SQN) could be used to enhance the detection sensitivity to single microwave-photons. Recently, a device, arranged in a transistor-like geometry as in Fig. 3, was tested at LNF within the Supergalax project: an SQN working as a coupling element between two perpendicular resonators such that the transmission properties of the device are modified by the presence of few microwave photons (48). The advantage of using a SQN over a single qubit is that of a predicted scaling of the signal-to-noise ratio as N instead of \sqrt{N} , where N is the number of qubits in the network (49, 50).

The device was tested at LNF in a Leiden Cryogenics CF-CS110-1000 dilution refrigerator at a temperature of 15 mK. The third-harmonic absorption-peak of the R-resonator at 7.74 GHz was considered. The VNA output-power

was set to -40 dBm, corresponding to about -100 dBm at the device, and the through transmission (S_{21}) was measured. At the same time, a single tone of frequency 7.743 GHz was sent to the R-resonator with the Rohde&Schwarz SMA100B connected to the Port 3, and the output power of the generator varied from -40 to -20 dBm (Fig. 4). By increasing the power sent to Port 3 a variation of the resonant-drop frequency in the through transmission-spectrum (S_{21}) was clearly observed, confirming the feasibility of the device, but further optimization and engineering is needed to reach the single photon sensitivity.

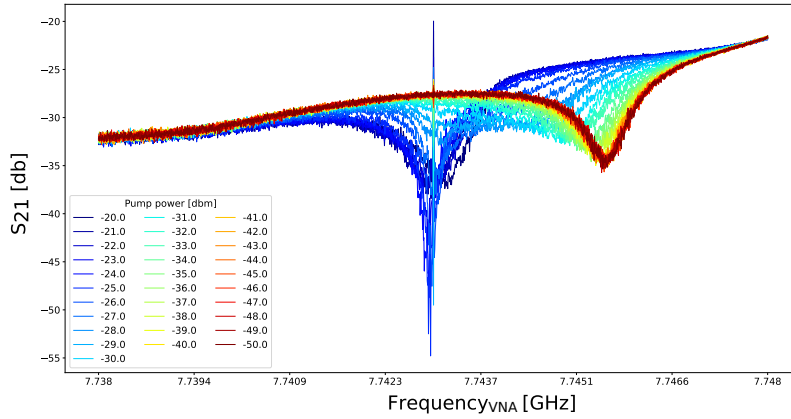


Figure 4: *Two-tone spectra measurements at frequency 7.74 GHz. First-tone through-transmission (S_{21}) vs VNA-frequency dependencies recorded at different powers of the second-tone signal of frequency of 7.743 GHz applied to the Port 3.*

3 FLASH

The FLASH experiment (FLASH, Finuda magnet for Light Axion Search), previously called KFLASH⁵¹, proposes the realization of a haloscope devoted to the detection for sub- μeV axion by recycling the no-longer used FINUDA^{52, 53} magnet and the DAΦNE cryogenic-plant, at LNF. The FINUDA

magnet is an iron-shielded solenoid-coil made from an aluminium-stabilised niobium-titanium superconductor providing an homogeneous axial field of 1.1 T with very large size bore, able to accommodate a cryogenic resonant cavity with a diameter of up to 2.1 m. The FLASH haloscope will be composed of such a large resonant cavity made of OFHC copper, inserted in a cryostat cooled down to 4.5 K hosted inside the FINUDA magnet. The operation frequency will be tuned by three metallic movable-rods and the signal will be amplified by a Microstrip SQUID cooled down to 300 mK, for a total temperature noise of 4.9 K. With this setup, it would be possible to search for KSVZ-axions scanning in the frequency range 117-360 MHz, corresponding to the well motivated mass region between 0.5 and 1.5 μeV (Fig. 5) in a total integrated time of about two years.

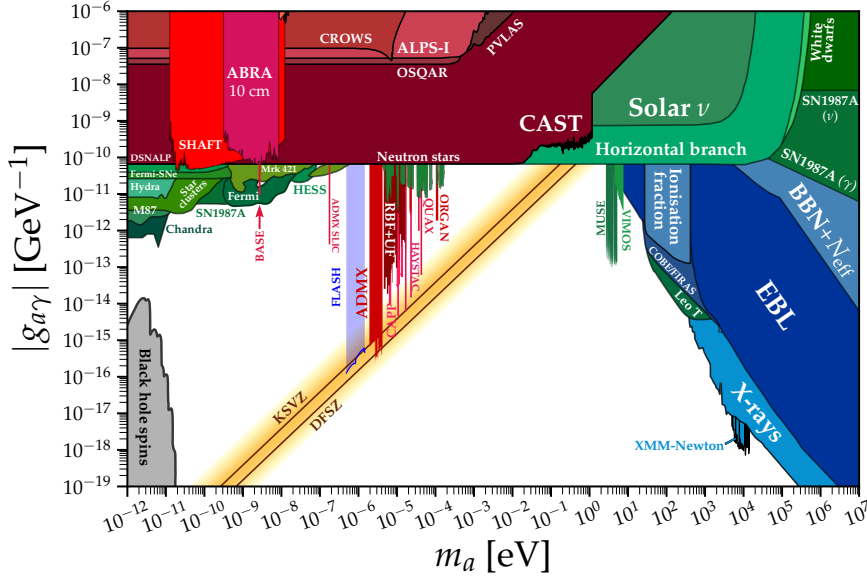


Figure 5: *Projection for axion searches with the FLASH haloscope is shown by the shaded area. Image realized with $\text{\textit{4}^2}$)*

FLASH will be sensitive also to dark matter composed of dark photons with kinetic-mixing parameter down to few 10^{-17} , and to high-frequency

gravitational-waves with strain of about few 10^{-22} .

In a possible second phase of the experiment, the cavity will be cooled to 100 mK. This will increase the axion sensitivity of about 1 order of magnitude, down to $g_{a\gamma\gamma} \sim 2 \times 10^{-17} \text{ GeV}^{-1}$, allowing us to probe the existence of DFSZ-axions in this mass range.

References

1. Steven Weinberg. *Phys. Rev. Lett.*, 40(4):223, 1978.
2. Frank Wilczek. *Phys. Rev. Lett.*, 40(5):279, 1978.
3. C. Abel et al. *Phys. Rev. Lett.*, 124:081803, Feb 2020.
4. Roberto D Peccei and Helen R Quinn. *Phys. Rev. Lett.*, 38(25):1440, 1977.
5. John Preskill, Mark B Wise, and Frank Wilczek. Cosmology of the invisible axion. *Phys. Lett. B*, 120(1-3):127–132, 1983.
6. Igor G Irastorza and Javier Redondo. *Prog. Part. Nucl. Phys.*, 102:89–159, 2018.
7. M Buschmann et al. *Nat Commun*, 13:1049, 2022.
8. Katharina-Sophie Isleif. *arXiv preprint arXiv:2202.07306*, 2022.
9. F. Della Valle et al. *The European Physical Journal C*, 76(1):1–15, 2016.
10. Pierre Sikivie. *Phys. Rev. Lett.*, 51(16):1415, 1983.
11. P. Sikivie. *Phys. Rev. D*, 32:2988–2991, Dec 1985.
12. S Al Kenany et al. *Nucl. Instr. Meth. Phys. Res. A*, 854:11–24, 2017.
13. P. A. Zyla et al. (*Particle Data Group*), *Prog. Theor. Exp. Phys.*, 2020(8), 08 2020. 083C01.
14. Daniele Di Gioacchino et al. *IEEE Trans. App. Sup.*, 29(5):1–5, 2019.
15. Danho Ahn and et al. *arXiv:1904.05111*, 2019.
16. D Alesini et al. *Rev. Sci. Instr.*, 91(9):094701, 2020.

17. D Alesini et al. *Nucl. Instr. Meth. Phys. Res. A*, 985:164641, 2021.
18. D. Alesini and et al. *Phys. Rev. D*, 106:052007, Sep 2022.
19. T Braine et al. *Phys. Rev. Lett.*, 124(10):101303, 2020.
20. N Du et al. *Phys. Rev. Lett.*, 120(15):151301, 2018.
21. C Boutan et al. *Phys. Rev. Lett.*, 121(26):261302, 2018.
22. C Bartram et al. *Phys. Rev Lett.*, 127(26):261803, 2021.
23. K Backes et al. *Nature*, 590(7845):238–242, 2021.
24. L Zhong et al. *Phys. Rev. D*, 97(9):092001, 2018.
25. Ben T McAllister and et al. *Phys. Dark Univ.*, 18:67–72, 2017.
26. Jihoon Choi et al. *Nucl. Inst. Meth. Phys. Res. A*, 1013:165667, 2021.
27. Soohyung Lee et al. *Phys. Rev. Lett.*, 124(10):101802, 2020.
28. Junu Jeong et al. *Phys. Rev. Lett.*, 125(22):221302, 2020.
29. Ohjoon Kwon et al. *Phys. Rev. Lett.*, 126(19):191802, 2021.
30. Youngjae Lee et al. *Phys. Rev. Lett.*, 128(24):241805, 2022.
31. Thierry Grenet et al. *arXiv:2110.14406*, 2021.
32. Alejandro Álvarez Melcón et al. *JHEP*, 07(2020):084, 2020.
33. Alejandro Álvarez Melcón et al. *JCAP*, 05(2018):040, 2018.
34. Alejandro Álvarez Melcón et al. *JHEP*, 10(2021):075, 2021.
35. Hsin Chang et al. *arXiv:2205.05574*, 2022.
36. D Alesini et al. *Phys. Rev. D*, 99(10):101101, 2019.
37. D Alesini et al. *Phys. Rev. D*, 103(10):102004, 2021.
38. R Barbieri et al. *Phys. Dark Univ.*, 15:135–141, 2017.
39. N Crescini et al. *Eur. Phys. J. C*, 78(9):1–9, 2018.

40. N Crescini et al. *Phys. Rev. Lett.*, 124(17):171801, 2020.
41. N. Roch et al. *Phys. Rev. Lett.*, 108:147701, Apr 2012.
42. Ciaran O'Hare. `cajohare/axionlimits: Axionlimits.`
<https://cajohare.github.io/AxionLimits/>, July 2020.
43. C Braggio et al. *Review of Scientific Instruments*, 93(9):094701, 2022.
44. A Rettaroli et al. *Nuc. Instr. Meth. A*, 1046:167679, 2023.
45. D Alesini et al. *Phys. Rev. D*, 106:052007, Sep 2022.
46. E Albertinale et al. *Nature*, 600:434–438, 2021),.
47. L S Kuzmin et al. *IEEE Trans. App. Sup.*, 28(7):1–5, 2018.
48. A D'Elia et al. *IEEE Trans. App. Sup.*, 33(1):1–9, 2023.
49. M. V. Fistul et al. *Phys. Rev. B*, 105:104516, Mar 2022.
50. P. Navez et al. *Phys. Rev. B*, 103:064503, Feb 2021.
51. D Alesini et al. *arXiv:1911.02427*, 2019.
52. M Bertani et al. *Nuclear Physics B Proc. Supp.*, 78(1-3):553–558, 1999.
53. M. Modena. *LNF-97-046-IR*, 12 1997.

SEARCHES FOR ULTRA LONG-LIVED PARTICLES

P. Camarri

Università degli Studi di Roma "Tor Vergata" and INFN Sezione di Roma Tor Vergata
on behalf of the MATHUSLA collaboration

Abstract

In the quest for particle dark matter and physics beyond the Standard Model, the possibility of the existence of neutral long-lived particles (LLPs) has been proposed. The MATHUSLA project has been designed as a surface experiment to detect possible LLPs produced in collisions at the CERN Large Hadron Collider (LHC). The MATHUSLA detector will cover a 10^4 m² surface and will have 9 layers of scintillating-detector planes, with a 25 m high LLP decay volume. The detector will be installed above the CMS interaction region of the LHC before the beginning of the Phase-2 high-luminosity operation. By adding a full-coverage layer of Resistive Plate Chambers (RPCs), the MATHUSLA experiment can extend its initial goal and give contributions to several unresolved issues in cosmic-ray physics: the unique spatial and temporal definition of extensive air showers provided by this extended set-up will give detailed information for studying the energy spectrum and composition of cosmic rays, as well as their arrival directions. This information will be crucial for testing hadronic-interaction models and studying the origin and propagation of

primary cosmic rays. The potentialities of MATHUSLA in LLP searches and cosmic-ray physics will be presented.

1 INTRODUCTION

The search for physics “Beyond the Standard Model” (BSM) motivates the possible existence of so-far-undiscovered Long-Lived Particles (LLPs). The main approaches to this search are the following:

- “top-down”: various BSM theories (e.g. supersymmetry) constructed to explain the physics of fundamental interactions naturally include LLPs:
- “bottom-up”: LLPs are included in the Standard Model (e.g. muons) and new LLPs can appear via similar mechanisms when adding new particles to the model.

Particles with long lifetime produced in collisions at the Large Hadron Collider (LHC) could be invisible to the main detectors, for several possible reasons:

- if $c\tau \gg \gg$ detector size (where τ is the LLP lifetime) most of such particles escape the detector;
- LLPs which decay inside the detector, but a significant distance away from the interaction point, are difficult to detect;
- if the decay rate of LLPs inside the detector is very small, such particles are swamped by the background.

For such reasons, in order to detect possible LLPs produced in collisions at the LHC, dedicated, suitably designed experiments must be conceived.

2 MATHUSLA: AN EXTERNAL LLP DETECTOR AT THE HIGH LUMINOSITY - LHC

The MATHUSLA (MAssive Timing Hodoscope for Ultra-Stable neutraL pAr-ticles) project foresees the deployment of a surface detector above the LHC interaction point of the CMS experiment [?]). The MATHUSLA detector will not be a part of CMS, and its construction and operation will not interfere with any other LHC experiments. The MATHUSLA structure will rise up to 9

m above the ground and will extend down to about 20 m underground. It will cover a horizontal surface of $100 \times 100 \text{ m}^2$ and the LLP decay volume will have a vertical thickness of 25 m. The detector will have a horizontal displacement of about 70 m and a vertical displacement of about 60 m with respect to the LHC interaction point, as shown in the scheme of Fig. ??.

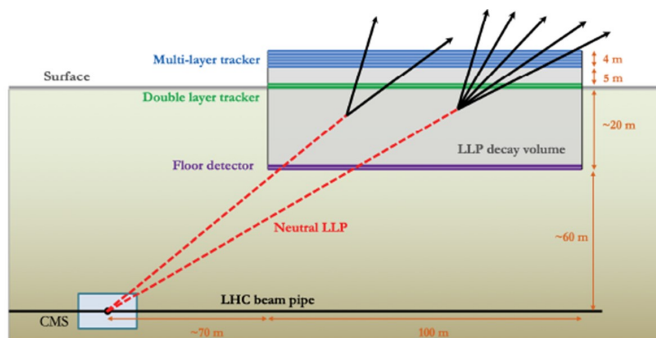


Figure 1: *Schematic vertical section of the MATHUSLA detector and its position with respect to the CMS interaction point at the HL-LHC.*

Due to the experiment large area, it will be deployed using a modular structure: 100 modules, each with a horizontal square area of $10 \times 10 \text{ m}^2$, as shown in the scheme of Fig. ??; each module will be further subdivided into four detector units, each with a horizontal square area of $5 \times 5 \text{ m}^2$.

Each module is composed of 6 tracking layers on top, 2 floor layers and 2 mid-level layers, as shown in the scheme of Fig. ??.

The tracking layers will be composed of extruded scintillator bars with wavelength-shifting fibers coupled to Silicon Photo Multipliers (SiPMs). The scintillator bars will be produced by the extrusion facilities at FNAL, already used for several other experiments. The size of each scintillator bar will be either $2.4 \text{ m} \times 3.5 \text{ cm} \times 1.5 \text{ cm}$ with readout at both ends, or 2.5 m long with looped fiber as the readout at one end. The expected transverse spatial resolution is about 1 cm, and the expected longitudinal spatial resolution (related to the resolution of the time difference between two ends) is about 15 cm. A

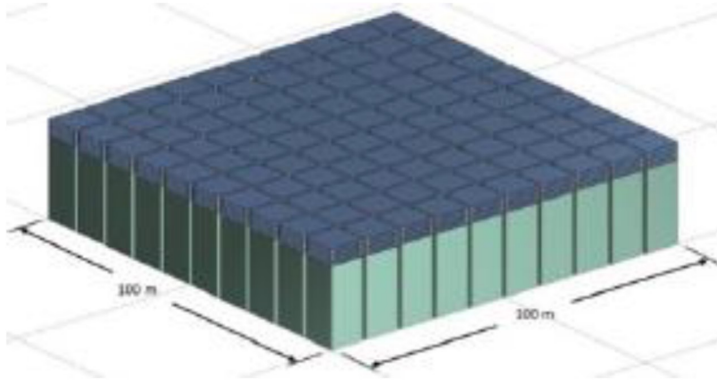


Figure 2: *Schematic view of the whole MATHUSLA setup showing its modular structure.*

test of the 5-m scintillator bars gave a 1-ns time resolution for cosmic-ray hits. R&D activities are going on concerning several items: wavelength-shifting fibers (attenuation, light collection), SiPMs (dark counts), scintillator-bar geometry.

The identification of LLP decays in MATHUSLA will be based upon the following considerations:

- since there will be no magnetic field in the decay volume, MATHUSLA will not be able to measure the particle momentum or energy, but the reconstruction of decay vertices geometrically compatible with long-lived neutral particles coming from the LHC interaction point will allow to evaluate the LLP Lorentz boost (Fig. ??);
- the synchronization of the MATHUSLA LLP candidate events with the CMS Level-1 trigger will allow off-line event-info correlation so that it will be possible to classify the LLP production mode (Fig. ??).

Based on that, two analysis steps follow:

- if the production mode is known, then the LLP mass can be derived from the experimental boost distribution;
- if the LLP mass is known, then the LLP decay mode can be established from the experimental track multiplicity.

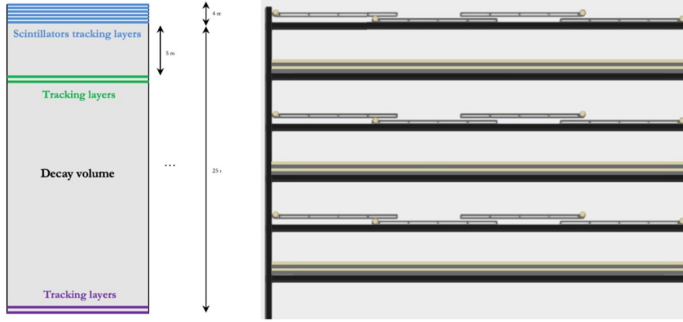


Figure 3: *Schematic vertical section of a MATHUSLA module (left), and details of the layout of its uppermost tracking layers (right).*

Under specific hypotheses, the combined MATHUSLA+CMS analysis could obtain some model parameters (e.g. mass of the parent particle, LLP mass) with just 100 observed LLP events.

In the search for new particles, a precise, reliable evaluation of the backgrounds is mandatory. A preliminary consideration in this respect is that LLP displaced vertices have to satisfy many stringent geometrical (~ 1 cm precision) and timing (~ 1 ns precision) requirements. Fig. ?? shows a schematic vertical section of MATHUSLA with examples of the main possible background events. These requirements, plus a few extra geometrical and timing cuts, will provide almost negligible background for neutral LLP decays (less than 1 background event per year expected). Here are more details about the expected background events:

- the background due to cosmic rays was estimated with Test-Stand measurements performed on the surface above the LHC P1 interaction point in 2018; about 3^{14} downward-going tracks are expected in MATHUSLA over the whole HL-LHC run: these can be distinguished from LLPs by using timing cuts; about 2^{10} upward-going events due to cosmic-ray inelastic backscattering from the floor or to the decay of stopped muons in the floor are expected in MATHUSLA over the whole HL-LHC run:

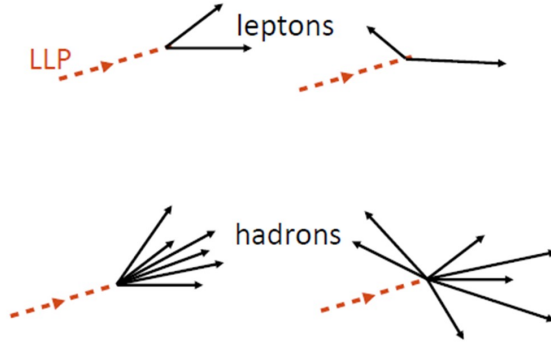


Figure 4: Schemes of possible *LLP* decay vertices, in the case of two-body leptonic decay and many-body hadronic decay.

a negligible fraction of these could produce fake decay vertices in the MATHUSLA decay volume; possible rare K_L^0 produced in the floor can be vetoed with various strategies, which are under study;

- the background due to upward-going muons from HL-LHC collisions reaching MATHUSLA will amount to $\sim 10^{11}$, mostly from W and $b\bar{b}$ decays, from 3 ab^{-1} of HL-LHC collisions; most of these tracks can be vetoed with floor detectors, with just a very tiny fraction generating displaced vertices due to scattering or rare decays; overall, this kind of background can be handled without difficulty;
- the background due to charged tracks generated by neutrino scattering in the MATHUSLA decay volume can be estimated reliably: neutrinos from HL-LHC collisions are expected to produce $\ll 1$ fake decay vertex per year, and atmospheric neutrinos are expected to produce ~ 30 fake decay vertices per year, which can be reduced to less than one with geometrical and timing cuts.

The sensitivity of MATHUSLA to LLP detection depends on the physical properties of the LLP (e.g. mass, lifetime, production cross section) and on the detector geometry. Here are the expected MATHUSLA sensitivities to a few

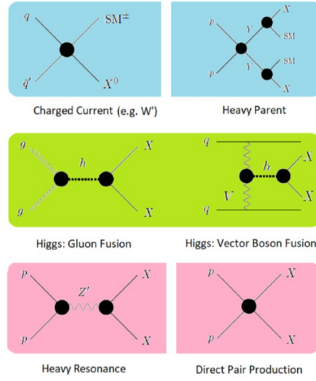


Figure 5: *Diagrams of possible LLP production modes in pp collisions at the HL-LHC.*

LLP benchmark models.

- hadronically-decaying LLPs produced in exotic-Higgs decay; the process $pp \rightarrow h \rightarrow XX$ can be studied with sensitivity improved by a factor of $\sim 10^3$ with respect to the LHC main detectors; an LLP production process of this kind with cross section $\gtrsim 1$ fb can be detected in MATHUSLA (Fig. ?? ?);
- in scenarios where the long-lifetime limit is accessible ($\gtrsim 100$ m), MATHUSLA is complementary to other planned experiments for LLP detection; for instance, the exclusion plots for the case of a singlet dark scalar S mixing with the Standard-Model Higgs boson through a θ mixing angle are shown in Fig. ?? ? ?);
- LLP two-body decay to a Standard-Model particle and a “Dark-Matter” particle, as foreseen by a “freeze-in” Dark-Matter model, where the LLP (χ_2 mass eigenstate of the model) existed in thermal equilibrium with primordial plasma, then decaying to a final state including a Dark-Matter particle (χ_1 mass eigenstate of the model) ? ?).

More benchmark models for LLP search can be found in the Physics Beyond Colliders CERN report, and more sensitivity projections for MATHUSLA can

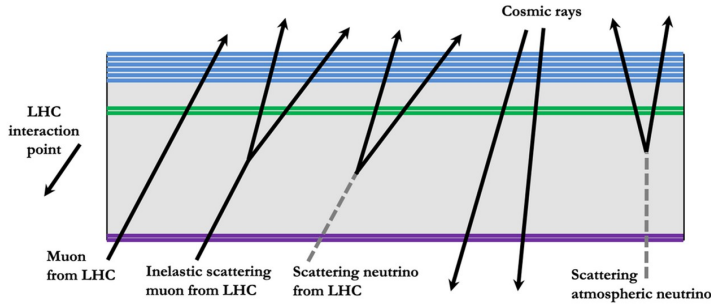


Figure 6: *Schematic vertical section of the MATHUSLA setup with the main possible backgrounds to LLP detection.*

be found in

3 PROPOSAL FOR AN ADDITIONAL LAYER OF RESISTIVE PLATE CHAMBERS IN MATHUSLA

The good performance and the important scientific results of the ARGO-YBJ experiment, based on a full-coverage single layer of Resistive Plate Chambers (RPCs), suggested the possibility of exploiting the wide area covered by the MATHUSLA experiment to install a full-coverage layer of RPCs. This additional layer of detectors can obviously provide additional information to the LLP measurement of the MATHUSLA experiment, and can contribute to specific studies in cosmic-ray physics which could not be easily done with other experiments.

RPCs provide the following additional information:

- Lower multi-hit probability in one strip due to the finer segmentation of the RPC read-out strips
- Estimation of the pulse charge from the “time-over-threshold” measurement; this give an approximate evaluation of the hit multiplicity in one

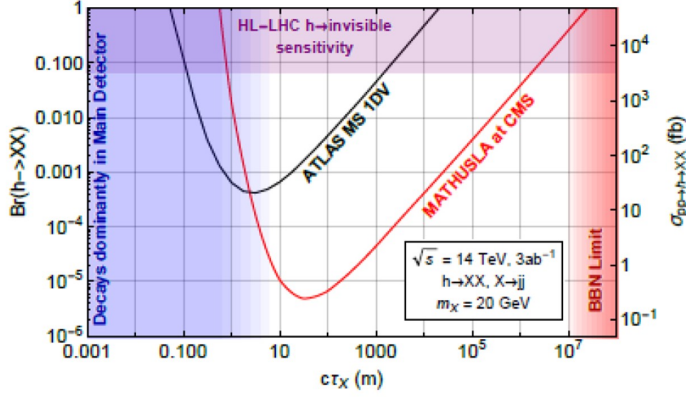


Figure 7: Comparison of the exclusion plots for LLP detection in ATLAS and MATHUSLA for the whole HL-LHC run, in the case of an LLP mass of 20 GeV decaying into two jets, coming from exotic-Higgs decay. The excluded regions, in case of null detection, are the one above the curves.

strip provided the number of simultaneous hits is significantly greater than one.

- Crucial information for cosmic-ray studies with MATHUSLA: linear response for hit density up to more than 10^4 hits/m² in the detection of air-shower cores thanks to the “big-pad” analog readout, to be compared to the saturated response (at high hit density) of a digital strip readout.

Here are the main features of the RPCs that would be used in MATHUSLA:

- Big-Pad size: 1.1×0.9 m²; the big-pad signal is proportional to the local charge density crossing the detector;
- Read-out strip area: 242 cm² (11-mm pitch);
- Operating mode: saturated avalanche;
- Gas-gap width: 1 mm (as the ATLAS BI RPCs).

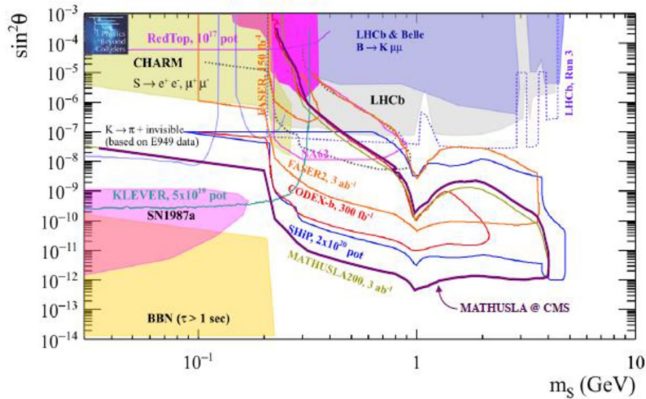


Figure 8: Comparison of the exclusion plots for LLP detection in several experiments, with different statistics, in the case of a dark scalar LLP S mixing with the Standard-Model Higgs boson through a θ mixing angle. The exclusion plots are now represented in the $(m_S, \sin^2 \theta)$ plane.

4 THE MATHUSLA TEST STAND

A small-scale experiment, the MATHUSLA test stand, was constructed and installed on the surface above the interaction point of the ATLAS detector (LHC Point 1) and collected data during 2018 (?). The test stand was operational both during LHC pp collisions and when the LHC was not operating. The goal was to measure the rate of muons from LHC pp collisions reaching the surface, as well as the rate of inelastic backscattering from cosmic rays that could create upwardgoing tracks, and to determine how well simulation models could reproduce the data. This information is a very useful input for future studies on the background expectations for the proposed MATHUSLA experiment. The test stand used scintillation counters recovered from the Tevatron Run II $D0$ forward muon trigger system; they were arranged to form two planes of $2.5 \times 2.5 \text{ m}^2$ area each. Spare RPCs of the ARGO-YBJ experiment were arranged in six layers between the scintillator planes, and used to track charged particles crossing the test stand. The height of the whole setup was about 6.5 m. A scheme and a picture of the MATHUSLA Test Stand

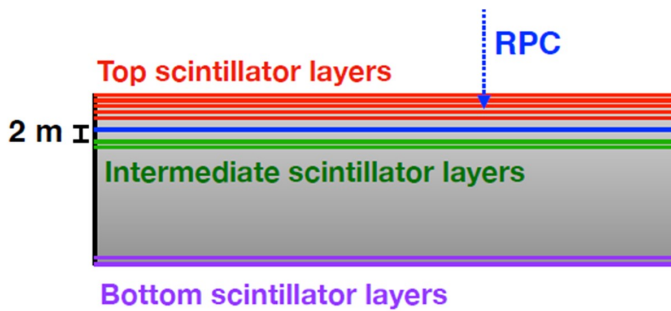


Figure 9: *Schematic vertical section of the MATHUSLA setup with the insertion of the proposed RPC layer.*

are shown in Fig. ??

The test-stand results confirm the background assumptions in the MATHUSLA proposal and demonstrate that there are no unexpected sources of background. These results give confidence in the MATHUSLA projected physics reach.

5 COSMIC-RAY PHYSICS WITH MATHUSLA

We already pointed out the features of the additional RPC layers connected to cosmic-ray studies with MATHUSLA. Nevertheless, there are a few important constraints to such studies: the very modest altitude of the experimental site (374 m above sea level), and a sensitive area not exceeding 10^4 m^2 .

Taking everything into account, cosmic-ray studies with MATHUSLA may be focused on the following items (?):

- Cosmic-ray composition (measurement of the atomic number Z of the primary particle);

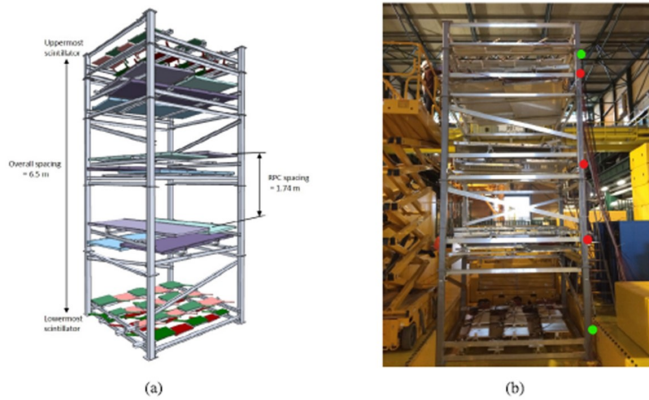


Figure 10: *Left: schematic view of the MATHUSLA Test Stand of 2018. Right: picture of the MATHUSLA Test Stand taken at the experimental site, above the LHC P1 interaction point.*

- Bundles of parallel muons. They can be observed when the electro-photonic component of the shower is absorbed before the shower hits the detector (“pure muonic shower”). For vertical showers they can be seen only at low energy, while for inclined or almost horizontal showers they can be observed also at high or very high energy due to the larger thickness of the atmosphere. This study is crucial both again for cosmic-ray composition studies and for discriminating among different high-energy hadronic interaction models.

The space-time-charge information provided by the RPC big pads allow the EAS front reconstruction, its inclination with respect to the horizontal plane and the local hit density.

As an example of the RPC-plane response to an extensive air shower, fig. ?? shows the bidimensional distribution of the induced charge on the RPC big pads in one simulated event (primary proton of 263 GeV with a zenith angle of 11.37) and the bidimensional map of the big-pad time delays with respect to the first hit in the event.

If the EAS arrival direction is greater than about 65, muons are the main

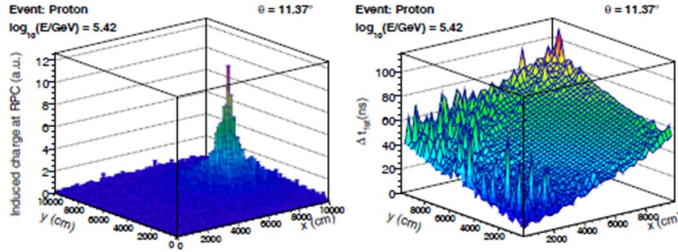


Figure 11: *Left: bidimensional distribution of the induced charge on the RPC big pads in one simulated event (primary proton of 263 GeV with a zenith angle of 11.37). Right: bidimensional map of the big-pad time delays with respect to the first hit in the event.*

component of the EAS. At the MATHUSLA site, inclined EAS from H and Fe primary nuclei of $\sim 1 \div \sim 100$ PeV have an average muon content of about 80 ± 1 %, as predicted by QGSJET-II-04 MC simulations.

The average value and the spectrum of the local muon density D in MATHUSLA for inclined EAS events generated by H and Fe primaries in the $1 \div 100$ PeV energy range have been simulated and studied using several high-energy hadronic interaction models, assuming that the primary energy spectra have a behaviour $\sim E^{-2}$. Above 10 PeV the local magnitude of D increases linearly with the primary energy in log scale and it is greater for heavy primaries than for light ones. The D spectra for EAS with a high content of muons are harder than the D spectra for EAS with a low muon multiplicity, and a slight spread is observed depending on the high-energy hadronic interaction model: so, such curves can be used to test the prediction of different models and discriminate among them. The results of the simulation studies are shown in Fig. ??.

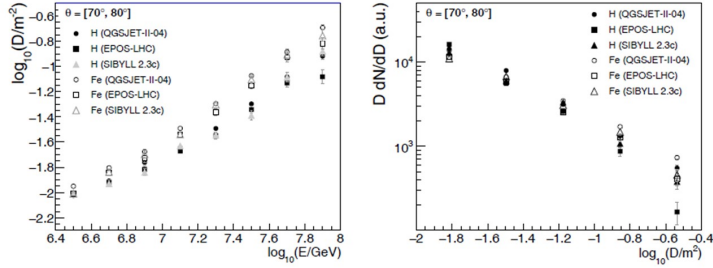


Figure 12: *Left: local muon density reaching MATHUSLA vs. primary energy, in log-log scale, for showers induced by protons (H) and iron nuclei (Fe) according to several hadronic-interaction models. Right: muon-density spectrum on MATHUSLA vs. primary energy, for showers induced by protons (H) and iron nuclei (Fe) according to several hadronic-interaction models.*

6 THE MATHUSLA PROGRESS STATUS AND CONCLUSIONS

The Letter of Intent (2019 + addendum in 2020) was signed by 83 researchers from USA (Spokesperson: Prof. Henry Lubatti, University of Washington, Seattle), Canada, Europe (11 from Italy), Israel, Central and South America. The Technical Design Report is being written and is expected to be presented to CERN by the end of 2022, followed by a prototype module and the full detector for the HL-LHC run.

References

1. H. Lubatti *et al.*, arXiv:1001.04040
2. A. Ibarra, arXiv:1809.01683
3. M. Hirsch, arXiv:2001.04750
4. D. Curtin, arXiv:1806.07396

5. J. Beacham *et al.*, J.Phys.G 47 (2020) 1, 01501
6. M. Alidra *et al.* (the MATHUSLA collaboration), Nucl.Instr.Meth. A 985 (2021) 164661
7. C. Alpigiani *et al.*, “Cosmic-ray searches with the MATHUSLA detector”, in preparation.

**NEW PHYSICS SEARCH IN HIGH PRECISION
MEASUREMENTS:
THE MUON $g - 2$ FACTOR**

Marco Incagli
Istituto Nazionale di Fisica Nucleare (INFN) – Pisa
for the E989 (Muon $g - 2$) experiment at Fermilab

Abstract

The Fermilab Muon $g-2$ experiment measures the muon anomalous magnetic moment with high precision. Together with recent improvements on the theory front, the first results of the experiment confirm the long-standing discrepancy between the experimental measurements and the Standard Model predictions. The observed value of $a_\mu(\text{FNAL}) = 116\,592\,040(54) \times 10^{-11}$ (0.46 ppm), combined with the previous experimental measurement, results in a discrepancy of $(251 \pm 59) \times 10^{-11}$ with the theoretical prediction, corresponding to 4.2σ . This note presents the first results, the current status and the future prospects of the Muon $g-2$ experiment at Fermilab.

1 The g -factor and the muon magnetic anomaly

The g factor relates the magnetic moment of a particle to its angular momentum and charge-to-mass ratio.. For a charged lepton, g relates its magnetic moment

to its spin:

$$\vec{\mu} = -g \frac{e}{2m} \vec{S}. \quad (1)$$

Experimentally, it was found that $g = 2$, but only in 1928 this value was derived by Dirac starting from his famous formula. A spectacular success of the Quantum Theory.

The *magnetic anomaly* is the fractional difference of g from the value 2: $a = \frac{g-2}{2}$. Experimental evidence that $g \neq 2$ began mounting by 1947 through measurements such as the Lamb shift ¹⁾ and preliminary measurements of g factors in gallium by Kusch and Foley ²⁾ indicating an incomplete understanding of electrodynamics at atomic scales. These and other results drove Schwinger, Feynman, Tomonaga and others to combine electromagnetism with the quantum theory and thereby provide the foundation of Quantum Electrodynamics (QED). QED predicted the possibility for charged particles to emit and reabsorb particles from the quantum vacuum, thus modifying the effective coupling constants. This manifestly quantum effect enhances the g factor to a value larger than 2, resulting in a non-zero anomaly. The famous Schwinger term, published in 1948,

$$a = \frac{\alpha}{2\pi} \sim 0.00116, \quad (2)$$

provides the leading contribution to the muon and electron magnetic anomaly¹. Earlier that same year, Kusch and Foley ³⁾, studying the Zeeman effect in Gallium atoms, published their definitive measurement of a non-null value of the magnetic anomaly for the electron, finding

$$a^{exp} = 0.00119 \pm 0.00005. \quad (3)$$

Schwinger's prediction aligned in perfect agreement with the measurement and together they confirmed the existence of these *radiative corrections*. Another important success of QED.

Since then, many more diagrams contributing to a_μ have been evaluated. These include the theoretical *tour de force* of the QED contributions to 5 loops (12,672 diagrams) and the important weak interaction contributions. Many efforts have contributed to the evaluation of the QCD contributions in the

¹Higher order contributions depend on the mass and thus are different for the two leptons

report of the Muon $g-2$ Theory Initiative (see ⁴⁾ and references therein). Their consensus value of

$$a_{\mu}^{theo} = (116,591,810 \pm 43) \times 10^{-11}, \quad (4)$$

corresponding to 370 parts per billion (ppb), represents an impressive precision.

Similarly, the average of the published result ⁵⁾ by the E989 collaboration (*Fermilab $g-2$*) and the previous value published by the E821 collaboration ⁶⁾ at Brookhaven National Laboratory (BNL) yields the experimental value,

$$a_{\mu}^{exp} = 116,592,061 \pm 41) \times 10^{-11} \quad (5)$$

corresponding to 350 ppb. Theory and experiment show a difference of $(251 \pm 59) \times 10^{-11}$, which corresponds to 4.2 standard deviations. This difference can hide additional terms which are not accounted for by the current Standard Model of Particle Physics. As discussed in section 5, a recent lattice calculation of the QCD contribution to a_{μ} ⁷⁾ reduces this discrepancy. The value presents a 2.2σ tension with the current theoretical determination, as reported in ⁴⁾, therefore it is going through a close scrutiny within the theoretical community.

2 The muon $g-2$ strategy

The storage ring measurement of the muon anomaly relies on the spin precession and cyclotron motion of a charged particle orbiting in a uniform magnetic field. For a particle with momentum and spin vectors in a plane perpendicular to \vec{B} , a classical calculation of the difference of these frequencies yields

$$\omega_a = \omega_s - \omega_c = g \frac{e}{2m} B - \frac{e}{m} B = a_{\mu} \frac{e}{m} B \quad (6)$$

so that

$$a_{\mu} = \frac{\omega_a m}{B e} \quad (7)$$

A relativistic calculation modifies the expression for ω_s and ω_c , but the difference in Eq. 6 remains unaffected. Thus, for $a_{\mu} = 0$, that is $g = 2$, the two vectors rotate with the same frequency, while for $a_{\mu} > 0$, the spin vector rotates faster than the momentum vector (see fig. 1). In the Fermilab $g-2$ setup, the spin advances by approximately 12° with respect to the momentum each orbit. An observable sensitive to this relative precession rate would therefore provide a direct measurement of a_{μ} . This approach can be realized using a beam of

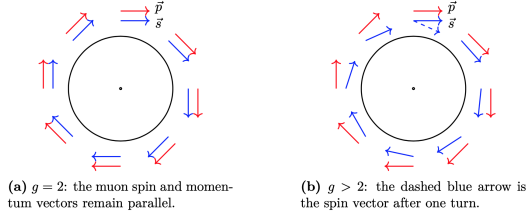


Figure 1: Spin and momentum vectors for a muon orbiting in a magnetic field (a) when $a_\mu = 0$, so the spin does not rotate relatively to the muon momentum, and (b) when $g > 2$.

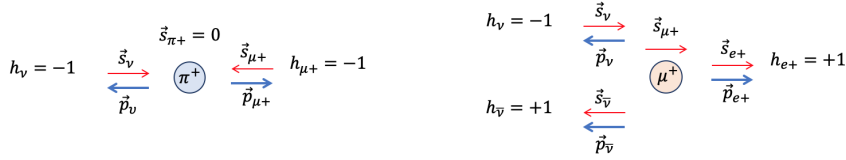


Figure 2: Schematic representation of pion (left) and muon (right) decays. Blue arrows (\vec{p}) and red arrows (\vec{s}) represent the momentum and spin vector, respectively, while h is the particle helicity.

polarized muons that evolve in a very stable and precisely measured magnetic field. Parity violation from the V-A structure of weak decays provides both a source of polarized muons and a way to statistically identify the muon spin direction (see fig. 2).

Storage of the muon beam requires vertical focusing from a quadrupole system, but the complicated spin precession in magnetic quadrupoles would render precision measurement impossible. The experiment therefore employs electrostatic quadrupoles. The electric field adds a $\vec{\beta} \times \vec{E}$ term, corresponding to a \vec{B} field in the muon rest frame, to the expression in Eq. 6. With an "out of plane" (vertical) momentum component also considered, the spin evolves as ⁸):

$$\frac{d(\hat{\beta} \cdot \vec{S})}{dt} = -\frac{q}{m} \vec{S}_T \cdot \left[a_\mu \hat{\beta} \times \vec{B} + \beta \left(a_\mu - \frac{1}{\gamma^2 - 1} \right) \frac{\vec{E}}{c} \right] \quad (8)$$

where $\vec{S}_T = \vec{S} - (\hat{\beta} \cdot \vec{S}) \hat{\beta}$ is the spin component perpendicular to the momentum direction $\hat{\beta}$. With $\vec{E} = 0$ and the spin and momentum restricted to a plane

perpendicular to \vec{B} , Eq. 8 reduces to the simple Eq. 6.

Farley, Picasso and collaborators ⁹⁾ realized in the 70s that the strategic choice of $\gamma = \sqrt{(a_\mu + 1)/a_\mu} \sim 29.3$ corresponding to a muon momentum $p_0 = 3.094 \text{ GeV}/c$, would minimize the electric field contribution to ω_a . At this *magic momentum*, the prefactor of the \vec{E} term vanishes. Because of the finite Storage Ring momentum acceptance of

$$\delta p/p = 0.15\%, \quad (9)$$

the cancellation occurs only at first order, but it allows treatment of the E-field contribution as a correction to the measured ω_a .

Utilizing comagnetometry Measurement of the magnitude of the field $|\vec{B}|$ by nuclear magnetic resonance (NMR) probes, as detailed in the next section, allows its expression in terms of the precession frequency of protons shielded in water $\tilde{\omega}'_p(T)$ as

$$\tilde{B} = \frac{\hbar \tilde{\omega}'_p(T)}{2\mu'_p(T)} = \frac{\hbar \tilde{\omega}'_p(T)}{2} \frac{\mu_e(H)}{\mu'_p(T)} \frac{\mu_e}{\mu_e(H)} \frac{1}{\mu_e}, \quad (10)$$

with the last three factors known precisely. The tilde in \tilde{B} and $\tilde{\omega}'_p(T)$ indicates the average of the field over the muon distribution weighted by the detected decays over time. Combining Eqs. 6, 10, and $\mu_e = \frac{g_e}{2} \frac{e}{m_e} \frac{\hbar}{2}$ yields

$$a_\mu = \frac{\omega_a}{\tilde{\omega}'_p(T)} \frac{\mu'_p(T)}{\mu_e(H)} \frac{\mu_e(H)}{\mu_e} \frac{m_\mu}{m_e} \frac{g_e}{2}. \quad (11)$$

The Muon g-2 experiment thus provides the ratio

$$\mathcal{R}'_\mu = \frac{\omega_a \cdot (1 + C)}{\tilde{\omega}'_p \cdot (1 + B)} \quad (12)$$

as its primary experimental output, where C and B represent small corrections to the measured frequencies, related to beam dynamics (C) and to the presence of transient fields (B) as discussed in the next two sections.

The external factors – the ratio of the magnetic moment of a proton shielded in a spherical water sample at a reference temperature of $T = 34.7^\circ\text{C}$ to the magnetic moment of an electron bound in hydrogen ($\mu'_p(T)/\mu_e(H)$), the ratio $\mu_e(H)/\mu_e$, the ratio of the muon to the electron mass and the g factor of the electron g_e – are known with a combined uncertainty of 25 ppb (see details in ⁵⁾).

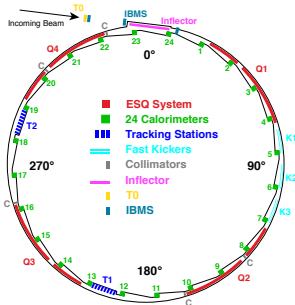


Figure 3: Layout of the Muon $g-2$ experiment at Fermilab

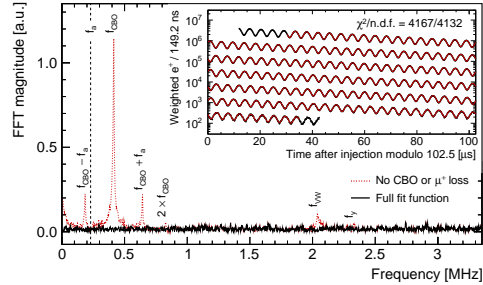


Figure 4: Fourier transform of the residuals from a fit following Eq. 13.

3 Measuring the anomalous precession frequency

The Fermilab complex delivers a sequence of 16 polarized muon bunches every 1.4 seconds to the Muon $g-2$ storage ring, where each bunch circulates for $700 \mu\text{sec}$ (a “fill”), about 11 muon lifetimes. A suite of 24 PbF_2 crystal calorimeters¹⁰ situated uniformly around the interior of the storage ring (see Fig. 3) detect the positrons from beam muon decay. Every calorimeter consists of a 9×6 array of crystals, each with a Silicon Photomultiplier (SiPM) photodetector.

The variation of the positron energy spectrum as the spins in a monochromatic polarized muon beam precess leads to a rate time-dependence of the precession signal described by

$$N(t) = N_0 e^{-t/\gamma\tau_\mu} (1 + A(E_{thr}) \cos(\omega_a t + \phi_{\text{ens}})), \quad (13)$$

where γ is the standard boost factor (about 29.3 for muons at the magic momentum), τ_μ is the muon lifetime, ω_a is the anomalous precession frequency, and $A(E_{thr})$ is the asymmetry amplitude of the sinusoidal variation, which depends on the energy threshold applied to the detected positrons. The phase ϕ_{ens} represents the ensemble average precession phase for the muons with detected daughter positrons. That average phase receives several contributions: the phase distribution within the injected beam, the longer drift distance for higher energy positrons vs lower energy positrons because of their different curvatures in the \vec{B} field, and the detector acceptance as a function of the

transverse decay position of beam muons. Any effect correlated with time after beam injection that changes the makeup of muons with detected daughter positrons can lead to a time dependent drift $\phi_{\text{ens}} \rightarrow \phi_{\text{ens}}(t) \sim \phi_0 + \phi_1 t$. The latter term would directly bias the value of ω_a extracted from the data. A rate-dependent drift of the gains, for example, would change the effective energy threshold for detected positrons and lead to such a drift. A laser system¹¹⁾ overlays well-characterized pulses on top of 10% of our muon fills that allow monitoring of and correction for such gain drifts. The pileup of positrons close in time and space in a calorimeter, whose probability varies as muons decay, can also lead to such a drift.

The collaboration utilizes two complementary techniques to reconstruct positron candidates from the waveforms, which bring different optimizations for resolving pileup. A third technique reconstructs the total measured energy versus time, which inherently eliminates bias from pileup. All told six independent analysis groups contributed 11 different measurements of ω_a (see¹²⁾).

Fitting with only the basic decay model of Eq. 13 results in set of residuals that show distinct frequencies in their fast Fourier transform (FFT) shown in Fig. 4. These frequencies correspond to well-understood horizontal and vertical oscillations of the stored beam particles about their nominal circular orbits, which then couple to the acceptance of the detector system to modulate the observed rates. Appropriate modification of the basic model to account for these effects results in excellent quality fits that match the data well (see Fig. 4), have residuals with a featureless FFT spectrum, and χ^2 values consistent with the number of degrees of freedom. Combination of the four data subsets in Run-1, which correspond to different operating conditions, provides an overall statistical precision of 434 parts per billion (ppb).

Beam dynamics corrections The measured ω_a value requires three significant corrections to allow its interpretation as the frequency of Eqs. 7 or 11. The largest correction comes from the spread of stored muon energies in the beam, which results in imperfect suppression of the electric field term in Eq. 8. A second correction results from vertical momentum distribution of the beam muons, which alters the horizontal precession rate. A straw tracking system in the vacuum reconstructs the beam motion by extrapolation of the decay positrons back to the storage region. Finally, in Run-1 two faulty high voltage

resistors controlling the quadrupoles caused the beam to change shape and to slowly drift downward during the time interval used to determine ω_a . When coupled with acceptance effects, these changes resulted in a drift in the ensemble average phase, thus biasing ω_a . This effect has been modelled and understood well.

These corrections add up to a total shift $C \simeq 500$ ppb, with an uncertainty of 93 ppb, on the measured ω_a value as reported in the summary table 2.

4 The Magnetic Field $\tilde{\omega}'_p$

The 1.45 T field is generated by a C -shaped superconducting dipole magnet represented in figure 5. The magnetic field in the 4.5 cm radius storage region, described in detail in ¹³⁾, is highly uniform in order to reduce the uncertainty on the determination of the field experienced by the muons. The uniformity is achieved by a long process of shimming that locally modifies the field direction. On top of this, an active feedback system modifies the coils current in order to keep the magnetic field stable, for example for hall temperature variations.

Tracking the magnetic field The magnetic field is measured by using pulsed proton Nuclear Magnetic Resonance (NMR) probes. A cylindrically shaped *trolley*, which can run on rails inside the storage region when muons are not present, hosts 17 NMR probes. Each probe is filled with petroleum jelly and the Larmor precession frequency of the protons within this jelly is measured. Each probe is carefully calibrated in terms of a precision calibration probe containing a pure water sample. The in-vacuum trolley runs in the Storage Ring and measures the magnetic field experienced by the muons in $\simeq 9000$ azimuthal locations.

The field's evolution between trolley runs is tracked by a set of 378 probes which are mounted in 72 azimuthal stations regularly spaced around the ring. The measurement from the trolley probes at a given azimuthal position θ , is determined by the solution of the source-free Laplace equation:

$$B = A_0 + \sum_{n=1} \left(\frac{r}{r_0} \right)^n [A_n \cos(n\theta) + B_n \sin(n\theta)] \quad (14)$$

expressed in polar coordinates (r, θ) with respect to the center of the muon ideal orbit, where $r_0 = 4.5$ cm is the radius of the storage region. The A_n

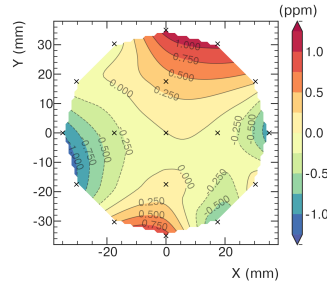
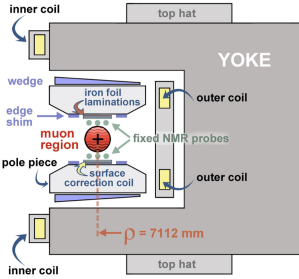


Figure 5: Cross section of the Muon $g-2$ magnet. It's a C -shaped superconducting magnet that provides a 1.45 T field. Figure 6: Relative variation of the magnetic field. The locations of the 17 trolley probes are indicated by (x).

and B_n parameters are the multipole strengths, also known as the normal and the skew multipole, respectively. The average over the azimuthal angle of the observed field, relative to the dominant dipole component, is shown in Fig. 6, together with the location of the measuring probes.

The fixed probes are used to track the field in between trolley runs.

Calibration procedure The trolley probes are calibrated by means of an external probe hosting a cylindrical water sample which is installed on a translation stage in the Storage Ring vacuum. The translation stage allows the calibration probe to be moved to each trolley probe position at a specific azimuthal location. The calibration and the trolley probes are then swapped several times to obtain a calibration constant for each of the 17 probes.

Muon weighting The magnetic field map has to be averaged over the muon transverse distribution at each azimuthal slice. The muon distribution is measured at $\sim 180^\circ$ and $\sim 270^\circ$ with respect to the injection point by two tracker stations. The in-vacuum straw tracker stations measure the trajectories of the decay positrons and trace them back to their radial tangency point within the storage ring. These profiles are propagated to other azimuthal locations using beam dynamics simulation.

Transient fields On top of the main static field, additional fields are induced by the fast switching storage ring elements that define the muon trajectory: the kicker and the electrostatic quadrupoles. An eddy current induced locally by the kicker system produces a transient magnetic field in the storage volume. A magnetometer, installed between the kicker plates, measures the Faraday rotation of a polarized laser light in a terbium-gallium-garnet (TGG) crystal. The second transient arises from charging the electrostatic quadrupoles, where the Lorentz forces induce mechanical vibrations in the plates that generate magnetic perturbations. Customized NMR probes measure these transient fields at several positions to determine the average field throughout the quadrupole volumes.

5 Result and perspectives

The recently published result ⁵⁾ comprises four data subsets collected between April and July 2018 with distinct beam storage conditions, and totals 10^{10} positrons in the analysis. Table 1 lists the values of the muon and proton precession angular frequencies, ω_a and $\tilde{\omega}'_p$, for the four subsets along with the combined value for the ratio \mathcal{R}'_μ . The systematic uncertainties correlate strongly among the four measurements, but the statistical term, which is uncorrelated among the subsets, dominates the total error. Combining \mathcal{R}'_μ with the external input in Eq. 7 yields a muon anomaly of

$$a_\mu(\text{FNAL}) = 116\,592\,040(54) \times 10^{-11} \quad (0.46 \text{ ppm}), \quad (15)$$

Table 2 summarizes the statistical and systematic contributions to the final result. The observed a_μ value is fully compatible with the previous BNL result, and combine to give an experimental average of

$$a_\mu(\text{Exp}) = 116\,592\,061(41) \times 10^{-11} \quad (0.35 \text{ ppm}). \quad (16)$$

The E989 experiment has already collected over 10 times the statistics used for this first measurement, and continues to collect additional data with the goal of reducing the statistical error to ~ 100 ppb. The systematic uncertainty currently sits at 157 ppb, a factor of 2 lower than in the previous BNL experiment. Work in progress should reduce this uncertainty down to the ~ 100 ppb level, which will allow E989 to reach its proposed total uncertainty goal

Run	$\omega_a/2\pi$ [Hz]	$\tilde{\omega}'_p/2\pi$ [Hz]	$\mathcal{R}'_\mu \times 1000$
1a	229081.06(28)	61791871.2(7.1)	3.7073009(45)
1b	229081.40(24)	61791937.8(7.9)	3.7073024(38)
1c	229081.26(19)	61791845.4(7.7)	3.7073057(31)
1d	229081.23(16)	61792003.4(6.6)	3.7072957(26)
			3.7073003(17)

Table 1: Run-1 group measurements of ω_a , $\tilde{\omega}'_p$, and their ratios \mathcal{R}'_μ multiplied by 1000.

Quantity	Correction (ppb)	Uncertainty (ppb)
ω_a^m (statistical)	–	434
ω_a^m (systematic)	–	56
C	500	93
$\langle \omega'_p(x, y, \phi) \times M(x, y, \phi) \rangle$	–	56
B	-44	99
Total external factors	–	25
Totals	544	462

Table 2: Summary table of uncertainties and corrections.

of a $\sigma^{tot} \sim 140$ ppb, a factor of 4 more precise than the previous experimental result.

Discussion The new result confirms the value of a_μ found previously by the BNL E821 experiment. The new world average shows a discrepancy of 4.2 standard deviations with the theoretical prediction recommended by the Muon $g-2$ Theory Initiative ⁴⁾. In April 2021, the Budapest-Marseille-Wuppertal (BMW) collaboration published a prediction of the QCD contribution to the muon anomaly based on lattice calculation ⁷⁾. This new prediction, which has a precision of 0.8%, more than a factor of two better with respect to the previous ones, hint at a reduced discrepancy with the observed anomaly. Recently, three other groups provided preliminary results on the same quantity measured in a reduced energy region, which accounts for $\sim 30\%$ of the total correction due to QCD loops ^{15, 16, 17)}, all in agreement with the BMW value. This new prediction, however, is in tension with the current one, which is based on a dispersion integral of experimental $e^+e^- \rightarrow$ hadrons cross section

measurements⁴⁾. As Ref. ¹⁴⁾ notes, an increase in the measured hadronic cross section below $\sqrt{s} \sim 1$ GeV could reconcile the two predictions, although the required increase would be an order of magnitude larger than the current experimental precision. Additional contributions above ~ 1 GeV are excluded at the 95% Confidence Level as they result in tension with the prediction of fundamental parameters from the global electroweak fits, like the Higgs and W masses. Because of this, the theory community continues to push both calculational approaches to test the compatibility of different predictions in some detail. The tension that is now consolidating between the two theoretical approaches for the estimation of a_μ^{HVP} is being referred as *the new $g-2$ puzzle* and remains unexplained as of today.

Should the current a_μ prediction based on the dispersion integral hold, and assuming the current experimental central value also holds, the expected improvement in precision would ascertain the current discrepancy of 251×10^{-11} with an uncertainty in the $40 - 50 \times 10^{-11}$ range, which would provide strong evidence of physics beyond the Standard Model (BSM physics). Such a discrepancy, of the same order of magnitude as the electroweak contribution to a_μ (154×10^{-11}), would indicate a TeV scale for the BSM physics. Even if the prediction and experimental determination should agree in the end, the improvement in a_μ will provide a powerful constraint on any model extending the Standard Model. The next few years will provide exciting opportunities as the Muon $g-2$ experiment and the theory community continue to push on this precision frontier.

Acknowledgments

The Muon $g-2$ Experiment was performed at the Fermi National Accelerator Laboratory, a U.S. Department of Energy, Office of Science, HEP User Facility. Fermilab is managed by Fermi Research Alliance, LLC (FRA), acting under Contract No. DE-AC02-07CH11359. Additional support for the experiment was provided by the Department of Energy offices of HEP and NP (USA), the National Science Foundation (USA), the Istituto Nazionale di Fisica Nucleare (Italy), the Science and Technology Facilities Council (UK), the Royal Society (UK), the European Union’s Horizon 2020 research and innovation programme under the Marie Skłodowska-Curie grant agreements No. 101006726, No. 734303, the National Natural Science Foundation of China

(Grant No. 11975153, 12075151), MSIP, NRF and IBS-R017-D1 (Republic of Korea), the German Research Foundation (DFG) through the Cluster of Excellence PRISMA+ (EXC 2118/1, Project ID 39083149).

References

1. W. E. Lamb, R. C. Retherford, *Phys. Rev.* **72** (1947) 241–243. doi:10.1103/PhysRev.72.241.
2. P. Kusch, H. M. Foley, *Phys. Rev.* **72** (1947) 1256–1257.
3. P. Kusch, H. M. Foley, *Phys. Rev.* **74** (1948) 250–263. doi:10.1103/PhysRev.74.250.
4. T. Aoyama, et al., *Phys. Rept.* **887** (2020) 1–166. arXiv:2006.04822.
5. B. Abi, et al., *Phys. Rev. Lett.* **126** (14) (2021) 141801. arXiv:2104.03281.
6. G. W. Bennett, et al., *Phys. Rev. D* **73** (2006) 072003.
7. S. Borsanyi, et al., *Nature* **593** (7857) (2021) 51–55. arXiv:2002.12347.
8. J. D. Jackson, 3rd Edition, Wiley, New York, NY, 1999.
9. J. Bailey, et al., *Nucl. Phys. B* **150** (1979) 1–75.
10. J. Kaspar, A. Fienberg, D. Hertzog, M. Huehn, P. Kammel, K. Khaw, D. Peterson, M. Smith, T. V. Wechel, A. Chapelain, L. Gibbons, D. Sweigart, C. Ferrari, A. Fioretti, C. Gabbanini, G. Venanzoni, M. Iacovacci, S. Mastroianni, K. Giovanetti, W. Gohn, T. Gorringer, D. Pocanic, Design and performance of sipm-based readout of PbF_2 crystals for high-rate, precision timing applications, *Journal of Instrumentation* **12** (01) (2017) P01009.
URL <http://stacks.iop.org/1748-0221/12/i=01/a=P01009>
11. A. Anastasi, et al., *JINST* **14** (2019) P11025. arXiv:1906.08432.
12. T. Albahri, et al., *Phys. Rev. D* **103** (2021) 072002.
13. T. Albahri, et al., *Phys. Rev. A* **103** (2021) 042208.

14. A. Keshavarzi, W. J. Marciano, M. Passera, A. Sirlin, Phys. Rev. D 102 (3) (2020) 033002. arXiv:2006.12666.
15. M. Cè et al. <https://arxiv.org/pdf/2206.06582.pdf>;
16. C. Aleaxndrou et al. <https://arxiv.org/pdf/2206.15084.pdf>;
17. C. Lehner (on behalf of RBC & UKQCD collaborations), “The hadronic vacuum polarization”, Talk at Fifth Plenary Workshop of the Muon $g-2$ Theory Initiative, <https://indico.ph.ed.ac.uk/event/112/contributions/1660/attachments/1000/1391/talk-nobackup.pdf>;